Pretreatment of TiO_2-supported Fe, Co and Ru Catalysts: An *In Situ* Powder Diffraction Study

Matthew Kyle Rayner

A thesis submitted to the Faculty of Science, University of the Witwatersrand, Johannesburg, in fulfillment of the requirements for the Degree of Doctor of Philosophy.

Johannesburg, 2011

Declaration

I declare that this thesis is my own, unaided work. It is being submitted for the Degree of Doctor of Philosophy in the University of the Witwatersrand, Johannesburg. It has not been submitted before for any degree or examination in any other University.

Signature of candidate

……day of ……..2011

Abstract

There has been increasing interest in *in situ* or *in operando* studies of heterogeneous catalysts in the past two decades. This drive has seen the invention and modification of analytical instruments that allow for the investigation of certain catalyst properties under realistic reaction conditions. Powder X-ray diffraction has been used to investigate the structural properties of heterogeneous catalysts for many years and has not escaped the *in situ* revolution. Reaction cells have been designed, tested and used, both on laboratory-based instruments and at neutron and synchrotron facilities. The experiments performed at these institutions have yielded information regarding the active solid-state phases of heterogeneous catalysts used in a multitude of different reactions, often with surprising results. Little attention has, however, been given to the use of the technique during catalyst preparation and its importance in such investigations is highlighted in this work in conjunction with whole-pattern Rietveld refinement techniques.

This study focused on the use of *in situ* PXRD as a means of monitoring the structural properties of TiO_2-supported metal catalysts during heat treatment, or calcination, and reduction, or activation. The TiO_2 supports included Degussa P25, Sigma-Aldrich anatase and nanosized anatase prepared using a sol gel method. The metals of interest were those shown to be active in the Fischer-Tropsch reaction, namely Fe, Co and Ru.

In situ heat treatment of the supports was used to measure thermal stability and to monitor the anatase to rutile phase transition in terms of concentration and particle size. We were able to show that the Sigma anatase was the most stable of the three supports, while Degussa P25 was the least stable. By calculating the rates of change of concentration between each collection, a reasonably accurate determination of the phase transition temperature in each support was possible. Our results confirmed the growth of anatase particles before the phase transition and the rapid agglomeration of rutile particles after the transition, both of which had been discussed elsewhere. During the course of the heat treatment of the supports, mathematical corrections were developed to eliminate the effects of sample penetration and diffraction from the sample holder that affect the quantitative phase analysis.

In situ heat treatment experiments were employed to determine the ideal calcination temperature of each catalyst in terms of maximum metal oxide concentration and particle size. By using an internal standard (spike), we were able to monitor the crystallization of the amorphous metal precursors to form supported metal oxides. The addition of the metal oxide phases was shown to affect the anatase to rutile phase transition in various ways, depending on the support and metal oxide species. The effect of excessive heat treatment was also investigated and provided insight into the formation of metal titanates. Using the rates of change of concentration between collections, we were able to determine if anatase and/or rutile took part in the formation of the metal titanates.

In situ activation experiments were conducted in order to determine the ideal reduction procedure for each catalyst. The reduction results confirmed that the concentration of H_2 in H_2/N_2 gas mixtures had an effect on the reduction profile of a Degussa-supported Fe catalyst. We were able to monitor the formation of amorphous phases, which form during the second stages of reduction of both hematite and cobalt(II) oxide. It is thought that these amorphous materials represent the interfacial region between the support and the metal particles. This is the first time that the quantification of this interface material has been performed and its presence has been used to explain the poor degrees of reducibility observed for these types of catalysts. We found that the Ru and Co particles were less sensitive to elevated reduction temperatures than the Fe particles, which demonstrated a massive degree of sintering even at low temperatures.

Acknowledgements

This work would not have been possible without the following people and institutions:

- My supervisors, Professors Neil Coville and David Billing, for giving me the opportunity to realize my potential
- My good friend, Doctor Manuel Fernandes, for meaningful input and conversations
- Professor Michael Witcomb and Paul Franklyn for their assistance with electron microscopy
- Professor Michael Claeys for acting as our research group leader
- My mother, Lesley Moodie, and stepfather, Raymond Moodie, for providing the opportunity to attend university and complete my postgraduate degrees
- Samantha Birtles for all her support over the past five years
- My good friend, Roy Forbes, for his continued support and meaningful conversations
- The University of the Witwatersrand
- The School of Chemistry at the University of the Witwatersrand for providing the research facilities
- The CATOMMAT and Structural Chemistry research groups within the School of Chemistry
- The School of Chemical Engineering at the University of Cape Town for the use of their *in situ* PXRD equipment and their hospitality
- The DST-NRF Centre of Excellence in Catalysis (c*change) for funding

Presentations and Publications

Poster Presentations

1. CATSA Conference 2008, Parys, South Africa

Fe / TiO2 Fischer-Tropsch Catalysts: X-ray Diffraction Studies Under Non-ambient Temperatures and Pressures

2. CATSA Conference 2009, Worcester, South Africa

Quantitative Rietveld Analysis of Fe/TiO_2 Catalysts During *In Situ* X-ray Diffraction Experiments

3. CATSA Conference 2009, Bloemfontein, South Africa

Gas-dependent reduction profiles of Degussa P25-supported Fe Catalysts

Oral Presentations

1. University of the Witwatersrand Fischer-Tropsch Symposium 2010, Johannesburg, South Africa

In situ PXRD for the Activation of Titania-supported Iron Catalysts

2. University of the Witwatersrand Postgraduate Symposium 2010, Johannesburg, South Africa

Catalyst Pretreatment: An *In Situ* PXRD Study

3. University of Kwazulu-Natal 2009, Westville, South Africa

The Anton Paar XRK900 – *In situ* X-ray Diffraction Made Possible at the Laboratory Scale

Publications Resulting From This Work

1. M. K. Rayner, N. J. Coville and D. G. Billing, "Identifying the reactive polymorph in solid-state reactions" (in preparation).
2. M. K. Rayner, N. J. Coville and D. G. Billing, "*In situ* heat treatment of titania-supported catalysts to identify optimum calcination temperatures" (in preparation).
3. M. K. Rayner, N. J. Coville and D. G. Billing, "*In situ* activation of titania-supported catalysts and the quantification of amorphous interfacial materials" (in preparation).
4. M. K. Rayner, N. J. Coville and D. G. Billing, "Changes in reduction pathways induced by the H_2 concentration in H_2/N_2 gas mixtures" (in preparation).

Publications Resulting From Side Projects

1. H. Xiong, M. Moyo, M. K. Rayner, L. L. Jewell, D. G. Billing and N. J. Coville, "Autoreduction and Catalytic Performance of a Cobalt Fischer-Tropsch Synthesis Catalyst Supported on Nitrogen-Doped Carbon Spheres," *CHEMCATCHEM*, **2**, 514 (2010).
2. M. K. Rayner, D. G. Billing, "Poly[1,4-bis(ammoniomethyl)cyclohexane [di-mu-bromido-dibromidoplumbate(II)]]," *Acta Crystallographica Section E*, **66**, M658 (2010).
3. M. K. Rayner, D. G. Billing, "Poly[1,4-bis(ammoniomethyl)cyclohexane [di-mu-chlorido-dichloridoplumbate(II)]]," *Acta Crystallographica Section E*, **66**, M659 (2010).
4. M. K. Rayner, D. G. Billing, "Poly[1,4-bis(ammoniomethyl)cyclohexane [di-mu-iodido-diiodidoplumbate(II)]]," *Acta Crystallographica Section E*, **66**, M660 (2010).

Contents

Table of Contents

List of Tables

Chapter 1

Chapter 2

Chapter 3

List of Figures

Chapter 1

Chapter 2

Chapter 3

Abbreviations and Acronyms

Barrels (of oil)	bbl
Barrels of oil equivalent	BOE
Body-centered cubic	BCC
Debye function analysis	DFA
evolved gas analysis	EGA
extended X-ray absorption fine structure	EXAFS
Face-centered cubic	FCC
Fischer-Tropsch	FT
Fixed divergence slit	FDS
Full width at half maximum	FWHM
Gas chromatography-mass spectrometry	GCMS
Goodness of fit	GoF
High resolution transmission electron microscopy	HRTEM
High temperature Fischer-Tropsch	HTFT
isobutyric acid	IBA
Low temperature Fischer-Tropsch	LTFT
methacrylic acid	MAA
Nanosized anatase	NSA
National Institute for Standards and Technology	NIST
Not attributed to the transition	NAT
Not consumed by reduction	NCBR
Parallel plate avalanche counter	PPAC
Position sensitive detector	PSD
Powder X-ray diffraction	PXRD
Pressure acid leaching	PAL
Quantitative phase analysis	QPA
Standard reference material	SRM
Suid Afrikaanse Steenkool en Olie (Afrikaans for South African Coal and Oil)	SASOL
Synthesis gas	Syngas
Temperature-programmed reduction	TPR
Thermogravimetric analysis	TGA
Total pattern analysis solution	TOPAS
Transmission electron microscopy	TEM
University of Cape Town	UCT
University of the Western Cape	UWC
University of the Witwatersrand	WITS
Water gas shift	WGS
X-ray diffraction	XRD

CHAPTER 1: INTRODUCTION

1.1. A BRIEF HISTORY OF THE FISCHER-TROPSCH PROCESS

Franz Fischer and Hans Tropsch, working at the Kaiser Wilhelm Institute for Chemistry in Germany, published data relating to catalytic reactions that convert mixtures of carbon monoxide (CO) and hydrogen (H_2), now referred to as synthesis gas (or syngas), into liquid hydrocarbons.[1] These liquid hydrocarbons can be used for liquid fuels. Prior to World War II, Germany was unable to secure reliable supplies of crude oil for liquid fuel production. Germany did however have large, accessible coal deposits, which would prove invaluable in the production of syngas via a process known as coal gasification. The lack of crude oil, abundance of coal and the development of coal gasification plants made the Fischer-Tropsch (FT) process highly attractive as an alternate source of liquid fuels.[2] As a result, plants were built to produce liquid hydrocarbons for fuel use based on the discoveries of Fischer and Tropsch in the 1920's, which reduced the demand for crude oil substantially.

The FT process also found favor in Apartheid South Africa in 1973, when an oil embargo significantly decreased supplies of crude oil to the country.[3] South Africa, with its large coal deposits, was able to produce a sizable amount of syngas via the gasification of coal, which could then be converted to liquid fuels. SASOL, which is now an international company, commissioned the first FT plant in 1955, which produced mainly waxes (which can be cracked to form gasoline and diesel) and gasoline. A second plant was commissioned in 1980, which utilized new reactor technology to produce mainly gasoline and diesel fuels.[4] SASOL is still one of the world leaders in the production of synthetic fuels from syngas and is set to maintain that status for many years to come.

It seems the FT process is a product of both human ingenuity and political circumstances and to this day the popularity of the process has fluctuated in parallel with the price of crude oil. Recent volatility in crude oil prices, with a high of 150 US$/barrel in July of 2008 and a low of 30 US$/barrel in December 2008, raised concerns about the production of liquid fuels all over the world.[5] Steynberg and Dry (2004) determined that the FT process is commercially viable when the price of crude oil exceeds US$20/barrel, since at this price FT products compete with liquid fuels produced from crude oil.[6] Figure 1.1 is a graph of the year-average oil price for the past 64 years and shows that in 1998 the average price of oil was $15.93 (inflation adjusted), marking the first and last time the price dipped below the 20 US$/barrel mark in 48 years.[7] The high price of oil and the relatively low cost of production of synthetic fuel will probably secure the future of the FT process for many years to come.

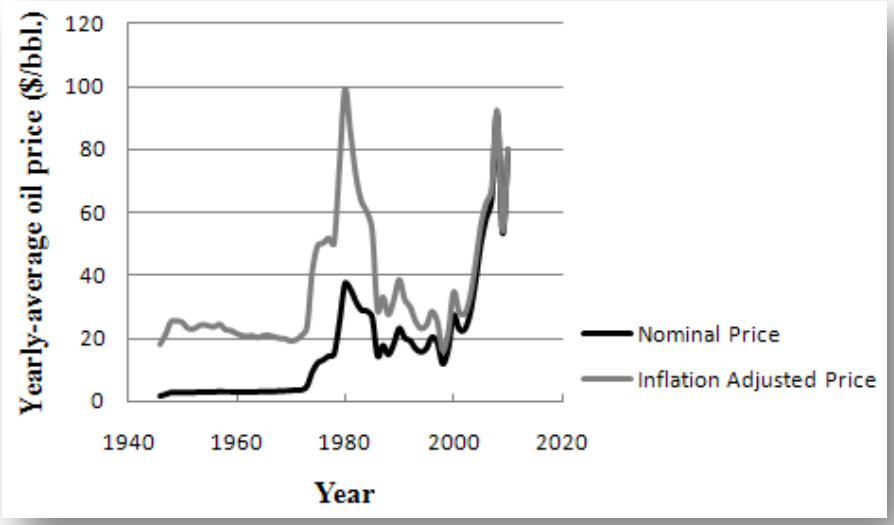

Figure 1.1. Yearly-average oil price 1946-2010[7]

Current estimates of the worlds accessible oil reserves are in the range of 1.4 x 10^{12} barrels (bbl),[8] which equates to 40 – 50 years supply at current consumption rates.[9] Estimates also predict a further 1.9 x 10^{12} bbl still to be found, although this figure may be a severe overestimate.[8] Focus is, therefore, being directed towards alternate methods of liquid fuel production. As a consequence the FT process, being fairly mature, well understood and relatively cheap, is standing out as a clear favorite to provide for the worlds ever increasing demand for liquid fuels. A great advantage of the FT process is the fact that almost any carbon source can be used to generate syngas and thus hydrocarbons. These sources include; natural gas, with an estimated accessible reserve of 1.1 x 10^{12} BOE (barrels of oil equivalent),[10] oil sands (0.3 x 10^{12}),[8] oil shales (1.9 x 10^{12} BOE),[8] heavy oil (0.5 x 10^{12} BOE),[8] coal (4.2 x 10^{12} BOE)[11] and biomass (variable).

The popularity and availability of the above mentioned carbon sources for the FT process has recently seen the commissioning of modern FT plants in many different locations all over the world. A methane-based plant, aimed at producing waxes, high quality diesel fuels and kerosene, is already operational in Malaysia with, a capacity of 3.7 x 10^{6} bbl per year.[12-13] A joint venture between SASOL and Chevron has seen the development of a similar plant, which is currently under construction in Nigeria. Exxon and SASOL, in a joint venture, have recently started production in a new plant in Qatar.[13] Currently heavy oil, coal and methane are used as carbon sources in FT processes. Methane-based FT processes are favored due to a considerably lower (50%) capital investment over coal-based FT processes. Other factors have an influence on the choice of process, such as availability and security of the carbon source.[14]

1.2. CHEMISTRY OF THE FT PROCESS

1.2.1. Syngas Production

Gasification of coal is usually completed either endothermically using steam at high temperature and high pressure, described by equation **(1)**, or exothermically (industrially favored) via the addition of oxygen, outlined in equation **(2)**. The latter process can be modified to produce the required ratio of H_2 to CO and the ratio can be further controlled by the water-gas shift reaction in equation **(3)**. 50% of the carbon in coal is completely oxidized to carbon dioxide (CO_2), making the process relatively inefficient.[13] However, CO_2 and methane are converted to syngas in downstream reactors and recycled. These extra reactors increase the cost of building a coal-based FT plant.

Steam-reforming of methane is achieved via the use of high temperature, high pressure steam, as described by equation **(4),** in the presence of a nickel (Ni) catalyst. This process is relatively efficient (only producing 20% CO_2) and often results in a syngas mixture that needs to be enriched with CO.[4]

$$C(s) + H_2O(g) \rightarrow CO + H_2 \quad \textbf{(1)}$$

$$5C(s) + O_2(g) + 3H_2O(g) \rightarrow 3CO(g) + CO_2(g) + H_2(g) + CH_4(g) \quad \textbf{(2)}$$

$$CO + H_2O \rightarrow CO_2 + H_2O \quad \textbf{(3)}$$

$$CH_4(g) + H_2O(g) \rightarrow CO(g) + 3H_2(g) \quad \textbf{(4)}$$

1.2.2. FT Reaction and Gas Ratio Effects

Different gas ratios are used to produce hydrocarbons of different molecular weights, as is seen by the range of FT reactions shown in equations **(5)** to **(10)**.[4] When a gas with a high H_2/CO ratio is used, lighter hydrocarbons are produced and vice versa. Reactors and catalysts are optimized to produce hydrocarbons of a certain molecular weight, however, the polymeric nature of this reaction results in a distribution of products. The unwanted products are often cracked, if the carbon chains are longer than desired, to form the desired products, while the light fractions are recycled back to the steam reformers to be converted to syngas. The simplified FT reaction in equation **(11)** shows a H_2/CO ratio of 2.15, which is the consumption ratio of cobalt FT catalysts. Using a reactant gas mixture with a ratio equal to that of the consumption ratio ensures high CO conversions.[14]

$$nCO + 2nH_2 \rightarrow (CH_2)_n + nH_2O \quad \textbf{(5)}$$

$$nCO + (2n+1)H_2 \rightarrow C_nH_{2n+2} + nH_2O \quad \textbf{(6)}$$

$$nCO + 2nH_2 \rightarrow C_nH_{2n+1}OH + (n-1)H_2O \quad \textbf{(7)}$$

$$2nCO + nH_2 \rightarrow (CH_2)_n + nCO_2 \quad \textbf{(8)}$$

$$2nCO + (n+1)H_2 \rightarrow C_nH_{2n+2} + nCO_2 \quad \textbf{(9)}$$

$$(2n-1)CO + (n-1)H_2 \rightarrow C_nH_{2n+1}OH + (n-1)CO_2 \quad \textbf{(10)}$$

$$2.15H_2 + CO \rightarrow \text{hydrocarbons} + H_2O \quad \textbf{(11)}$$

1.2.3. Fischer-Tropsch Catalysts

Research into FT catalysts has been ongoing for decades. Iron (Fe), ruthenium (Ru), cobalt (Co) and nickel (Ni) show the highest FT activity amongst the transition metals. Ru is not commercially used due to its price (180.00 US$/ounce or 45207.11 ZAR/kg).[15] Ni (12.83 US$/lb or 41.44 ZAR/kg)[16] is highly active but has two intrinsic problems. It is steadily lost from the FT reactors due to nickel carbonyl [$Ni(CO)_4$] formation at elevated temperatures and pressures. It is also one of the best known hydrogenation catalysts, which means it tends to form low molecular weight hydrocarbons and large amounts of methane.[14] Fe (350.00 US$/tonne or 2.49 ZAR/kg)[17] provides, by far, the best value of all four metals, since it has good FT activity and is not expensive. The unfortunate property that Fe has, in regards to the FT processes, is that it is also a relatively good catalyst for the water gas shift (WGS) reaction, given in equation **(3)**, which leads to decreased H_2/CO consumption ratios.[13] Fe catalysts in low temperature Fischer-Tropsch (LTFT) processes, operating at 230 °C, have a H_2/CO consumption ratio of 1.7. Fe catalysts in high temperature Fischer-Tropsch (HTFT) processes, operating at 340 °C, force the water-gas shift reaction to equilibrium and make it possible to convert CO_2 to FT products via the reverse of equation **(3)**, which enhances the efficiency of the process.[14]

Commercial iron based FT catalysts are prepared via the addition of a hot solution of Fe and copper (Cu) nitrates to a hot solution of sodium carbonate (Na_2CO_3). The precipitate formed is washed with water to eliminate sodium. A solution of potassium silicate (K_2SiO_3) is added to the resulting mixture followed by nitric acid to remove any excess potassium. The resulting slurry is partially dried and extruded to form the catalyst pellets. The product is then further dried to a water-weight percentage of less than 10 %. The Cu aids in the reduction of the Fe_2O_3 by lowering the reduction temperature and minimizing metal crystallite growth, a process which is also aided by the presence of silica (SiO_2). Potassium (K) acts as a promoter, lowering the dissociation energy of CO during the FT reaction, leading to higher molecular weight hydrocarbons.[6,18,19]

Co (39595.00 US$/tonne or 281.92 ZAR/kg)[20] catalysts are industrially prepared by simple dispersion on a high area support, followed by calcination and reduction to leave the active Co(0) phase present as nanoparticles. Co has a higher consumption ratio than Fe, as explained previously, but this increase in activity comes at a price since Co is approximately 113 times more expensive than Fe at the current prices. However, newer plants are preferentially using these catalysts in slurry-phase LTFT reactors, since they have a lower affinity for the water-gas shift reaction than the Fe catalysts and therefore provide higher first-pass conversions and thus increased efficiency.

1.2.4. Reactor Designs

The highly exothermic FT process has been performed in four types of reactors (Fig. 1.2), all of which have to remove the heat generated during the reaction in order to prevent catalyst deactivation and light hydrocarbon production.[21] The first is referred to as a multi-tubular fixed-bed reactor (Fig. 1.2**A**) and is an assembly of long, narrow, catalyst-containing tubes surrounded by a water-filled cooling jacket. The water temperature is controlled by maintaining the pressure of the steam in the jacket, while syngas is forced through the tubes under pressure.[21] The second type is the slurry bubble column reactor (Fig. 1.2**B**), which utilizes a solid catalyst in a liquid medium or supercritical fluid, making up the slurry.[22-23] The synthesis gas is bubbled through the slurry while it is vigorously stirred. The gaseous products are collected by convection, while the waxes or heavy fractions are separated from the slurry. The slurry-type reactors display better thermal conduction, making it easier to control the temperature of the reaction. The fixed-fluidized-bed reactors (Fig. 1.2**C**) are similar to the slurry reactors with the exception of the liquid medium. The solid catalytic material is supported by a porous plate, referred to as a distributor. The syngas is forced through the distributor and the solid catalyst at high velocity, giving the catalytic particles fluid-like properties. This reactor benefits from decreased diffusion limitations when compared to slurry-type reactors, since there is no liquid phase. The final reactor is the circulating fluidized bed reactor. Syngas is forced through the catalyst hopper (left side of figure 1.2**D**) at high velocity, a process referred to as "dense phase mode." When the gas reaches the bottom of the hopper, it is allowed to fluidize the catalyst particles (with the help of incoming syngas), which are carried to the heated region of the reactor (right side of figure 1.2**D**) where the FT reaction occurs. This second process is referred to as "lean phase mode." The gas can be circulated constantly in order to ensure good conversions and selectivity.

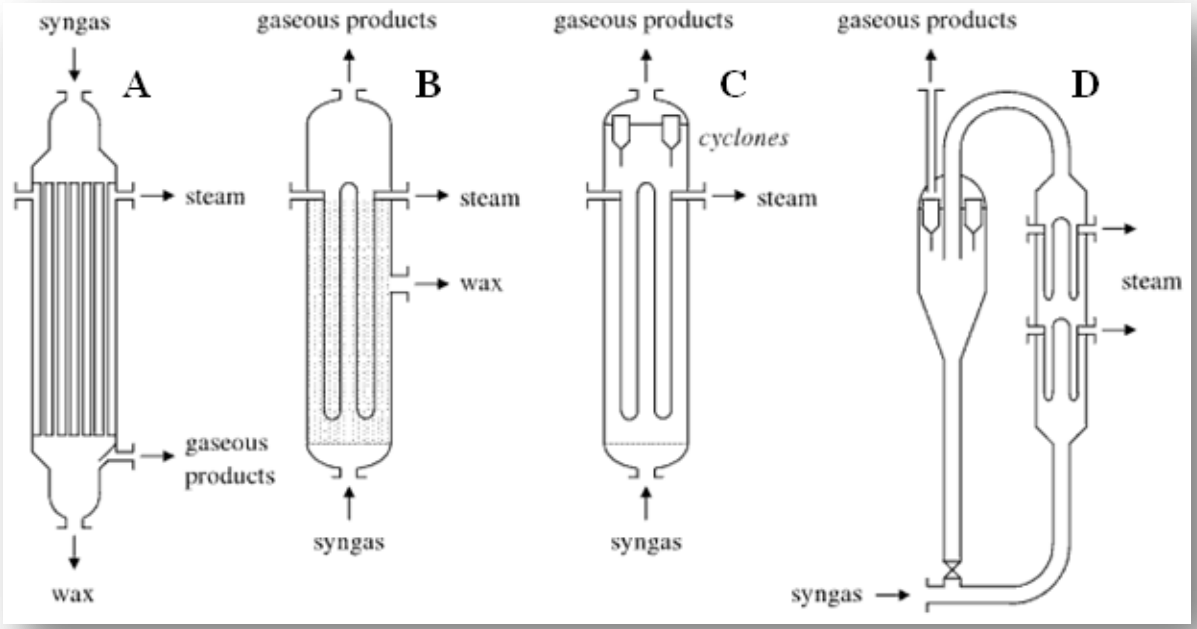

*Figure 1.2. Reactors used in FT synthesis: **A** – multi-tubular fixed bed reactor, **B** – slurry bubble column reactor, **C** – circulating fluidized bed reactor and **D** – fixed fluidized bed reactoR*[21]

Fe-based HTFT synthesis, for the production of gasoline and diesel, is almost exclusively performed in fixed fluidized bed reactors, due to their increased ability to dissipate heat, lower construction and operating costs and their higher capacities.[14] They also produce a very similar product distribution to multi-tubular fixed bed reactors.[21] The Fe-based LTFT product distribution, which is geared toward wax production, is affected by reactor type. Satterfield *et al*.[22] and Jager and Espinoza[23] showed that the alkene to alkane ratio produced by fixed-bed reactors is significantly lower than that produced by slurry bubble column reactors. The slurry bubble column reactor required 30 % less catalytic material to produce the equivalent amount of FT products, when compared to the fixed bed reactor. Fixed bed reactors were found to be up to two times less sensitive to catalyst poisoning by sulfur. As with most processes there are pros and cons for using different reactor types.

1.2.5. Fischer-Tropsch Selectivity

The FT process does not result in a single product but rather a range of products of varying molecular weights.[24-25] Highly branched alkanes are ideal for high octane gasoline (referred to as petrol in South Africa), while linear alkanes are best suited for high quality, or high cetane, diesel.[14] Octane numbers of gasoline or petrol mixtures are calculated using the degree of engine knock in test engines relative to mixtures of iso-octane (2,2,4-trimethylpentane), which has an octane rating of 100 (no knock), and heptane, which has an octane rating of 0. If a fuel mixture, synthetic or otherwise, generates the same knock as a 95 : 5 mixture of the previously mentioned hydrocarbons, the fuel is given an octane rating of 95. Engine knock is generated when pockets of fuel/air mixtures resist uniform combustion upon ignition by the spark plug. These pockets are ignited out of sequence, causing a shock-wave and an increase in cylinder pressure. The effects can range from negligible to entirely destructive. Cetane numbers represent a measure of the ignition delay of diesel fuels. Higher numbers represent shorter ignition delays and better efficiency. Cetane numbers of 40-55 are most common, since values above 55 show no benefits for emission or efficiency. Cetane numbers are derived by comparison to mixtures of cetane, rated at 100, and 1-methylnaphthalene, rated at 0.[26]

The FT process conditions, such as partial pressures of the reactant gases, temperature, catalyst type and presence of promoters, help to narrow the range of products and thus allow for some product distribution control.[14] The exact reaction mechanism of the FT reaction is still unknown and is an area of controversy and debate in the field of catalysis. The one aspect that most scientists have come to agree upon is that the mechanism is similar to that of polymerization of individual monomers to form carbon chains of varying lengths. The disagreement relates to how the CO species are initially modified to form CH_2 (or other) monomers to allow for hydrocarbon chain growth.[27-30] Figure 1.3 indicates how the FT process always gives a mixture of products.[14] It shows that there are three competing reactions that can occur after an initial insertion. The first is the immediate desorption of an alkene (1), the second is an insertion of another monomer (2) and the third is hydrogenation to form an alkane (3). This interpretation does not

explain the presence of alcohols, ketones, acids and aldehydes that are present in product mixtures. These compounds are produced by insertion of other monomer species, a process which is little understood.

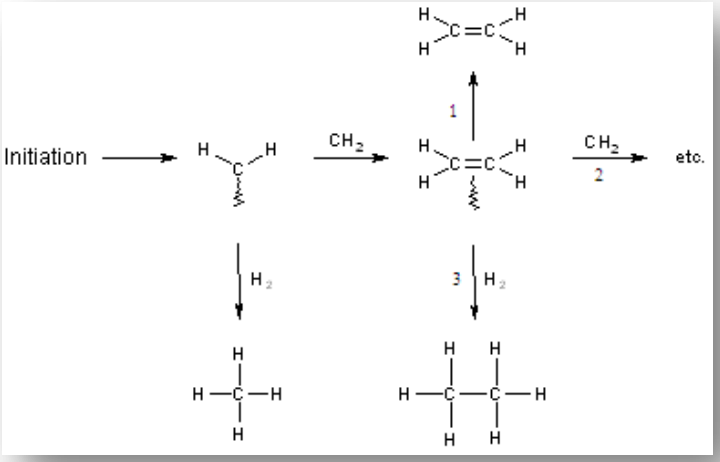

Figure 1.3. Polymerization-like growth process during FT reactions (modified from Dry)[14]

Increasing the temperature of any FT process reduces the probability of monomer insertion and leads to the preferential formation of methane and other light hydrocarbons.[14] As already mentioned the larger the H_2/CO ratio the lighter the hydrocarbon products. In LTFT reactors Co catalysts produce higher molecular weight hydrocarbons under higher total pressures, up to 20 bar,[31] while Fe catalysts are not significantly affected by increasing the overall pressure.[32] In HTFT processes where only Fe catalysts are used, increasing the overall pressure leads to a product distribution biased towards higher molecular weight hydrocarbons.[31]

1.2.5. Kinetic Aspects of the Fischer-Tropsch Process

The kinetic equations **(12)** and **(13)** represent those for Co and Fe FT catalysts respectively. It must be noted that the rate equation for Co contains no water (H_2O) term while that for Fe does.[33-34] This confirms the fact that Fe catalysts are considerably affected by water formation via the WGS reaction leading to a decrease in the rate of the overall reaction.

$$rate = kp_{H_2}p_{CO} \Big/ \left(1 + bp_{CO}\right)^2 \qquad \textbf{(12)}$$

$$rate = mp_{H_2}p_{CO} \Big/ \left(p_{CO} + ap_{H_2O}\right) \qquad \textbf{(13)}$$

Figure 1.4 presents the calculated conversion profiles of iron- and cobalt-based catalysts in a fixed-bed LTFT reactor.[14] The constants *k* and *m*, in equations **(12)** and **(13)**, were chosen to yield the same percent conversion for both Fe and Co catalysts at the surface of the catalyst bed. When pressures were increased, so were the gas flow rates so that the residence time was the same. The calculations indicate that an increase in the catalyst bed length, an increase in pressure and the presence of promoters lead to significantly improved conversions. They also suggest that cobalt catalysts outperform iron catalysts by a significant margin under optimized conditions.

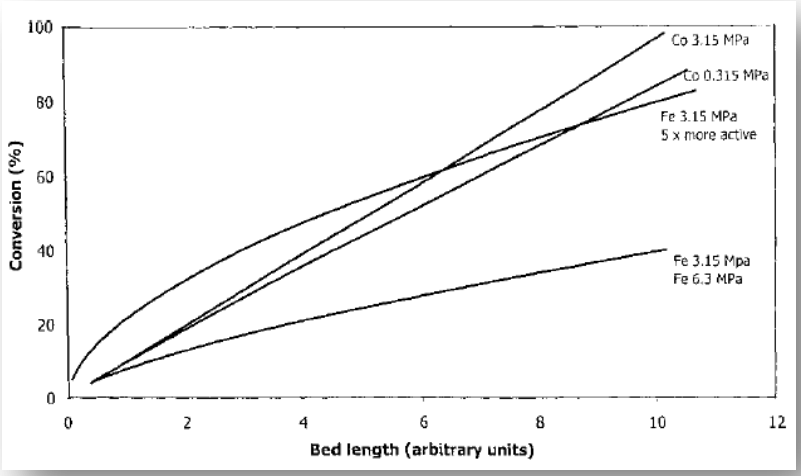

Figure 1.4. Calculated conversion profiles of iron- and cobalt-based catalysts used in LTFT reactors[14]

1.3. POWDER X-RAY DIFFRACTION (PXRD)

Many textbooks present the fundamentals of PXRD in exquisite detail.[35-38] However, such a theoretical evaluation is unnecessary for the purposes of this work. For this reason, only the very basics are discussed in line with explanations put forward by Dinnebier and Billinge.[39]

1.3.1. Sine Wave Theory

X-rays form part of the electromagnetic spectrum with wavelengths (λ) in the order of 0.01 x 10^{-9} m (0.1 Å) to 10 x 10^{-9} m (100 Å), approximately 2 orders of magnitude smaller than the wavelengths of visible light.[26] The wave follows a classical optical sine function that repeats every 2π radians (1 radian = 57.3°). If two waves, with identical wavelength, are not synchronized, they are said to have a "phase shift," which can be measured in terms of length (Δ) or on an angular scale (δφ), where $\delta\varphi = \frac{2\pi}{\lambda}\Delta$ (Fig. 1.5).[39] The intensity of a single detected sine wave (I) is proportional to the square of the amplitude (A). When two waves are present and are completely in phase, i.e. δφ = 0, the resulting intensity is proportional to the square of the sum of the amplitudes [equation **(14)**] and this is referred to as constructive interference. When two waves are completely out of phase, i.e. δφ = π, destructive interference occurs where equation **(15)** is satisfied. Equation **(16)** describes the intensity for two waves with 0 < δφ < π, while equation **(17)** describes the condition for more than two waves and their relative phase shifts.

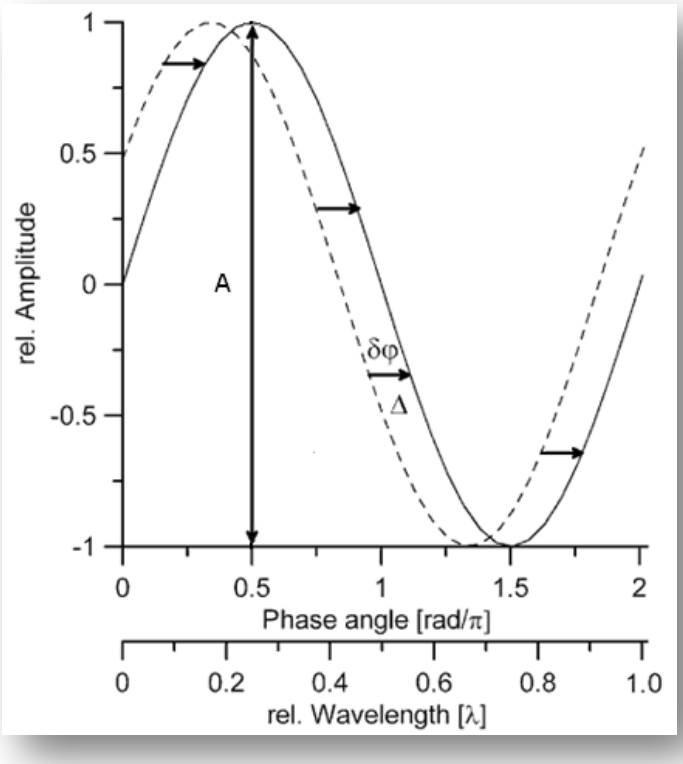

Figure 1.5. Illustration of the phase shift between two sine waves of equal amplitude (adapted from Dinnebier and Billinge)[39]

$$I = (A_1 + A_2)^2 \quad \textbf{(14)}$$

$$I = (A_1 - A_2)^2 \quad \textbf{(15)}$$

$$I = (A_1 + A_2 e^{i\delta\varphi})^2 \quad \textbf{(16)}$$

$$I = (\sum_j A_j \, e^{i\varphi_j})^2 \quad \textbf{(17)}$$

X-rays incident on a sample can be scattered elastically, referred to as coherent scattering, or inelastically, referred to as Compton scattering, by the electrons that surround atoms in all matter. Coherent scattering occurs when the wavelength of the scattered photons is equal to that of the incident photons. Compton scattering occurs when the wavelength of the scattered photons is longer (lower energy) than the incident photons. Photons scattered by electron clouds of different atoms at different positions arrive at the detector with a relative phase shift. The detected intensity (I) and the phase shift (φ_j) in equation **(17)** are dependent on the direction of the incident and diffracted photons and the position of the atoms (j) in the sample and since j is the only unknown parameter in **(17)** it becomes the subject of the equation, allowing for the determination of atomic positions. This only holds true if the incident wavelength has amplitude similar in size to the separation of the scattering atoms.

1.3.2. The Bragg Equation

The Bragg equation describes the reflection of X-rays by sets of lattice planes.[40] Crystallographic lattice planes are described using Miller indices, referred to as *hkl* values. They describe the planes in a crystalline or semi-crystalline material that arise due to the arrangement of atoms in a unit cell (the smallest repeating unit of a crystal). An (*hkl*) plane describes a plane through a unit cell with intersections at $\left(\frac{h}{a},\frac{k}{b},\frac{l}{c}\right)$, where a, b and c are the lattice parameters of the unit cell. Parallel planes within a crystal or powder have the same *hkl* value and are equally spaced by a distance, or d-spacing, d_{hkl}. Unlike low-energy visible light, X-rays penetrate the sample and are reflected by multiple parallel planes in the same direction, leading to superposition of the reflected waves. Figure 1.6 is a simplified representation of the diffraction process, used to derive the famous Bragg Equation.[39] It shows that photon *2* penetrates plane A and interacts with the electron cloud of an atom centered at *N* and in doing so has had to travel a distance of *PN* further than photon *1*. Upon reflection of the photon at point *N*, the photon had to travel an addition distance *NQ*, when compared to photon *1*. This extra distance can be described by equation **(18)**. Constructive interference of the reflected photons will occur only when *PN* + *NQ* is a multiple of *n* numbers of the wavelength (n = 0, ±1, ±2…), i.e. n = 0 indicates no phase shift, while n = +1 indicates one full phase shift in the positive direction resulting in a net zero phase shift. This condition is represented in equation **(19)**.

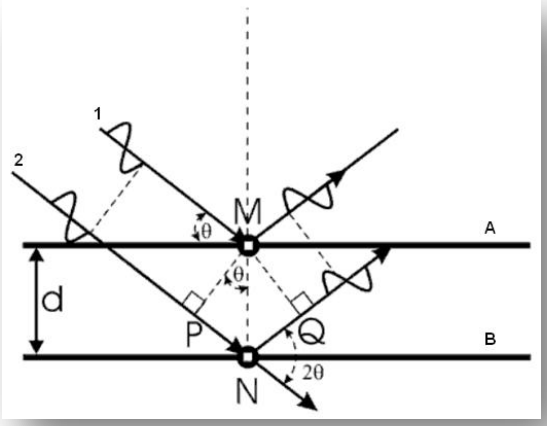

$$\Delta = PN + NQ \qquad \textbf{(18)}$$

$$\Delta = n\lambda \qquad \textbf{(19)}$$

Figure 1.6. Geometry of diffraction used for the simplified derivation of Bragg's law (adapted from Dinnebier and Billinge)[39]

Destructive interference occurs when Δ is not a multiple of the wavelength, i.e. from other planes, with total destructive interference occurring when $n = \pm\frac{1}{2}, \pm\frac{3}{2}\ldots$ This results in the detection of diffracted photons that satisfy equation **(19)**. Simple geometric calculations result in formulation of equation **(20)**, which is the Bragg equation for X-ray diffraction.

$$n\lambda = 2d\sin\theta \qquad \textbf{(20)}$$

This simplified derivation, although resulting in the correct answer, assumes that X-rays are reflected by planes within the sample when, in fact, they are scattered by the electrons associated with the atoms that make up the sample. Atoms in planes with the same Miller indices are usually offset relative to one another, unlike the idealized situation depicted in figure 1.6. Bloss described a more general derivation in order to account for this observation.[41] He was able to show that equation **(20)** still applies when an atom in one plane is shifted relative to its equivalent atom in another plane with the same Miller index, as is the case in figure 1.7.[39]

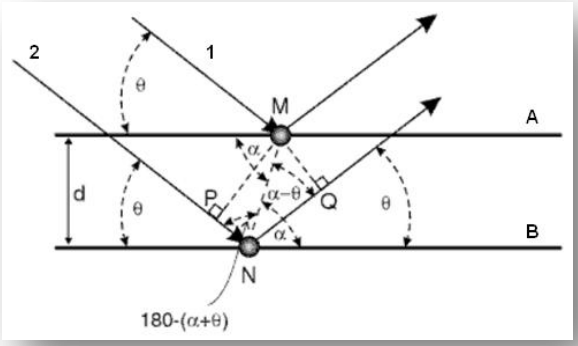

Figure 1.7. Geometry of diffraction in the more common case, where atoms do not occupy identical positions in consecutive planes (adapted from Dinnebier and Billinge)[39]

The phase shift for this case can be calculated in the following way:

$$\begin{aligned} n\lambda &= MNcos[180° - (\alpha + \theta)] + MNcos(\alpha - \theta) \\ &= MN[-\cos(\alpha + \theta) + cos(\alpha - \theta)] \end{aligned} \qquad \textbf{(21)}$$

Which reduces to:

$$n\lambda = MN(2\sin\alpha\sin\theta) \qquad \textbf{(22)}$$

Since:

$$\begin{aligned} \cos(\alpha + \theta) &= \cos\alpha\cos\theta - \sin\alpha\sin\theta \\ \cos(\alpha - \theta) &= \cos\alpha\cos\theta + \sin\alpha\sin\theta \end{aligned} \qquad \textbf{(23)}$$

However:

$$d = MN\sin\alpha \qquad \textbf{(24)}$$

Resulting in the original Bragg equation:

$$n\lambda = 2d\sin\theta \qquad \textbf{(20)}$$

1.3.3. The Reciprocal Lattice

Crystals contain atoms or molecules arranged in a particular repeating order. The crystal can be divided into three-dimensional repeating units referred to as unit cells, with lattice parameters *a*, *b*, and *c* (in units of length) and *α*, *β* and *γ* (the angles between *b* & *c*, *a* & *c* and *a* & *b* respectively in units of degrees). There are four types of unit cells, namely *primitive* (*P*), *body-centered* (*I*), *face-centered* (*F*) and *side-centered* (*C*), and seven possible lattice systems to form 14 Bravais lattices (Fig. 1.8).[42] Combination of the 14 Bravais lattices with all possible symmetry elements gives rise to 230 possible space groups.

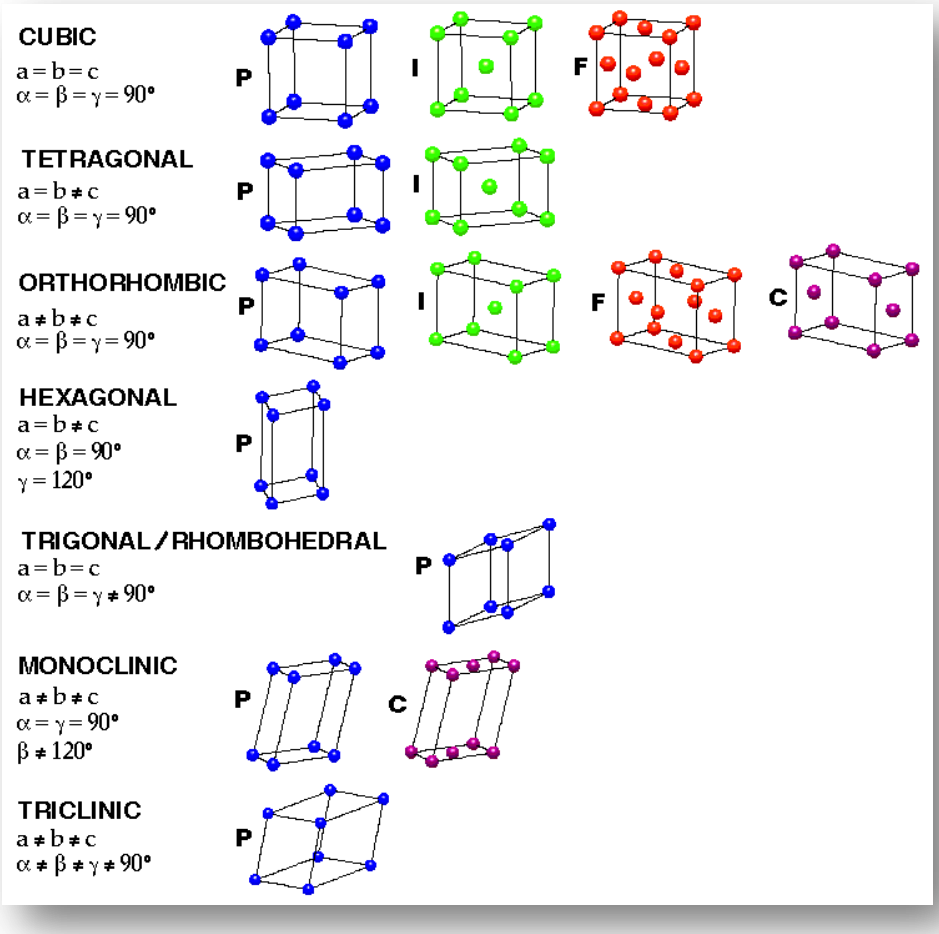

Figure 1.8. Lattice systems and Bravais lattices (adapted from Brown et al.)[42]

A lattice, with the same origin and parameters *a**, *b**, *c**, *α**, *β**, *γ** and *V** (volume), such that the vectors (in bold):

$$\mathbf{a}\cdot\mathbf{b}^* = \mathbf{a}\cdot\mathbf{c}^* = \mathbf{b}\cdot\mathbf{c}^* = \mathbf{a}^*\cdot\mathbf{b} = \mathbf{a}^*\cdot\mathbf{c} = \mathbf{b}^*\cdot\mathbf{c} = 0$$

and

$$\mathbf{a}\cdot\mathbf{a}^* = \mathbf{b}\cdot\mathbf{b}^* = \mathbf{c}\cdot\mathbf{c}^* = 1 \qquad \textbf{(25)}$$

represent the reciprocal lattice, which exists in reciprocal space.[39] Each point in reciprocal space is related to a vector defining a crystallographic plane or *hkl* index (Fig. 1.9).

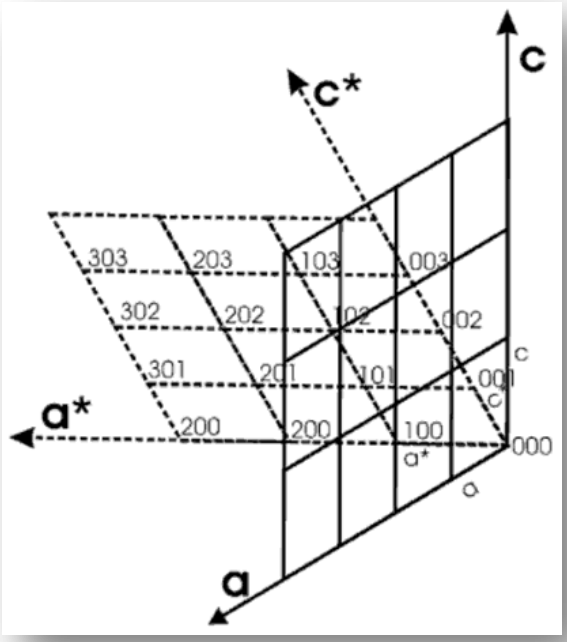

Figure 1.9. Two-dimensional representation of a monoclinic lattice and its corresponding two-dimensional reciprocal lattice[39]

A vector from the origin in reciprocal space to any reciprocal lattice point (*hkl*) is referred to as a reciprocal lattice vector ($\mathbf{h}_{hkl}$) and is defined by:

$$\mathbf{h}_{hkl} = h\mathbf{a}^* + k\mathbf{b}^* + l\mathbf{c}^*; \; h, k \text{ and } l \text{ are all integers.} \qquad \textbf{(26)}$$

The length of the reciprocal base vectors is calculated using:

$$\mathbf{a}^* = x(\mathbf{b} \times \mathbf{c}) \qquad \textbf{(27)}$$

where the scale factor *x* can be determined using equation **(25)**:

$$\mathbf{a}^*\mathbf{a} = x(\mathbf{b} \times \mathbf{ca}) = xV \Rightarrow x = \frac{1}{V} \qquad \textbf{(28)}$$

leading to:

$$\mathbf{a}^* = \frac{1}{V}(\mathbf{b} \times \mathbf{c}), \;\; \mathbf{b}^* = \frac{1}{V}(\mathbf{c} \times \mathbf{a}), \;\; \mathbf{c}^* = \frac{1}{V}(\mathbf{a} \times \mathbf{b}) \qquad \textbf{(29)}$$

and vice versa:

$$\mathbf{a} = \frac{1}{V^*}(\mathbf{b}^* \times \mathbf{c}^*), \;\; \mathbf{b} = \frac{1}{V^*}(\mathbf{c}^* \times \mathbf{a}^*), \;\; \mathbf{c} = \frac{1}{V^*}(\mathbf{a}^* \times \mathbf{b}^*) \qquad \textbf{(30)}$$

The relationship between the reciprocal and the real lattice parameters is:

$$a^* = \frac{bc\sin\theta}{V} \quad b^* = \frac{ac\sin\beta}{V} \quad c^* = \frac{ab\sin\gamma}{V}$$

$$\cos\alpha^* = \frac{\cos\beta\cos\gamma - \cos\alpha}{\sin\beta\sin\gamma} \quad \cos\beta^* = \frac{\cos\alpha\cos\gamma - \cos\beta}{\sin\alpha\sin\gamma} \quad \cos\gamma^* = \frac{\cos\alpha\cos\beta - \cos\gamma}{\sin\alpha\sin\beta}$$

$$V = abc\sqrt{1 + 2\cos\alpha\cos\beta\cos\gamma - \cos^2\alpha - \cos^2\beta - \cos^2\gamma} \qquad \textbf{(31)}$$

Rederiving Bragg's law in vector notation assumes elastic scattering (no change in λ) of the incident wave vectors (**s_0**) to give scattered vectors (**s**), as shown in figure 1.10.[39] The vectors point in the direction of the propagation of the wave and their length depends on λ.

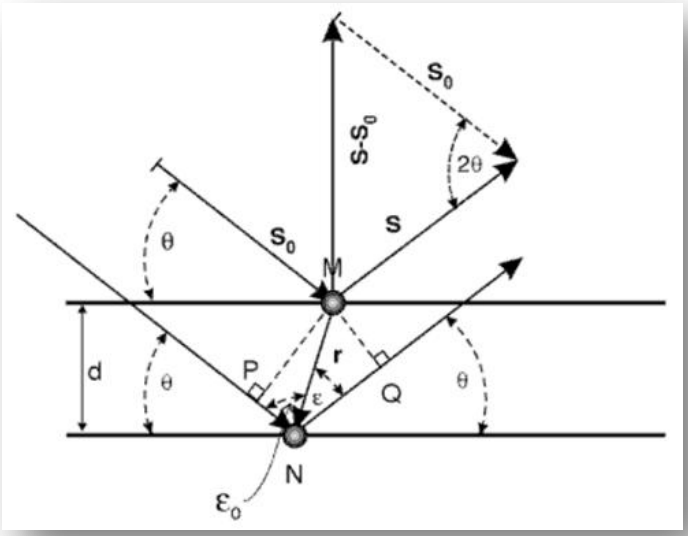

Figure 1.10. Wave and scattering vectors in elastic Bragg scattering[39]

The direction and length of the scattering vector is defined by:

$$\boldsymbol{h} = (\boldsymbol{s} - \boldsymbol{s}_0) \qquad \textbf{(32)} \qquad \frac{h}{s} = 2\sin\theta \qquad \textbf{(33)}$$

which is always perpendicular to the scattering plane for a specular reflection. Combination of equation **(33)** with the original Bragg equation **(20)** gives:

$$\frac{n\lambda}{d} = \frac{h}{s} \qquad \textbf{(34)}$$

By setting the magnitude of vector **s** to 1/λ, equation **(34)** simplifies to give the Bragg equation in terms of the length or magnitude of the scattering vector *h*:

$$h = \frac{n}{d} \qquad \textbf{(35)}$$

Equation **(35)** shows that diffraction occurs when the magnitude of the scattering vector **h** is an integral number of 1/*d* reciprocal lattice spacings. Vector **d*** is defined such that it is perpendicular to the lattice planes and is 1/λ in length giving:

$$\mathbf{h} = n\mathbf{d}^* \qquad \textbf{(36)}$$

This result indicates that diffraction can occur from the same planes at different 2θ scattering angles, giving the different orders (*n*) of diffraction. If *n* is incorporated into the indexing of lattice planes, such that:

$$nd^*_{hkl} = d^*_{nh,nk,nl} \qquad \textbf{(37)}$$

an alternative of Braggs equation is generated:

$$\mathbf{h} = \mathbf{d}^*_{hkl} \qquad \textbf{(38)}$$

$\boldsymbol{d}^*_{hkl}$ vectors are incident on real space lattice planes and to determine the reciprocal space basis vectors, **a***, **b*** and **c***, $\boldsymbol{d}_{hkl}$ has to be defined in terms of real space basis vectors **a**, **b** and **c** (Fig. 1.11):

$$\boldsymbol{OA} = \frac{1}{h}\mathbf{a} \;\;,\;\; \boldsymbol{OB} = \frac{1}{k}\mathbf{b} \;\;,\;\; \boldsymbol{OC} = \frac{1}{l}\mathbf{c} \qquad \textbf{(39)}$$

These integers are the Miller indices of the intersected plane.

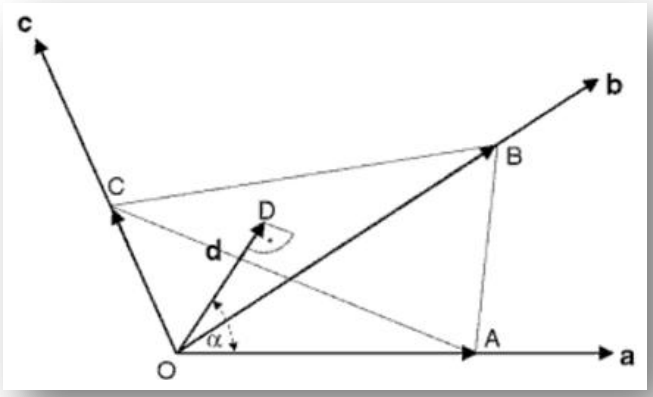

Figure 1.11. Lattice plane in terms of real space basis vectors[39]

The $\boldsymbol{d}_{hkl}$ vector originates on one plane and terminates on the following parallel plane so that $\mathbf{OA} \cdot \mathbf{d} = (OA)d\cos\alpha$. Geometrically $(OA)\cos\alpha = d$ therefore $\mathbf{OA} \cdot \mathbf{d} = d^2$, which, when substituted into **(39)**, gives:

$$\frac{1}{h}\mathbf{a} \cdot \mathbf{d} = d^2 \qquad \textbf{(40)}$$

And inevitably:

$$h = \mathbf{a} \cdot \frac{\mathbf{d}}{d^2} \quad , \quad k = \mathbf{b} \cdot \frac{\mathbf{d}}{d^2} \quad , \quad l = \mathbf{c} \cdot \frac{\mathbf{d}}{d^2} \qquad \textbf{(41)}$$

h, *k* and *l* are always divided by their largest common integer to yield the Miller index of a plane. The $\mathbf{d}^*_{hkl}$ vector, form equation **(38)**, is incident on the plane, parallel to **d**, but has a magnitude of 1/*d*. This provides a means to define $\mathbf{d}^*_{hkl}$ in terms of **d**:

$$\mathbf{d}^*_{hkl} = \frac{\mathbf{d}}{d^2} \qquad \textbf{(42)}$$

which gives:

$$\mathbf{d}^*_{hkl} = h\mathbf{a} + k\mathbf{b} + l\mathbf{c} \qquad \textbf{(43)}$$

since:

$$\begin{aligned} \mathbf{d}^*_{hkl} \cdot \mathbf{a}^* &= h\mathbf{a} \cdot \mathbf{a}^* + k\mathbf{b} \cdot \mathbf{a}^* + l\mathbf{c} \cdot \mathbf{a}^* = h \\ \mathbf{d}^*_{hkl} \cdot \mathbf{b}^* &= h\mathbf{a} \cdot \mathbf{b}^* + k\mathbf{b} \cdot \mathbf{b}^* + l\mathbf{c} \cdot \mathbf{b}^* = k \\ \mathbf{d}^*_{hkl} \cdot \mathbf{c}^* &= h\mathbf{a} \cdot \mathbf{c}^* + k\mathbf{b} \cdot \mathbf{c}^* + l\mathbf{c} \cdot \mathbf{c}^* = l \end{aligned} \qquad \textbf{(44)}$$

Comparison of equation **(43)** with equation **(26)** proves the identity of $\mathbf{d}^*_{hkl}$ and the reciprocal lattice vector $\mathbf{h}_{hkl}$ and the Bragg equation **(38)** can be restated as:

$$\mathbf{h} = \mathbf{h}_{hkl} \qquad \textbf{(45)}$$

Equation **(45)** merely states that diffraction occurs whenever the scattering vector **h** equals a reciprocal lattice vector $\mathbf{h}_{hkl}$.

1.3.4. Ewald Construction

Equation **(45)** indicates that diffraction occurs when the scattering vector, **h**, equals a reciprocal lattice vector, $\mathbf{h}_{hkl}$. The magnitude and direction of the scattering vector depends on the experimental geometry, while that of the reciprocal lattice vector is dependent on the lattice parameters and their orientation within the crystalline sample.[39] An Ewald's construction demonstrates the relationship between the wavelength of the radiation (λ), the diffraction angle of a given reflection and the reciprocal lattice of a crystalline system. The aim of an Ewald's construction is to determine which lattice planes, represented by points on a reciprocal lattice (Fig. 1.12), will result in constructive interference of the scattered photons and ultimately the detection of a diffraction peak.[43]

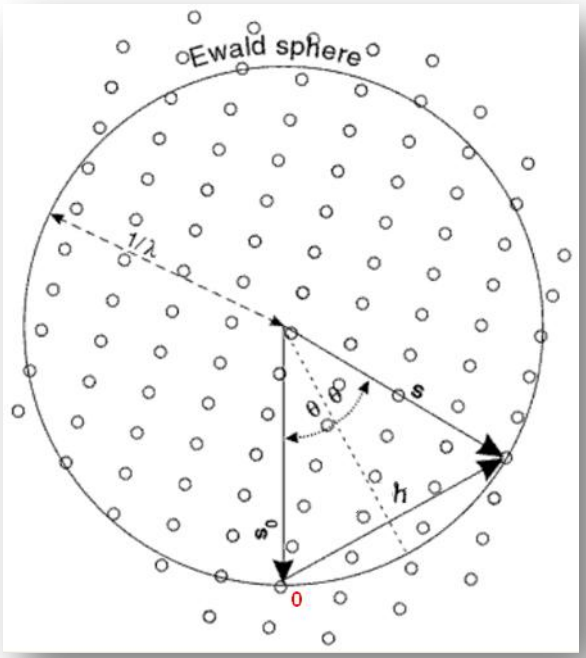

Figure 1.12. Simplified 2-dimensional reciprocal lattice (origin at 0) with geometrical construction of an Ewald circle (adapted from Dinnebier and Billinge)[39]

The incident wave vector ($\mathbf{s}_0$) falling on a single crystal has a magnitude of $1/\lambda$ and is drawn in the direction of the incident radiation. A sphere with a radius of $1/\lambda$ is drawn centered at the tail of this vector. This is referred to as the Ewald sphere. The scattered wave vector (**s**) has the same magnitude (elastic scattering) and originates from the same place as $\mathbf{s}_0$ and is directed toward the detector. The scattering vector (**h**), where $\mathbf{h} = \mathbf{s} - \mathbf{s}_0$ completes the triangle at the ends of $\mathbf{s}_0$ and **s**, which both lie on the surface of the sphere. The reciprocal lattice is then drawn with the origin at the terminal point of $\mathbf{s}_0$. The sphere is constructed in such a way that reciprocal lattice points that lie on the surface of the sphere satisfy the Bragg equation, resulting in diffraction. A zero-dimensional detector, usually referred to as a scintillation counter, is moved along the imaginary surface of the sphere detecting the diffracted intensity at the lattice points intersecting the sphere. In the case of two-dimensional detectors, used for single crystal experiments, multiple diffraction vectors are detected simultaneously. The crystal is then rotated, reorientating the reciprocal lattice to bring different reciprocal lattice points onto the surface of the Ewald sphere.[39]

Ideal powder samples are made up of randomly orientated crystallites, which results in the smearing of all the reciprocal lattice points onto the surface of a sphere centered at the origin of reciprocal space during Ewald construction (Fig. 1.13).[39] Ideally there should be so many, randomly orientated, crystallites that the reciprocal lattice points smear into continuous rings that surround the origin of reciprocal space. The three-dimensional orientation of the $\mathbf{d}^*_{hkl}$ vector is reduced to just one dimension, representing the modulus of the $\mathbf{d}^*_{hkl}$ vector.

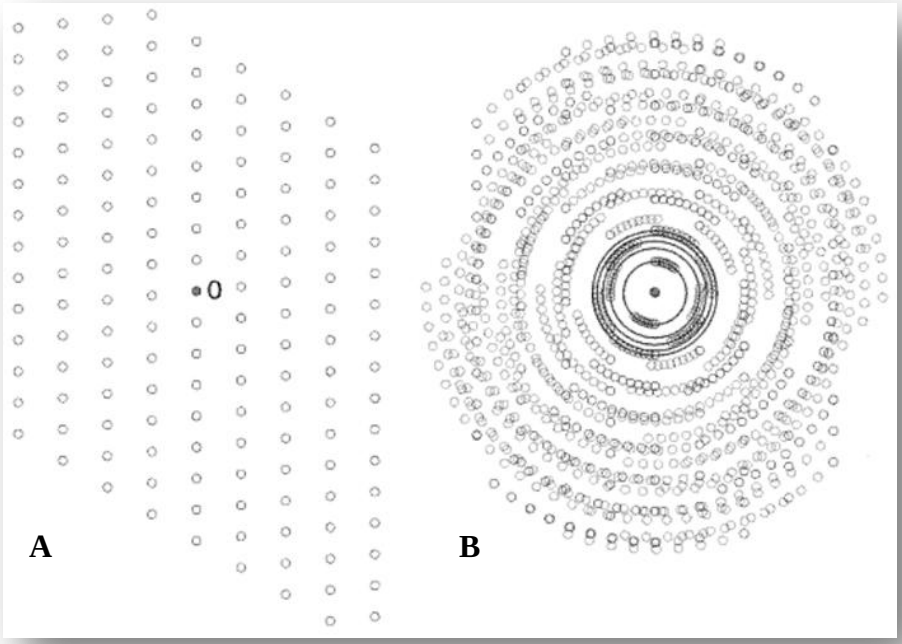

*Figure 1.13. 2-dimensional illustrations of **A** – the reciprocal lattice of an individual single crystal and **B** – and a large number of randomly orientated crystallites present in a powder sample (adapted from Dinnebier and Billinge)*[39]

Figure 1.14 shows how a two-dimensional Ewald sphere is generated for polycrystalline samples.[39] Diffracted beams are detected in the directions where the reciprocal lattice rings intersect the Ewald sphere. The lowest accessible d-spacing reflections are dependent on the diameter of the sphere $\left(\frac{2}{\lambda}\right)$. A decrease in the incident wavelength results in an increase in the number of accessible reflections.

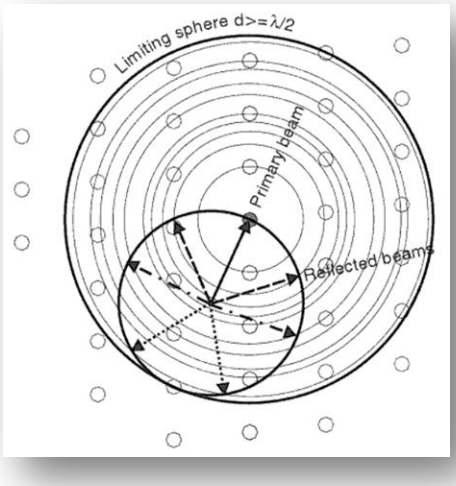

Figure 1.14. Accessible region of reciprocal space in a powder diffraction measurement[39]

In three dimensions, the intersection of reciprocal lattice rings and the Ewald sphere correspond to diffraction from *hkl* planes. Diffraction takes the shape of coaxial cones, which are referred to as Debye-Scherrer cones, instead of individual reflections observed during single crystal measurements (Fig. 1.15).[39]

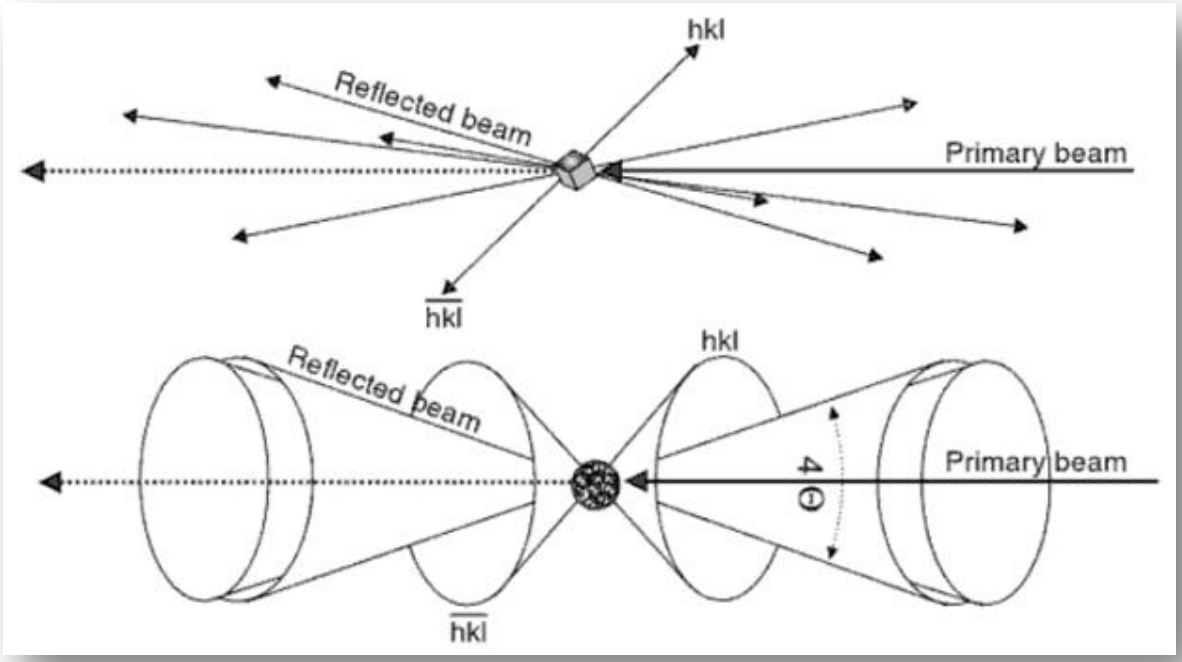

*Figure 1.15. Comparison between diffraction from **A** – a single crystal and **B** – a randomly orientated powder sample with Debye-Scherrer cones*[39]

The presence of reciprocal lattice rings in powder experiments, instead of individual points, results in a loss of information, due to the loss of three-dimensional resolution. Reflections representing different lattice planes with the same d-spacing often overlap, since the absolute directions of the representative vectors cannot be resolved. Some overlaps occur due to symmetry and are referred to as systematic overlaps, while others are entirely accidental. Accidental overlaps can often be deconstructed by increasing the resolution of the experiment, either by decreasing the wavelength (by changing the source anode for example) or by collecting the data at low temperatures, thus decreasing the effects of thermal lattice parameter redundancy.[39]

Powder diffraction data can be collected using a two-dimensional detector, which is placed perpendicular to the incident beam after the sample. An ideal powder sample would result in the detection of smooth, concentric circles at the varying cone angles. Imperfections in the diffraction rings provide information about sample texture (preferred orientation) and crystalline strain. Zero- and one-dimensional detectors operate by measuring a slice of one half of the diffraction cones, often resulting in the loss of information regarding crystallinity, texture and strain. Powder samples are often rotated about the axis normal to the surface (φ) in order to minimize this effect and ensure limited information is lost.[39]

1.3.5. Derivatives of the Bragg Equation

Some important relationships in crystallography can be deduced by taking the derivative of the Bragg equation **(20)**. Redefining the Bragg equation in terms of d gives:

$$d = \frac{n\lambda}{2\sin\theta} \qquad \textbf{(45)}$$

The uncertainty of the measured *d*-spacing is given by the total derivative d*d*, which is written according to the chain rule:

$$\mathrm{d}d = \frac{\partial d}{\partial \theta}\mathrm{d}\theta + \frac{\partial d}{\partial \lambda}\mathrm{d}\lambda \qquad \textbf{(46)}$$

therefore:

$$\mathrm{d}d = \frac{n\lambda}{2\sin\theta}\frac{\cos\theta}{\sin\theta}\mathrm{d}\theta + \frac{n}{2\sin\theta}\mathrm{d}\lambda \qquad \textbf{(47)}$$

and ultimately:

$$\frac{\mathrm{d}d}{d} = -\frac{\mathrm{d}\theta}{\tan\theta} + \frac{\mathrm{d}\lambda}{\lambda} \qquad \textbf{(48)}$$

Equation **(48)** is graphically represented in figure 1.16 and illustrates the effect of minor misalignments on the determination of the *d*-spacings.[39] Crystallographic strain, whether induced by external forces or internal defects, causes the *d*-spacings to vary. Macroscopic strain causes uniform changes in the *d*-spacings, resulting in a shift of the average peak position of $\Delta\theta$. Microscopic, or localized strain, results in a distribution of similar *d*-spacings, which broaden the observed diffraction peak by $\delta\theta$. A constant angular offset, introduced through minor misalignment of the diffractometer, results in a non-linear error in the determination of d_{hkl}, which affects low angle reflections more than high angle reflections. The ability to resolve partially overlapping peaks, separated by Δd_{hkl}, is limited by the finite angular resolution ($\Delta\theta$) of the diffractometer. Therefore, a misalignment of the diffractometer can lead to incorrect determination of the d-spacings and the presence or magnitude of crystallographic strain.

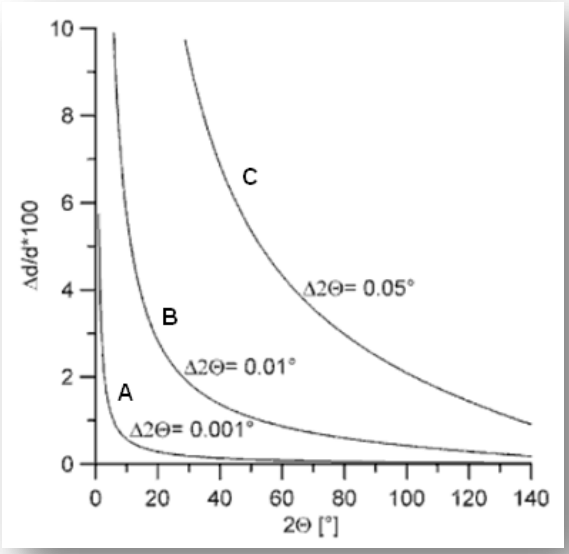

*Figure 1.16. Error in measured d-spacings as a function of 2-theta from a **A** – well aligned, **B** – typically aligned and **C** – poorly aligned diffractometer (modified from Dinnebier and Billinge)*[39]

Experimental variations have the most marked impact on the angular resolution of a diffraction instrument. The wavelength spread of the X-ray source ($\Delta\lambda$) can be described using:

$$\frac{\mathrm{d}\theta}{\mathrm{d}\lambda} = \frac{\tan\theta}{\lambda} \qquad \textbf{(49)}$$

which is depicted in figure 1.17.[39] It shows that the resolution, due to a finite spread in λ, decreases with increasing 2-theta, i.e. it is more difficult to resolve two semi-overlapping adjacent peaks at high diffraction angles, when the wavelength of the X-rays is not 100 % monochromatic.

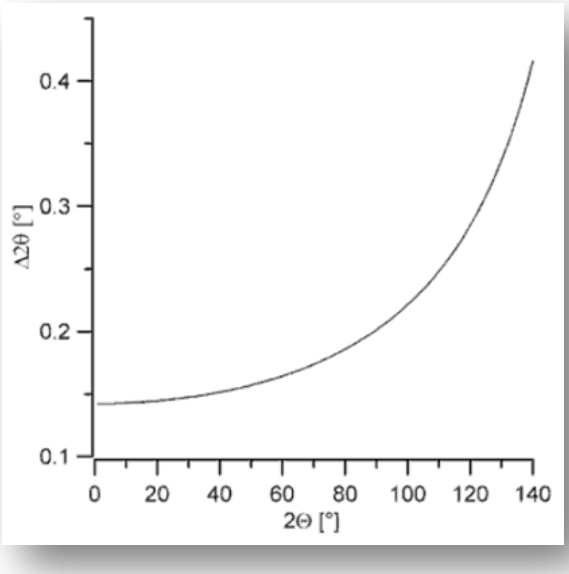

Figure 1.17. Angular dependence of resolution due to the wavelength spread between Cu-Kα_1 and Cu-Kα_2[39]

Even a well aligned, monochromatic instrument will generate data with instrumental line broadening. The data can either be corrected using standard reference materials, for which instrumental effects can be derived, or the instrumental effects can be modelled during Rietveld refinement of the data.

1.3.6. Bragg's Law and Crystallite Size

The final important property of the Bragg equation is the ability to use it to calculate the average crystallite size of a powder sample. Bragg's equation calculates the position of powder diffraction peaks if the sample contains a large number of randomly orientated crystallites. If the crystallites have a finite size, the diffraction peaks they generate will have a finite width. The relationship between particle size and the width of a diffraction peak is described by the Scherrer equation.[44] The simplified derivation of the Scherrer equation is reproduced from Dinnebier and Billinge,[39] which, in turn, was reproduced from Klug and Alexander.[37]

Figure 1.18 shows the variation in path length of diffracted X-rays as a function of the depth of the equivalent lattice planes.[39] When the angle between the incident X-rays and the lattice plane differs by an amount ε from the Bragg diffraction angle, there is always a lattice plane (in a sample containing large crystallites) where the extra path length Δ corresponds to λ/2, resulting in destructive interference. This minimizes the detectable reflections at angles above and below the Bragg diffraction angle. This explains the sharp diffraction peaks observed for samples containing large crystallites. For small crystallites the extinguishing plane for which $\Delta = \left(n + \frac{1}{2}\right)\lambda$ will not be present. No destructive intereference extinguishes reflections about the Bragg diffraction angle, which results in broad diffraction peaks. This sample broadening phenomenon was modelled by Scherrer to estimate the average crystallite particle size.

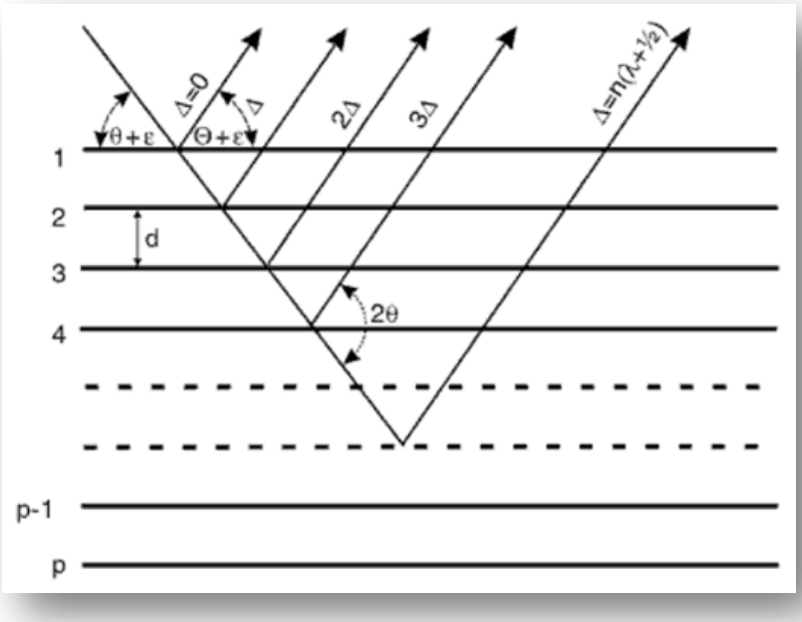

Figure 1.18. Variation in path length of diffracted X-rays as a function of depth of the equivalent lattice planes[39]

The thickness of a crystallite, measured perpendicular to the diffracting planes (*p* in figure 1.18) and with *d*-spacing equal to d_{hkl}, is:

$$L_{hkl} = pd_{hkl} \quad \textbf{(50)}$$

The additional path length between two consecutive lattice planes at the angle $\theta + \varepsilon$ is:

$$\begin{aligned}\Delta &= 2d\sin(\theta+\varepsilon)\\ &= 2d(\sin\theta\cos\epsilon+\cos\theta\sin\epsilon)\\ &= n\lambda\cos\varepsilon+\sin\varepsilon 2d\cos\theta\\ &\approx n\lambda+\sin\varepsilon 2d\cos\theta\end{aligned} \quad \textbf{(51)}$$

The corresponding phase shift is then:

$$\delta\varphi = 2\pi\frac{\Delta}{\lambda} = 2\pi n + \frac{4\pi}{\lambda}\epsilon d\cos\theta = \frac{4\pi\varepsilon d\cos\theta}{\lambda} \quad \textbf{(52)}$$

The phase shift between first and last plane is then:

$$\delta\varphi = p\frac{4\pi\epsilon d\cos\theta}{\lambda} = \frac{4\pi L_{hkl}\varepsilon\cos\theta}{\lambda} \quad \textbf{(53)}$$

Making ε the subject of the equation:

$$\varepsilon = \frac{\lambda\delta\varphi}{4\pi L_{hkl}\cos\theta} \quad \textbf{(54)}$$

gives an equation linking the misallignment angle, the crystallite size and the phase shift between the reflections from the first and last plane. Intuitively, the maximum intensity is observed where $\delta\varphi = 0$ ($\varepsilon = 0$) and increasing ε results in a decrease in intensity, giving rise to diffraction peaks of a particular width. Perfect destructive interference occurs between the diffracted waves from the first and last planes when $\delta\varphi = \pm\pi$, corresponding to $\varepsilon = \pm\frac{\lambda}{4L_{hkl}\cos\theta}$. The measured angular width between these points (referred to as the full width at half maximum or FWHM) is:

$$\beta_{hkl} = 4\varepsilon = \frac{\lambda}{L_{hkl}\cos\theta} \quad \textbf{(55)}$$

providing some measure of the peak width (in radians), due to the particle size. If the correct form for the intensity distribution is taken into account, equation **(55)** becomes:

$$L_{hkl} = 4\varepsilon = \frac{K\lambda}{\beta\cos\theta} \quad \textbf{(56)}$$

where K is a scale factor representing the shape of the crystallites ($K = 0.89$ for perfect spheres and $K = 0.94$ for cubes).

1.4. THE RIETVELD METHOD

The Rietveld Method is described in a number of modern textbooks in superb detail.[45-47] Here we discuss the absolute basics described by Robert Von Dreele, one of the developers of the GSAS Rietveld refinement suite and one of the leading specialists in powder diffraction and the Rietveld method.[47]

1.4.1. History of the Rietveld Technique

Before the development of the Rietveld technique, powder diffraction analysis involved the extraction of individual structure factors (a structure factor describes how an incident beam is scattered by the atoms in a unit cell and takes into account the variations in the scattering power of different types of atoms or ions) before standard single crystal methods were applied to elucidate structural information. This method could only be used for simple structures, since diffraction patterns from more complex structures would have significant peak overlap. The loss of three-dimensional reflection information in a powder pattern results in a drastic reduction of information, required to calculate structural parameters and atomic positions.[47]

Hugo Rietveld was the first scientist to consider a neutron powder diffraction pattern as a smooth curve made up of Gaussian peaks on top of a smooth background.[48] He realized that a mathematical expression could be derived to calculate the intensity (Y_c) at every point in a powder pattern, using contributions from the background (Y_b) and the Bragg reflections ($Y_{hkl} = Y_{\mathbf{h}}$), resulting in equation **(57)**.

$$Y_c = Y_b + \sum Y_{\mathbf{h}} \qquad \textbf{(57)}$$

Y_b and $Y_{\mathbf{h}}$ are the results of mathematical models that incorporate both crystalline and instrumental parameters in a PXRD experiment. These adjustable parameters are refined by a least-squares minimization of the weighted differences between the observed and calculated intensities to yield a calculated powder pattern as close to the observed pattern as possible.[49] It is this process that is referred to as "Rietveld Refinement." A Rietveld refinement is, therefore, a complex curve fitting problem.

1.4.2. Least Squares

Equation **(57)**, referred to as the model function, contains terms that are parameterized *via* mostly nonlinear and complex analytical expressions. These expressions take into account both the crystal structure of the sample and instrumental contributions. The physical properties of the probe form part of the instrumental contribution and cannot be omitted. When using particle (X-ray photons or neutrons) counting techniques, as is the case for powder diffraction, the model has to take in to account the Poisson distribution of the detected intensities about the exact diffraction angle, which, in itself, is a form of instrumental line broadening. When the number of powder profile points exceeds the number of parameters, a minimization of

$$M = \sum w(Y_o - Y_c)^2 \qquad \textbf{(58)}$$

by least squares, will give estimates of the parameters with the minimum amount of variance in any linear combination.[50] The weight function (w) is calculated from the variance in Y_o and it is usually assumed that there are no nonzero covariances between different Y_o values throughout the powder pattern. The calculated powder profile intensity is calculated using:

$$Y_c = K|F_{\mathbf{h}}|^2 H(\Delta T_{\mathbf{h}}) \qquad \textbf{(59)}$$

where K is the product of the various correction and scaling factors to the reflection intensities $|F_{\mathbf{h}}|^2$ and $H(\Delta T_{\mathbf{h}})$ is the value of the profile function for the location of profile point relative to the Bragg reflection position.[47] Equation **(58)** can be visualized as a slightly noisy three-dimensional surface with a small number of deep minima that correspond to possible solutions to the problem. Some of the minima will be false and represent incorrect solutions, while there will be one "global" minimum that represents the most correct solution.

The fact that equation **(59)**, is nonlinear and transcendental, i.e. invokes trigonometric functions, makes the use of standard linear least-squares analysis inappropriate. For this reason, the method used is to approximate the expression for Y_c as a Taylor series and only retain the first term:

$$Y_c(p_i) = Y_c(a_i) + \sum_i \frac{\partial Y_c}{\partial p_i} \Delta p_i \qquad \textbf{(60)}$$

The minimum is found by taking the first derivative of equation **(58)**:

$$\sum w(Y_o - Y_c) \frac{\partial Y_c}{\partial p_j} = 0 \qquad \textbf{(61)}$$

or by substitution:

$$\sum w \left[\Delta Y - \sum_i \frac{\partial Y_c}{\partial p_i} \Delta p_i \right] \frac{\partial Y_c}{\partial p_j} = 0 \qquad \Delta Y = Y_o - Y_c(a_i) \qquad \textbf{(62)}$$

which reduces to:

$$\sum w \frac{\partial Y_c}{\partial p_j} \left(\sum_i \frac{\partial Y_c}{\partial p_i} \Delta p_i \right) = \sum w \Delta Y \frac{\partial Y_c}{\partial p_j} \qquad \textbf{(63)}$$

Equations **(61)** and **(62)** represent the suite of normal equations and there is one for each parameter shift (Δp_i). The parameters in question can include the fractional coordinates of the atoms in the unit cell, the thermal parameters of the atoms, the occupancy factors (the probability of an atom occupying a given location in the unit cell), the scale factors (a factor that relates the calculated structure factors to the observed values), the lattice parameters, peak profile parameters, background coefficients, texture parameters, absorption of the sample and others.

Equations **(61)** and **(62)** can be rewritten in matrix form using the following three equations:

$$a_{i,j} = \sum w \frac{\partial Y_c}{\partial p_i} \frac{\partial Y_c}{\partial p_j} \quad , \quad x_j = \Delta p_j \quad and \quad v_i = \sum w\,(\Delta Y) \frac{\partial Y_c}{\partial p_i} \qquad \textbf{(64)}$$

to give:

$$\mathbf{Ax} = \mathbf{v} \qquad \textbf{(65)}$$

This matrix equation is solved for the desired parameter shifts by:

$$\mathbf{A^{-1}Ax} = \mathbf{A^{-1}v} \quad , \quad \mathbf{x} = \mathbf{A^{-1}v} = \mathbf{Bv} \quad \text{and} \quad x_j = \Delta p_j \qquad \textbf{(66)}$$

The inverse matrix (**B**) is normalized by the reduced χ^2 value [equation **(69)**] to give the variance-convergence matrix. The square roots of the diagonal elements of this normalized matrix are the estimated errors in the values of the shifts and, therefore, the errors of the parameters themselves. These calculated errors are based on the statistical errors in the experimental diffraction intensities and not on the discrepancies arising from systematic flaws in the model. Because of this, the models used to develop the calculated pattern must accurately represent a close correlation to the scattering process that gives rise observed pattern in order to avoid significant systematic errors.

An initial Taylor series approximation results in calculated shift values (Δp_i), which do not yield a completely minimized solution to the problem, but rather represent more realistic approximations, which are then used in subsequent refinements until the parameter shifts are less than some fraction of the estimated errors, calculated from the diagonal elements of the **B** matrix.[47] This approach, therefore, requires an initial estimate of each parameter to be refined [a_i in equation **(60)]**.

The quality of the least-squares refinement is usually reported as residual functions (also referred to as *R*-indices or *R*-factors):

$$R_p = \frac{\sum |Y_o - Y_c|}{\sum Y_o} \quad \text{and} \quad R_{wp} = \sqrt{\frac{M}{\sum w Y_o^2}} \qquad \textbf{(67)}$$

The weighted residual function (R_{wp}) is affected by the minimized factor (M) and is, therfore, the only statistically relevant residual function. The reduced χ^2 value, or the so-called "goodness of fit," is defined from the minimization function as:

$$\chi^2 = \frac{M}{(N_{obs} - N_{var})} \quad \textbf{(68)}$$

while the "expected R_{wp}" or R_{exp} is calculated using:

$$R_{exp} = \frac{R_{wp}}{\sqrt{\chi^2}} \quad \textbf{(69)}$$

The value of χ^2 will be unity in a perfect refinement. In reality values slightly higher than unity are observed if the weights for the observations are chosen correctly, i.e. as reciprocal variances. Incorrectly scaled variances will force the value of χ^2 away from unity, without affecting the value of R_{wp}.[47] Therefore, the "goodness of fit" value is one of the most important figures of merit in a Rietveld refinement.

1.5. *IN SITU* X-RAY DIFFRACTION

1.5.1. Brief History of *In Situ* X-ray Diffraction

The term "*in situ*" in PXRD refers to the collection of diffraction data under non-ambient or non-standard conditions. The first *in situ* investigations focussed on phase transitions at elevated temperatures, while low temperature and high pressure studies followed soon after. Much of the development of *in situ* experiments and instrumentation occurred at neutron sources, since neutrons were the only particles capable of penetrating the solid metal sample containers used at that time.[51-54] The low neutron flux, produced by the nuclear reactors at the time, limited the time resolution of the experiments dramatically. In addition to the flux problem, large samples were needed, since neutrons tend to destroy solid samples over a period of time. The development of synchrotron X-ray sources revolutionized *in situ* diffraction, due to the incredibly high flux and the range of the incident wavelengths that could be accessed. The relatively non-destructive X-rays, and the development of high quality optics, allowed for the analysis of small samples in more and more complex environments. The concurrent development of increasingly more efficient detectors made it possible to collect excellent diffraction data in a very short amount of time, which has led to the use of the technique to determine solid state reaction kinetics.[55]

The *in situ* technologies developed at neutron and synchrotron sources inevitably filtered through to laboratory instruments. Most laboratory instruments use a sealed tube to produce X-rays, the most common of which is the Cu tube, which produces $CuK\alpha_1$ and $CuK\alpha_2$ radiation. The relatively low flux produced by these types of sources results in difficulties during the collection of diffraction data due to absorption by the reaction cell and the sample. The low flux also limits the time resolution of an experiment, due to the increased time required to collect a diffraction pattern of good quality. These problems can be minimized by optimizing the experimental configuration. This can be achieved through a wide range of system changes that depend on the available budget of the project. Some examples of the more dramatic changes that can be implemented could include the installation of a rotating anode source that provides up to 50 times more flux than a conventional sealed tube.[56] Another option is to use tubes made from different anode materials, yielding X-rays with higher energies (shorter λ), which would have better reaction cell penetration characteristics. Table 1.1 lists common anode materials and their characteristic wavelengths.[57]

Table 1.1. Principle emission lines for various anode materials[57]

Anode	Cu	Mo	Cr	Fe	Co	Ag	W
λ Kα (Å)	1.54	0.71	2.29	1.94	1.79	0.56	0.21

Less dramatic, though still rather expensive, options include using X-ray mirrors and collimators to focus the divergent X-ray beam coming from the source, providing more flux per unit surface area and an increase in diffracted intensity from the sample.

The difficulties and expense associated with laboratory-based *in situ* setups have forced researchers to be creative in the way they collect diffraction data. An elegant example of this is the use of a one-dimensional detector, which is usually used to collect diffraction data through a wide range of two-theta angles, in static mode, collecting "snap-shots" of a single portion of the two-theta range, monitoring the development or change of a few reflections instead of the entire diffraction pattern. The use of a one-dimensional position sensitive detector in static mode allows researchers to obtain a time resolution of below 1 minute, enabling the determination of reaction kinetics on laboratory instruments.[51]

1.5.2. *In Situ* Cell Design

The flexibility of the diffraction technique has encouraged the development of custom-made *in situ* attachments for specific types of experiments. Early *in situ* cells, discussed briefly above, were merely pressurized metal tubes that could be heated by an external source. This design required the use of neutrons or high-energy X-rays that could penetrate the metal tube and interact with the sample material in transmission geometry.[51] The evolution of this technique resulted in the development of the capillary-based micro-reaction cell, which allowed transmission diffraction experiments to be performed on solid catalyst samples under reaction conditions.[58-59] The cell was designed using a single quartz capillary mounted in Swagelok fittings, through which gases could flow. The capillary was heated or cooled by passing a stream of hot or cold gas (air or nitrogen) over the capillary. This setup was, and still is, used to monitor the structural changes that occur in solid catalysts under reaction conditions. The installation of mass-flow controllers on the inlet side of the capillary and gas analysis systems, such as gas chromatography-mass spectrometry (GCMS), allowed researchers to monitor the exhaust gases and correlate observed changes in catalytic activity with the structural changes observed in the diffraction experiment. Standard glass capillaries can withstand pressures between 50 and 100 bar and the thin walls of the capillaries limit X-ray absorption.[51] Single crystal sapphire (corundum) capillaries have also been used when higher pressures are required but the increased wall thickness limits their use on lab-based intruments.[60]

In situ cells for X-ray reflection geometry are much more complicated in their design, since the incident and reflected X-rays have to reach the sample and the detector after penetrating some material designed to maintain the pressure and/or heat around the sample. Early designs incorporated the use of heating strips, onto which the sample was deposited. The sample and heating strip were usually sealed by a dome, made from X-ray transparent or weakly scattering materials, such as graphite or boron nitride (Fig. 1.19).[61] The dome shape ensured that both incident and reflected X-rays travelled through the dome perpendicularly, minimising absorption. These cells could be flushed or filled with inert gases in order to prevent corrosion of the heating strip. Other gases could also be introduced during the experiment as long as they did not attack the filament. The large surface area, and relative weakness of the transparent materials it was made of, limited the pressure profile of the dome enclosure.[51] Modern cells of this type are capable of

reaching temperatures of 1100 °C at pressures between 10^{-2} mbar and 0.25 bar above atmospheric pressure.

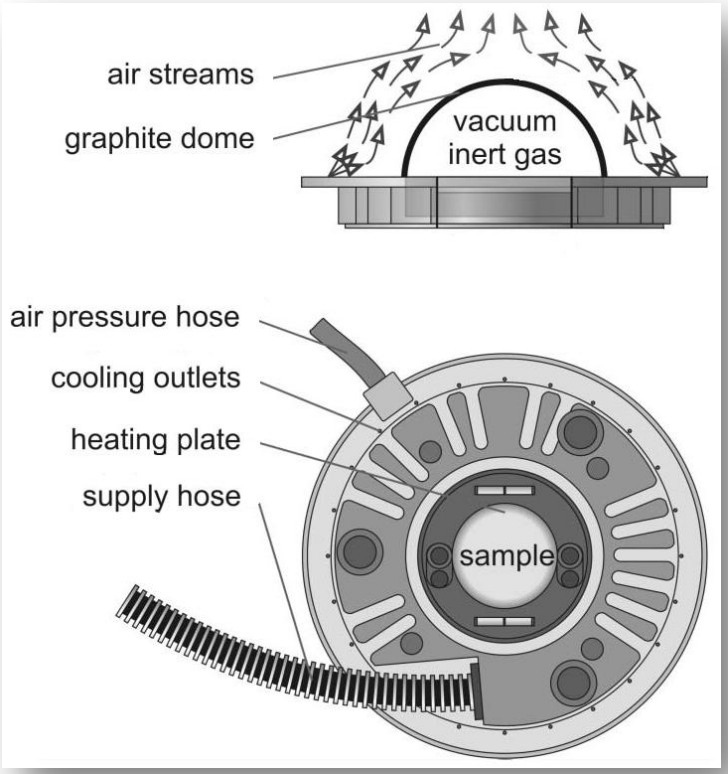

Figure 1.19. Schematic diagram of a Domed Hot Stage 1100 (DHS1100) attachment for high temperature XRD (Anton Paar GmbH)[61]

A number of designs have been successfully commercialized and implemented in X-ray laboratories worldwide. Currently, the largest supplier of *in situ* X-ray attachments is the Austrian-based company Anton Paar. They provide a number of cells with varying temperature and pressure ranges, which are listed in table 1.2.[62] They also manufacture cells for X-ray analysis of materials under various conditions of humidity and temperature (the Cryo and Humidity Chamber – CHC plus^{+}) and mechanical load and temperature (the Tensile Stage TS600). The majority of the cells available today are based on "chamber" designs. The XRK 900 is of particular interest, since this was the cell used to collect the *in situ* diffraction data in this study. The XRK 900 is constructed in three main parts, namely the housing, the lid supporting the furnace and the sample holder (Fig. 1.20).[63] The removable sample holder, made from stainless steel or Macor (a non-expanding aluminosilicate), is coaxially surrounded by heating elements in the furnace. The entire furnace is surrounded by heat shielding, which has two transparent beryllium windows to allow incident X-rays to strike the sample and reflected X-rays to leave the cell and strike the detector. The furnace is attached to the lid, which delivers current to the heating elements. The lid also houses the sockets for the thermocouples that measure the heat inside the furnace and at the sample. The heat shielding is surrounded by a cooling water jacket, which forms the major part of the housing. The housing has windows, covered with a transparent capton foil, that are aligned with the windows in the heat shielding. The housing attaches directly to the goniometer of the diffractometer and can be aligned in a relatively short amount of time. The XRK 900 has the added advantage that gases, at pressures up to 10

bar, can be forced over or through the sample. With gases flowing through the sample, the cell resembles a fixed bed reactor for catalytic reactions.

Table 1.2. Anton Paar in situ attachments and their temperature and pressure ranges[62]

CELL DESIGN	MODEL	MIN TEMPERATURE (°C)	MAX TEMPERATURE (°C)	MIN PRESSURE (mbar)	MAX PRESSURE (bar)
High-Temperature Oven-Chamber	HTK 1200N	25	1200	0.0001	ATM + 1
	HTK 1200N Capillary Extension	25	1000	N/A	N/A
Reactor Chamber	XRK 900	25	900	1.00	10
Low-Temperature Chamber	TTK 450	-193	450	0.0001	ATM + 1
High-Pressure Chamber	HPC 900	25	900	1.00	100
High-Temperature Chambers	HTK 16 - Platinum	25	1600	0.0001	ATM + 1
	- Graphite	25	1500	0.0001	ATM + 1
	HTK 2000 - Tungsten	25	2300	0.0001	N/A
	- Platinum	25	1600	0.0001	ATM + 1
Domed Hot Stage for Four-Circle Goniometers	DHS 900	25	900	ATM	ATM + 0.3
	DHS 1100	25	1100	0.01	ATM + 0.25
Domed Cooling Stage for Four-Circle Goniometers	DCS 350	-100	350	0.05	ATM + 0.3

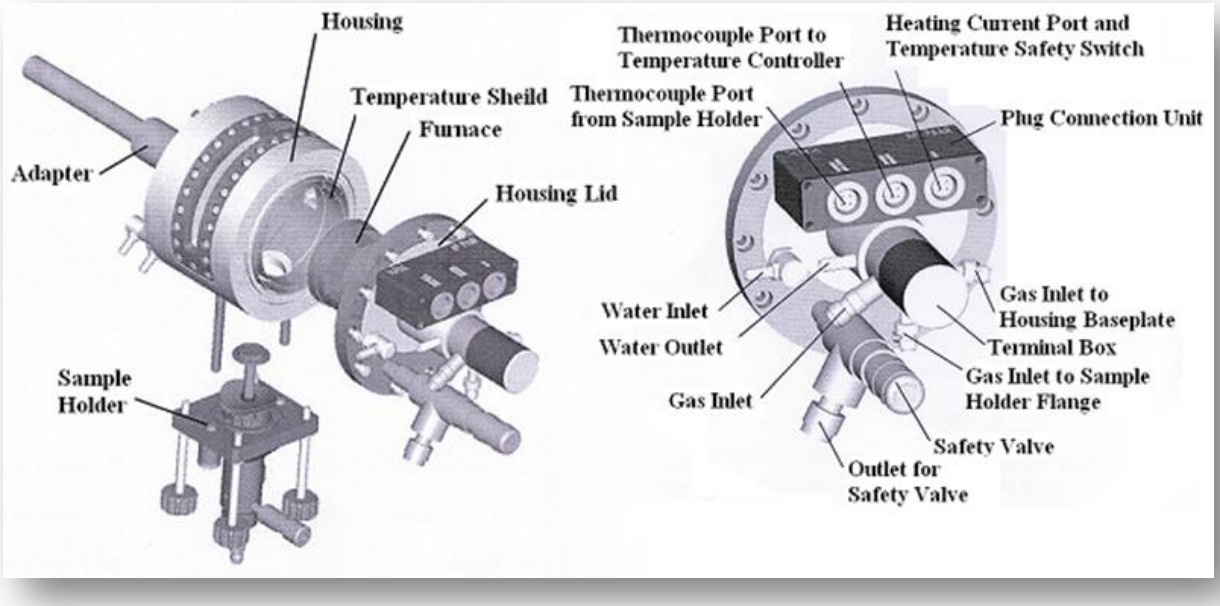

Figure 1.20. Schematic diagram of the Anton Paar XRK 900 in situ attachment[63]

1.6. LITERATURE REVIEW

In order to show the diversity of *in situ* experiments currently being performed, we provide some examples which demonstrate unique experiments on lab-based *in situ* PXRD systems. The collection of experiments also demonstrates the evolution of the *in situ* PXRD technique and the changes in research directions that have occurred over the past decade.

1.6.1. Decomposition of Ag_2O and the Active Phase of Oxydehydrogenation Catalysts

The need for lab-based *in situ* XRD investigations in heterogeneous catalysis was first voiced in a paper published by Herzog *et al. i*n 1994,[64] although they had touched on the subject in 1990.[65] They made mention of the importance of analyzing the bulk phases in catalysts under reaction conditions, even though the catalytic reactions occur only at the surface. They understood that minor structural changes in the catalyst could explain changes in activity or selectivity over time and that the active phase of the catalyst may not be present under normal analytical conditions. They evaluated the thermal decomposition of silver(I)oxide (Ag_2O) to elemental silver (Ag) and investigated the behaviour of the heteropoly catalyst $H_4[PVMo_{11}O_{40}]\cdot 32H_2O$ during the oxydehydrogenation of isobutyric acid (IBA) to methacrylic acid (MAA). They were able to monitor the reduction of Ag_2O to Ag between 200 °C and 400 °C, while quantifying the loss of molecular oxygen by evolved gas analysis (EGA), using a mass spectrometer downstream of the reactor. Their results suggested that the active phase of the oxydehydrogenation catalyst was an anhydrous phase, an observation that had never been considered before. They also monitored catalyst deactivation by decomposition of the catalyst to the inactive molybdenum(VI) oxide (MoO_3) phase.

1.6.2. Iron and "Ammonia Iron" Catalysts for Ammonia Synthesis

In 1996, the same authors investigated the microstructure of activated iron catalysts used for ammonia synthesis.[66] It was well known that standard bulk iron was inefficient in the ammonia synthesis reaction, while iron specially prepared using oxidic precursors, referred to as "ammonia iron," was extremely active.[67-68] Since the chemical composition of the two catalysts was the same, researchers began to focus on the structural differences between them. Initial investigations involved discussions about "paracrystallinity," which was developed using XRD data.[69-70] Paracrystallinity was defined as the normalised standard deviation of the *d*-spacings in a material and was determined using line profile analysis of an XRD reflection (currently referred to as stress-strain analysis).[71] The proposal was that a three-dimensional, edotactic incorporation of $FeAl_2O_4$ into the α-iron lattice caused substitutional point defects, which, in turn, caused strain within the lattice resulting in the modification of the bulk and surface structure of the activated catalyst. This proposal was later rejected by Mössbauer spectroscopy studies[72] and extended X-ray absorption fine structure (EXAFS) studies.[73-74] The two techniques actually confirmed the chemical similarities between the inactive and the active catalysts. Earlier chemisorptions results suggested that the activity of the catalysts was not a function of the nature of the active sites but rather their abundance.[75-76]

With all of the above in mind, Herzog *et al.* set out to perform *in situ* XRD measurements on the two catalysts. They focussed on the activation of the iron precursors using a 1:1 mixture of nitrogen and hydrogen, the average microstructure of the catalysts and the effects of oxygen poisoning of the catalyst. They found that the active catalyst precursor was mostly magnetite (Fe_3O_4) with small, but detectable, amounts of wuestite (FeO) and promoter compounds. *In situ* XRD activation (reduction) was used to monitor the reduction profile of FeO and texture analysis proved that the initial iron nuclei were formed by thermal decomposition of FeO ($4FeO \rightarrow Fe + Fe_3O_4$) and not by direct reduction of FeO ($FeO + H_2 \rightarrow Fe + H_2O$). They also determined that the formation of these iron nuclei was essential to activate the reduction of Fe_3O_4 at low temperatures, since they set up an electrochemical gradient enabling the diffusion of Fe^{2+} ions to the iron nuclei. This explains why iron shells are not formed around magnetite particles, limiting the degree of reduction. This mechanism of activation results in a significant amount of restructuring, resulting in an iron phase that has significantly different textural properties than the parent magnetite phase, which was observed during line profile analysis. By monitoring the anisotropic rates of decrease in peak intensity of the magnetite phase, they were able to show that Fe^{2+} diffusion along different directions occurs at different rates. They were also able to show that the activity of the catalyst only increased at the very end of the activation process and, therefore, was not a function of bulk activation. The observed peak intensity ratios were significantly different from isotropic α-iron, suggesting that there was significant texturing in the "ammonia iron." By changing the gas composition, they were able to show that nitrogen atoms diffused into the iron lattice under reaction conditions, increasing the *d*-spacing of the surface layers. These observations conclusively proved that heterogeneous catalysts may not be as homogeneous under reaction conditions as they appear to be, even if only one phase is present.

They then turned their attention to investigating the deactivation of the catalyst by oxygen. They witnessed the formation of magnetite and hematite upon introduction of a small amount of oxygen under reaction conditions, confirming the catalysts affinity for oxygen and lending credibility to the presence of multiple types of iron that can interact with oxygen in different ways. In addition to the formation of the iron oxides, the presence of oxygen had an effect on the iron phase (table 1.3).[66] It is clear that the oxygen affected the bulk texture of the iron as well as the average particle size. The initial addition of oxygen actually increased the production of ammonia, which was attributed to fracturing of the active surface phase, in the presence of oxygen, leading to a temporary increase in the surface area of the active phase. This process caused restructuring of the ammonia iron to form inactive normal iron in the long term. They found that this restructuring process occured quite slowly and if the catalyst was re-reduced immediately after exposure to oxygen the activity of the catalyst is little affected. The multitude of results obtained during the course of this study demonstrated the power of the *in situ* XRD technique.

Table 1.3. Crystallographic changes of the iron phase during oxygen poisoning of an "ammonia iron" catalyst[66]

State of Reaction	Texture Ratio (200)/(110)	FWHM (°2θ)		Particle Size (nm)	
		(110)	(200)	(110)	(200)
Before oxidation	0.07	0.41	0.80	263	147
During oxidation after 15 h	0.20	0.42	0.52	257	227
During oxidation after 30 h	0.20	0.47	0.51	229	231
After oxidation	0.08	0.25	0.46	431	256

1.6.3. The Temperature Difference between the Support and Active Metal Particles

In 2002, a paper was published by Plyasova *et al.* describing a method for the determination of the actual temperature of supported catalyst particles.[77] This investigation was prompted by numerical calculations suggesting that the actual temperature of a supported catalyst particle may be tens or even hundreds of degrees higher than the average temperature of the catalyst measured using a thermocouple.[78] Calculations suggested that the temperature difference between 10 nm platinum (Pt) particles and a gamma-alumina (γ-Al_2O_3) support in a common hydrocarbon oxidation catalyst, could be as much as 200 °C when the catalyst was at an operational temperature of 620 °C. Plyasova *et al.* developed their method using a nickel-magnesia (Ni/MgO) catalyst, commonly used for the hydrogenation of carbon monoxide (CO). The catalyst was prepared via coprecipitation of aqueous Ni and Mg nitrate solutions, mixed in a 1:1 molar ratio. The precipitate was calcined in argon (Ar) at 500 °C to produce a mixed Ni-Mg oxide, which was then activated using hydrogen (H_2) at the same temperature. This yielded supported nickel particles with an average size of 8 nm. Preliminary XRD results suggested that the activation process was incomplete and that the support was, in fact, an inhomogeneous solid solution of Ni^{2+} in MgO. Additional heat treatment in a reducing environment, resulted in increased homogeneity of the solid solution, which was witnessed using *in situ* PXRD.

The authors compared the thermal expansion behaviour of the *a* lattice parameter of the mixed metal oxide phase with the calculated values for pure MgO phase, both under reaction conditions. They found that the two materials have an almost identical thermal expansion coefficient but the length of the *a* lattice parameter for the mixed metal oxide was consistently smaller at each temperature interval (Fig. 1.21**A**). Using this information, they were able to determine the degree of reduction of Ni^{2+} to be approximately 35 %. The fact that the lattice parameter of the mixed metal oxide increased to the same extent as the calculated MgO lattice parameter at every temperature interval, meant that the temperature of the support was equal to, or very close to, the temperature of the reactor under reaction conditions. Curve *1* in figure 1.21**B** represents the linear expansion of the *a* lattice parameter of metallic nickel during heating under H_2, while curve *2* represents the non-linear expansion of *a* when heated in the reaction gas mixture.[77] The increase in the lattice parameter, between 200 °C and 300 °C, was attributed to the absorption of heat generated by the active exothermic hydrogenation reaction outlined in equation **(70)**. The differences in the thermal conductivity coefficients of the Ni particles (λ_{Ni} = 58.6 $Wm^{-1}K^{-1}$) and the support (λ_{MgO} = 0.61

$Wm^{-1}K^{-1}$) retards heat transfer form the Ni particles to the support, which means that any heat produced at the sites cannot be conducted away from the sites, leading to a large temperature gradient between the two phases. Using the linear thermal expansion trend in figure 1.21**B**, the difference in temperature between the particles and the support (ΔT) at 300 °C was estimated to be +250 ± 25 °C.[77] The authors acknowledged the possible formation of an interstitial solid solution of carbon in nickel,[79] which would also increase the lattice parameter, and adjusted their initial estimate to give a ΔT value of 150-170 °C. The decrease in a_{Ni} at temperatures above 300 °C was attributed to the formation of graphitic materials with a much higher thermal conductivity coefficient, which acted as a heat sink, conducting heat away from the Ni particles.

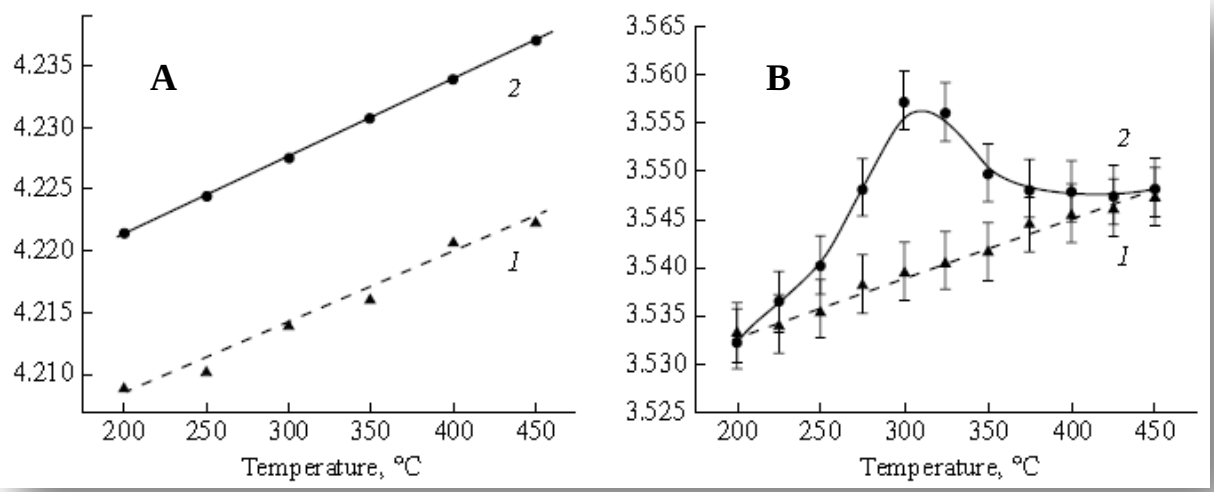

*Figure 1.21. **A** – thermal expansion of the a lattice parameter of 1 – the Ni-Mg mixed-metal oxide support and 2 –pure MgO (calculated) and **B** – thermal expansion of the a lattice parameter of metallic Ni under 1 – H_2 and 2 – a 3:2 reaction mixture of H_2 and CO*[77]

$$CO + 3H_2 \rightarrow CH_4 + H_2O \qquad \Delta H^{\circ}_{298°C} = -210 \text{kJ.mol}^{-1} \qquad \textbf{(70)}$$

1.6.4. The Structure of Pt and PtRu Particles on a Carbon Support

In 2008, Walter Vogel completed an *in situ* PXRD analysis on carbon-supported platinum (Pt/C) and bimetallic platinum-ruthenium (PtRu/C) electrocatalysts, which are used as reference materials in fuel cell applications.[80] He demonstrated the *in situ* reduction of the surface oxides present on the highly dispersed Pt particles in the Pt/C catalyst in a vacuum at room temperature, using incredibly small pulses of H_2 (1 ml). Figure 1.22 relates the intensity of the Pt-111 peak to time and surface temperature.[80] The exact time of the H_2 pulses can be determined by monitoring the increase in temperature of the catalyst, as was shown in the previous section. The results show that two H_2 pulses increased the intensity of the Pt-111 peak by 10.5 %, resulting in complete reduction. The time resolution achieved for this experiment was five seconds, i.e. a fixed 1° 2-theta range (focussed on the Pt-111 peak) was collected every 5 s. This was made possible with the use of a high resolution diffractometer, equipped with an advanced image plate detector.

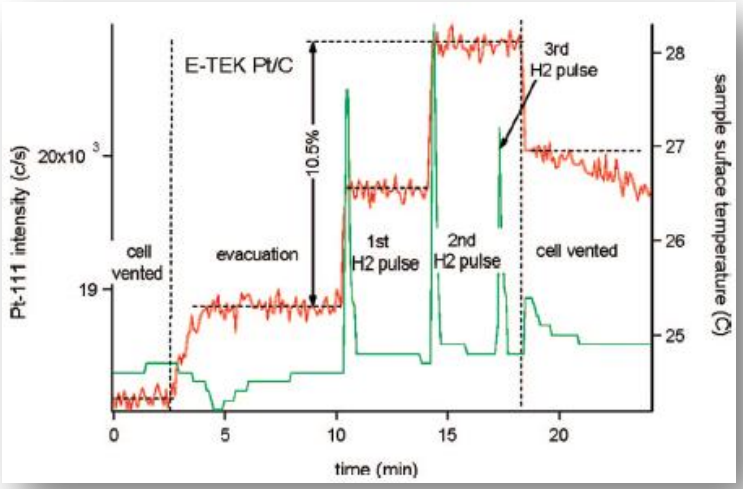

Figure 1.22. Reduction of the E-TEK Pt/C catalyst in a vacuum using 1 ml injections of H_2 (red line – Pt-111 intensity and green line – sample surface temperature)[80]

A similar treatment of the PtRu/C catalyst demonstrated significant differences from the Pt/C catalyst discussed above (Fig. 1.23).[80] In this case, five H_2 pulses were required to complete the surface reduction and each pulse resulted in a less distinct increase in intensity of the Pt-111 peak. Figure 1.23 also shows that the PtRu/C catalyst was much less efficient at releasing the heat generated during reduction, which is indicated by the slow decay of the temperature curve after each H_2 pulse.

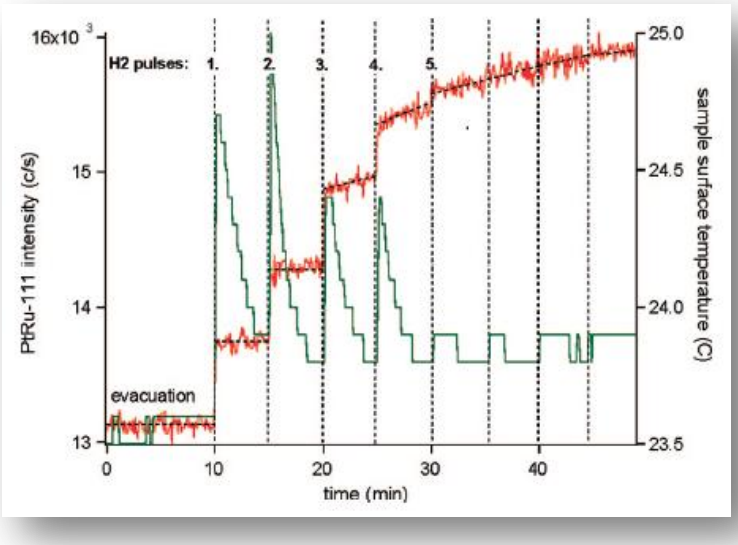

Figure 1.23. Reduction of the E-TEK PtRu/C catalyst in a vacuum using 1 ml injections of H_2 (red line – Pt-111 intensity, green line – sample surface temperature)[80]

The author used Debye function analysis (DFA), which is a direct method of structure analysis capable of yielding information about the size and structure of crystalline domains and identify noncrystalline structures,[81-84] to simulate diffraction data representing various crystal morphologies for the determination of the structure of the PtRu particles. His results showed that the activated PtRu catalyst particles were present as a perfect alloy on the surface of the support. He was also able to show that the lattice contraction of the Pt and PtRu particles, with a value of 0.80 % for both species, was a quantum size effect, which had been debated for some time.

1.6.5. Pressure Acid Leaching (PAL) of Nickel Laterite Ores

In 2005 Madsen *et al.* performed *in situ* PXRD experiments to investigate pressure acid leaching (PAL) of nickel laterite ores in Australia.[85] The process involves the treatment of laterite ores with sulfuric acid at high temperatures and pressures in order to dissolve nickel and cobalt bearing phases. The acid solution is then treated with solvents to extract the metals and the acid is recycled. The process has been extensively studied,[86-87] however, all of the analyses were performed *ex situ* and it was thought that the cooling of the sample, resulted in the formation of artefacts, especially for saprolite (a type of laterite ore). These characteristics, and the industrial importance of the process, made this system a perfect candidate for *in situ* PXRD analysis.

Two slurry mixtures of saprolite ore (30 wt%) and sulfuric acid were prepared with acid concentrations of 19.4 wt% (referred to as "low acid") and 32.7 wt% (high acid). The authors added an internal standard, in the form of 0.5 μm industrial diamond powder (20 wt% in the ore-acid-spike mixture), which enabled the calculation of any undefined crystalline phases and amorphous material in the sample at any given time using the Rietveld method. The internal standard (also referred to as a spike) also allowed the authors to calculate the absolute, rather than the relative, phase concentrations regardless of whether all of the phases included in the analysis. This topic will be covered in the sections to come, since the evaluation of amorphous material content in a sample forms a large part of this study. The diffraction experiments were performed in a capillary reactor, to minimise the texturing problems associated with lizardite (a type of laterite ore), heated to 220 °C at a hydrothermal pressure of 24 bar. Highly monochromatic MoKα radiation was used in conjunction with a curved position-sensitive detector, which could collect diffraction information over a range of 120 °2θ simultaneously, with a time resolution of 2 min.

Figure 1.24 shows the quantitative results obtained during the PAL experiments. For the first time, the dissolution of lizardite [$Mg_3Si_2O_5(OH)_4$] could be monitored as its concentration decreased with the simultaneous increase in the amorphous concentration (solution). It is clear that the dissolution occurred significantly faster under high acid conditions (Fig. 1.24**A**) than low acid conditions (Fig 1.24**B**). Jarosite, with the general formula $(Na,H_3O)(Al,Fe)_3(SO_4)_2(OH)_6$, and kieserite ($MgSO_4 \cdot H_2O$) precipitated from the solution soon after the start of the dissolution of lizardite. In both the high and low acid experiments, precipitation of kieserite occurred once the rate of precipitation of jarosite had slowed. The authors explained this sequential formation by acknowledging that the precipitation of jarosite would require a lower concentration of iron than the concentration of magnesium required to precipitate kieserite. The precipitation of these minerals resulted in a decrease in concentration of the amorphous component, which is expected since a solution containing dissolved ions will be more amorphous in nature before precipitation begins. The maghemite concentration was unaffected throughout both experiments, suggesting that it is the only stable phase under these conditions. After 190 minutes, the reactor was allowed to cool to room temperature, while data collection continued. The cooling resulted in the dissolution of kieserite and a proportional increase in the amorphous component. This drastic change

highlights the importance of *in situ* measurements, since an *ex situ* diffraction pattern collected after the PAL process would not be representative of the sample. This is not always the case, since some solid materials are irreversibly altered under reaction conditions and *ex situ* analysis would provide the correct answer.

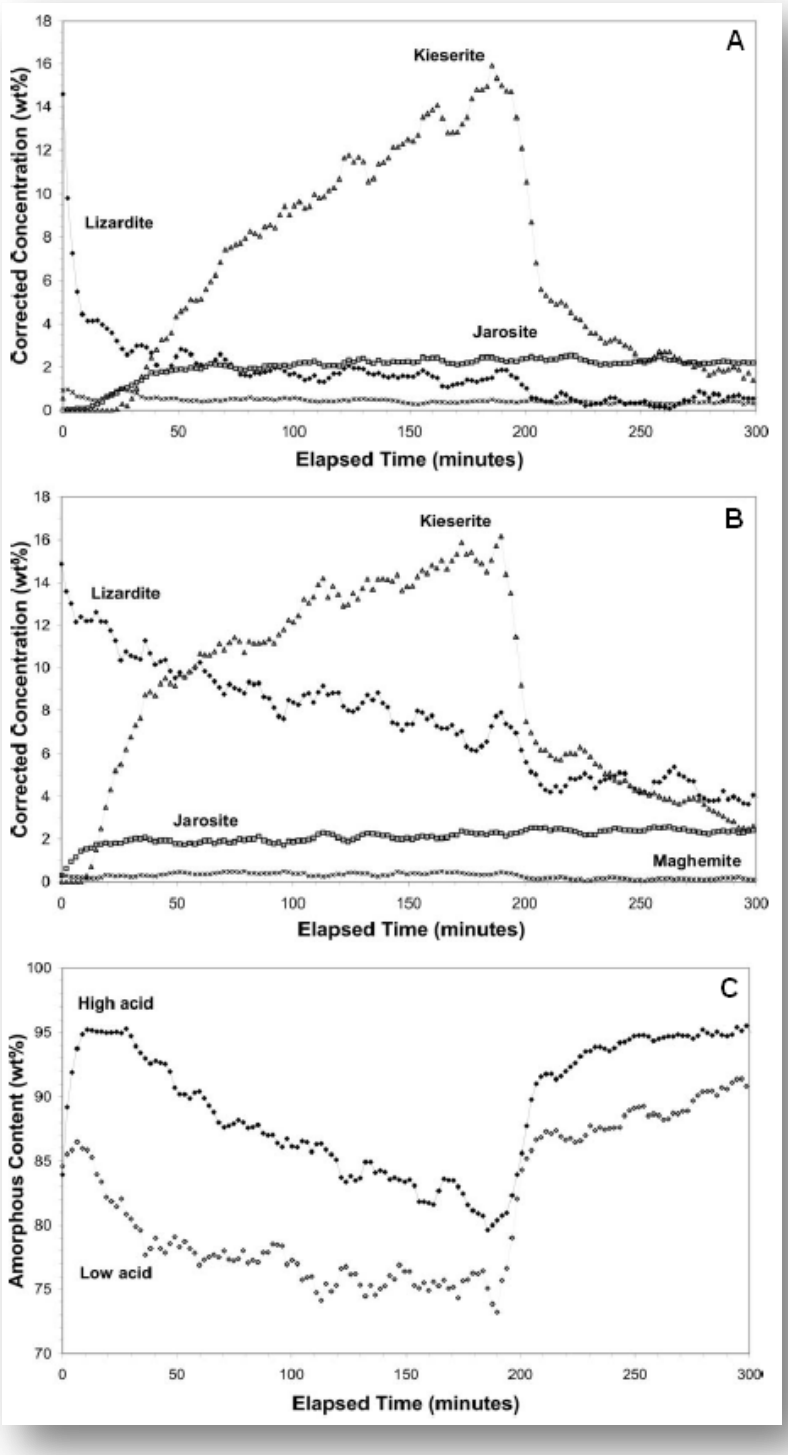

*Figure 1.24. Results of the Rietveld-based quantitative phase analysis (QPA) during pressure acid leaching (PAL) of saprolite ore at 220 °C and 24 bar in **A** – high acid and **B** – low acid environments, while **C** is the calculated concentration of amorphous or unknown components (solid and liquid) during the two PAL experiments (the reactor was cooled to room temperature after 190 min)*[85]

1.6.6. Body-centred Cubic Cobalt in the FT Reaction

In 1989, Colley *et al*. used lab-based *in situ* PXRD to monitor the behaviour of cobalt/manganese oxide, mixed spinel-type FT catalysts during activation and under reaction conditions.[88] They were unable to definitively determine if the phase of cobalt produced by activation was face-centred cubic (FCC) or a mixture of FCC and body-centred cubic (BCC). However, they were able to show that BCC cobalt began to form after 24 h of exposure to syngas (1:1 ratio of H_2/CO at 0.82 bar and 220 °C) and continued to increase in concentration with increasing time (Fig. 1.25). The BCC phase was shown to be stable upon cooling and exposure to air, however, milling the sample in air resulted in the transformation of the majority of BCC cobalt back to FCC cobalt. The authors made mention of the fact that the kinetics of formation of BCC cobalt correlate well with the activity and selectivities observed as a function of time for this catalyst system, which suggests that the BCC phase is the catalytically active species in the FT reaction.

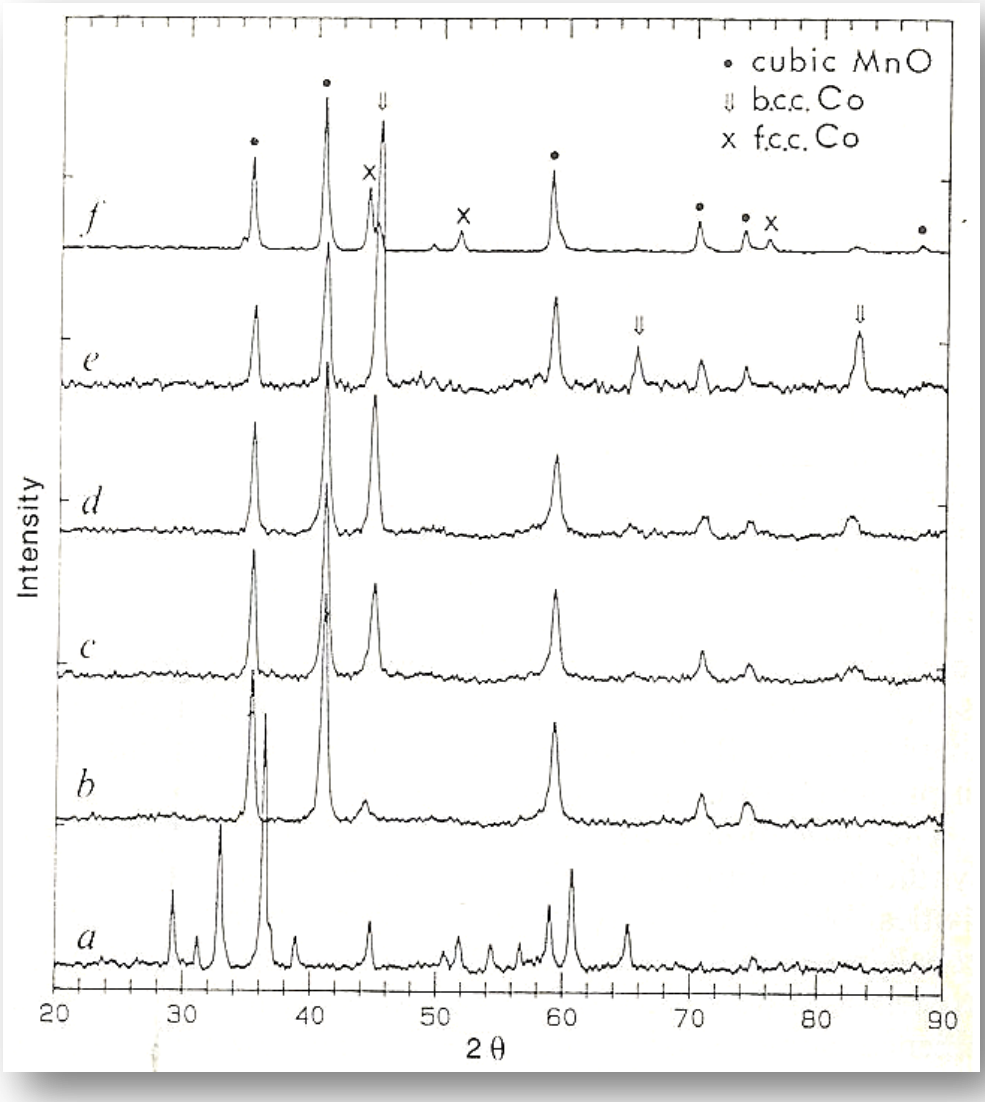

Figure 1.25. In situ PXRD patterns of the Co/MnO FT catalyst a – before reduction, b – after reduction with H_2 at 450 °C, c-e – after 24 h, 72 h, and 112 h reaction with synthesis gas at 220 °C and f – resulting sample milled in air[88]

1.6.7. Silica (SiO_2)-, Alumina (Al_2O_3)- and Titania (TiO_2)-supported Cobalt Catalysts

The final experimental example comes from the work published by Ducreux *et al.*.[89] The authors performed similar *in situ* reduction experiments to those discussed above and arrived at a similar result. However, a new cobalt-carbide (Co_2C) phase was observed during the *in situ* FT experiments performed on the Co/Al_2O_3 catalyst (Fig. 1.26**A**) and the bimetallic $Co\text{-}Ru/TiO_2$ catalyst (Fig. 1.26**B**) after only 70 h on stream. The formation of this new phase resulted in a parallel decrease in the peak intensity of metallic Co. The Co/SiO_2 catalyst and bulk cobalt(II/III) oxide (Co_3O_4) showed no carbide formation even after 310 h on stream.

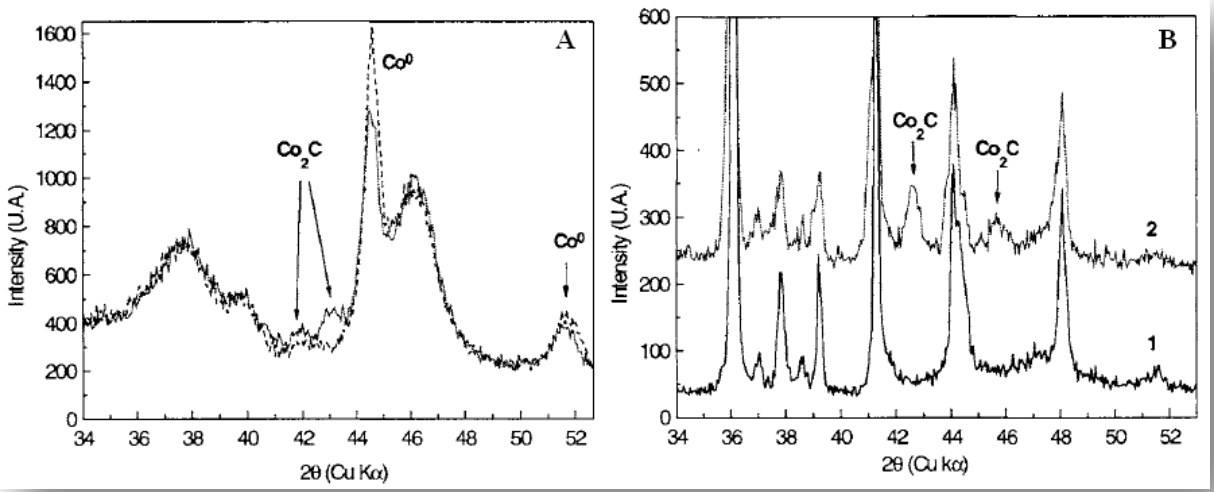

*Figure 1.26. The formation of Co_2C in **A** – the Co/Al_2O_3 catalyst and **B** – the $Co\text{-}Ru/TiO_2$ catalyst (1 – after activation and 2 – after 180 h on stream)*[89]

The authors were able to show a decrease in CO conversion with increasing Co_2C peak intensity and a selectivity shift towards $C_5 - C_9$ products for the $Co\text{-}Ru/TiO_2$ catalyst. The formation of the carbide phase and the decrease in activity occurred at a significantly slower rate for the Co/Al_2O_3 catalyst, while no deactivation or change in selectivity was observed during the treatment of the Co/SiO_2 catalyst. This work clearly demonstrates the relationship between structure modification and activity/selectivity and its importance to industrial processes.

1.7. OBJECTIVES OF THIS STUDY

Much of the work that has been published using *in situ* PXRD in catalysis has focussed on the solid state changes that occur under catalytic conditions. Our work focuses on the pretreatment stages of TiO_2-supported metal catalysts, namely calcination and activation. These processes differ for every catalytic system and are usually developed using non-structural information, such as thermogravimetric analysis (TGA) for calcination procedures and temperature-programmed reduction (TPR) for activation procedures. We will show that structural information gathered during *in situ* heat treatment and activation experiments can lead to the development of better pretreatment procedures and ultimately a good degree of control of the structural properties of a solid state catalyst. The objectives of this study are, therefore, as follows:

- Prepare TiO_2-supported Fe, Co and Ru precatalysts using three different TiO_2 materials and the incipient wetness impregnation method. The supports of interest are Degussa P25, Sigma-Aldrich anatase (referred to as Sigma anatase), and a nanosized anatase (NSA), prepared using a sol gel method.
- Develop *in situ* PXRD heat treatment experiments to monitor the structural changes induced by exposure of the supports and catalysts to temperatures of up to 900 °C.
- Monitor the crystallization of the metal oxide phases and amorphous phase concentrations, using internal standard (spike) addition and whole pattern Rietveld methods.
- Determine the ideal calcination procedure for each catalyst in terms of maximum metal oxide concentration and particle size.
- Develop *in situ* PXRD activation experiments to monitor the reduction of the supported metal oxide phases and possible interactions with the supports.
- Determine the ideal reduction procedure for each catalyst in terms of maximum M^0 concentration and particle size.

1.8. REFERENCES

1. F. Fischer and H. Tropsch, *U.S. Patent 1,746,464* (1930).
2. B. H. Davis and M. L. Occelli, *Fischer-Tropsch Synthesis, Catalysts and Catalysis*, Elsevier, Boston, 1-27 (2007).
3. S. R. Lewis, *The Economics of Apartheid*, Council on Foreign Relations Press, New York, 127-134 (1990).
4. J. M. Thomas and W. J. Thomas, *Principles and Practise of Heterogeneous Catalysis*, Wiley-VCH, New York, 524-548 (1997).
5. *Oil prices*, oil-price.net, updated: 18/01/2008 and accessed: 18/01/2008, <www.oil-price.net/index.php?lang=en>
6. A. Steynbeg and M. Dry, *Fischer-Tropsch Technology*, Elservier, Amsterdam, 406-413 (2004).
7. L. M. McMahon, *Historical Crude Oil Prices (Table)*, Capital Professional Services, updated: 21/07/2010 and accessed: 20/02/2011, <http://inflationdata.com/inflation/inflation_rate/historical_oil_prices_table.asp>
8. USGS World Energy Assessment Team, U.S. Geological Survey World Petroleum Assessment 2000 – D*escription and Results – Executive Summary*, USGS Information Services, Denver, 1-4 (2010).
9. S. T. Sie, *Studies in Surface Science and Catalysis Volume 85*, Elsevier, Amsterdam, 587-631 (1994).
10. *The CIA World Fact Book 2011*, Skyhorse Publishing, New York (2010).
11. A. W. Clarke and J. A. Trinnaman, *2010 Survey of Energy Resources*, World Energy Council, London (2010).
12. H. M. V. van Wecham and M. M. G. Sendon, *Studies in Surface Science and Catalysis Volume 81*, Elsevier, Amsterdam, 43 (1994).
13. J. Eilers, S. A. Posthuma and S. T. Sie, *Catalysis Letters* **7**, 253 (1990).
14. M. E. Dry, *J. Chem. Technol. Biotechnol.* **77**, 43 (2001).
15. *Precious Metal Prices*, The Bullion Desk, updated: 18/02/2011 and accessed: 20/02/2011, <www.thebulliondesk.com/>
16. *Ferrous Metal Prices*, Metals News, updated: 18/02/2011 and accessed: 20/02/2011, <www.metalprices.com>
17. M. Creamer, *ICD, Palabora Mining Partner Technology Minnow in Pilot Iron Project*, Mining Weekly.com, updated: 08/08/2010 and accessed: 24/02/2011, <http://www.miningweekly.com/article/idc-palabora-mining-partner-technology-minnow-in-pilot-metallic-iron-project-2010-10-08>
18. M. E. Dry, *Catalysis Today* **6**, 183 (1990).
19. H. Schulz, G. Schaub, M. Claeys and T. Riedel, *Applied Catalysis A: General* **186**, 215 (1999)
20. *Latest LME Cobalt Prices*, London Metal Exchange, updated: 23/02/2011 and accessed: 24/02/2011, < http://www.lme.com/minormetals/Cobalt_Prices.asp>
21. A. de Klerk and E. Furimsky, *Catalysis in the Refining of Fischer-Tropsch Syncrude*, RSC Publishing, Cambridge (2010).
22. K. Woo, S. Kang, S. Kim, J. Bae and K. Jun, *Fuel Process. Technol.*, **91**, 434 (2010).

23. H. R. Khakdaman and K. Sadaghiani, *Chem. Eng. Res. Des.*, **85**, 263 (2007).
24. M. E. Dry, *Catalysis-Science and Technology Volume 1*, Springer-Verlag, Berlin, 159-255 (1981).
25. R. B. Anderson, *The Fischer-Tropsch Synthesis*, Academic Press, New York (1984).
26. T. L. Brown, H. E. Lemay Jr., B. E. Bursten and J. R. Burdge, *Chemistry Central Science 9th Edition*, Pearson Education Inc., New Jersey (2003).
27. R. B. Anderson, *The Fischer-Tropsch Synthesis*, Academic Press, New York (1984).
28. M. E. Dry, *Applied Catalysis A: General* **138**, 319 (1996).
29. M. E. Dry, *Catalysis Today* **6**, 183 (1990)
30. H. Schulz, G. Schaub, M. Claeys and T. Riedel, *Applied Catalysis A: General* **186**, 215 (1999)
31. M. E. Dry, *The Fischer-Tropsch Synthesis in Catalysis-Science and Technology Volume 1*, Springer-Verlag, Berlin (1981).
32. P. J. van Berge, *Studies in Surface Science and Catalysis Volume 107*, Elsevier, Amsterdam (1997).
33. M. E. Dry, *Applied Catalysis A: General* **138**, 319 (1996).
34. I. C. Yates and C. N. Satterfield, *Energy and Fuels* **5**, 168 (1991).
35. B.E. Warren, *X-ray Diffraction*, Addison-Wesley Publishing, Reading (1969).
36. L. V. Azároff, R. Kaplow, N. Kato, R. J. Weiss, A. J. C. Wilson and R. A. Young, *X-ray Diffraction*, McGraw-Hill, New York (1974).
37. H. P. Klug and L. E. Alexander, *X-ray Diffraction Procedures for Polycrystalline and Amorphous Materials*, Wiley, New York (1974).
38. V. K. Pecharsky and P. Y. Zavalij, *Fundamentals of Powder Diffraction and Structural Characterization of Materials*, Kluwer Academic Publishers, Boston (2003).
39. R. E. Dinnebier and S. J. L. Billinge, *Principles of Powder Diffraction* in *Powder Diffraction Theory and Practice*, RSC Publishing, Cambridge (2009).
40. W. L. Bragg, *Proc. Cambridge Philos. Soc.*, **17**, 43 (1913).
41. F. D. Bloss, *Crystallography and Crystal Chemistry. An Introduction*, Holt, Rinehart and Winston, Austin (1971).
42. P. Atkins, T. Overton, J. Rourke, M. Weller and F. Armstrong, *Inorganic Chemistry 4th Edition*, Oxford University Press, United Kingdom (2006).
43. P. P. Ewald, *Acta Crystallogr.*, **A25**, 103 (1969).
44. P. Scherrer, *Gőttinger Nachrichten*, 98 (1918).
45. R. A. Young (Ed.), *The Rietveld Method*, Oxford Science Publications, Oxford (1993).
46. G. Will, *Powder Diffraction: The Rietveld Method and the Two-Stage Method*, Springer-Verlag, Berlin (2006).
47. R. B. Von Dreele, *Rietveld Refinement* in *Powder Diffraction Theory and Practice* (Ed. R. E. Dinnebier and S. J. L. Billinge), RSC Publishing, Cambridge, (2009).
48. H. M. Rietveld, *Acta Crystallogr.*, **22**, 151 (1967).
49. H. M. Rietveld, *J. Appl. Crystallogr.*, **2**, 65 (1969).
50. W. C. Hamilton, *Statistics in Physical Science*, Ronald Press, New York (1964).

51. P. Norby and U. Schwarz, *Powder Diffraction under Non-ambient Conditions* in *Powder Diffraction Theory and Practice*, RSC Publishing, Cambridge (2009).
52. C. Riekel and R. Schollhorn, *Mater. Res. Bull.*, **11**, 369 (1976).
53. A. N. Christensen, M. S. Lehmann and J. Pannetier, *J. Appl. Crystallogr.*, **18**, 170 (1985).
54. A. N. Christensen, H. Fjellvåg and M. S. Lehmann, *Acta Chem. Scand. Ser. A*, **39**, 593 (1985).
55. D. D. L. Chung, P. W. DeHaven, H. Arnold and D. Ghosh, *X-Ray Diffraction at Elevated Temperatures: A Method for in Situ Process Analysis*, John Wiley and Sons, New York (1993).
56. *Technical Note SCD4: Characteristics and Relative Performance of Laboratory X-ray Sources for Protein Crystallography*, Bruker AXS (2007).
57. J. K. Cockcroft and A. N. Fitch, *Experimental Setups* in *Powder Diffraction Theory and Practice*, RSC Publishing, Cambridge (2009).
58. B. S. Clausen, G. Steffensen, B. Fabius, J. Villadsen, R. Feidenhans and H. Topsoe, *J. Catal.*, **132**, 524 (1991).
59. B. S. Clausen, L. Grabaek, G. Steffensen, P. L. Hansen and H. Topsoe, *Catal. Lett.*, **20**, 23 (1993).
60. D. G. Medvedev, A. Tripathi, A. Clearfield, A. J. Celestian, J. B. Parise and J. Hanson, *Chem. Mater.*, **16**, 3659 (2004).
61. Anton Paar GmbH, *J. Appl. Crystallogr.*, **40**, 202 (2007).
62. *X-ray Structure Analysis Products*, Anton Paar GmbH, accessed: 28/02/2011, <http://www.anton-paar.com/X-ray-Structure-Analysis-XRD/59_Corporate_en?productgroup_id=233&X-ray-Structure-Analysis-XRD>
63. *Anton Paar XRK 900 User* Manual, Anton Paar GmbH (2005).
64. B. Herzog, T. Ilkenhans and R. Schlögl, *Fresenius J. Anal. Chem.*, **349**, 247 (1994).
65. M. Muhler, J. Schütze, M. Wesemann, T. Rayment, A. Dent, R. Schlögl and G. Ertl, *J. Catal.*, **126**, 339 (1990).
66. B. Herzog, D. Herein and R. Schlögl, *Appl. Catal. A*, **141**, 71 (1996).
67. A. Nielsen, *Catal. Rev. Sci. Eng.*, **23**, 17 (1981).
68. R. Brill and S. Tauster, *Ber. Bunsen Ges. Phys. Chem.*, **67**, 390 (1963).
69. P. Stoltze and J. Norskov, *Phys. Rev. Lett.*, **55**, 2502 (1985).
70. R. Hosemann and H. Bagchi, *Direct Analysis of Diffraction by Matter*, North-Holland, Amsterdam (1962).
71. W. S. Borghard and M. Boudart, *J. Catal.*, **80**, 194 (1983).
72. H. Topsoe, J. A. Dumesic and M. Boudart, *J. Catal.*, **28**, 477 (1973).
73. W. Niemann, B. S. Clausen and H. Topsoe, *Ber. Bunsen Ges. Phys. Chem.*, **91**, 1292 (1987).
74. R. Schlögl, *Catalytic Ammonia Synthesis - Fundamentals and Practice*, Plenum Press, New York (1991).
75. N. D. Spencer, R. C. Schoonmaker and G. A. Somorjai, *J. Catal.*, **74**, 129 (1982).
76. P. Stoltze and J. Norskov, *Phys. Rev. Lett.*, **55**, 2502 (1985).
77. L. M. Plyasova, T. A. Kriger, A. A. Khassin, and V. N. Parmon, *Dokl. Phys. Chem.*, **382**, 47 (2002).

78. V. N. Parmon, *Kinet. Katal.*, **37**, 476 (1996).
79. A. Barbier, E. Brum Pereira and G. A. Martin, *Catal. Lett.*, **45**, 221 (1997).
80. W. Vogel, *J. Phys. Chem. C*, **112**, 13475 (2008).
81. V. Gnutzmann and W. Vogel, *J. Phys. Chem.*, **94**, 4991 (1990).
82. W. Vogel, *Cryst. Res. Technol.*, **33**, 1141 (1998).
83. W. Vogel, J. Bradley, O. Vollmer and I. Abraham, *J. Phys. Chem. B*, **102**, 10853 (1998).
84. W. Vogel, B. Rosner and B. Tesche, *J. Phys. Chem.*, **97**, 11611 (1993).
85. I. C. Madsen, N. V. Y. Scarletta and B. I. Whittington, *J. Appl. Crystallogr.*, **38**, 927 (2005).
86. B. I. Whittington, R. G. McDonald, J. A. Johnson and D. M. Muir, *Hydrometallurgy*, **70**, 31 (2003).
87. B. I. Whittington, J. A. Johnson, L. P. Quan, R. G. McDonald and D. M. Muir, *Hydrometallurgy*, **70**, 47 (2003).
88. S. E. Colley, R. G. Copperthwaite, G. J. Hutchings, S. P. Terblanche and M. M. Thackeray, *Nature*, **339**, 129 (1989).
89. O. Ducreux, J. Lynch, B. Rebours, M. Roy and P. Chaumette, *Stud. Surf. Sci. Catal.*, **119**, 125 (1998).

CHAPTER 2: EXPERIMENTAL METHODS

2.1. TiO_2 SUPPORTS

Three titania (TiO_2) support materials were used in this study. They were; AEROXIDE TiO_2 P25 (±21 nm, ≥99.5 % purity), produced by Evonik Degussa (referred to as Degussa P25),[1] Anatase (325 mesh, ≥99 % purity),[2] produced by Sigma-Aldrich (referred to as Sigma anatase) and a nano-sized anatase support (referred to as NSA), prepared using the method developed by Sivakumar *et al.*, which is described below.[3]

2.1.1. NSA Synthesis

Titanium(IV) oxysulfate ($TiOSO_4$) [63.972 g (0.400 mol)], produced by Sigma-Aldrich,[4] was dissolved in 2.00 L of distilled water to produce a 0.20 M solution. A 2.85 M aqueous solution of ammonium hydroxide (NH_4OH), produced by Sigma-Aldrich,[5] was added drop wise to the $TiOSO_4$ solution, while stirring at room temperature, until the solution achieved a pH of 7.5. The precipitate, [$TiO(OH)_2$], was separated by filtration, and washed repeatedly with distilled water until no sulfate ions could be detected in the washings, using the barium chloride ($BaCl_2$) test. The precipitate was converted to a stable sol by dispersing it in 4.00 L of distilled water at 90 °C, after which a 1.59 M solution of nitric acid (HNO_3), prepared using Sigma-Aldrich nitric acid with ≥99 % purity,[6] was added drop wise until the sol achieved a pH of 2, causing polymerization of the precipitate. This sol was aged for 12 h at room temperature, after which it was converted to a gel by raising the pH to 6 via the drop wise addition of the aqueous 2.85 M NH_4OH solution. The gel was again aged for 24 h and then dried at 90 °C for 24 h. The product was gently milled to produce a homogeneous white powder.

2.2. CATALYSTS

The incipient wetness impregnation technique was used to load 10 wt% of metal, where the metals were Fe, Co or Ru, onto each of the three TiO_2 support materials to yield 10 g of each catalyst.

2.2.1. 10 % Fe Catalysts

Three, room-temperature saturated solutions of ferric nitrate were prepared by dissolving 7.230 g (18 mmol) ferric nitrate nonahydrate [$Fe(NO_3)_3 \cdot 9H_2O$], Sigma-Aldrich ≥98 % purity,[7] in deionized water. Degussa P25, Sigma anatase and NSA [9.000 g (113 mmol)] were individually added to each of the solutions while stirring. The slurries were stirred for 1 hour and dried at 120 °C for 24 h. The products were gently milled to form homogeneous 10 % Fe/TiO_2 precatalysts (untreated catalysts).

2.2.2. 10 % Co Catalysts

Three, room-temperature saturated solutions of cobalt(II) nitrate were prepared by dissolving 4.938 g (17 mmol) cobalt(II) nitrate hexahydrate [$Co(NO_3)_2 \cdot 6H_2O$], Sigma-Aldrich 98 % purity,[8] in deionized water. Degussa P25, Sigma anatase and NSA [9.000 g (113 mmol)] were individually added to each of the solutions while stirring. The slurries were stirred for 1 hour and dried at 120 °C for 24 h. The products were gently milled to form homogeneous 10 % Co/TiO_2 precatalysts.

2.2.3. 10 % Ru Catalysts

Ruthenium(III) acetate [$Ru(CH_3COO)_3$] was prepared by dissolving 2.051 g (8 mmol) ruthenium(III) chloride trihydrate ($RuCl_3 \cdot 3H_2O$), Sigma-Aldrich technical grade,[9] and 4.036 g (30 mmol) anhydrous sodium acetate (CH_3COONa), Sigma-Aldrich ≥99.0 % purity,[10] in 50 ml absolute ethanol (CH_3CH_2OH), Sigma-Aldrich ACS reagent grade,[11] and 50 ml glacial acetic (CH_3COOH), Sigma-Aldrich ACS reagent grade,[12] and refluxing for 12 h. The solvents were removed by evaporation and the product was purified by ethanol extraction and subsequent evaporation.

Three, room-temperature saturated solutions of $Ru(CH_3COO)_3$ were prepared by dissolving 2.735 g (10 mmol) $Ru(CH_3COO)_3$ in deionized water. Degussa P25, Sigma anatase and NSA [9.000 g (113 mmol)] were individually added to each of the solutions while stirring. The slurries were stirred for 1 hour and dried at 120 °C for 24 h. The products were gently milled to form homogeneous 10 % Ru/TiO_2 powders.

2.3. CATALYST CHARACTERIZATION

2.3.1. X-RAY DIFFRACTION

2.3.1.1. Instrument Configuration

The majority of the *in situ* diffraction experiments were executed on a diffractometer based at the University of the Witwatersrand (WITS). However, a number of experiments were repeated on a similar diffractometer based at the University of Cape Town (UCT) to ensure reproducibility and accuracy.

The instrument based at WITS is a Bruker D8 Advance with a Cu source operated at 40 kV and 40 mA. The X-rays (predominantly $CuK\alpha_1$ with $\lambda = 1.5405929$ Å) produced by the Cu tube pass through a line focus slit (12 mm x 6 mm) and impinge a multi-purpose Göbel mirror transforming the divergent X-ray beam into a quasi-parallel beam. The parallel beam passes through a 2.5 ° soller and a 0.6 mm fixed divergence slit (FDS) before striking the sample. The Göbel mirror was used to increase the incident intensity of the X-ray beam and limit the effects of surface roughness and sample height changes with increasing temperature.[13] The role of the soller and FDS was to decrease axial divergence and to minimize peak shifts and asymmetric peak broadening. The cell used was an Anton Paar XRK 900 (discussed previously), capable of reaching 900 °C at a rate of 10 °C/min and handling pressures of 10 bar.[14] A Makor sample holder was used for both the heat treatment and reduction experiments, the

properties of which are discussed in reference 16. A basic gas reticulation system was installed (Fig. 2.1) to supply the cell with various gases and gas mixtures.

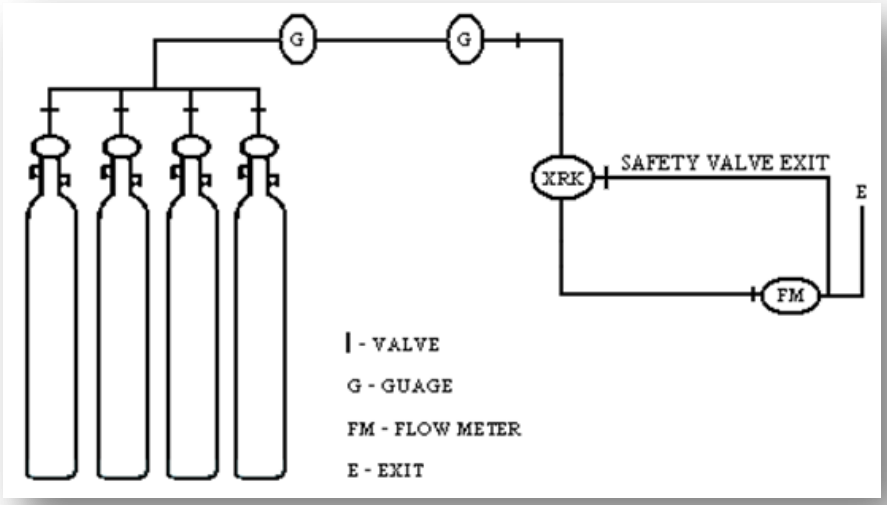

Figure 2.1. Diagrammatic representation of the gas reticulation system that feeds the XRK reaction cell

A 2.5 ° radial soller, a nickel filter and a 3 mm antiscatter slit precede a Bruker VÅntec-1 linear position sensitive detector (PSD), which collects the diffracted X-rays. The detector was operated with a 3 °2θ window. The detector incorporates resistive anode parallel plate avalanche counter (PPAC) technology and operates using the principle that X-ray photons ionize inert gas atoms, such as argon (Ar) or xenon (Xe), liberating electrons, which accelerate towards an anode set to a potential of approximately 1000 V (Fig. 2.2).[15] The accelerating electrons cause further ionization of the gas, which enhances the signal (gas amplification). The amplified electrons can impact multiple readout electrodes (multiple strip detector), positioned in parallel, which determine the angle of incidence of the X-ray photon. To decrease the probability of discharges, a common problem associated with conventional PPAC's, the VÅntec-1 detector incorporates a thin resistive layer, deposited on an insulator placed between the amplification region and the readout electrode, which increases the stability of the detector. A computer using Bruker's *Diffrac*^{Plus} software controls the diffractometer and the XRK 900.[17]

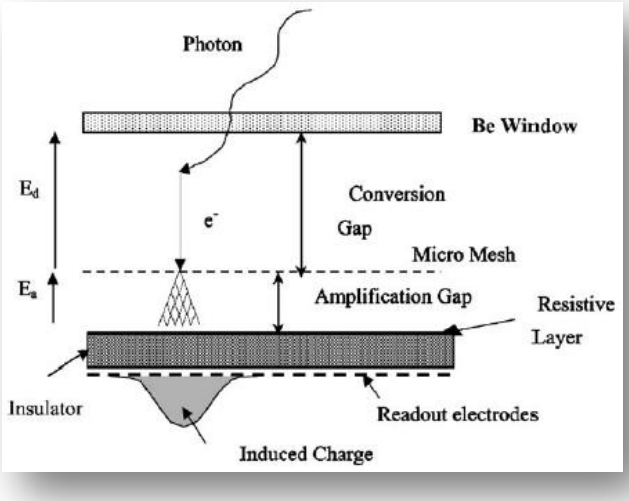

Figure 2.2. Resistive anode PPAC used in the Bruker VÅntec-1 detector[15]

The D8 at UCT employs the use of a cobalt (Co) sealed tube and an iron filter to produce CoKα_1 radiation with λ = 1.78897 Å. Beside these two differences, the two systems were identical.

2.3.1.2. Calibration of the D8 Diffractometer at WITS

The maximum window width of the VÅntec-1 detector is 12 °2-theta, which means that 12 °2-theta can be collected simultaneously, decreasing collection times dramatically. However, the use of such a wide window results in significant peak broadening, due to the detection of X-rays outside the main beam path (axial divergence), resulting in decreased resolution. It was mentioned previously that the VÅntec-1 detector on the WITS D8 was operated using a window width of 6 °2-theta. This width proved to be the best compromise between intensity and resolution.

Lanthanum hexaboride (LaB_6), a cubic $Pm\bar{3}m$ phase prepared by the National Institute for Standards and Technology (NIST), was used as a reference material for benchmarking the diffractometer.[18] This material has a certified lattice parameter of 4.1569162 ± 0.0000097 Å when CuKα_1 radiation, with λ = 1.5405929 Å, is used. A diffraction pattern of the LaB_6 was collected on the WITS D8 and refined using TOPAS and the fundamental parameters approach. The refinement yielded a lattice parameter of 4.1560890 ± 0.0002116 Å, which represents a negligible 0.02 % deviation from the standard reference material (SRM). Figure 2.3 is a plot of the difference between the WITS D8 peak positions and the NIST-certified peak positions (Δ2-theta) as a function of 2-theta. It shows that the accuracy of the peak positions decreases with increasing 2-theta. Bruker reported negligible errors throughout the 2-theta range, while using a highly optimized system and a zero-dimensional detector (scintillation counter).[19] This difference in trends has been observed before and is attributed to the wide collection window of the PSD detector and inflated accuracy of the Bruker results in order to improve sales.[20] However, the fact that the refinement of the WITS D8 data gave the correct lattice parameter, and the fact that the differences between the observed and calculated peak position is so small (0.03 % at most), is enough evidence that the system is well aligned.

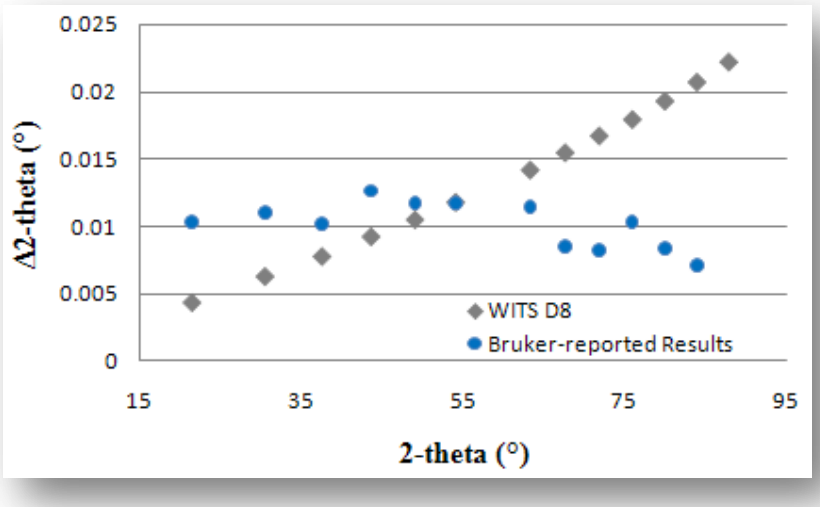

Figure 2.3. The difference between the observed peak position and the certified peak positions of NIST LaB_6 (SRM640a) as a function of 2-theta collected on the WITS D8 and reported by Bruker

Figure 2.4 compares the intensities of the 1 1 0 LaB_6 peak as a function of the FDS size. Small slit sizes provide the best resolution of the $CuK\alpha_1/K\alpha_2$ doublet at the expense of intensity. Since the materials in this investigation are well known and have a large amount of symmetry (few peaks), we chose to use the 0.6 mm slit in order to extract the maximum possible intensity to improve the quantitative analysis statistics.

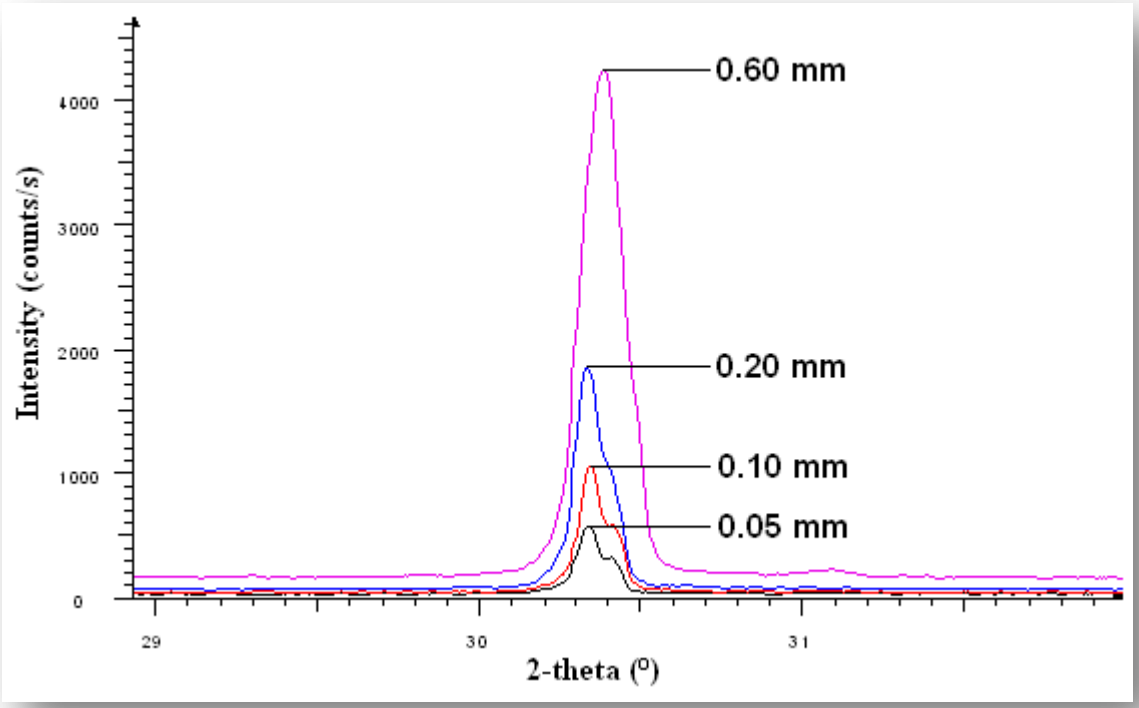

Figure 2.4. The variation in intensity of the LaB_6 1 1 0 peak as a function of (FDS) size

The 2-theta dependence of the full width at half maximum (FWHM) is shown in figure 2.5. The highly optimized Bruker system shows an exponential relationship between FWHM and 2-theta, while the data collected on the WITS D8, using the VÅntec detector and a 0.6 mm FDS, appears to be unaffected over the angular range used in this investigation.

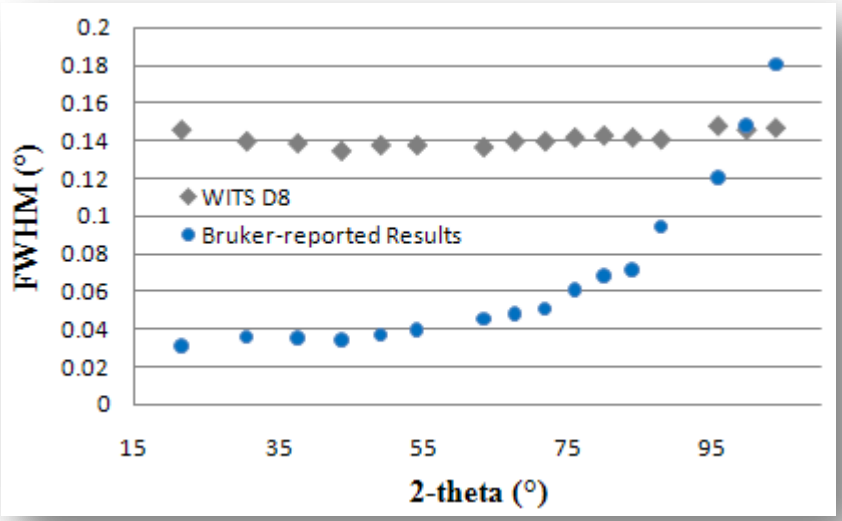

Figure 2.5. 2-theta dependence of FWHM of the optimised Bruker system and the WITS D8

A similar procedure was repeated with silicon (Si), NIST SRM640c, since it was used as an internal standard, or spike, in almost all of the data presented in this work. The certified lattice parameter is 5.4311946 ± 0.0000092 Å, while the refined lattice parameter we obtained was 5.4306793 ± 0.0001068 Å, representing a 0.01 % difference. The difference in calculated (NIST) and refined peak positions is given in figure 2.6 and shows that the differences are even smaller than for the LaB_6 SRM.

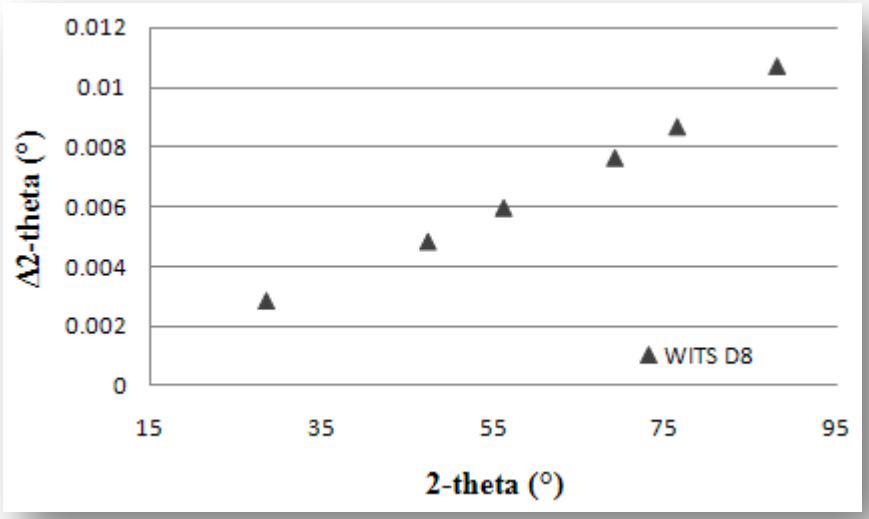

Figure 2.6. The difference between the NIST silicon peak positions and the refined peak positions from the WITS D8

The FWHM values of the NIST Si (Fig. 2.7) show a similar trend to the optimized Bruker data presented for LaB_6 (Fig. 2.5), in that the FWHM increases with increasing 2-theta. Unfortunately, we were unable to find the equivalent set of calibration data performed by Bruker on the NIST Si for reference purposes.

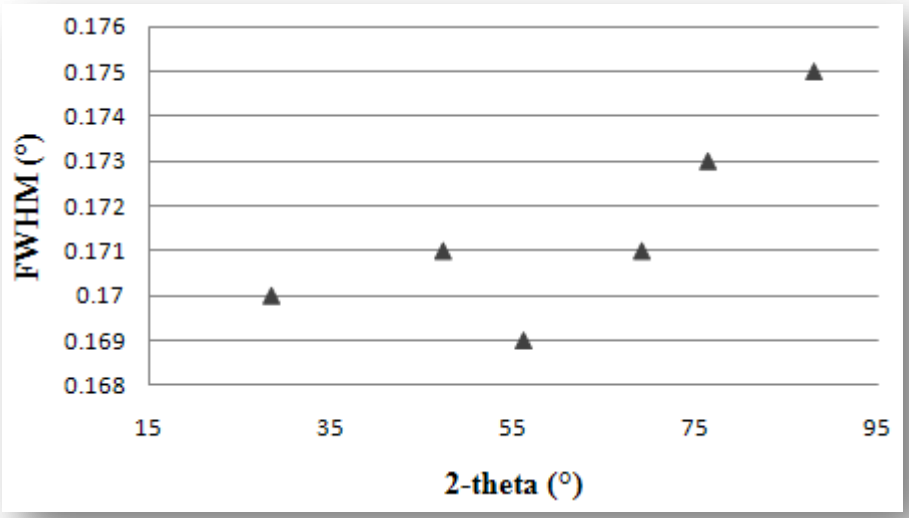

Figure 2.7. The variation of the FWHM of the NIST Si (SRM640c) diffraction peaks, collected on the WITS D8, with increasing 2-theta

2.3.1.3. Calibration of the XRK 900

Temperature calibration of the XRK 900 is usually required, since the thermocouple that measures the "sample temperature" is situated at a distance of approximately 3 mm from the sample. This results in slight temperature variations between the reported temperature and the sample temperature. In order to quantify the difference a reference material with known thermal expansion behaviour is heated in the cell, while diffraction patters are collected at regular temperature intervals. In this case NIST Si was heated under normal ambient conditions from 30 °C to 900 °C in 30 °C intervals, with a diffraction pattern collected at every interval. The diffraction data was then refined using the fundamental parameters approach in TOPAS with seven independent parameters, namely one background coefficient, a histogram scale factor, a single lattice parameter, two crystallite size descriptions, a zero point error description and an absorption correction. Figure 2.8 shows the difference between the calculated NIST Si lattice parameters, determined by Okada and Tokumaru,[21] and our refined values with increasing temperature. It shows that the temperature of the sample is cooler than expected from the thermocouple measurements, i.e. the lattice parameter is smaller than expected, at temperatures below 500 °C and higher than expected at temperatures above 500 °C. However, the largest difference between the lattice parameters, observed at 900 °C, represents a difference in temperature of only 0.52 °C, or 0.06 %, which was considered negligible in this study.

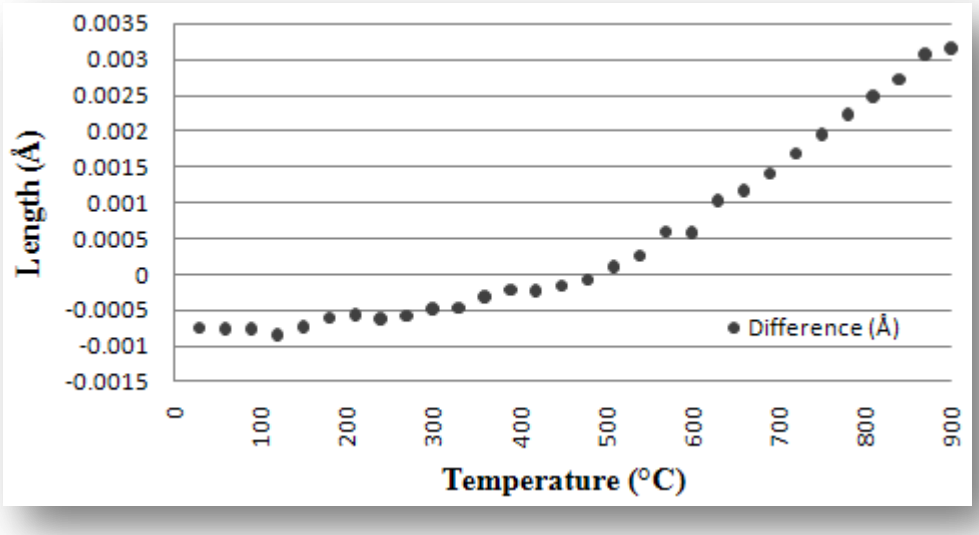

Figure 2.8. The difference between the calculated (Okada and Tokumaru method)[21] and observed lattice parameter of NIST Si with increasing temperature

2.3.1.4. *In situ* PXRD Experiments

Due to the number of *in situ* experiments performed in this study, the details of the diffraction experiments and Rietveld refinements are summarized in tables 2.1 through 2.8. Table 2.1 summarizes the experimental details and parameters used for the *in situ* heat treatment of the three supports. Tables 2.2 through 2.4 summarize the details of the heat treatment experiments on the catalysts, while tables 2.5 through 2.8 summarize the reduction experiments.

An internal standard, in the form of NIST silicon (discussed above), was added to each sample. This is often referred to as spiking, a process which will be discussed in more detail below. The samples were loaded into the Makor sample holder and gently smoothed using a glass slide. The experiments were performed at atmospheric pressure, with compressed air, hydrogen (H_2) or hydrogen/nitrogen mixtures (H_2/N_2), flowing through the sample bed at a rate of 30 ml/min. Reduction experiments required the flow of hot water (90 °C) through the cooling jacket of the XRK to limit condensation of water inside the cell. The temperature parameters in the table show the temperature range of the experiment and incremental increases. These increases represent the temperature difference between each collection. Using the heat treatment of the Degussa P25 support as an example, the first collection would take place at 30 °C, the second at 60 °C (30 °C increment) and so on. The increases in temperature were executed at a rate of 10 °C/min in all of the experiments. The cell was allowed to equilibrate before each collection began. This is referred to as the "equilibration delay" in the tables. The collection and refinement details are also summarized in the tables below and are fairly self-explanatory. More information about the refinement is provided below.

Table 2.1. Experimental details for the in situ heat treatment of the TiO_2 supports

	Degussa P25	Sigma Anatase	NSA
Temperature Range (°C)	30 - 900	400 - 900	30 - 870
Temperature/Collection Increment (°C)	30	30	30
Equilibration Delay (s)	500	500	500
Spike Phase	Silicon	Silicon	Silicon
Spike Concentration (wt%)	10	3	5
Angular Range (° 2θ)	8 - 90	8 - 90	8 - 90
Step Size (°2θ)	0.021	0.021	0.021
Time per step (s)	1	1	1
Number of Patterns Collected	30	18	29
Average Number of Parameters Refined / Pattern	25	30	25
Average Rwp (%)	15.75	11.30	13.99
Average GoF	1.12	1.25	1.12

Table 2.2. Experimental details for the in situ heat treatment of the Fe/TiO_2 catalysts

	Fe/Degussa P25	Fe/Sigma Anatase	Fe/NSA
Temperature Range (°C)	30 - 900	400 - 900	30 - 900
Temperature/Collection Increment (°C)	30	30	30
Equilibration Delay (s)	500	500	500
Spike Phase	Silicon	Silicon	Silicon
Spike Concentration (wt%)	5	10	5
Angular Range (° 2θ)	8 - 90	8 - 90	8 - 90
Step Size (°2θ)	0.021	0.021	0.021
Time per step (s)	1	1	1
Number of Patterns Collected	30	18	30
Average Number of Parameters Refined / Pattern	22	38	27
Average Rwp (%)	10.81	7.82	10.48
Average GoF	1.06	1.12	1.08

Table 2.3. Experimental details for the in situ heat treatment of the Co/TiO_2 catalysts

	Co/Degussa P25	Co/Sigma Anatase	Co/NSA
Temperature Range (°C)	100 - 900	30 - 900	30 - 900
Temperature/Collection Increment (°C)	50	30	30
Equilibration Delay (s)	250	500	500
Spike Phase	Baddeleyite	Silicon	Silicon
Spike Concentration (wt%)	25	3	10
Angular Range (° 2θ)	27 - 119	5 - 90	8 - 90
Step Size (°2θ)	0.029	0.036	0.021
Time per step (s)	1	1.5	1
Number of Patterns Collected	17	30	30
Average Number of Parameters Refined / Pattern	54	33	21
Average Rwp (%)	4.66	6.41	2.86
Average GoF	1.24	1.08	1.03

Table 2.4. Experimental details for the in situ heat treatment of the Ru/TiO_2 catalysts

	Ru/Degussa P25	Ru/Sigma Anatase	Ru/NSA
Temperature Range (°C)	30 - 900	30 - 900	30 - 900
Temperature/Collection Increment (°C)	30	30	30
Equilibration Delay (s)	500	500	500
Spike Phase	Baddeleyite	Silicon	Silicon
Spike Concentration (wt%)	25	5	10
Angular Range (° 2θ)	8 - 90	8 - 90	8 - 90
Step Size (°2θ)	0.021	0.021	0.021
Time per step (s)	1	1	1
Number of Patterns Collected	30	30	30
Number of Patterns Refined	30	16	30
Average Number of Parameters Refined / Pattern	59	34	45
Average Rwp (%)	20.01	6.05	5.47
Average GoF	1.12	1.24	1.16

Table 2.5. Experimental details for the in situ reduction of the Fe/Degussa P25 catalyst that was incorrectly calcined at 600 °C

	Fe/Degussa P25 - Incorrectly Calcined at 600 °C		
	5%H2/N2	10%H2/N2	100%H2/N2
Temperature Range (°C)	100 - 540	100 - 540	100 - 540
Temperature/Collection Increment (°C)	20	20	20
Equilibration Delay (s)	250	250	250
Spike Phase	Silicon	Silicon	Silicon
Spike Concentration (wt%)	5	5	5
Angular Range (° 2θ)	20 - 85	20 - 50	20 - 85
Step Size (°2θ)	0.021	0.036	0.021
Time per step (s)	1	3.5	1
Number of Patterns Collected	23	23	23
Average Number of Parameters Refined / Pattern	34	31	31
Average Rwp (%)	9.79	5.10	9.42
Average GoF	1.04	1.13	1.05

Table 2.6. Experimental details for the in situ reduction of the Fe/TiO_2 catalysts

	Fe/Degussa P25	Fe/Sigma Anatase	Fe/NSA
Temperature Range (°C)	100 - 540	100 - 540	100 - 323 (hold)
Temperature/Collection Increment (°C)	20	20	20
Gas (atmospheric pressure)	H2	H2	H2
Equilibration Delay (s)	250	250	250
Spike Phase	Silicon	Silicon	Silicon
Spike Concentration (wt%)	5	10	5
Angular Range (° 2θ)	20 - 85	20 - 85	20 - 85
Step Size (°2θ)	0.021	0.021	0.021
Time per step (s)	1	1	1
Number of Patterns Collected	23	23	23
Average Number of Parameters Refined / Pattern	31	32	21
Average Rwp (%)	4.12	4.65	4.18
Average GoF	1.13	1.22	1.23

Table 2.7. Experimental details for the in situ reduction of the Co/TiO_2 catalysts

	Co/Degussa P25	Co/Sigma Anatase	Co/NSA
Temperature Range (°C)	100 - 500	100 - 540	100 - 310 (search)
Temperature/Collection Increment (°C)	20	20	20 & 1
Gas (atmospheric pressure)	H2	H2	H2
Equilibration Delay (s)	250	250	250
Spike Phase	Baddeleyite	Silicon	Silicon
Spike Concentration (wt%)	25	3	10
Angular Range (° 2θ)	25 - 120	20 - 85	20 - 85
Step Size (°2θ)	0.029	0.021	0.021
Time per step (s)	1	1	1
Number of Patterns Collected	21	23	21
Average Number of Parameters Refined / Pattern	51	31	21
Average Rwp (%)	4.16	3.56	3.09
Average GoF	1.27	1.19	1.08

Table 2.8. Experimental details for the in situ reduction of the Ru/TiO_2 catalysts

	Ru/Degussa P25	Ru/Sigma Anatase	Ru/NSA
Temperature Range (°C)	100 - 540	100 - 540	100 - 540
Temperature/Collection Increment (°C)	20	20	20
Gas (atmospheric pressure)	H2	H2	H2
Equilibration Delay (s)	250	250	250
Spike Phase	Baddeleyite	Silicon	Silicon
Spike Concentration (wt%)	25	5	10
Angular Range (° 2θ)	20 - 85	20 - 85	20 - 85
Step Size (°2θ)	0.021	0.021	0.021
Time per step (s)	1	1	1
Number of Patterns Collected	23	23	23
Average Number of Parameters Refined / Pattern	62	27	28
Average Rwp (%)	5.49	6.19	5.91
Average GoF	1.36	1.24	1.19

2.3.1.5. Benchtop Bruker D2 Diffractometer

A very small number of diffraction patterns were collected on a benchtop Bruker D2 diffractometer equipped with a sealed Cu tube, operated at 30kV and 10mA. The D2 employs the use of a LynxEye PSD detector (angular range of 5 °) with primary and secondary beam radial soller slits (2.5 °) and a secondary beam nickel filter. The measuring circle of the instrument is set at a constant value of 141.4 mm.

2.3.1.6. Input Files and Refinement Parameters

A refined TOPAS input file, for the first diffraction pattern (at 30 °C) collected during the heat treatment of the Degussa P25 support, is given as an example with accompanying explanations (Fig. 2.9). Green text is used for names, such as file names, structure names and space group names. Light blue text represents parameters that are not to be refined. The figures of merit are not refinable parameters but rather measures of the accuracy of the refinement, so they can change. Red text represents parameters that are to be refined, where @ is the refine operator in TOPAS. This example contains 19 independent parameters. All other input files are merely variations of this with minor differences in the number of parameters, due to the different types and number of structures and preferred orientation parameters that are often required for certain phases due to their morphology. The data (raw) files and refinement or project (pro) files can be found on the CD submitted with this thesis.

The number of refinable parameters was kept as low as possible for every refinement. The errors associated with each parameter (also calculated by TOPAS) were monitored in order to ensure that the standard deviation was always less than 10 %, ensuring the accuracy of the refinement.

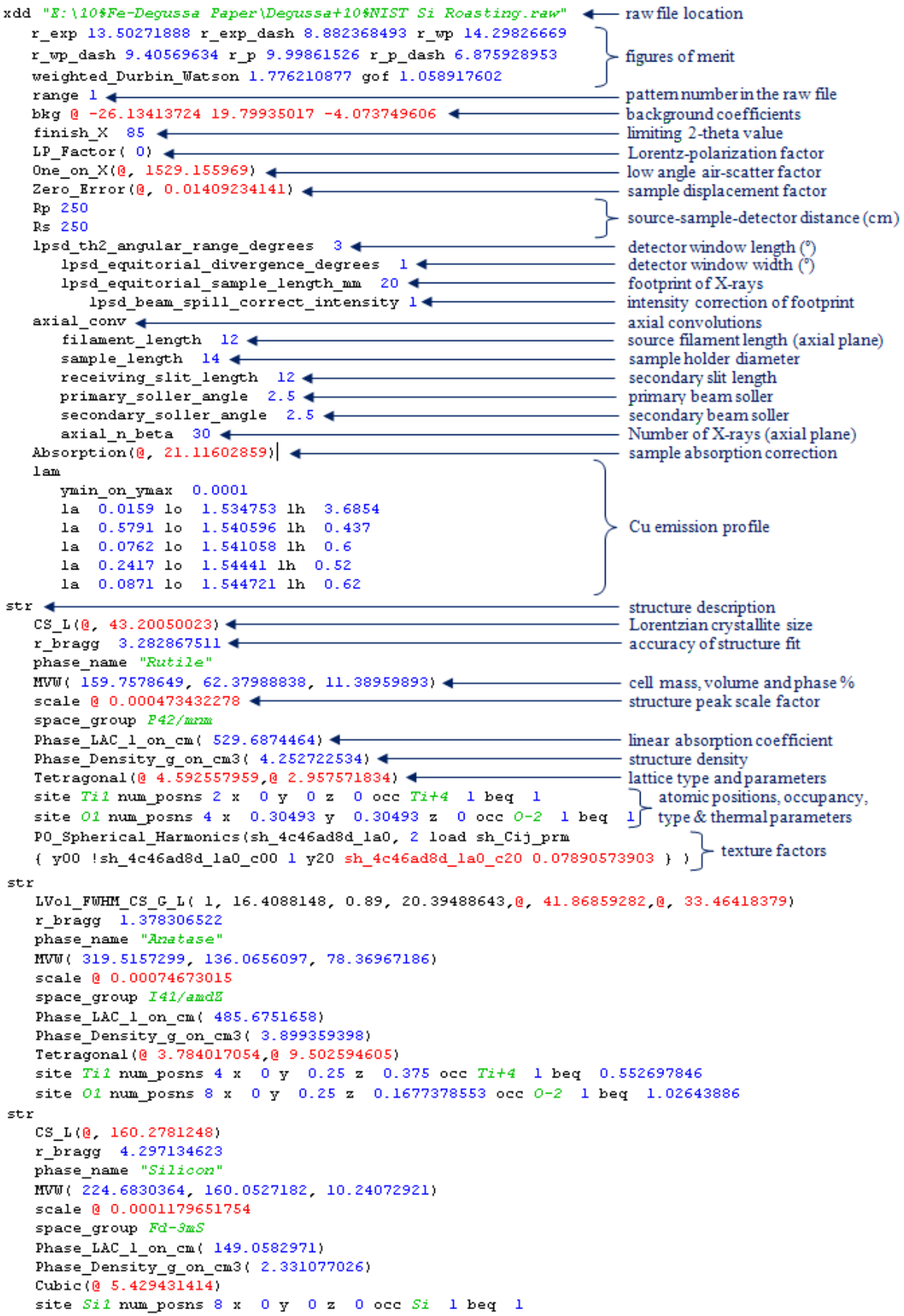

Figure 2.9. Example of a TOPAS input file used to refine the pattern collected from the Degussa P25 support at 30 °C

2.3.1.7. Rietveld-based Quantitative Phase Analysis (QPA)

Although the Rietveld method was initially developed for the refinement of crystal structures and structure solution, some of the non-structural parameters used in the refinement provide non-structural information. The most important of these parameters, for this work, is the Rietveld scale factor, which relates to the amount of a particular phase in a multiphase mixture (denoted "scale" in each of the structure files in figure 2.9).[22]

The integrated intensity (I) of an *hkl* reflection for phase α in a multiphase mixture can be calculated using:

$$I_{(hkl)\alpha} = \left[\frac{I_0\lambda^3}{32\pi r}\frac{e^4}{m_e^2c^4}\right]\cdot\left[\frac{M_{hkl}}{2V_\alpha^2}\left|F_{(hkl)\alpha}\right|^2\left(\frac{1+\cos^2 2\theta\cos^2 2\theta_m}{\sin^2\theta\cos\theta}\right)\right]\cdot\left[\frac{W_\alpha}{p_\alpha\mu_m^*}\right] \qquad \textbf{(71)}$$

where I_0 is the incident beam intensity, e is the charge on an electron, m_e is the mass of an electron, r is the distance from the scattering electron and the detector, c is the speed of light, M is the multiplicity of the *hkl* reflection, V is the unit cell volume, F is the structure factor of the *hkl* reflection, θ and θ_m are the diffraction angles for the *hkl* reflection and monochromator respectively, W_α is the weight fraction, p_α is the density of phase α and μ_m^* is the mass absorption coefficient of the sample.[22] The expression in the first square bracket in equation **(71)** describes the instrumental setup and can, therefore, be reduced to a constant during QPA. The expression in the second square bracket is a constant for reflection *hkl* of phase α. Equation **(71)** can, therefore, be rewritten as:

$$I_{i\alpha} = C_{i\alpha}\frac{W_\alpha}{p_\alpha\mu_m^*} \qquad \textbf{(72)}$$

where $I_{i\alpha}$ is the intensity of a reflection, or group of reflections (i), $C_{i\alpha}$ is a constant that combines both the instrumental and reflection expressions for a given reflection. Equation **(72)** can be rewritten using the fact that the constant C is inversely proportional to V^2, I is proportional to the Rietveld scale factor (S)[23] and the density of a phase can be calculated using:

$$p_\alpha = 1.6604\cdot\frac{ZM_\alpha}{V_\alpha} \qquad \textbf{(73)}$$

where Z is the number of formula units in the unit cell, M_α is the molecular mass of the formula unit and 1.6604 is the conversion factor from AMU.Å^{-3} to g.cm^{-3}. The resultant formula for QPA is therefore:

$$W_\alpha = \frac{S_\alpha(ZMV)_\alpha\mu_m^*}{K} \qquad \textbf{(74)}$$

where K is a scaling factor that is used to present W_α on a absolute basis. It has been shown that K is dependant only on the instrumental conditions and not on phase and sample-related parameters.[24] K is usually determined by performing a single measurement on a standard mixture, referred to as an external standard, where the weight fraction (W) of a particular phase is known. The calculated value for K is then used to determine W_α as long as the unknown sample is run under exactly the same instrumental conditions as the external standard.[22]

The need to measure K and μ_m^* can be eliminated by the addition of a known amount, W_s, of an internal standard (also referred to as a spike), s, to the unknown sample, in this case our supports and catalysts. Taking the ratio of W_α to W_s eliminates K and μ_m^* to give:

$$W_\alpha = W_s \frac{S_\alpha (ZMV)_\alpha}{S_s (ZMV)_s} \quad \textbf{(75)}$$

Hill and Howard[25] applied Chung's matrix flushing method[26-27] to Rietveld analysis and were able to show that W_α in a mixture made up of n phases can be given by:

$$W_\alpha = W_s \frac{S_\alpha (ZMV)_\alpha}{\sum_{k=1}^{n} S_k (ZMV)_k} \quad \textbf{(76)}$$

This method normalizes the sum of the analyzed weight fractions to 1.0. If the sample contains amorphous phases and/or minor concentrations of unidentified crystalline phases, the analyzed weight fractions will be overestimated. The inclusion of an internal standard allows for the modification of the measured W_α's via:

$$W_{\alpha(\text{abs})} = W_\alpha \times \frac{W_{s(\text{known})}}{W_{s(\text{measured})}} \quad \textbf{(77)}$$

and:

$$W_{(\text{unkown})} = 1.0 - \sum_{k=1}^{n} W_{k(\text{abs})} \quad \textbf{(78)}$$

giving absolute, rather than relative, phase percentages of all the crystalline phases present in the sample as well as an "amorphous" value for the total amount of amorphous materials and/or unidentified crystalline phases.

2.3.2. TRANSMISSION ELECTRON MICROSCOPY (TEM)

2.3.2.1. Low Resolution TEM

An FEI Tecnai Spirit TEM in BioTWIN lens configuration with a tungsten (W) filament, operated at 120 kV, was used to collect the majority of TEM images in this study.[28-29] Samples were loaded onto holey carbon films for analysis.

2.3.2.2. High Resolution TEM (HRTEM)

HR-TEM images were collected on an FEI Tecnai G2 F20 XTWIN STEM, based at the University of the Western Cape (UWC), with a tungsten filament operated at 200 kV, giving a point to point resolution limit of 1.9 Å.[30] The standard bright field imaging system houses a 4 k chip with an area of 2048x2048 pixels. Images were collected in spot-size 1 with beam spread to ensure low-dose conditions at 200 kV. Images were collected at (or as close to) the Sherzer defocus setting of the microscope. Samples were loaded onto holey carbon films for analysis.

2.3.3. THERMOGRAVIMETRIC ANALYSIS (TGA)

All TGA experiments were performed on a PerkinElmer TGA 4000 with a 45-position sample holder. The experiments were performed under atmospheric conditions in the 30-900 °C temperature range.[31] The sample was heated at a rate of 10 °C/min with measurements collected at a rate of 130 measurements/min.

2.3.4. SOFTWARE USED TO ANALYZE AND PRESENT DATA

- *Bruker AXS Evaluation Suite (EVA)*

  The diffraction data, plotted in 2- and 3-dimensions, presented in this study was prepared using the EVA software.[32]

- *Structural Databases*

  The search-match functionality in EVA used the Powder Diffraction File - 2 (PDF-2) database (2004 release), distributed by the International Center for Diffraction Data (ICDD).[33] Crystallographic information files (cif files) were obtained from the Inorganic Crystal Structure Database (ICSD – 2010 release) and used as initial structure files in the refinements.[34]

- *Diamond 3.2f*

  All structural diagrams presented in this study were generated using Crystal Impact's Diamond software (version 3.2f).[35]

- *Bruker AXS TOPAS 4.2*

  All Rietveld refinements were performed using TOPAS (version 4.2) in graphical user interface (GUI) mode.[36]

- *Gatan Microscopy Suite (GMS)*

  The GMS includes the DigitalMicrograph software, used to capture the digital TEM images.[37]

- *Image Processing and Analysis in Java (ImageJ)*

  ImageJ was used to convert the TEM images, in dm3 format, to jpg format for presentation in this thesis.[38]

- *PerkinElmer Pyris*

  PerkinElmer Pyris software, version 9.1.0.0202, was used to collect the TGA data.[39]

2.4. REFERENCES

1. *Information for AEROXIDE® TiO_2 P 25*, Evonik Industries, accessed: 04/03/2011, <http://www.aerosil.com/lpa-productfinder/page/productsbytext/faces/productdetails_1.jsp>
2. *Titanium(IV)oxide, anatase*, Sigma-Aldrich, accessed: 04/03/2011, <http://www.sigmaaldrich.com/catalog/ProductDetail.do?lang=en&N4=248576|ALDRICH&N5=SEARCH_CONCAT_PNO|BRAND_KEY&F=SPEC>
3. S. Sivakumar, P. Krishna Pillai, P. Mukundan and K. G. K. Warrier, *Mater. Lett.*, **57**, 330 (2002).
4. *Titanium(IV)oxysulfate*, Sigma-Aldrich, accessed: 04/03/2011, <http://www.sigmaaldrich.com/catalog/ProductDetail.do?lang=en&N4=14023|SIAL&N5=SEARCH_CONCAT_PNO|BRAND_KEY&F=SPEC>
5. *Ammonium hydroxide solution (10 % in H_2O)*, Sigma-Aldrich, accessed: 04/03/2011, < http://www.sigmaaldrich.com/catalog/ProductDetail.do?lang=en&N4=17837|FLUKA&N5=SEARCH_CONCAT_PNO|BRAND_KEY&F=SPEC>
6. *Nitric Acid (ACS reagent ≥ 90 %)*, Sigma-Aldrich, accessed: 04/03/2011, < http://www.sigmaaldrich.com/catalog/ProductDetail.do?lang=en&N4=258121|SIAL&N5=SEARCH_CONCAT_PNO|BRAND_KEY&F=SPEC>
7. *Iron(III)nitrate nonahydrate*, Sigma-Aldrich, accessed: 04/03/2011, < http://www.sigmaaldrich.com/catalog/ProductDetail.do?lang=en&N4=F3002|SIAL&N5=SEARCH_CONCAT_PNO|BRAND_KEY&F=SPEC>
8. *Cobalt(II)nitrate hexahydrate*, Sigma-Aldrich, accessed: 04/03/2011, < http://www.sigmaaldrich.com/catalog/ProductDetail.do?lang=en&N4=230375|SIAL&N5=SEARCH_CONCAT_PNO|BRAND_KEY&F=SPEC>
9. *Ruthenium (III)chloride trihydrate*, Sigma-Aldrich, accessed: 04/03/2011, <http://www.sigmaaldrich.com/catalog/ProductDetail.do?lang=en&N4=10452|ALDRICH&N5=SEARCH_CONCAT_PNO|BRAND_KEY&F=SPEC>
10. *Anhydrous sodium acetate*, Sigma-Aldrich, accessed: 04/03/2011, <http://www.sigmaaldrich.com/catalog/ProductDetail.do?lang=en&N4=S8750|SIAL&N5=SEARCH_CONCAT_PNO|BRAND_KEY&F=SPEC>
11. *Ethanol ACS reagent*, Sigma-Aldrich, accessed: 04/03/2011, < http://www.sigmaaldrich.com/catalog/ProductDetail.do?lang=en&N4=459844|SIAL&N5=SEARCH_CONCAT_PNO|BRAND_KEY&F=SPEC>

12. *Glacial acetic acid, ACS reagent*, Sigma-Aldrich, accessed: 04/03/2011, <http://www.sigmaaldrich.com/catalog/ProductDetail.do?lang=en&N4=242853|SIAL&N5=SEARCH_CONCAT_PNO|BRAND_KEY&F=SPEC>
13. Bruker AXS, *Spec Sheet XRD 30: Göbel Mirrors Properties and Potentials*, Karlsruhe (2007).
14. *Reactor Chamber: XRK 900*, Anton Paar GmbH, accessed: 05/03/2011, <http://www.anton-paar.com/Reactor-Chamber-XRK-900/X-ray-Structure-Analysis-XRD/60_Corporate_en?product_id=138>
15. M. Kocsis, P. Boesecke, D. Carbone, C. Herve, B. Becker, Y. Diawara, R. Durst, D. Khazins, B. He, S. Medved, V. Sedov, T. Thorson and G. Wachter, *Nucl. Instrum. Methods Phys. Res. A*, **563**, 172 (2006).
16. Corning, *Makor Machinable Glass Ceramic Technical Information* (2001).
17. *Diffrac^{Plus} v4.0: Software for Controlling Bruker Diffractometers*, Bruker AXS, Karlsruhe (1998).
18. J.P. Cline, R.D. Deslattes, J. Staudenmann, L.T. Hudson, A. Henins and R.W. Cheary, *NIST Standard Reference Material 660a: LaB_6 Powder as a Line Position and Line Shape Standard for Powder Diffraction*, Gaithersburg (2000).
19. *Evaluation of the D8 Advance Diffractometer using the NIST LaB_6 Line Position and Profile Shape standard (SRM660a)*, Bruker AXS, Karlsruhe (1998).
20. S. Allen, *Ph.D. Thesis: Thermoresponsive Behaviour of AM_2O_8 Materials*, Durham University (2003).
21. Y. Okada and Y. Tokumaru, *J.Appl. Phys.*, **56**, 314 (1984).
22. I. C. Madsen and N. V. Y. Scarlett, *Quantitative Phase Analysis* in *Powder Diffraction Theory and Practice* (Ed. R. E. Dinnebier and S. J. L. Billinge), RSC Publishing, Cambridge, (2009).
23. R. J. Hill, *Powder Diff.*, **6**, 74 (1991).
24. B. H. O'Connor and M. D. Raven, *Powder Diff.*, **3**, 2 (1988).
25. R. J. Hill and C. J. Howard, *J. Appl. Crystallogr.*, **20**, 467 (1987).
26. F. H. Chung, *J. Appl. Crystallogr.*, **7**, 519 (1974).
27. F. H. Chung, *J. Appl. Crystallogr.*, **7**, 526 (1974).
28. *Tecnai Spirit TEM Next Generation Microscopy for Life Sciences*, FEI, Oregon (2009).
29. *Tecnai Spirit Transmission Electron Microscope*, FEI, accessed: 09/03/2011, <http://www.fei.com/products/transmission-electron-microscopes/tecnai-spirit.aspx>
30. K. Ravenberg, *Keeping Pace in the Innovation Race*, FEI, Oregon (2008).
31. *TGA 4000*, PerkinElmer, accessed: 09/03/2011, <http://las.perkinelmer.com/Catalog/ProductInfoPage.htm?ProductID=N5370210>
32. *DIFFRAC.EVA: The Next Era in Phase Analysis*, Bruker AXS, Karlsruhe (2010).
33. *The International Center for Diffraction Data*, ICDD, accessed: 09/03/2011, <http://www.icdd.com/>
34. *ICSD – Inorganic Crystal Structure Database*, FIZ Karlsruhe, updated 19/10/2010 accessed: 09/03/2011, <http://www.fiz-karlsruhe.de/icsd.html>
35. W. T. Pennington, *J. Appl. Cryst.*, **32**, 1028 (1999).
36. A. A. Coelho, *TOPAS v4.2: General Profile and Structure Analysis Software for Powder Diffraction Data*, Bruker AXS, Karlsruhe (2007).

37. *Software Products*, Gatan Inc., accessed: 09/03/2011, <http://www.gatan.com/products/software/>
38. *Image Processing and Analysis in Java (ImageJ)*, ImageJ, accessed: 09/03/2011, <http://rsbweb.nih.gov/ij/>
39. *Pyris Software*, PerkinElmer, Massachusetts (2004).

CHAPTER 3 – RESULTS AND DISCUSSION

3.1. *IN SITU* HEAT TREATMENT OF SUPPORTS

The term "heat treatment" in this study refers to the heating of a sample from 30 °C to 900 °C in the presence of air, usually at atmospheric pressure and flowing at a rate of 30 ml/min through a sample. The heat treatment of Degussa P25 (the first support of interest) will be used as an example, in order to show the vast quantity of data that can be extracted from Rietveld refinement procedures. A discussion of this amount of data for each experiment performed would be overwhelming and extremely tedious to read. For this reason only data that highlights important properties or occurrences different from the norm are presented here. The heat treatment experiments performed on each sample will be divided into the following sections; Preliminary Discussion, Quantitative Analysis and Particle Size Analysis.

3.1.1. DEGUSSA P25

Preliminary Discussion

Degussa P25 is, by far, the most industrially important titania (TiO_2) support and, therefore, is the most logical place to begin the discussion. Degussa P25 is a mixture of two TiO_2 phases, namely anatase (tetragonal, *I*41/*amds*), which is comprised of highly distorted, edge-sharing TiO_2 octahedra,[1] and rutile (tetragonal, *P*42/*mnm*), which is comprised of undistorted, corner- and edge-sharing TiO_2 octahedra (Fig. 3.1).[2] The anatase to rutile ratio in Degussa P25 is usually in the region of 7:1, however, heat treatment procedures can affect the ratio, since anatase undergoes a solid-state phase transition to form the thermodynamically stable rutile phase after moderate energy input. The exact temperature at which the phase transition occurs is sample related, since factors such as impurities,[3-8] particle size,[9-12] pressure[13] and dopants,[14] have been shown to increase and decrease the temperature of the phase transition to varying degrees. There are, in fact, many different phases of titania that are stable under various conditions but the three most common phases are anatase, rutile and brookite (orthorhombic, *Pbca*). Brookite is thought to be the least stable of the three phases, transforming to anatase with little energy input.[15]

For a support to be useful in catalytic systems it must be stable under reactor conditions. Therefore, there should be no phase changes in the support at temperatures below and slightly above the reaction temperature of interest. Phase changes in the support could lead to accelerated catalyst deactivation and loss of profitability in metal/TiO_2 systems. Support-related deactivation of catalysts can occur due to a decrease in the surface area of the support, artificially sintering active metal particles leading to a decrease in activity and/or selectivity. Another deactivation route involves absorption of the metal catalyst by the support to form metal-support product phases such as metal titanates.

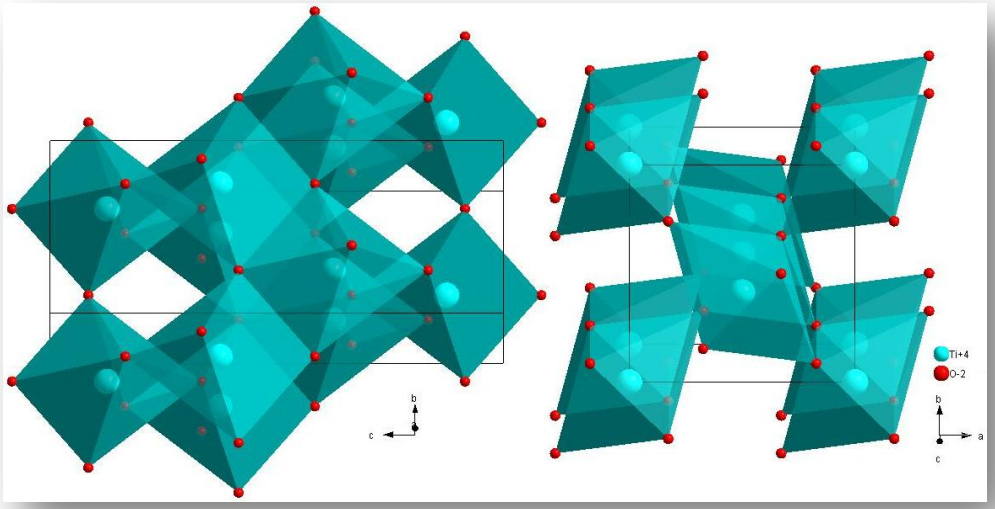

Figure 3.1. Crystallographic representations of anatase (tetragonal, I41/amds)[1] *and rutile (tetragonal, P42/mnm)*[2] *generated using DIAMOND 3.2f* [16]

Quantitative Analysis

Variable-temperature PXRD data is usually presented using three dimensions (Fig. 3.2). In this procedure a plot of intensity vs. 2-theta is shown as a function of increasing temperature or time. However, some of the detail, especially during the phase changes, may be lost in this orientation. In order to avoid this issue, the diffraction results can be displayed in two dimensions (Fig. 3.3), where a topographical view of the intensities of peaks is depicted in a colour code and the intensity axis, or y axis, is replaced by the pattern number or temperature at which the pattern was measured. This type of view is referred to as an intensity profile in this work. It is important to note that phases with low concentrations that develop during the experiment will have small diffraction peaks that may be lost in the background when using this orientation. A crystalline spike, either in the form of cubic silicon (Si) or monoclinic baddeleyite (ZrO_2), was added to every sample in order to calculate any amorphous material within the sample via methods mentioned previously.

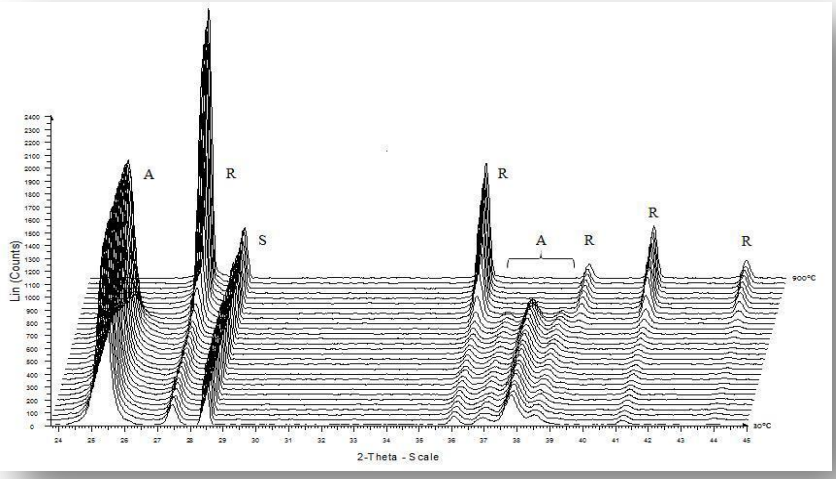

*Figure 3.2. 3-Dimensional view of the PXRD patterns collected during the heat treatment of Degussa P25, containing a 10 % silicon spike (**A** – anatase, **R** – rutile and **S** – silicon)*

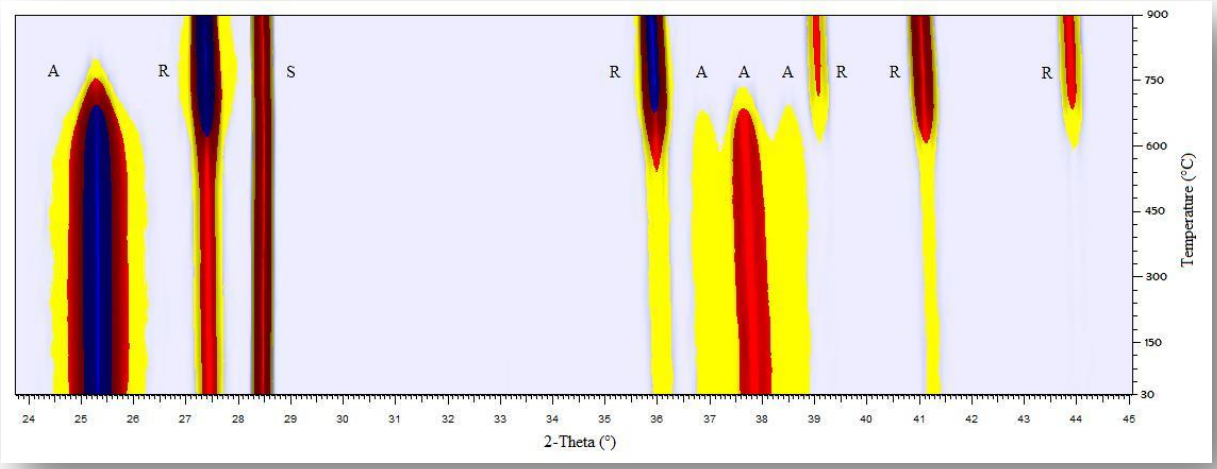

Figure 3.3. 2-Dimensional, or intensity profile, view of PXRD patterns collected during the heat treatment of the Degussa P25 support containing a 10 % silicon spike: ***A*** *– anatase,* ***R*** *– rutile and* ***S*** *– silicon*

Visual inspection of figures 3.2 and 3.3 suggests that anatase undergoes a phase transition to rutile at a temperature in the region of 540 °C, judging from the increase in peak intensity of the 0 1 1 rutile peak at 36.1 ° 2-theta. The speciation graph prepared using the quantitative results of the Rietveld refinement (Fig. 3.4) indicates that the anatase to rutile phase transition began at a temperature between 480 °C and 510 °C, although the curvature in the plot can lead to some uncertainty in the temperature range. The phase transition was complete at 810 °C, when no anatase peaks could be detected.

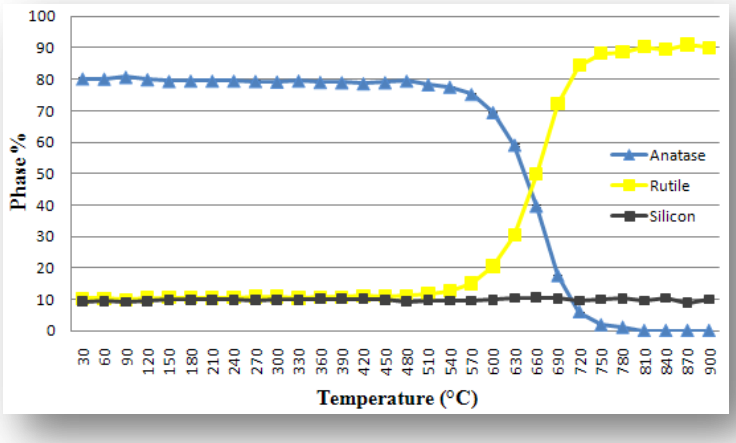

Figure 3.4. Phase composition of Degussa P25, containing a 10 % silicon spike, during heat treatment (average GoF value of 1.08)

It is important to note that the diffraction patterns collected during the phase transitions do not represent the sample at equilibrium, since the phase transition will continue while the diffraction pattern is collected, assuming that the transition is spontaneous at that temperature. However, the sample was allowed to "equilibrate" at each temperature interval for a minimum of five minutes before data collection began. It is also important to note that solid-state phase transitions are relatively slow at constant temperatures when compared to solution kinetics and can, therefore, be considered to be in some sort of semi-equilibrated state.

In this experiment, the silicon concentration was accurately calculated for each refinement in the series and, therefore, did not require constraint. It will be shown later that this was not always the case and constraint of the silicon percentage was sometimes required. This allowed the concentration of amorphous material present in the sample to be calculated.

Calculation of the derivative $\left(\frac{dy}{dx}\right)$ of the curves presented in figure 3.4 provides information on the instantaneous rates of change of phase concentrations as a function of temperature (Fig. 3.5), with the units %/°C, similar to that of a rate equation with units of mol/s. This graph provides a means for a more accurate determination of the start of a phase transition, since one can distinguish an increase in the rate of rutile formation (positive values) with an equal decrease in the rate of consumption of anatase (negative values) at temperatures of 510 °C and above. This indicates that our initial assessment of the transition temperature, of between 480 °C and 510 °C, was correct. The initial rate of rutile formation was slow but gradually gained momentum at higher temperatures, reaching a maximum of 0.7 %/°C at 690 °C, i.e. three and a half times faster than at 480 °C. The rate of formation of rutile should equal the rate of consumption of anatase, since this is a direct phase transition. This was the case, since the curve for anatase consumption is a mirror image of the rutile formation curve.

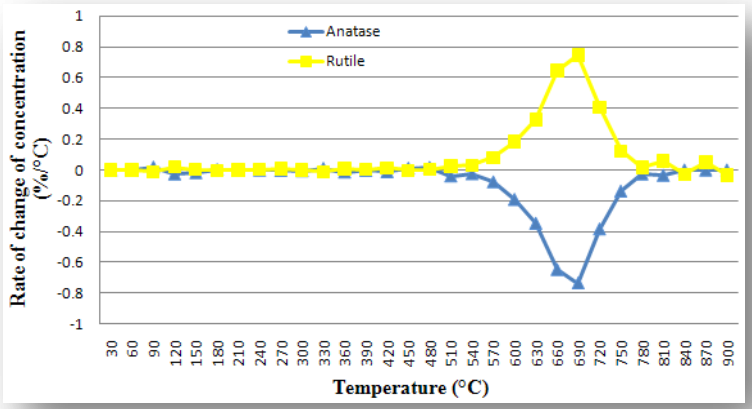

Figure 3.5. Instantaneous rates of change of concentration of anatase and rutile as a function of temperature during the heat treatment of Degussa P25

The quantitative data presented above has little meaning if the quality of the refinement is not reported. This is especially important since the Rietveld method is highly sensitive to user skill and understanding of the process. An excellent example of the user sensitivity of the Rietveld method was the incorrect refinement of γ-quinacridone using structural data for β-quinacridone, which had entirely different lattice parameters, molecular packing and molecular conformation when compared to the actual structure of γ-quinacridone (determined by single crystal XRD), even though the Rietveld method suggested that the structure was entirely reasonable.[17] Fortunately, the phases present in the samples discussed in this study are unambiguous and well known and there should be little problem identifying and monitoring the phases and the changes they undergo.

It is no simple task presenting figures of merit for these types of refinements, due to the large number of diffraction patterns collected and refined in a single file. One may encounter images like that presented in figure 3.6, where an individual pattern has been refined and the difference curve between the calculated and observed patterns is clearly seen. Figure 3.7 shows all of the calculated, observed and a difference pattern generated during the refinement of the 30 diffraction patterns and demonstrates the inadequacy of this type of presentation for variable-temperature data. For this reason, graphs of the GoF (Fig. 3.8), R_{exp} and R_{wp} (Fig. 3.9) values of each refinement could be generated to give an idea of the accuracy of the refinements at ever increasing temperatures. GoF is a function of R_{wp} and R_{exp} ($GoF = \frac{Rwp}{Rexp}$) and if refinements are completed accurately, the GoF value should remain relatively constant throughout the temperature range. For this reason GoF values will be averaged over the entire temperature range and quoted as such (Fig. 3.4). The Rwp and GoF graphs are useful during the refinement process, since any deviation from a relatively consistent value or slope, especially for GoF, indicates an omission or error made during the refinement of that pattern.

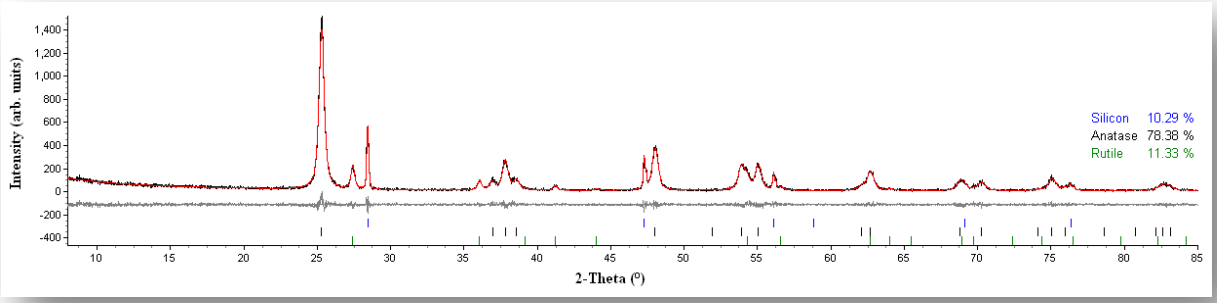

Figure 3.6. Individual Rietveld refinement of the pattern collected at 120 °C during heat treatment of Degussa P25 containing a 10 % silicon spike (black – experimental pattern, red calculated pattern and grey – difference curve)

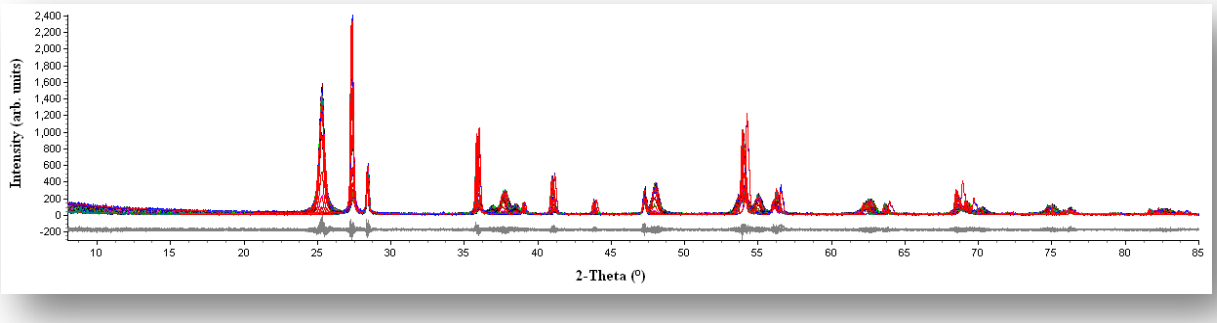

Figure 3.7. Rietveld refinements of all 31 patterns collected during the heat treatment of Degussa P25 containing a 10 % silicon spike (black – experimental patterns, red calculated patterns and grey – global difference curve)

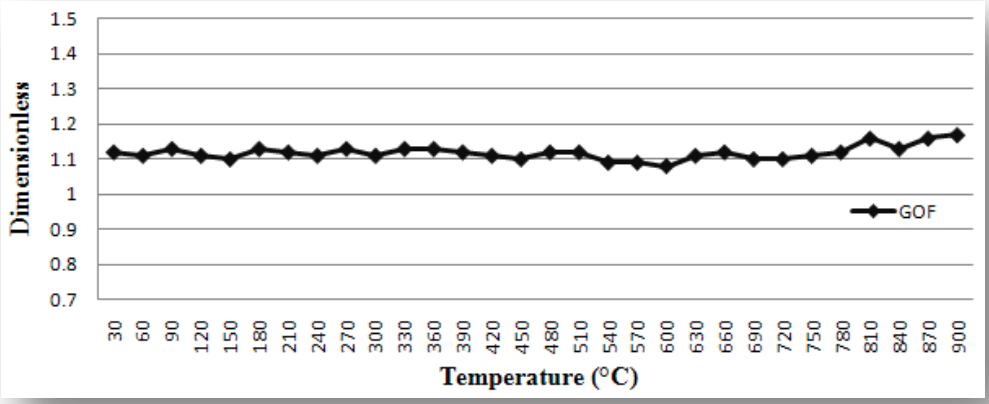

Figure 3.8. GoF values of all 30 patterns collected during the heat treatment of Degussa P25 containing a 10 % silicon spike

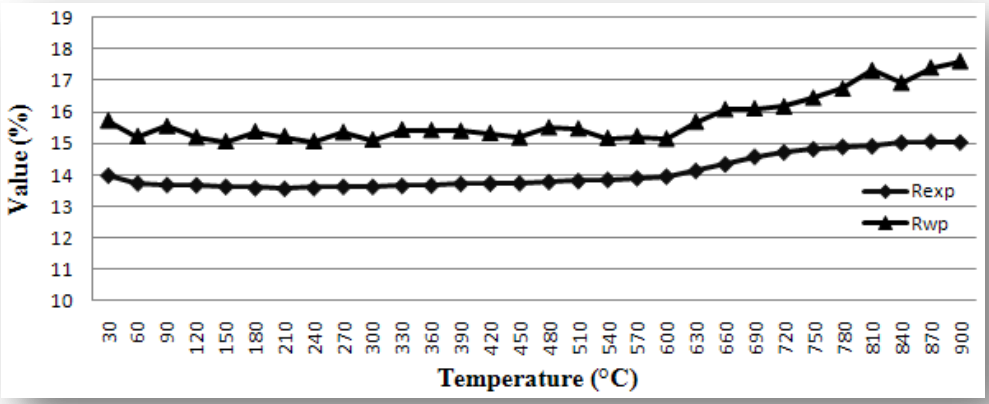

Figure 3.9. R_{exp} and R_{wp} values of all 30 patterns collected during the heat treatment of Degussa P25 containing a 10 % silicon spike

Particle Size Analysis

The average particle size of each of the constituent phases was calculated using the Scherrer formula (discussed in earlier sections), which is built into the TOPAS construct. This calculation provided a means to monitor changes in particle size as a function of temperature during our experiments (Fig. 3.10). The accuracy of the calculation is demonstrated by comparison of the calculated particle size values and the actual particle sizes observed in the TEM image given as figure 3.11**X**. The curve indicated that the average particle size, of both anatase and rutile, remained relatively constant until the reactor temperature exceeded 540 °C. At this point both the anatase and rutile phases appeared to increase in size. These findings are in agreement with those observed by Kim *et al.* using HRTEM.[18] They proposed that faceted anatase-anatase phase boundaries interact to form bridges (referred to as necks by the authors) at the appropriate temperature, resulting in severe lattice distortions. These points of high distortion are proposed to act as nucleation points for the phase transition to rutile. Although we can make no comment on the nucleation process, the observed increase in anatase particle size in our study, at the start of the

transition, lends credibility to the anatase-anatase bridging mechanism. The calculated increase in anatase particle size due to thermal expansion between 30 °C and 750 °C is approximately 2 %, which is significantly lower than the observed increase of 85 %. This comparison confirmed that the increase in particle size was due to agglomeration, or bridging, and not thermal expansion. The authors reported no decrease in anatase particle size once the transition had been allowed to progress. In our data we were able to show that the average anatase particle size did decrease as it was converted to rutile. The authors also noted the rapid grain growth of rutile, which we also observed, especially at temperatures above 630 °C. The rapid growth of the rutile particles has been attributed to the difference in surface tension between anatase (γ = 0.4 J/m^2) and rutile (γ = 2.2 J/m^2).[19] The high surface tension of the rutile particles drives the increase in particle size in order to minimize the surface area, and thus surface energy. The massive growth of the rutile particles was also confirmed by the TEM study of the sample after the heat treatment process (Fig. 3.11-**Y**).

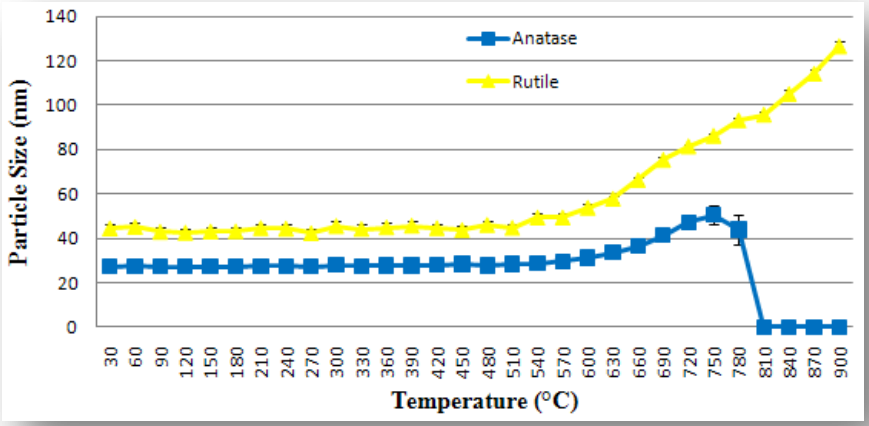

Figure 3.10. Particle size changes of anatase and rutile in Degussa P25 during the heat treatment process

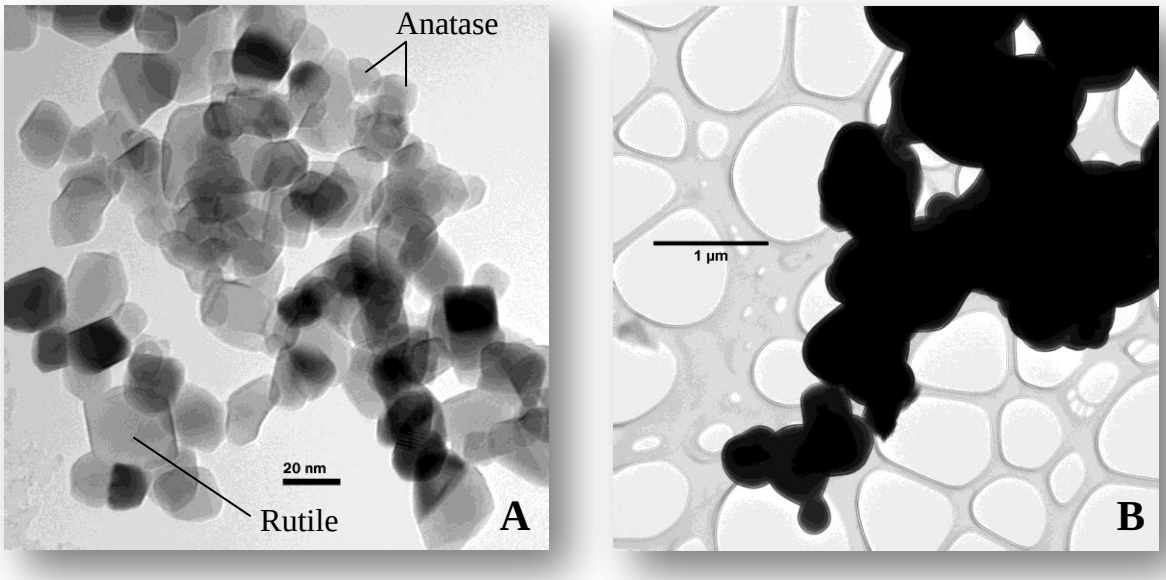

*Figure 3.11. TEM images of Degussa P25 before (**A**) and after (**B**) the heat treatment experiment*

Calculation of the instantaneous rates of change of particle size as a function of temperature (nm/°C) is given in figure 3.12. It should be noted that the errors were significantly larger for the particle size values than for phase percentage values, and thus these calculations indicate trends rather than exact numbers. Figure 3.12 shows that the rate of growth of rutile particles never exceeded 0.5 nm/°C, however, the rate of growth remained positive at reactor temperatures above 570 °C. The rate of anatase particle growth was weakly positive at temperatures between 540 °C and 750 °C and then became strongly negative, as the temperature exceeded 750 °C, reaching a maximum shrinkage rate of -1.5 nm/°C at 810 °C.

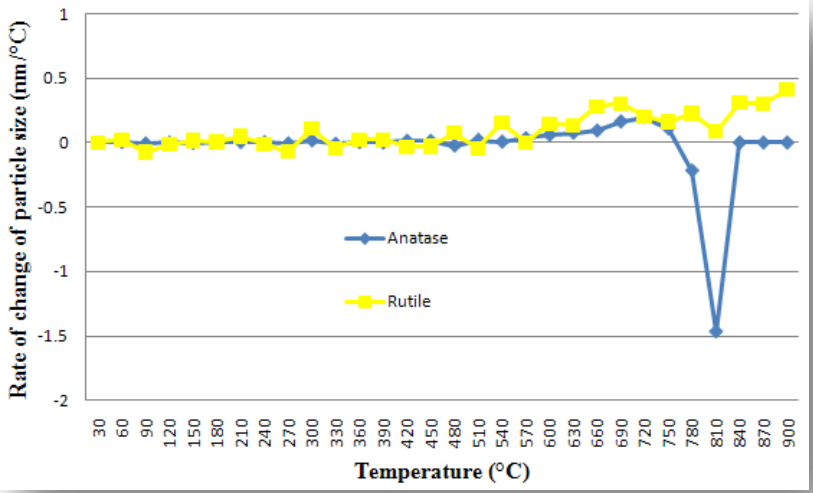

Figure 3.12. Instantaneous rates of change of particle size of anatase and rutile as a function of temperature during the heat treatment of Degussa P25

Degussa P25 was exposed to a similar heat treatment process under inert nitrogen (N_2) atmosphere in order to determine its effect on the phase transition and to verify if the trends observed above would be replicated under different conditions. Figure 3.13 shows the rates of increase of concentration rutile under both atmospheric environments. It was clear that the overall trend were similar, however, the starting point of the phase transition under N_2 was between 540 °C and 560 °C, compared to a temperature between 480 °C and 510 °C for the sample under air. The maximum rate of rutile formation under N_2 was approximately 50 % larger than under air. Additionally, the transition was complete at 810 °C and 760 °C for the samples heat treated under air and nitrogen respectively. These observations suggest that N_2 inhibits the transition until the temperature exceeds a certain value and then transition occurs rapidly.

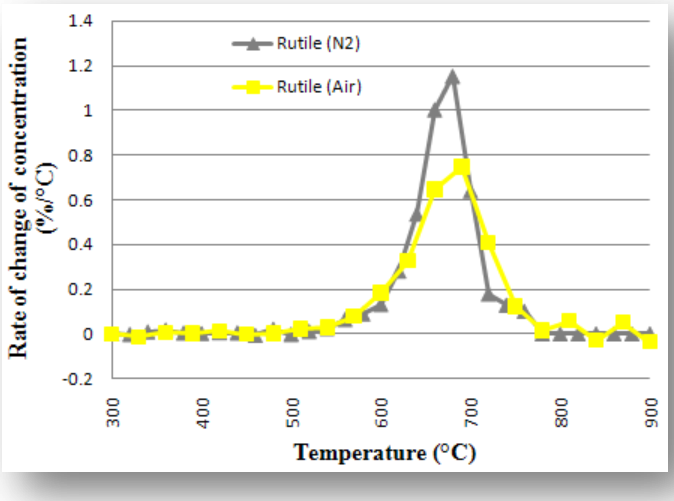

Figure 3.13. Rates of change of rutile concentration during heat treatment under air and nitrogen

The anatase particles present during the two experiments experienced similar growth patterns, as the anatase particles agglomerate (Fig. 3.14**A**), however, the decreases in anatase particle size occurred at different temperatures due to the significantly slower phase transition in the sample treated under air. The growth of rutile particles, although rather erratic (Fig. 3.14**B**), followed a similar pattern.

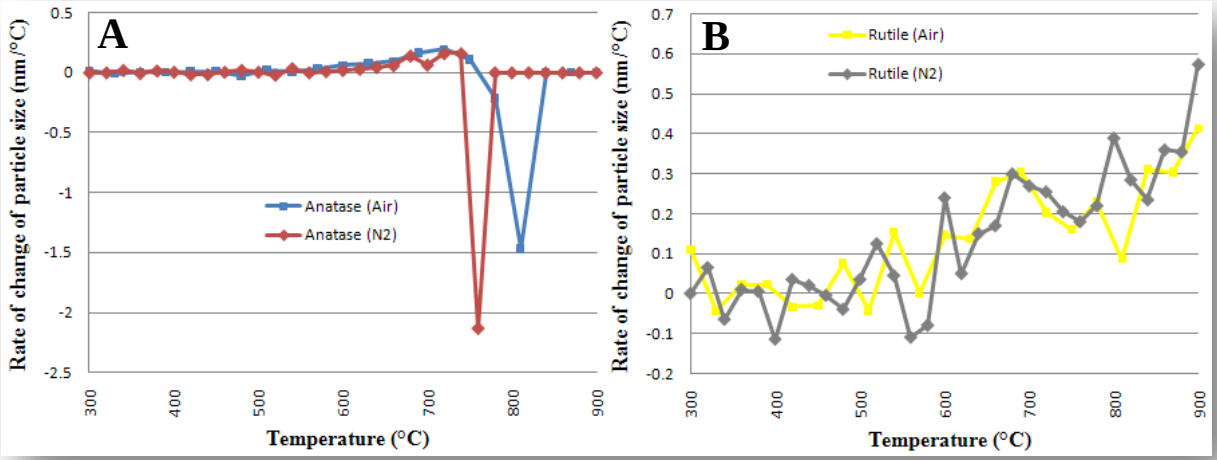

*Figure 3.14. Rates of change of particle size of **A** – anatase and **B** – rutile during heat treatment under air and nitrogen*

Lattice Parameter Analysis

Those with more critical eyes, and perhaps experience in the field, will have noticed the apparent shift in peak position in the intensity profile labeled figure 3.3. This is due to thermal expansion or contraction of the lattice parameters associated with those peaks. In the 2-dimensional figures a shift to the left, i.e. to lower 2θ values, indicates an increase in d-spacing between planes, since θ in the Bragg equation $d = {n\lambda}/{2\sin\theta}$ decreases. This increase is due to an expansion of the lattice parameter associated with that peak. Intuitively, a slope to the right indicates a contraction of the lattice parameter associated with that peak.

The lattice parameters shown in figures 3.15 and 3.16 indicate that the lattice parameters of anatase and rutile increase with an increase in temperature, corresponding to thermal expansion. This near linear trend is another indication of the accuracy of the refinement, since the changes in length are extremely small and highly affected by inaccuracies within the refinement.

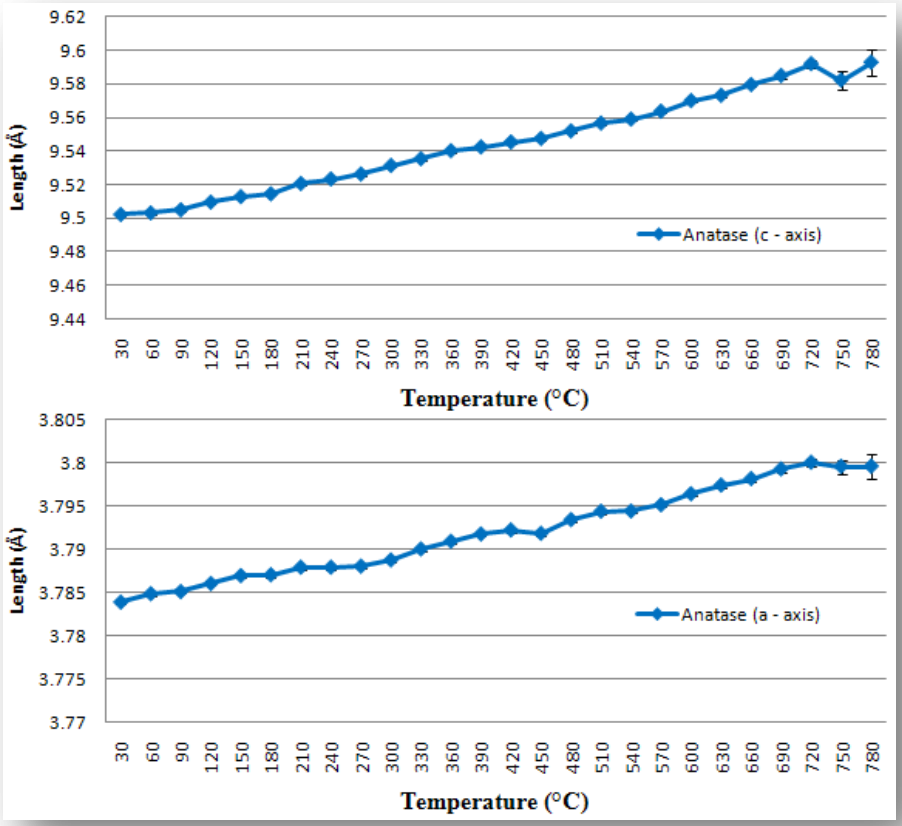

Figure 3.15. Lattice parameters of anatase during heat treatment

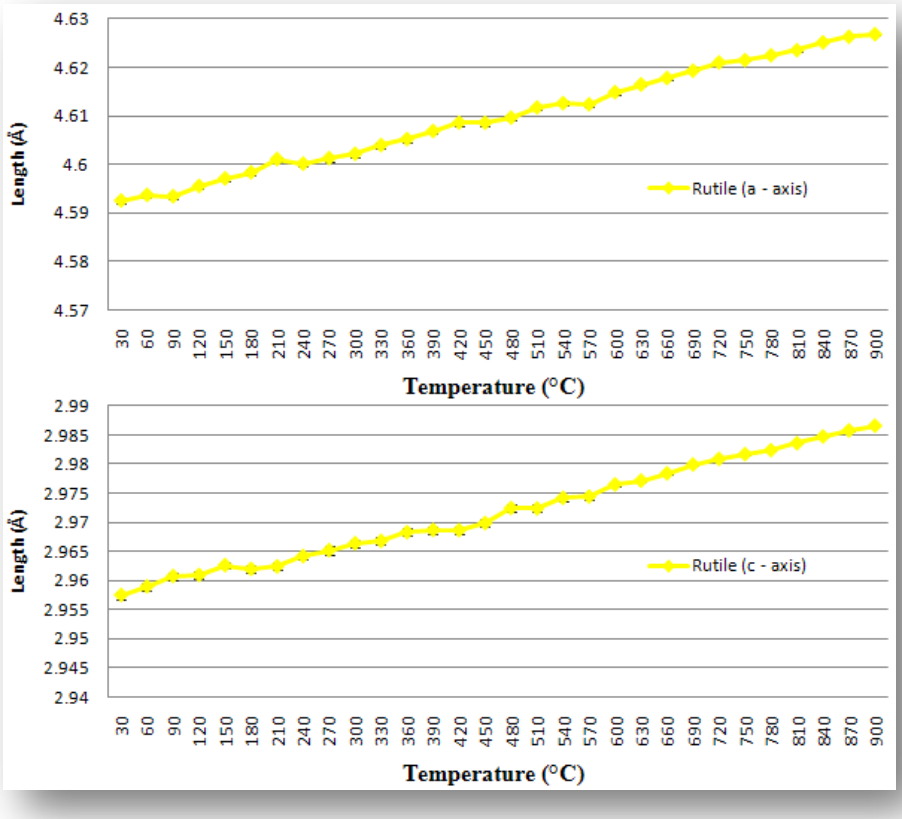

Figure 3.16. Lattice parameters of rutile during heat treatment

The lattice parameter value of the silicon, the unit cell of which is shown in figure 3.17, can be used as an accurate temperature reference during the experiment.[20-29] The difference between the calculated temperature of the sample, determined using the silicon lattice parameter and linear equations derived by Okada and Tokumaru,[30] and the observed temperature, obtained directly from a thermocouple near the sample bed is shown in figure 3.18. It is clear that at lower temperatures the observed temperature is underestimated, relative to the calculated temperature, while at higher temperatures the opposite is true. Ideally each dataset should be corrected for this difference. However, as the largest deviation between calculated and observed temperature values was 0.05 % so no corrections were made in this study.

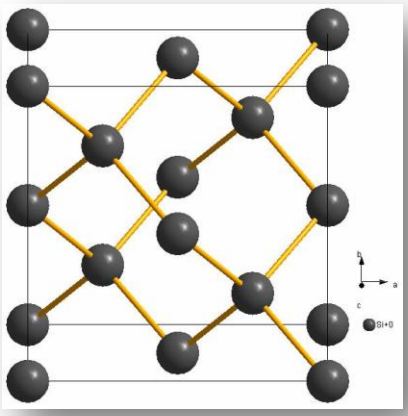

Figure 3.17. Crystallographic representation of silicon (cubic $Fd\bar{3}ms$)[31]

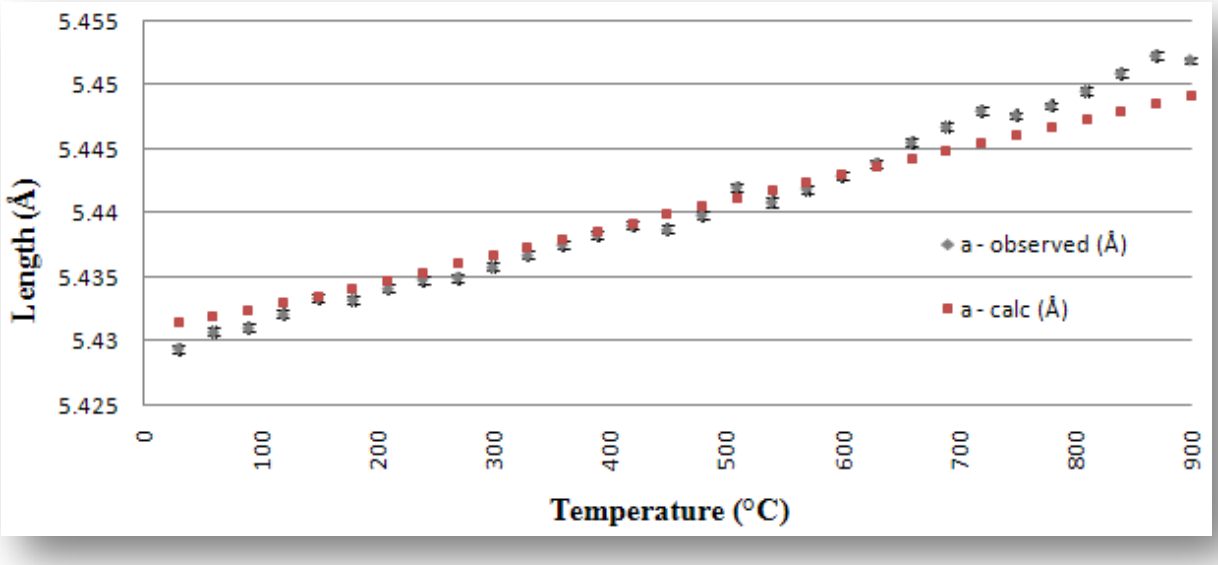

Figure 3.18. Comparison of observed (Rietveld method) and calculated (Okada and Tokumaru method)[30] *silicon lattice parameters used to describe differences in reported and calculated reactor temperature*

3.1.2. SIGMA ANATASE

Preliminary Discussion

The Sigma anatase support material contains a significantly larger anatase to rutile ratio (59:1) when compared to the Degussa P25 (7:1) titania (Fig. 3.19). It is clear that the anatase to rutile phase transition was negligible throughout the experiment, even at temperatures up to 900 °C. A kosnarite [$KZr_2(PO_4)_3$] phase appears in the data at temperatures above 490 °C, with major peaks at 18.96 °, 20.50 °, 23.47 ° and 30.54 ° 2-theta. Kosnarite crystallizes in a trigonal $R\bar{3}cH$ space group and is composed of ZrO_2 octahedra linked by PO_4 tetrahedra, with K^{+1} cations occupying the large voids formed by the cage-like structure (Fig. 3.20).[32] To confirm that kosnarite was present in the holder and not in the sample, a diffraction pattern was collected of the empty sample holder (Fig. 3.20). Using the Bruker Evaluation software (EVA) and the Powder Diffraction database (PDF) the kosnarite phase was identified. It was later discovered that this material had actually leached into the holder during a previous experiment unrelated to this project. The observation of kosnarite during the experiment indicates that the X-rays were penetrating the sample bed and diffracting from planes within the materials making up the sample holder. This was not surprising, since the sample is composed of relatively light elements (titanium, oxygen and silicon), which do not absorb and diffract X-rays as well as heavier elements. The density of the Sigma Anatase is quoted as 3.9 g/ml, which is similar to that of the Degussa P25 support with a value of 3.7 g/ml. This suggests that the density of the material has little effect on the X-ray penetration properties.

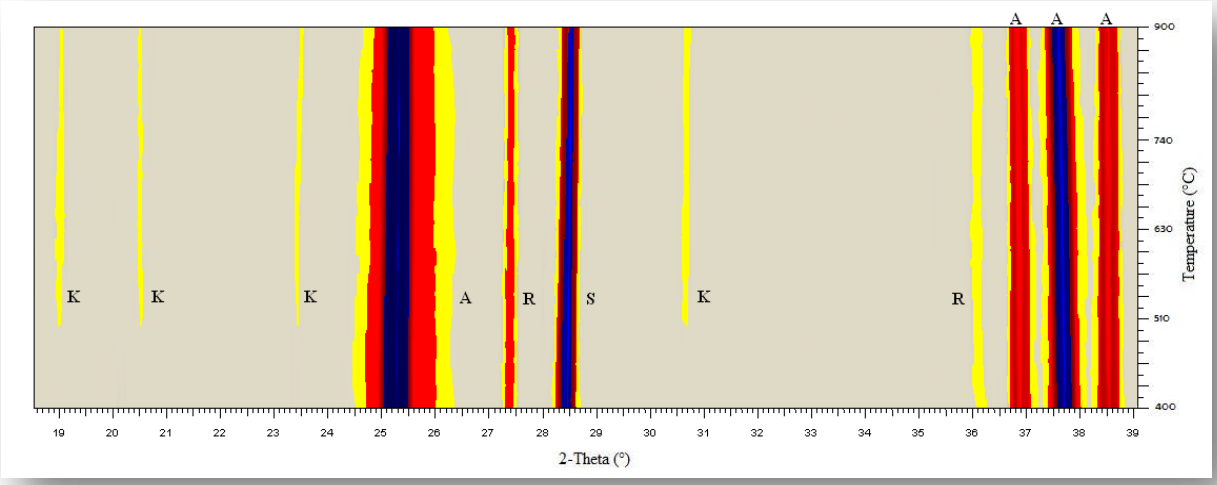

Figure 3.19. Intensity profile of the diffraction patterns collected during the heat treatment of the Sigma support: ***A*** *– anatase,* ***R*** *– rutile,* ***K*** *- kosnarite and* ***S*** *– silicon*

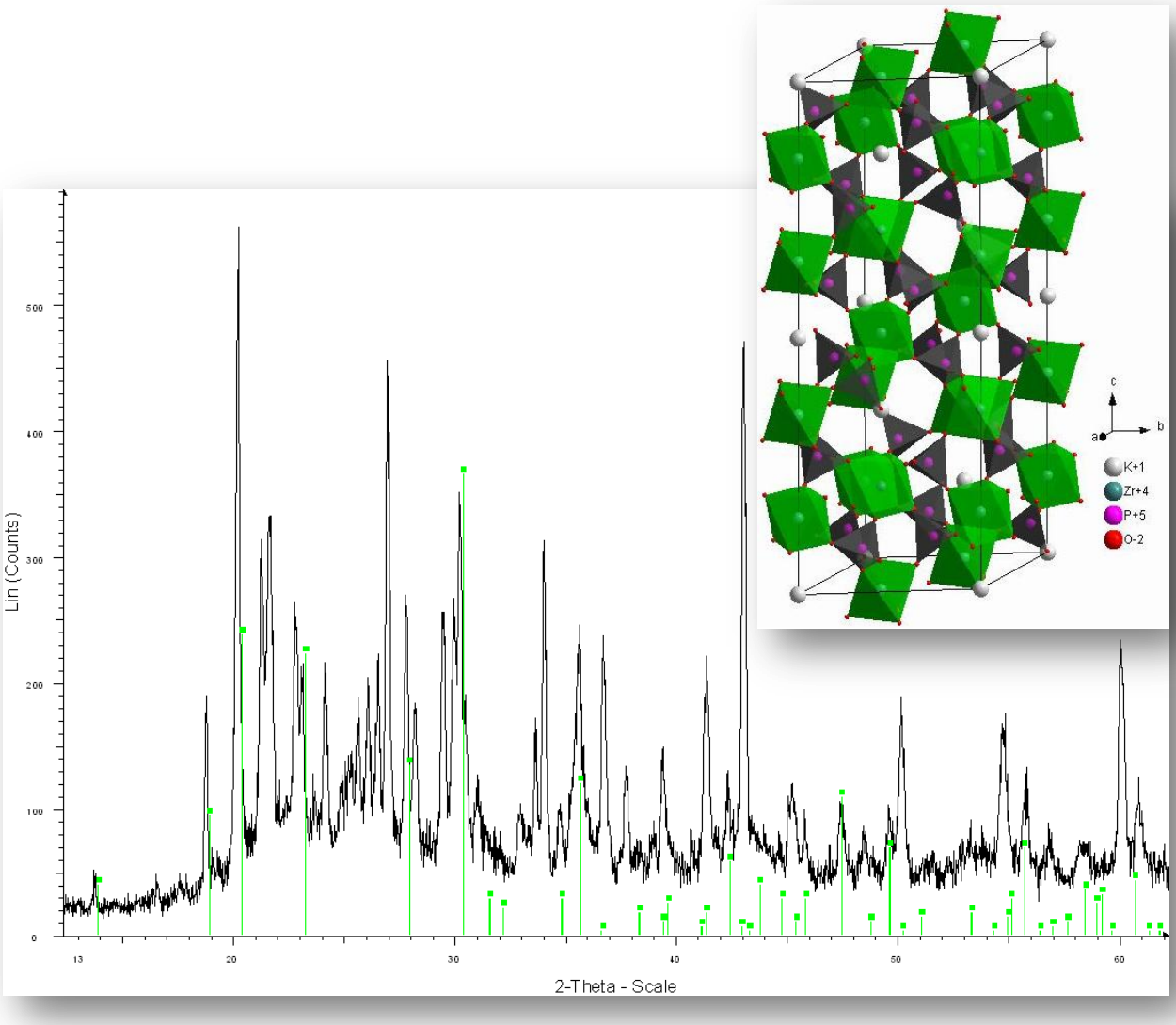

Figure 3.20. Diffraction pattern of the empty sample holder, showing matching kosnarite peaks while the inset shows a crystallographic representation of kosnarite (trigonal $R\bar{3}cH$)[32]

Quantitative Analysis

An unusual feature in the quantitative results depicted in figure 3.21 is the presence of an unexpected amorphous component within the sample. Figure 3.20, showing the diffraction pattern of the empty Makor[33] sample holder, had sharp diffraction peaks on top of broad diffraction peaks. These "bumps" are characteristic of amorphous materials. Thus, it is possible that the amorphous component that was calculated for our sample (Fig. 3.21) was actually a result of sample penetration and diffraction from the amorphous components within the sample holder. This would affect the noise and background of the pattern, which is used to calculate the amorphous contribution in the Rietveld method. To confirm this, a diffraction pattern was collected, using a sample holder known not to interact with X-rays, on another instrument with a similar Cu source (Fig. 3.22). The refinement of this data and the TEM image in figure 3.23, confirm that there was no amorphous material in this sample.

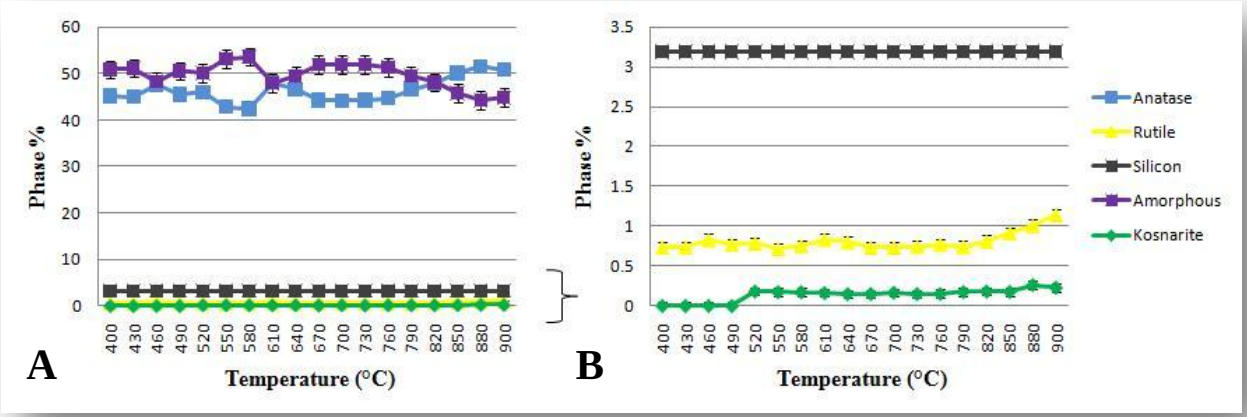

Figure 3.21. ***A*** *– phase composition of Sigma anatase during heat treatment and* ***B*** *– expansion of the 0 – 3.5 % region (average GoF value of 1.25)*

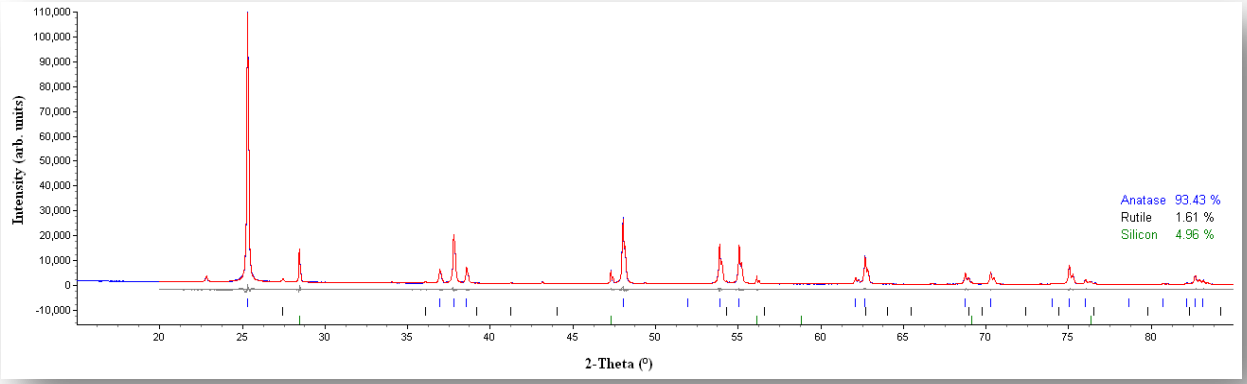

Figure 3.22. Rietveld refinement of the diffraction pattern collected from the Sigma support (5% silicon spike) at room temperature using the D2 diffractometer

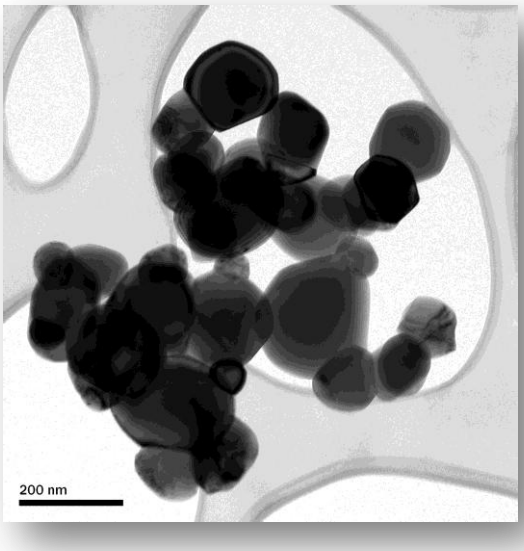

Figure 3.23. TEM image of the Sigma support before heat treatment

An attempt was made to correct the data. This was achieved by assuming that the diffraction from the amorphous material in the sample holder had a constant additive effect throughout the 2θ range. The ratios of the component phases were recalculated based on their contribution to the combined total of crystalline sample phases, calculated using the formula [100 % - silicon spike (%) – "amorphous content" (%)]. If we consider the first diffraction pattern collected at room temperature, the calculated anatase percentage was 47.43 %. However, subtraction of the "amorphous" and spike phase percentages from a possible 100 %, leaves a combined total of crystalline sample phases of 48.24 %, which corresponds to a recalculated anatase percentage of 98.32 %. This recalculated concentration was in agreement with the equivalent value obtained from the individual refinement in figure 3.22 with a value of 98.31 %. A complication arose when kosnarite became visible in the diffraction patterns (Table 3.1). The peaks for the kosnarite phase emerged at their characteristic 2-theta values and were, therefore did not affect the pattern as a whole, as was the case with the amorphous contribution from the sample holder. One can clearly see that the correction process worked effectively while the kosnarite phase is absent, but as soon as the peaks began to appear at 520 °C, it caused an over-calculation of the anatase and rutile phases, leading to a combined anatase and rutile total of more than 100 %.

Table 3.1. Recalculated anatase and rutile concentrations

	Refinement Results						***Adjusted Results***		
Temp (°C)	**Anatase (%)**	**Rutile (%)**	**Silicon (%)**	**Kosnarite (%)**	**Amorphous (%)**	**100-S-K-Am (%)**	**Anatase (%)**	**Rutile (%)**	**A+R (%)**
30	47.43	0.81	3.19	0.00	48.57	48.24	98.32	1.68	100.00
400	45.17	0.74	3.19	0.00	50.90	45.91	98.40	1.60	100.00
430	44.96	0.74	3.19	0.00	51.11	45.70	98.38	1.62	100.00
460	47.63	0.83	3.19	0.00	48.35	48.47	98.29	1.71	100.00
490	45.48	0.77	3.19	0.00	50.56	46.25	98.33	1.67	100.00
520	45.97	0.79	3.19	0.18	50.05	46.58	98.70	1.69	100.39
550	42.86	0.72	3.19	0.17	53.23	43.41	98.75	1.65	100.40
580	42.46	0.75	3.19	0.17	53.60	43.04	98.65	1.75	100.40
610	48.03	0.84	3.19	0.16	47.94	48.71	98.62	1.71	100.33
640	46.59	0.80	3.19	0.15	49.42	47.24	98.62	1.70	100.32
670	44.24	0.74	3.19	0.15	51.84	44.82	98.69	1.64	100.33
700	44.18	0.73	3.19	0.17	51.89	44.75	98.73	1.64	100.37
730	44.22	0.75	3.19	0.15	51.84	44.82	98.67	1.66	100.33
760	44.63	0.77	3.19	0.15	51.40	45.26	98.62	1.71	100.33
790	46.50	0.74	3.19	0.17	49.57	47.07	98.79	1.58	100.37
820	47.87	0.81	3.19	0.18	48.13	48.50	98.70	1.67	100.37
850	50.10	0.92	3.19	0.18	45.79	50.84	98.54	1.81	100.35
880	51.53	1.01	3.19	0.26	44.27	52.28	98.57	1.93	100.50
900	50.85	1.15	3.19	0.23	44.82	51.76	98.23	2.21	100.44

An aspect of this experiment was the stability of the support at high temperature. Figure 3.21**B** shows that only a small amount of anatase was converted to rutile at temperatures above 790 °C. It has been shown, by a number of authors,[9-12] that larger anatase particles resist the transition to rutile to a much greater extent than do smaller particles. The stability of this support, with anatase particles with an average size of 140 nm (discussed below), is thus expected.

We were interested to determine if the concentration of rutile in the support, at the start of the heat treatment, had an effect on the anatase transition temperature. To do this support samples containing increasing concentrations of added rutile (4 %, 6 % and 10 %) were subjected to the same heat treatment procedure. The experiments revealed that the transition temperature was unaffected by the added rutile, suggesting that rutile particles do not act as nucleation points for the anatase to rutile phase transition.

Particle Size Analysis

The data discussed above were used to determine parameters such as particle size, since these parameters are little affected by the background phenomena (Fig. 3.24**A**). The most notable difference between the Sigma and Degussa P25 support was the difference in the anatase particle size and the effect of temperature on the particle size. The average anatase particle size for the Degussa P25 support was approximately 33 nm, while that of the Sigma support was approximately 143 nm. There was little transformation of anatase to rutile so the particle sizes remained relatively constant throughout the experiment. The standard deviation for both anatase and rutile is large, indicating a large particle size distribution for both phases, a phenomenon also confirmed by variable sizes of the anatase particles shown in the TEM image presented in figure 3.24**B**.

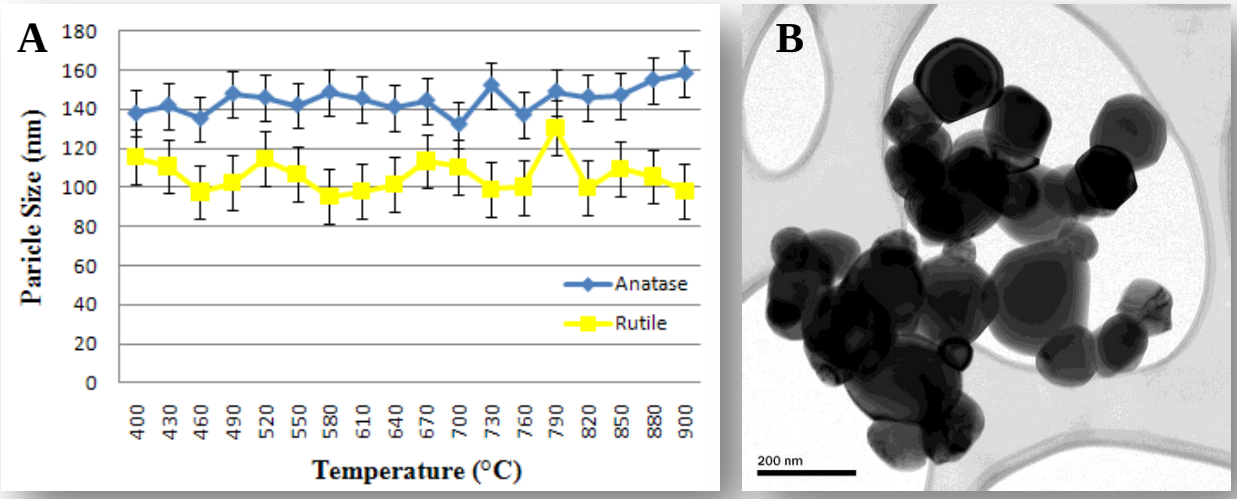

*Figure 3.24. Particle size changes of anatase and rutile in the Sigma support during heat treatment (**A**) and TEM image of the Sigma support before heat treatment (**B**)*

3.1.3. NANO-SIZED ANATASE (NSA)

Preliminary Discussion

The Sigma support phases had a large particle size, while the Degussa P25 support phases had a significantly smaller average particle size. The two supports also differ in rutile concentration. To complete the studies on titania, a phase pure anatase support was prepared as outlined by Sivakumar *et al.*.[34] The product, while not cantaining rutile, was, however, not phase pure and contained a large amount (± 30 %) of brookite (Fig. 3.25)[35] and some amorphous material (Fig. 3.26). The presence of brookite was not reported in the study by Sivakumar *et al.* but one of their PXRD patterns for a sample calcined at 400 °C had the equivalent peak at 30.8° 2-theta, to which they made no mention.

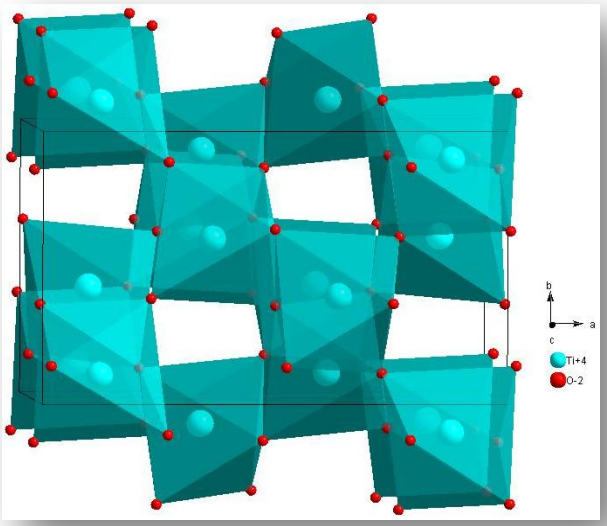

Figure 3.25. Crystallographic representation of brookite (orthorhombic Pbca)[35]

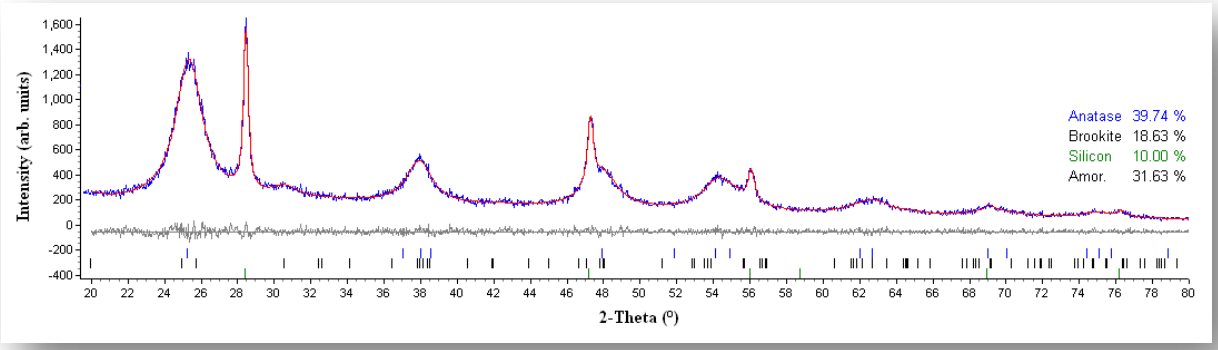

Figure 3.26. Refinement results of a diffraction pattern collected from the NSA support (10 % silicon spike) at room temperature on the D2 diffractometer

Heat treatment of this support (Fig. 3.27) showed that the anatase to rutile phase transition occurred from both the anatase and brookite parent phases even in the absence of rutile. The apparent sharpening of the anatase peaks with temperature indicates an increase in average particle size. These two observations are consistent with the idea that the phase transition can be initiated by severe strain in anatase-anatase bridges as proposed by Kim *et al.*.[18] Hu *et al.* also found that increasing concentrations of brookite tended

to decrease the starting and ending temperatures of the anatase to rutile phase transition, indicating that brookite acts as a solid-state catalyst for the transition.[36] This provides an explanation for the difference between the Sigma support, which did not undergo a phase transition to a significant extent, and the NSA support, which was almost entirely converted to rutile.

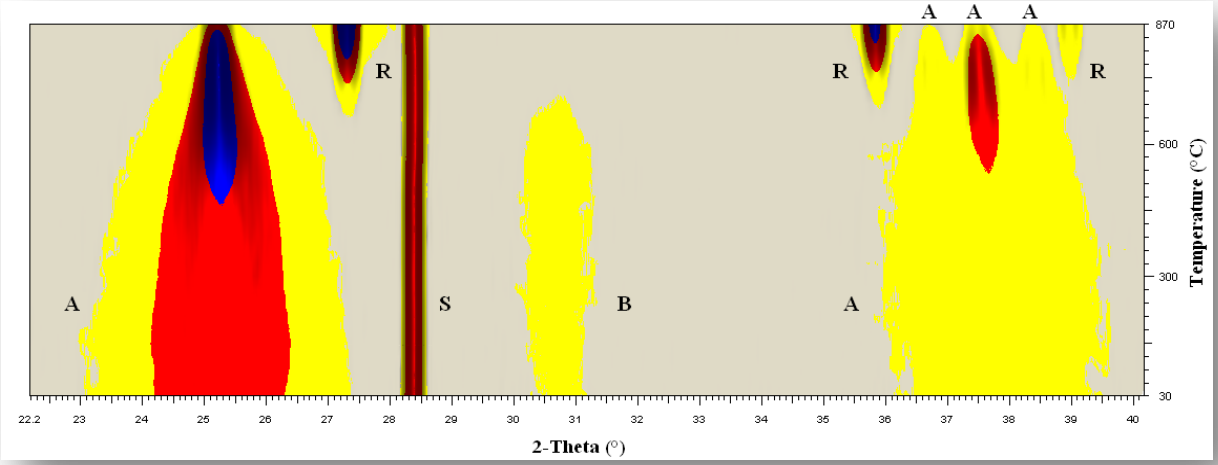

Figure 3.27. Intensity profile of the diffraction patterns collected during the heat treatment of the NSA support: ***A*** *– anatase,* ***B*** *– brookite,* ***R*** *– rutile and* ***S*** *– silicon*

Quantitative Analysis

Heat treatment of the support yielded some interesting results. The analysis was complicated by the presence of an "amorphous" contribution from the sample holder. This can be seen from the difference in the amorphous value of the refinement at 30 °C in figure 3.28**A** when compared to that given in figure 3.26. Thus a calculation to generate a representation of the amorphous component was not easy. For this reason, a correction procedure was employed to yield the ratios of the crystalline phases as a function of the combined total of anatase, brookite and rutile, the results of which are given as figure 3.28**B**.

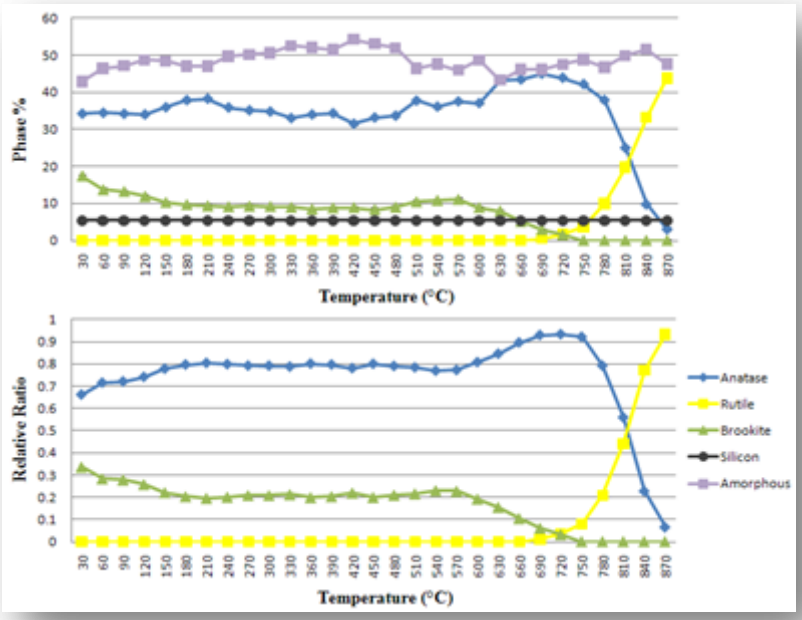

Figure 3.28. ***A*** *- quantitative phase analysis of the NSA support during heat treatment (average GoF of 1.12) and* ***B*** *- relative ratios of the constituent phases in the NSA support during the heat treatment*

Analysis of figure 3.28**B** revealed that at temperatures between 30 °C and 180 °C approximately 41 % of the brookite was converted to anatase. The remaining brookite was converted when the temperature exceeded 570 °C, a process that reached completion at 750 °C. The first rutile peaks appeared in the pattern collected at 690 °C, suggesting that the transition began at temperatures between 660 °C and 690 °C. All three phases coexisted in the temperature range of 660 °C to 750 °C.

The rate of formation and consumption of the various phases (Fig. 3.29) provided a means to determine if brookite was converted directly to rutile in this temperature range or if it had to pass through the anatase transition first. If anatase and brookite were both consumed to form rutile at 690 °C, the rates for both of the phases should have been negative, indicating consumption. However, the brookite rate was negative and the anatase rate was positive. This suggested that more anatase was formed from the transition from brookite than was consumed during the transition to rutile, suggesting the sequence brookite → anatase → rutile.

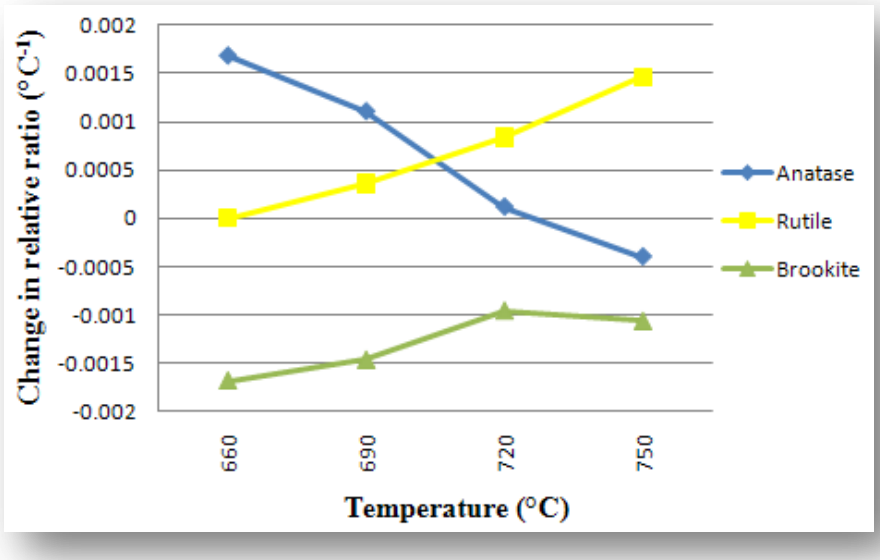

Figure 3.29. Instantaneous rates of change of relative ratios of anatase, brookite and rutile in the NSA support during heat treatment

Particle Size Analysis

The average anatase particle size for the NSA at room temperature was 8.6 ± 1 nm, while brookite had an average particle size of 3.3 ± 1 nm (Fig. 3.30). The particle sizes for both phases increased gradually as the temperature was increased. The TEM image of the NSA support material, given in figure 3.31, indicated that the particle sizes calculated during the refinement process were accurate, with the average particle size of both phases combined (since they were indistinguishable) of approximately 7 nm.

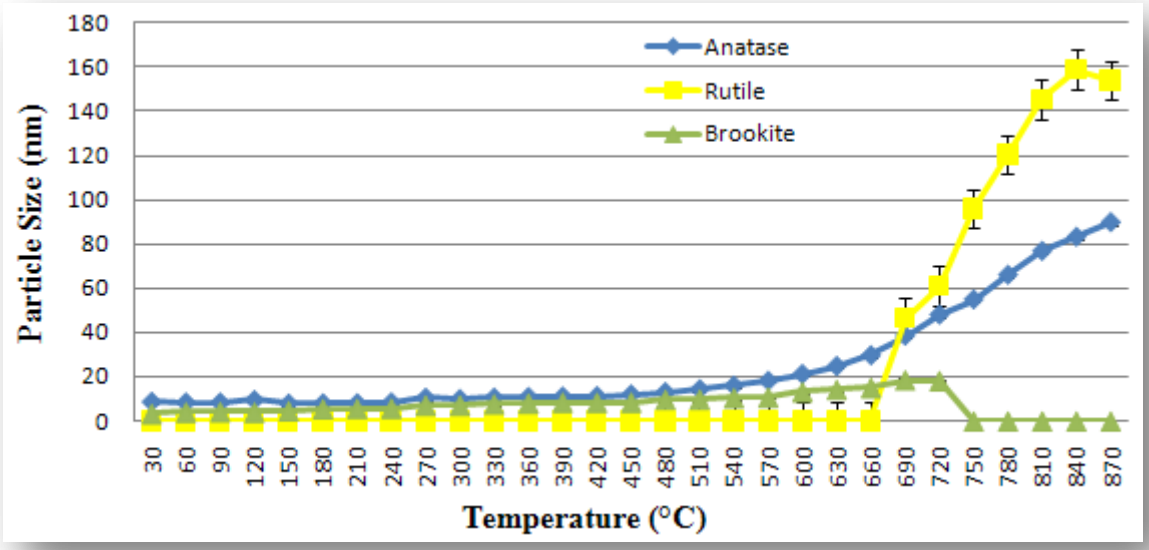

Figure 3.30. Particle size changes of the constituent phases in the NSA support during heat treatment

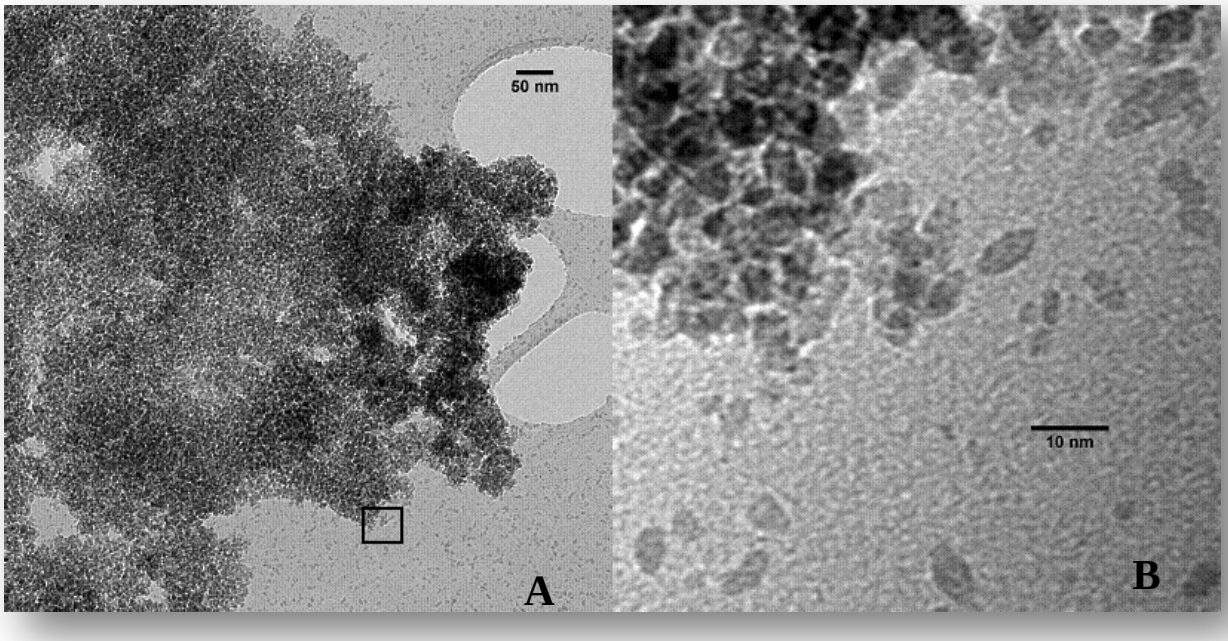

Figure 3.31. TEM images of the NSA support before heat treatment: ***A*** *– sample representation and* ***B*** *– magnified view showing individual support particles*

The rate of change of anatase particle size as a function of temperature is shown in figure 3.32. The rate of growth of anatase particles steadily increased, i.e. positive values, between 30 °C and 120 °C and then suddenly decreased, i.e. negative values, between 120 °C and 150 °C, meaning anatase particles grew more and more quickly and, at a temperature between 120 °C and 150 °C, fragmented (indicated by the negative value at 150 °C). The same was true for the region between 180 °C and 300 °C. Thermogravimetric analysis (TGA) shows that the NSA support lost mass constantly during heating (Fig. 3.33**A**). However, the derivative of the TGA curve (Fig. 3.33**B**) revealed the temperatures of maximum weight loss to be ± 73 °C, ± 247 °C and ± 347 °C. The first two temperatures of ± 73 °C and ± 247 °C fall within the two temperature regions discussed above. This indicates that the growth and subsequent shattering of the anatase particles (the major phase) was due to lattice expansion and violent escape of water and/or nitrate molecules respectively. At temperatures between 420 °C and 570 °C, the particles were not simply growing due to lattice expansion but due to agglomeration or sintering, the rate of which was temperature dependent, i.e. the higher the temperature, the higher the rate of sintering. When the temperature exceeded 570 °C brookite was converted to anatase, further increasing the average anatase particle size. At temperatures above 690 °C anatase particle growth, via brookite transformation and particle agglomeration, came into competition with rutile formation and the rate of growth became erratic, as witnessed in figure 3.32. A small amount of anatase remained in the system at 870 °C. The anatase particles that remained in the system had undergone extensive agglomeration and had a large average particle size (89.5 ± 1 nm), explaining the positive growth rates at these temperatures in figure 3.32.

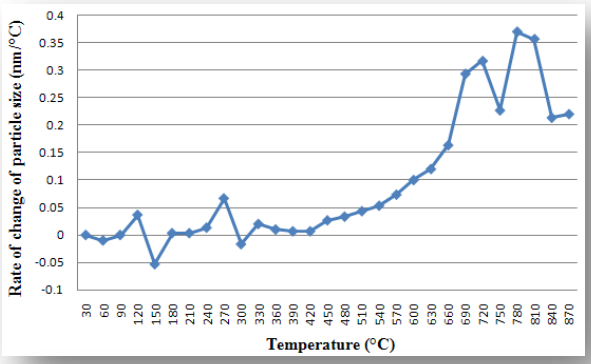

Figure 3.32. Instantaneous rates of change of anatase particle size in the NSA support during heat treatment

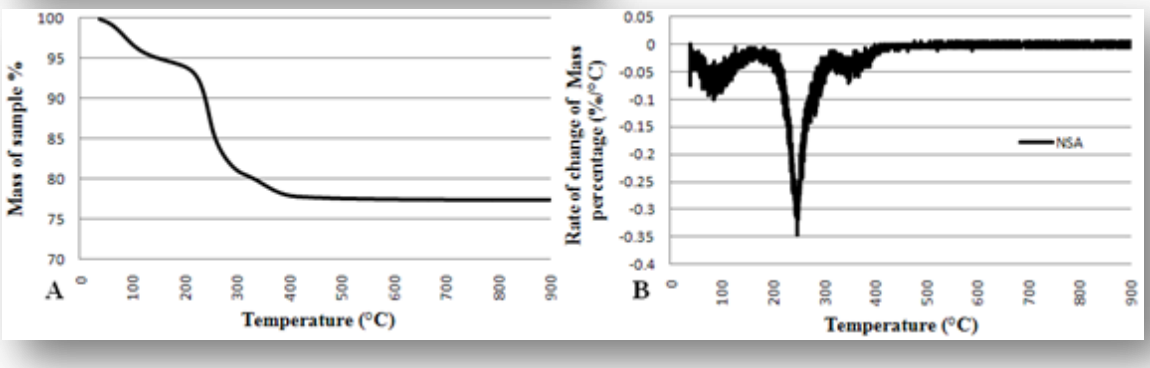

*Figure 3.33. **A** – mass loss of the NSA support during thermogravimetric analysis (TGA) and **B** – instantaneous rates of change of mass percentage of the NSA support*

3.2. HEAT TREATMENT OF CATALYSTS

Each of the support materials, discussed above, was used to prepare supported metal catalysts. The metals of interest were those that are active in the Fischer-Tropsch reaction, namely iron (Fe), cobalt (Co) and ruthenium (Ru), resulting in a matrix of samples that were studied that are presented in table 3.2. The catalysts were heat treated in a similar way to the supports discussed above (air at 1 bar with a flow rate of 30 ml/min) in order to monitor the formation of metal oxides (referred to as calcination), the effects of excess heat treatment and the particle size changes that occur during heat treatment. The heat treatment procedure was designed to determine the ideal calcination procedure for each catalyst in terms of maximum metal oxide concentration and particle size.

Table 3.2. Matrix of samples under investigation

	10% Fe
DEGUSSA-SUPPORTED CATALYSTS	10% Co
	10% Ru
	10% Fe
SIGMA-SUPPORTED CATALYSTS	10% Co
	10% Ru
	10% Fe
NSA-SUPPORTED CATALYSTS	10% Co
	10% Ru

3.2.1 Fe/DEGUSSA P25

Preliminary Discussion

Degussa P25 is the most common titania material used as a catalyst support, while iron is one of the most commonly used metal catalysts in FT synthesis. Unsupported Fe catalysts still dominate the FT industry and are used in both the HT- and LTFT processes.[37] The size of the metal particles, used in the FT reaction, has been known to affect the activity when the metal diameters are less than 10 nm.[38] Supported iron catalysts show highest activity when the metal particle size is larger than 10 nm.[39] The aim of the heat treatment experiments was, therefore, to determine the calcination procedure that resulted in the maximum concentration of iron oxide particles with an average particle size above 10 nm but less than 20 nm, with as small a size distribution as possible. Figure 3.34 shows the topographical view of the diffraction patterns collected during the heat treatment of the 10%Fe/Degussa P25 catalyst (for synthesis details see Chapter 2).

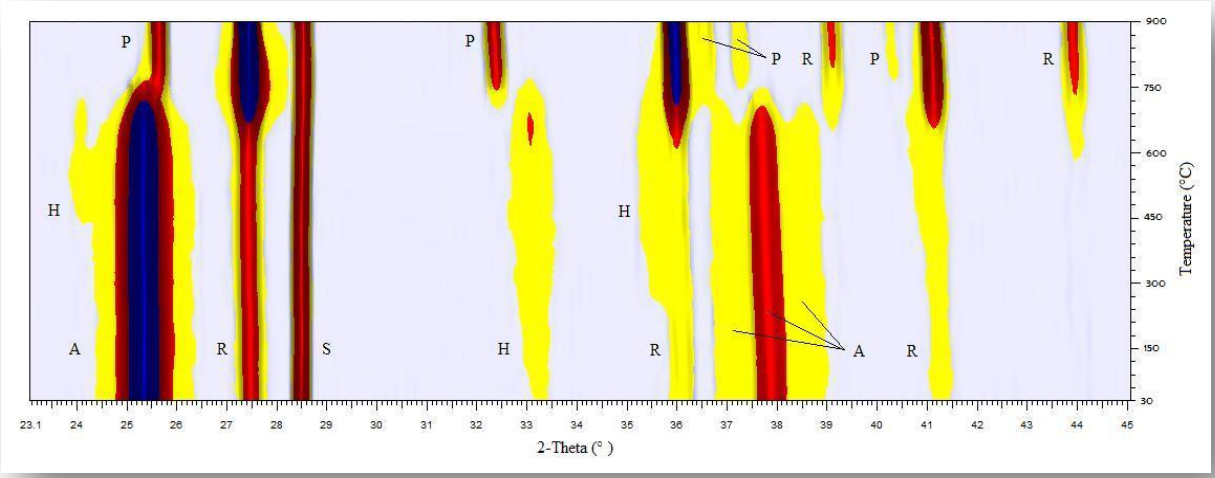

Figure 3.34. Intensity profile of the diffraction patterns collected during the heat treatment of the Fe/Degussa P25 catalyst: ***A*** *– anatase,* ***R*** *– rutile,* ***S*** *– silicon,* ***H*** *– hematite and* ***P*** *– pseudobrookite*

Quantitative Analysis

Determination of the ideal calcination temperature involved finding the temperature at which the hematite (Fe_2O_3) concentration reached a maximum and the iron particle size was between 10 nm and 20 nm. Hematite crystallizes in a trigonal, $R\bar{3}cH$ space group to form two-dimensional nets, made up of alternating Fe^{3+} and oxygen (O^{2-}) ions, extending parallel to the *b* axis (Fig. 3.35).[40] The major hematite powder diffraction peaks occur at a 2θ values of 33.2° and 35.6° when using a Cu radiation source (Fig. 3.34). Visual inspection of figure 3.34 suggests that the hematite peaks reached a maximum intensity at temperatures between 660 °C and 690 °C, however at those temperatures, anatase also undergoes the phase transition to rutile.

Another interesting observation was the formation of pseudobrookite (Fe_2TiO_5), which crystallizes in an orthorhombic *Ccmm* space group (Fig. 3.36).[41] Pseudobrookite forms via Ti^{4+} migration into the hematite phase at elevated temperatures, a process that was elegantly elucidated by Gennari *et al.*.[42] This occurs because the ionic radii for Ti^{4+} and Fe^{3+} (high spin) are 60.5 pm and 64.5 pm respectively and can therefore replace one another via a substitution-type process. The similarity in ionic radii leads to metal-site disorder, which means that Ti^{4+} positions cannot be distinguished from Fe^{3+} positions crystallographically. What is known, however, is that there are two Fe^{3+} ions for every Ti^{4+} ion, leading to occupancies for the two ions of 0.667 and 0.333 respectively.

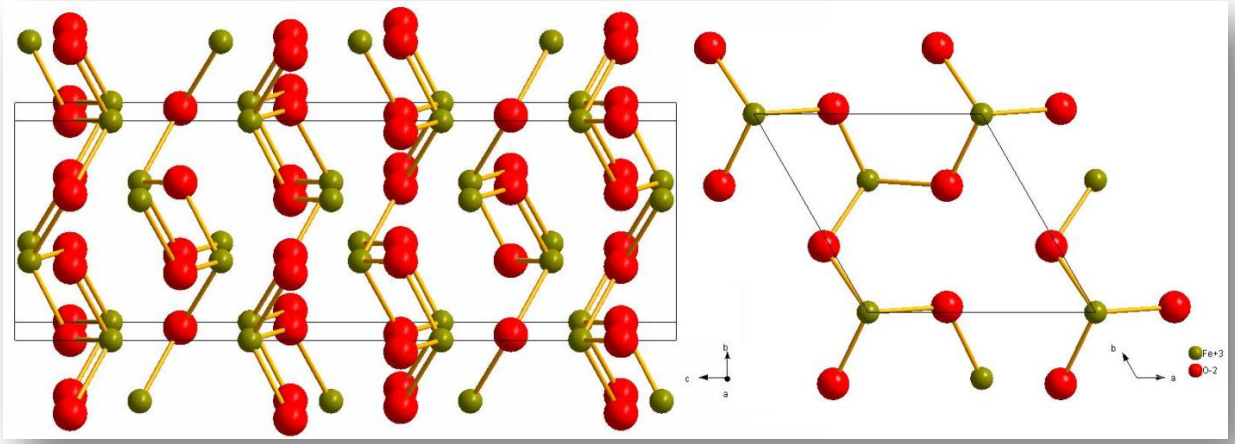

Figure 3.35. Crystallographic representation of hematite (trigonal $R\bar{3}cH$) as viewed down the a and c axis respectively[40]

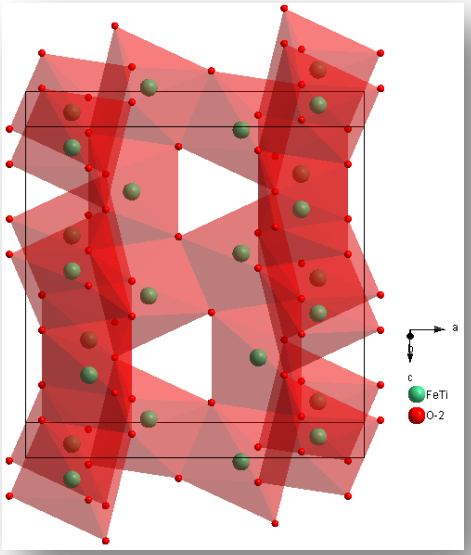

*Figure 3.36. Crystallographic representation of pseudobrookite (*orthorhombic *Ccmm)* [41]

Figure 3.37**A** provides a graphical view of the phase concentrations of the Fe/Degussa P25 catalyst as a function of temperature. It is clear that there was a large amorphous component due to the sample holder. Recalculation of the ratios of the phases, in an identical way to the heat treatment of the Sigma support, yielded the graph in figure 3.37**B**. The graph revealed an apparent decrease in anatase concentration as hematite was formed. This is obviously incorrect, since anatase is stable at these temperatures and hematite is not formed via the heating of anatase. In order to further correct the dataset, the behavior of the Fe species in the system had to be considered.

Fe^{3+} was loaded onto the support as iron nitrate [$Fe(NO_3)_3.9H_2O$]. The drying procedure converted roughly half (5.30 ± 0.3 %) of the iron nitrate to crystalline hematite. The remaining Fe^{3+} is present as an amorphous species, denoted Fe^{3+}AM. The amorphous nature of this material in the system is confirmed

by the absence of diffraction peaks for any other crystalline Fe^{3+} phase in figure 3.34. The calcination procedure involves the driving off of the remaining water and nitrate molecules present after the drying process, converting the remaining Fe^{3+}AM to hematite. By assuming that all the amorphous Fe^{3+}AM had been converted to hematite at 450 °C, the temperature at which hematite had reached its maximum concentration, corrections could be applied using the changes in concentration of hematite between each collection below 450 °C. The difference between each hematite value should be equal to the change in amorphous Fe^{3+}AM concentration and from these values a real amorphous component at each temperature interval could be calculated. The calculated amorphous component was then subtracted from the anatase values in order to maintain a realistic total phase composition of 100 %. The resulting graph is given as Figure 3.37**C**.

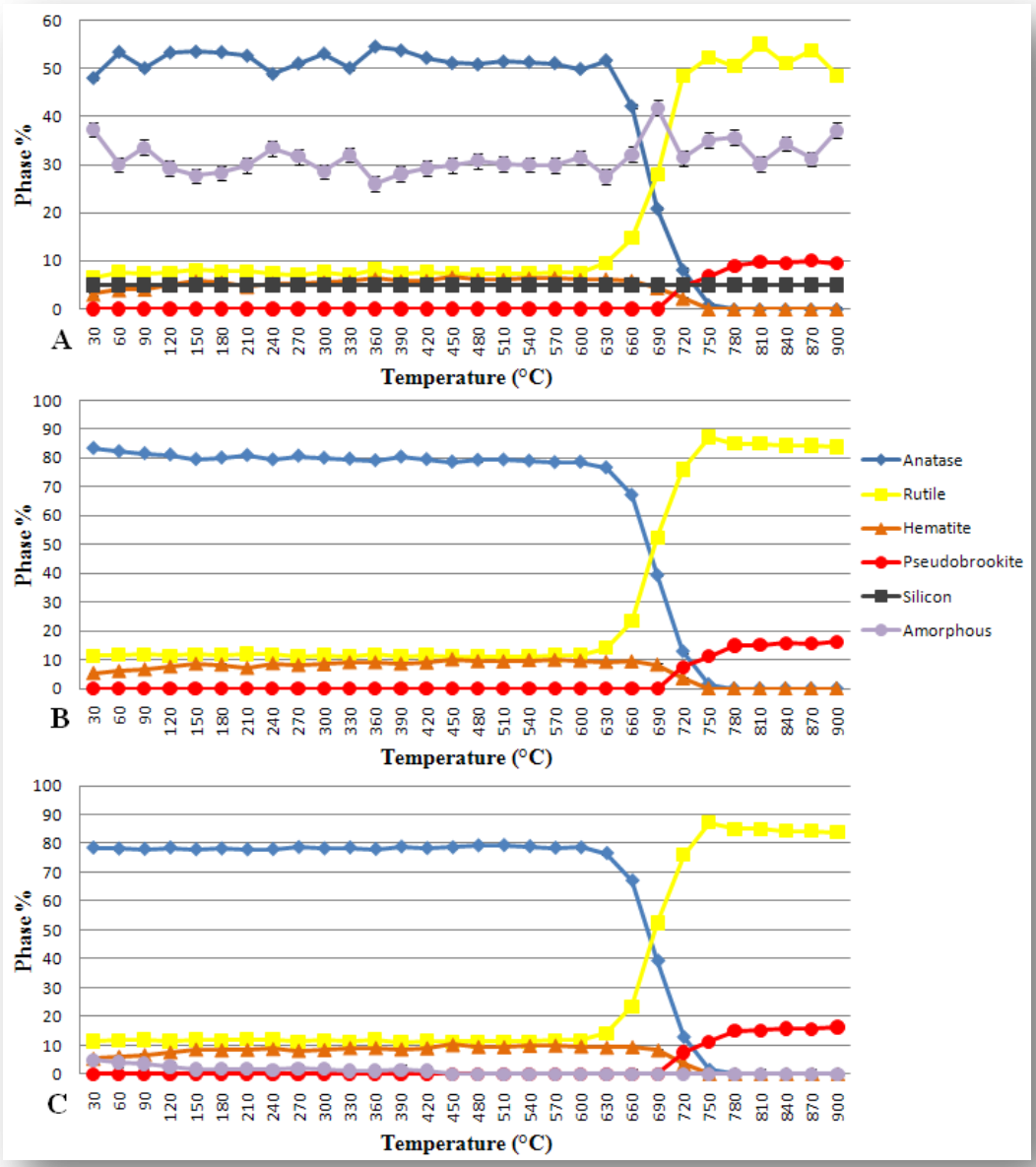

Figure 3.37. ***A*** *– original quantitative phase analysis of the Fe/Degussa P25 catalyst during heat treatment,* ***B*** *- primary correction of the quantitative phase analysis data and* ***C*** *- secondary correction of the quantitative phase analysis (average GoF of 1.06)*

The corrected refinement results indicate that the maximum hematite concentration of 10.19 ± 0.3 % had formed at 450 °C, which corresponds well with the calculated loading value of 10 %. The anatase to rutile phase transition began at a temperature between 600 °C and 630 °C, which was confirmed by the rates of change of anatase and rutile concentration graph, given as figure 3.38. Although the rates look like they mirror each other, there are very slight differences. The rate of consumption of anatase was found to be larger than the rate of formation of rutile at 720 °C (±10 % difference) and 750 °C (±2 % difference). It was shown previously that a direct phase change would result in equal rates of formation of the product phase and consumption of the reactant phase. The difference between the anatase and rutile rate curves in this temperature range, suggest that anatase was consumed in another process, i.e. not to form rutile. Literature has shown that the formation of pseudobrookite occurs via Ti^{4+} migration into hematite particles.[42] Since the rate of consumption of anatase exceeds that of the formation of rutile between 690 °C and 750 °C, it implies that the Ti^{4+} ions are likely to be exclusively generated by anatase. In order to confirm this, the rate of anatase consumption not attributed to the transition (denoted as NAT) was calculated and added to the rate of hematite consumption values at these temperatures, the results of which are shown in figure 3.39. The fact that the rate of formation of pseudobrookite mirrors the combined rates indicates that the Ti^{4+} migration reaction occurs exclusively between the hematite and anatase phases at temperatures between 690 °C and 750 °C.

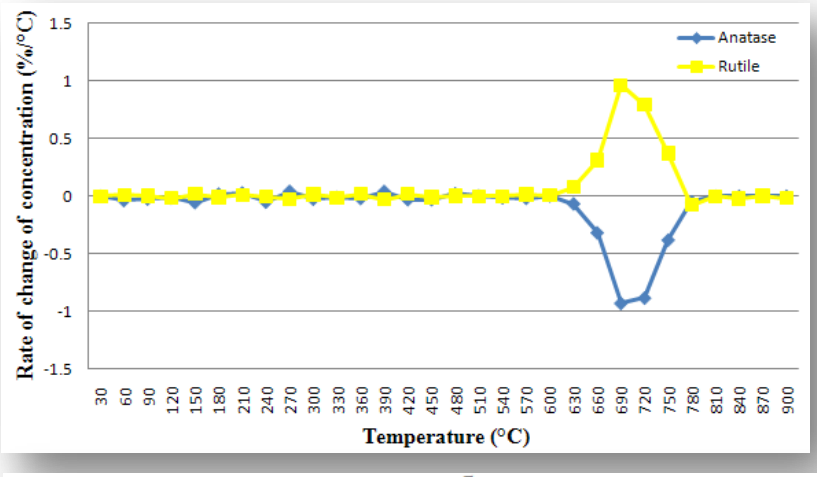

Figure 3.38. Instantaneous rates of change of anatase and rutile concentrations in the Fe/Degussa P25 catalyst during heat treatment

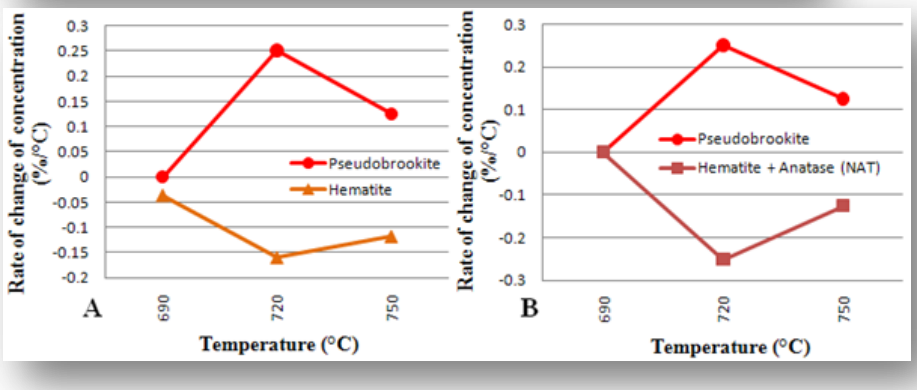

*Figure 3.39. Instantaneous rates of change of concentration of **A** – pseudobrookite and hematite and **B** – pseudobrookite and the combined rates of consumption of hematite and anatase not attributed to the phase transition (NAT)*

Particle Size Analysis

The hematite particles that were formed during the drying process had an average size of 8.5 ± 1 nm at the start of the heat treatment (Fig. 3.40). The average hematite particle size decreased as the Fe^{3+}AM was converted to crystalline hematite to yield a minimum average value of 5.4 ± 1 nm at 120 °C, which increased gradually as the temperature was increased. It was stated previously that the ideal calcination temperature for this particular catalyst, in terms of maximum concentration (10.19 ± 0.3 %), was 450 °C. The hematite particle size at 450 °C was well below the 20 nm goal with average values in the order of 12.4 ± 1 nm. Unfortunately, the hematite particle size was a third of the size of the anatase particle size, meaning that the dispersion of the hematite particles on the surface of the support phases was extremely low or the iron oxide particles were not supported at all. The TEM image, presented as figure 3.41**A**, suggested that the iron oxide particles were supported on anatase particles, but had a low degree of dispersion due to the similarity in size with the support particles. Figure 3.41**B** is a TEM image of a 10% Fe/rutile catalyst that we prepared in order to demonstrate an unsuccessful loading, in which iron oxide particles did not bind to the rutile support particles.

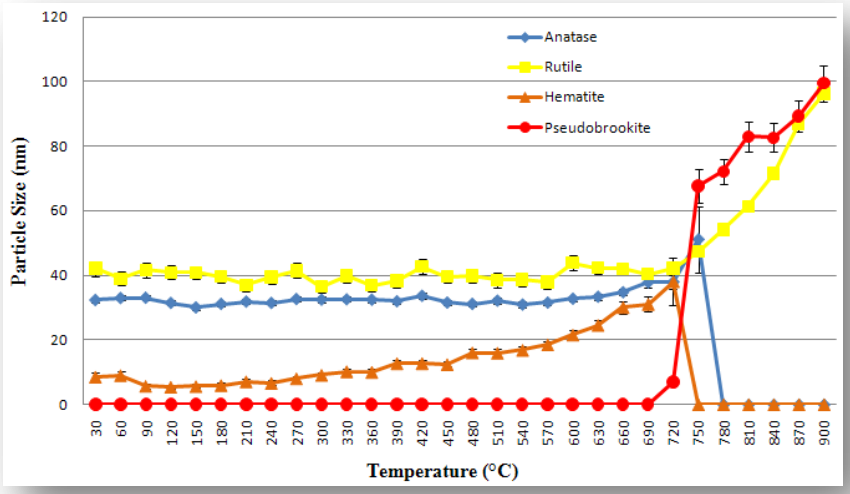

Figure 3.40. Particle size changes of the constituent phases in the Fe/Degussa P25 catalyst during heat treatment

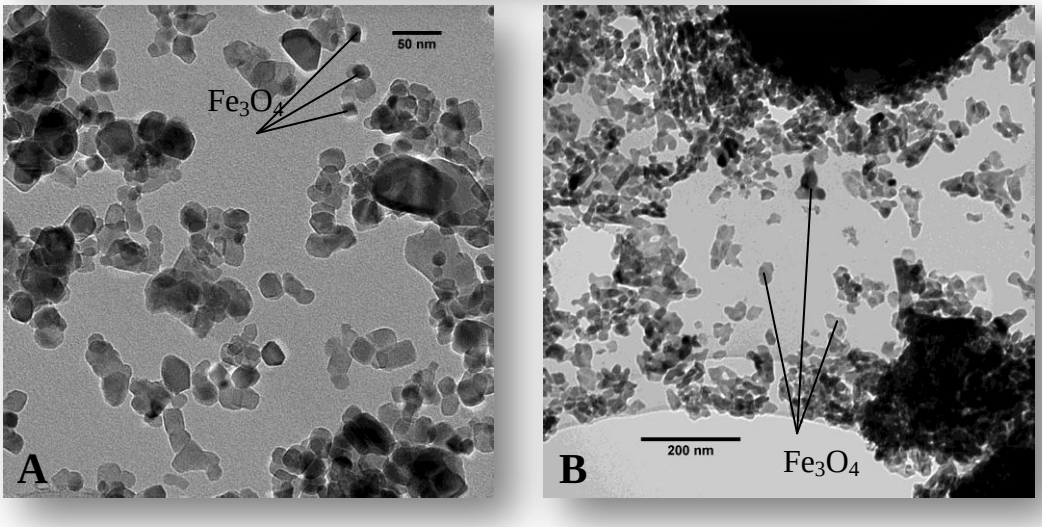

*Figure 3.41. TEM images of the Fe/Degussa P25 catalyst after calcination (**A**) and a similar Fe/Rutile catalyst for comparison (**B**)*

Hematite particle growth rate virtually ceased when pseudobrookite began to form at 690 °C. This was due to Ti^{4+} migration into the hematite particles, setting up a competitive process between hematite sintering and its conversion to pseudobrookite. At 720 °C the hematite particles increased in size prior to pseudobrookite formation. The majority of the solid-state reaction between anatase and hematite occurred between 720 °C and 750 °C, which was witnessed by the rates of change of particle size of anatase, hematite and pseudobrookite (Fig. 3.42). The average particle size of pseudobrookite and rutile continued to increase at elevated temperatures due to agglomeration.

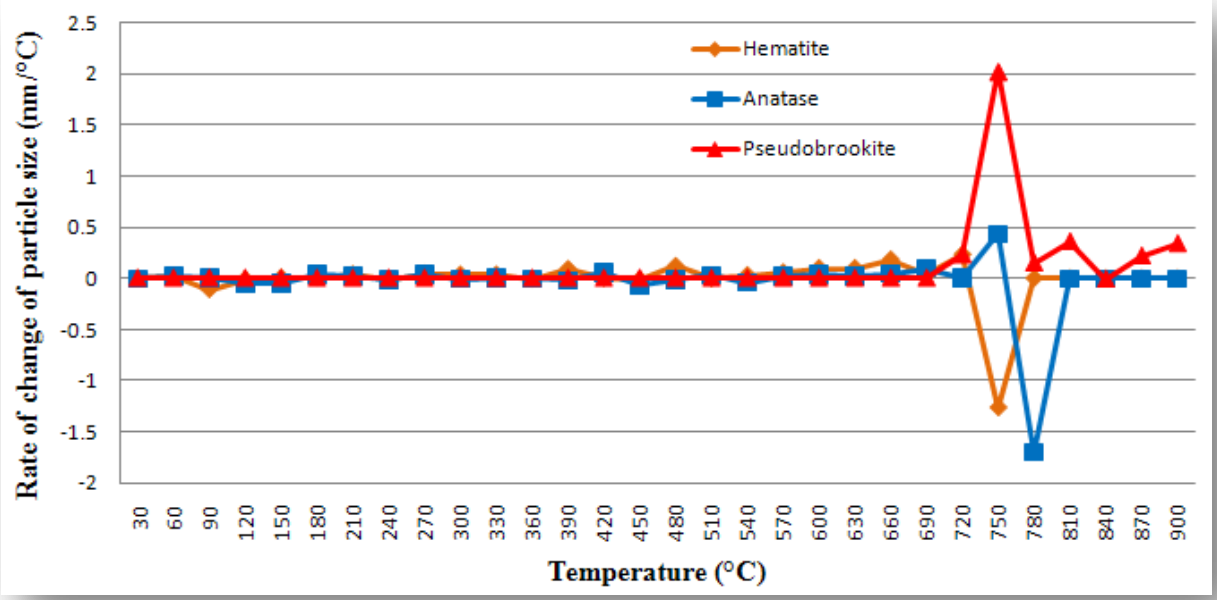

Figure 3.42. Instantaneous rates of change of particle size of anatase, hematite and pseudobrookite in the Fe/Degussa P25 catalyst during heat treatment

3.2.2. Fe/SIGMA ANATASE

Preliminary Discussion

The Sigma anatase support differed from the Degussa P25 support in that the average anatase particle size was approximately four times larger than that of Degussa P25. Secondly, the Sigma support displayed a significantly better thermal stability than Degussa P25, with very little anatase to rutile conversion even at temperatures of 900 °C (Fig. 3.21). Thirdly, the Sigma anatase was X-ray transparent and thus led to sample penetration and calculation of an unrealistic "amorphous" component. It was initially thought that the addition of iron, in the form of hematite, would aid in the X-ray absorption but unfortunately this did not alleviate this problem.

Quantitative Analysis

The intensity profile of the diffraction patterns collected during the heat treatment of this catalyst (Fig. 3.43) was similar to that of the Degussa P25-supported catalyst (Fig. 3.34). However, the Fe/Sigma catalyst revealed no hematite peaks at the start of the experiment. In this case none of the iron nitrate had been converted to hematite during the drying process and was therefore absent from the diffraction patterns. This meant that all Fe^{3+} was in the form of Fe^{3+}AM on the support. There was also significant sample penetration, leading to high and unrealistic amorphous material concentrations. This amorphous component was made up of contributions from the sample holder and from the real amorphous Fe^{3+}AM present at the start of the experiment. An identical correction procedure, to that described above, was employed to calculate accurate concentrations of each phase, resulting in the final speciation diagram given as figure 3.44.

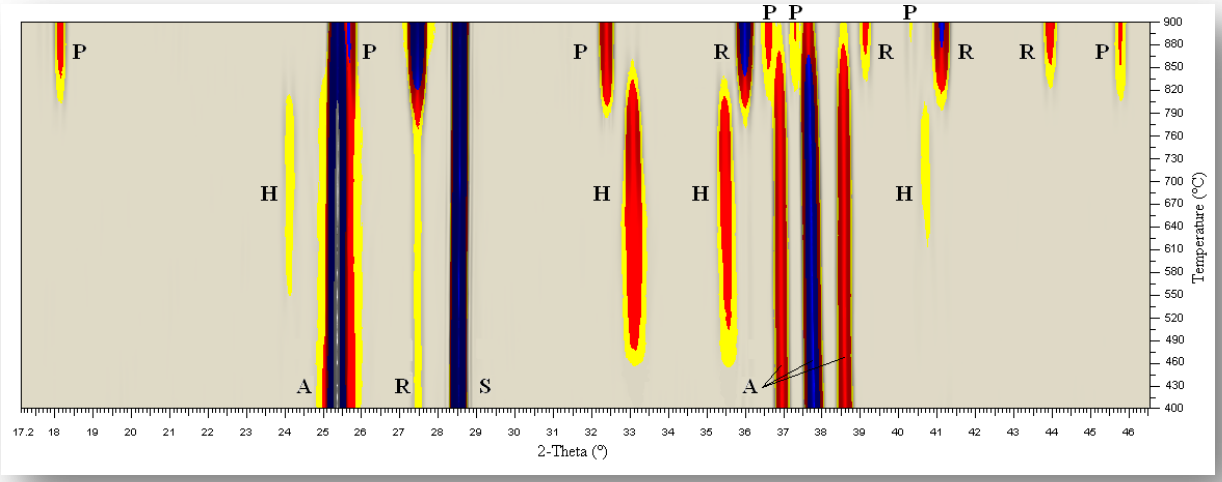

Figure 3.43. Intensity profile of the diffraction patterns collected during the heat treatment of the Fe/Sigma catalyst: ***A*** *– anatase,* ***R*** *– rutile,* ***S*** *– silicon,* ***H*** *– hematite and* ***P*** *– pseudobrookite*

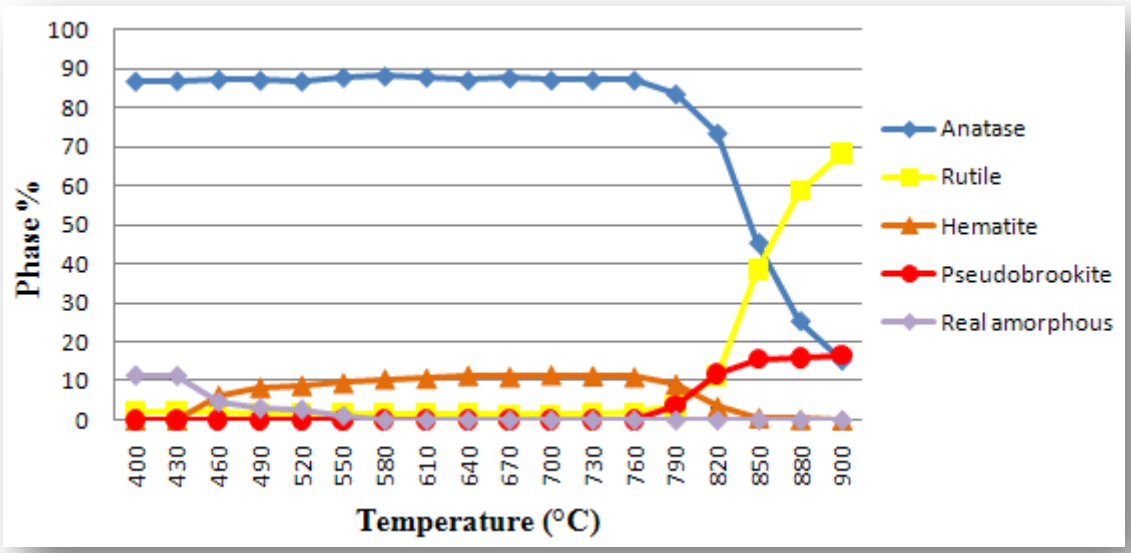

Figure 3.44. Quantitative phase analysis of the Fe/Sigma catalyst during heat treatment (average GoF of 1.12)

The conversion of Fe^{3+}AM to hematite began at temperatures above 430 °C and the maximum hematite concentration achieved was 11.48 ± 0.07 % at a temperature of 700 °C. The initial rate of conversion was relatively high, with values in the region of 0.22 %/°C, which decreased at higher temperatures (Fig. 3.45**A**). Heating the sample above 760 °C initiated the anatase to rutile phase transition with the simultaneous formation of pseudobrookite. It appears that the addition of hematite facilitated the anatase to rutile phase transition in the Sigma support. Heald and Weiss found that by adding hematite to anatase (Baker-analyzed, reagent grade, lot number 31310) even in concentrations as low as 0.087 %, the growth phase of the transition, at 1000 °C, was increased significantly, while the nucleation period was virtually unaffected.[5] This experiment relates to kinetic studies at constant temperature, while in our study the reaction was monitored at increasing temperature intervals. The addition of hematite to the Sigma anatase, especially in large concentrations, resulted in a transition that occurred at lower temperatures and to a much larger extent than for the unloaded support.

The rate of consumption of anatase exceeded the rate of formation of rutile at temperatures greater than 750 °C. The rate of consumption of anatase indicates, once again, that it was the preferred Ti^{4+} donor during the formation of pseudobrookite (Fig. 3.45**B**). The availability of anatase throughout the experiment allowed the pseudobrookite to form exclusively from the reaction between anatase and hematite. This indicates that Ti^{4+} diffusion from rutile into hematite is thermodynamically more difficult at temperatures below 900 °C, making anatase the kinetically favored reactant for this reaction.

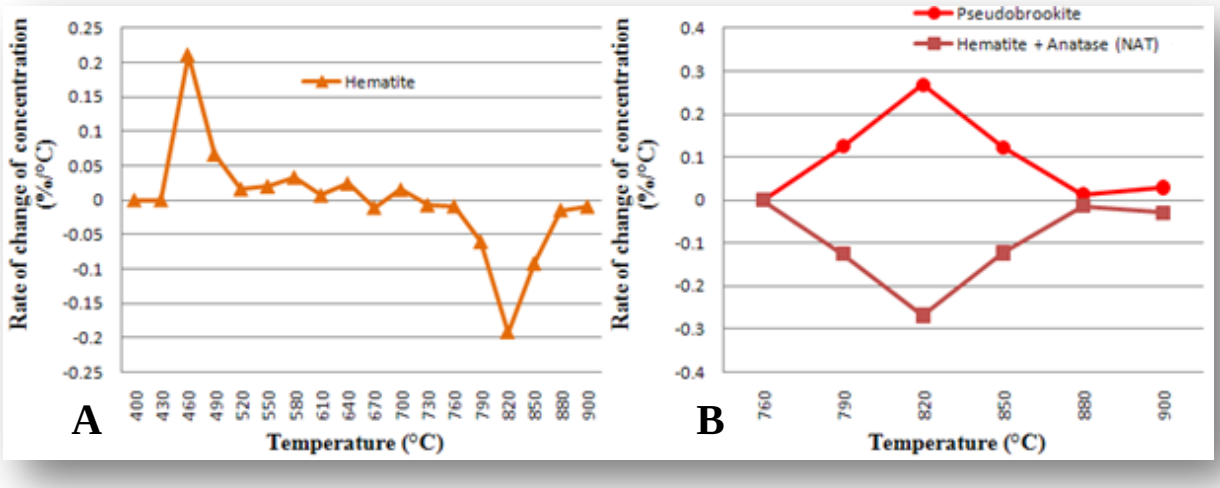

*Figure 3.45. Instantaneous rates of change of concentration of **A** – hematite and **B** – pseudobrookite compared to the combined rates of consumption of hematite and anatase not attributed to the phase transition (NAT)*

Particle Size Analysis

Figure 3.44 indicates that the maximum hematite concentration of 11.48 ± 0.1 % was achieved at a temperature of 700 °C. However, figure 3.46 indicates that the average hematite particle size at 700 °C was 35.2 ± 2 nm. In order to keep the average hematite particle size below the 20 nm limit, the catalyst would have to be calcined at 460 °C, giving an average particle size of 16.9 ± 2 nm, leading to a degree of oxidation of only 42 %. However, the TEM images, given in figure 3.47, show that the majority of the hematite particles were unsupported. This observation suggests that there was little Fe^{3+}AM / hematite – anatase interaction. Instead, the Fe^{3+}AM / hematite preferred to bind to similar particles in order to minimize surface energy.

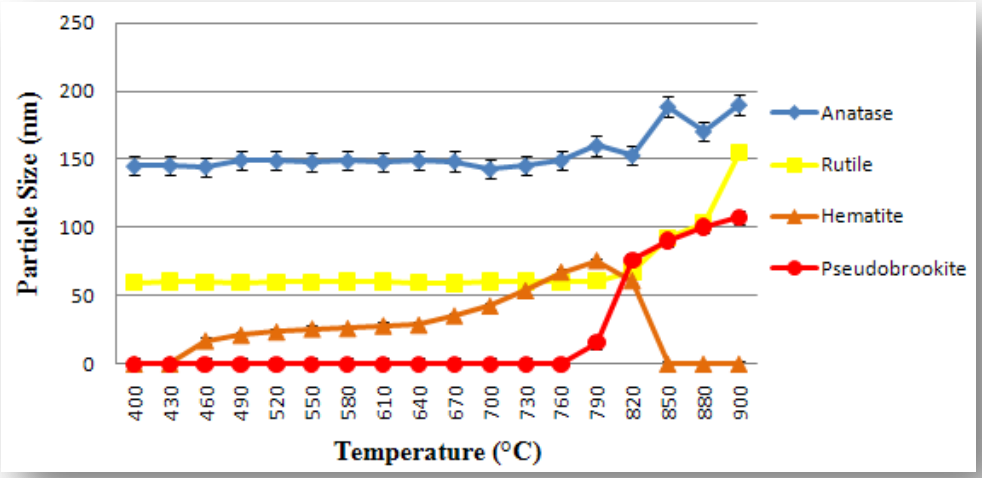

Figure 3.46. Particle size changes of the constituent phases in the Fe/Sigma catalyst during heat treatment

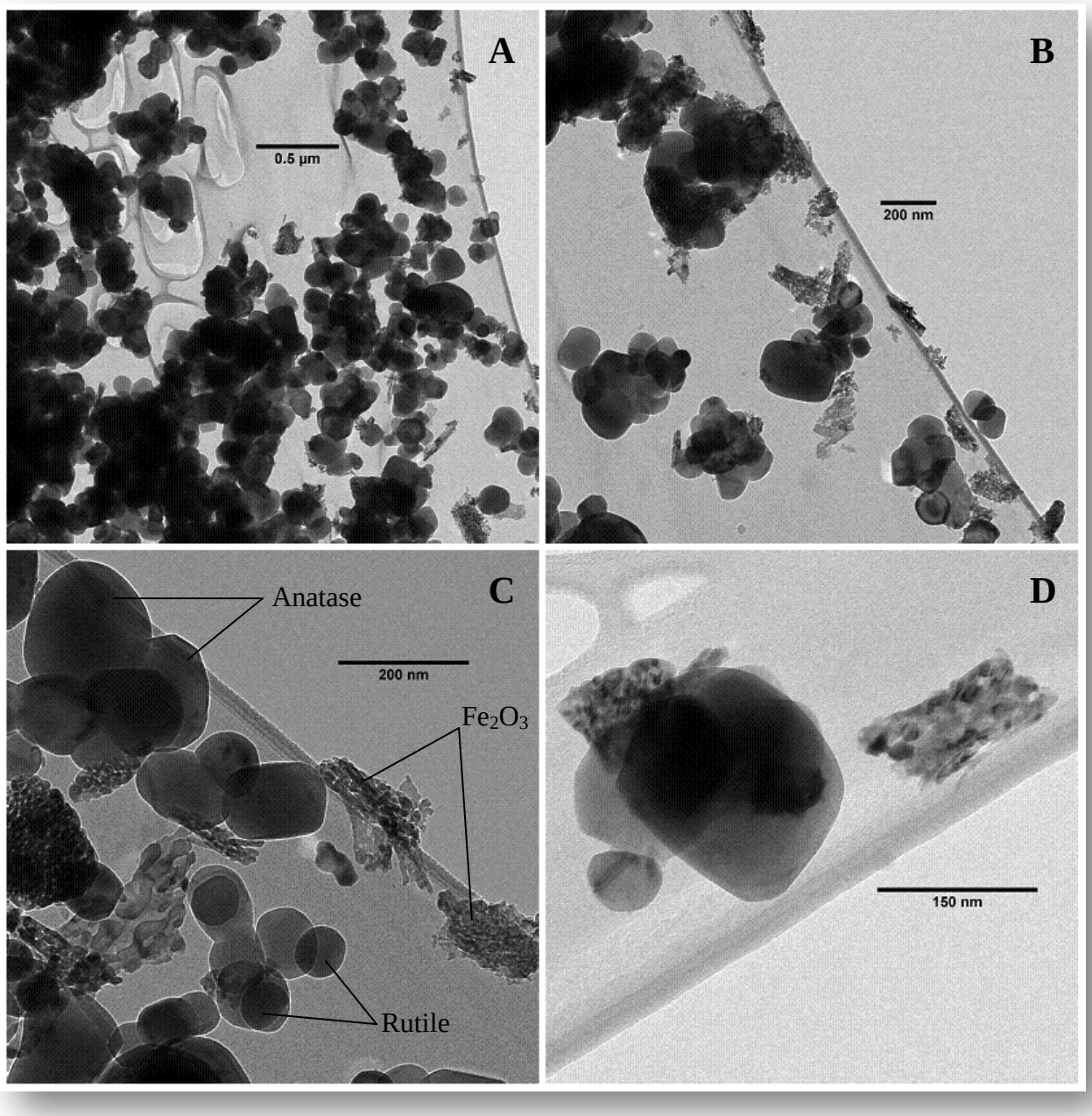

Figure 3.47. TEM images of the Fe/Sigma catalyst after calcination: ***A*** *– sample representation,* ***B*** *and* ***C*** *– images showing varying degrees of unsupported metal clustering and* ***D*** *– magnified view of a metal cluster*

Figure 3.48 gives the instantaneous rates of change of hematite and pseudobrookite particle size as a function of temperature. The hematite particle size initially increased at a relatively high rate of approximately 0.56 nm/°C at 460 °C as it began to crystallize from Fe^{3+}AM. The growth rate then decreased, but remained positive, until a temperature of 640 °C, after which the rate of growth increased steadily until it reached a second maxima of approximately 0.45 nm/°C. Hematite particles continued to grow at 790 °C, however the competing pseudobrookite reaction reduced the rate of growth and the hematite particles eventually disappear as the pseudobrookite reaction gained momentum. Figure 3.46 above shows that between 760 °C and 790 °C both hematite and pseudobrookite particles increased in

size, a fact confirmed by the positive values for both phases in figure 3.48. The pseudobrookite reached its highest rate of particle growth, approximately 2 nm/°C, at 820 °C but the hematite only reached a similar, negative rate at 850 °C. This phenomenon was not observed during the heat treatment of the Fe/Degussa P25 catalyst.

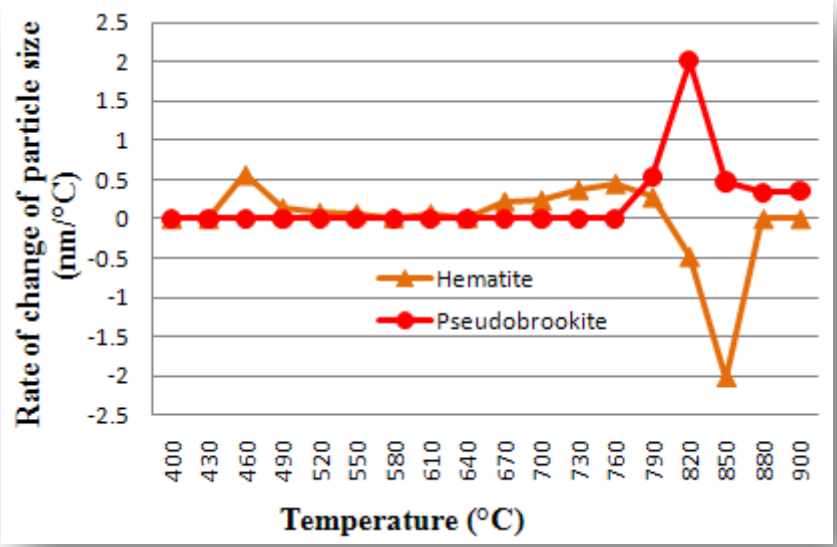

Figure 3.48. Instantaneous rates of change of hematite and pseudobrookite particle size in the Fe/Sigma catalyst during heat treatment

3.2.3. Fe/NSA

Preliminary Discussion

Heat treatment of the NSA support indicated that the support had an average particle size of approximately 9 nm. Unfortunately, the support was found to contain a significant amount of brookite and amorphous material.

Quantitative Analysis

The topographical view of the PXRD patterns collected during the heat treatment of the sample is given as figure 3.49, while the quantitative data for this experiment is given as figure 3.50.

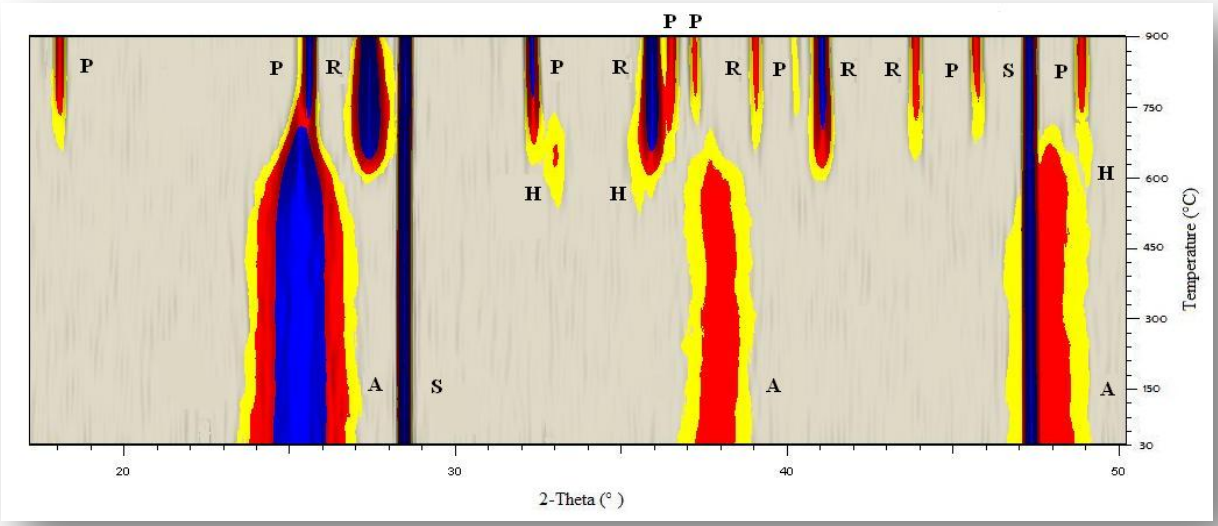

*Figure 3.49. Intensity profile of the diffraction patterns collected during the heat treatment of the Fe/NSA catalyst: **A** – anatase, **R** – rutile, **S** – silicon, **H** – hematite and **P** - pseudobrookite*

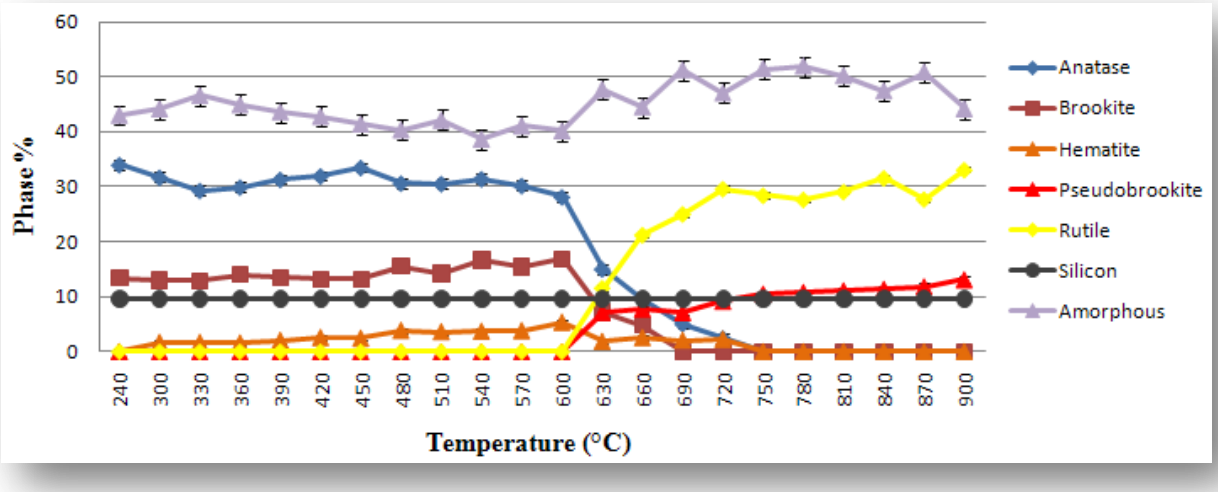

Figure 3.50. Quantitative phase analysis of the Fe/NSA catalyst during heat treatment (average GoF of 1.08)

It is clear that the quantitative results were far more complicated than observed for the previous samples. The problem with this dataset was the fact that there were three contributions to the "amorphous" content, i.e. the Fe^{3+}AM, the amorphous component in the support and the amorphous contribution coming from the sample holder. It was impossible to correct the data given the number of contributions to the amorphous value. For this reason, only quantitative trends are discussed.

Fe^{3+}AM was converted to hematite at temperatures above 240 °C and reached a maximum concentration at a temperature of 600 °C. The pseudobrookite reaction was found to occur at the same time as the start of the anatase to rutile transition at temperatures above 600 °C. The fact that the rate of consumption of anatase was smaller than the rate of formation of rutile at 630 °C, indicated that anatase was being consumed and formed simultaneously. It was assumed that brookite underwent the transition to anatase and then into rutile, which was shown during the heat treatment of the unloaded support. The rate of consumption of brookite was added to that of anatase, to give a value equivalent to the total consumption rate of anatase in the system (Table 3.3). Subtracting the rate of formation of rutile from this value yields the rate of consumption of anatase not attributed to the phase transition (NAT). Combination of this value with the rate of hematite consumption, resulted in the converse of the rate of formation of pseudobrookite, indicating that anatase was once again the preferred Ti^{4+} donor during the formation of pseudobrookite.

Table 3.3. Instantaneous rates of change of concentration of the phases present during the heat treatment of the Fe/NSA catalyst

	Rates of Change of Concentration (%/°C)							
Temp	Anatase	Brookite	Hematite	Pseudobrookite	Rutile	Total Anatase Consumption	Anatase Consumption NAT	NAT + Hematite
630	-0.699	-0.556	-0.207	0.560	0.902	-1.255	-0.353	-0.560
660	-0.475	-0.213	0.040	0.007	0.641	-0.688	-0.047	-0.007
690	-0.269	-0.346	-0.009	0.040	0.585	-0.615	-0.030	-0.040
720	-0.241	0.000	-0.004	0.097	0.149	-0.241	-0.092	-0.097
750	-0.184	0.000	-0.169	0.198	0.155	-0.184	-0.030	-0.198

Particle Size Analysis

Figure 3.51 shows the variation of particle size as a function of temperature during the heat treatment process. When hematite began to crystallize, at temperatures above 240 °C, it formed particles with sizes comparable to the support phases in a similar way as was observed for the Degussa P25-supported catalyst. This indicates that the metal particles were either unsupported or were joined to individual support particles as represented in figure 3.52. The average hematite particle size began to decrease as the temperature was increased beyond 330 °C, an effect that had not been observed in any of the previous catalyst samples. This observation indicates that larger Fe^{3+}AM particles are converted to hematite particles more readily, while smaller ones, which lower the average particle size, only form at higher temperatures. The hematite particles were at their smallest when the temperature was between 480 °C and

510 °C, with values in the region of 4.7 ± 2 nm. Anatase particles had sizes in the region of 12.3 ± 1 nm at the same temperature, which represented the largest anatase to rutile particle size ratio. Therefore, 510 °C marks the most practical calcination temperature for this system. The incomplete calcination at this temperature resulted in the formation of what seemed to be support, and possibly hematite, crystallites that were trapped in an amorphous Fe^{3+}AM matrix (Fig. 3.53). The anatase to rutile phase transition and the pseudobrookite reaction began at temperatures above 600 °C.

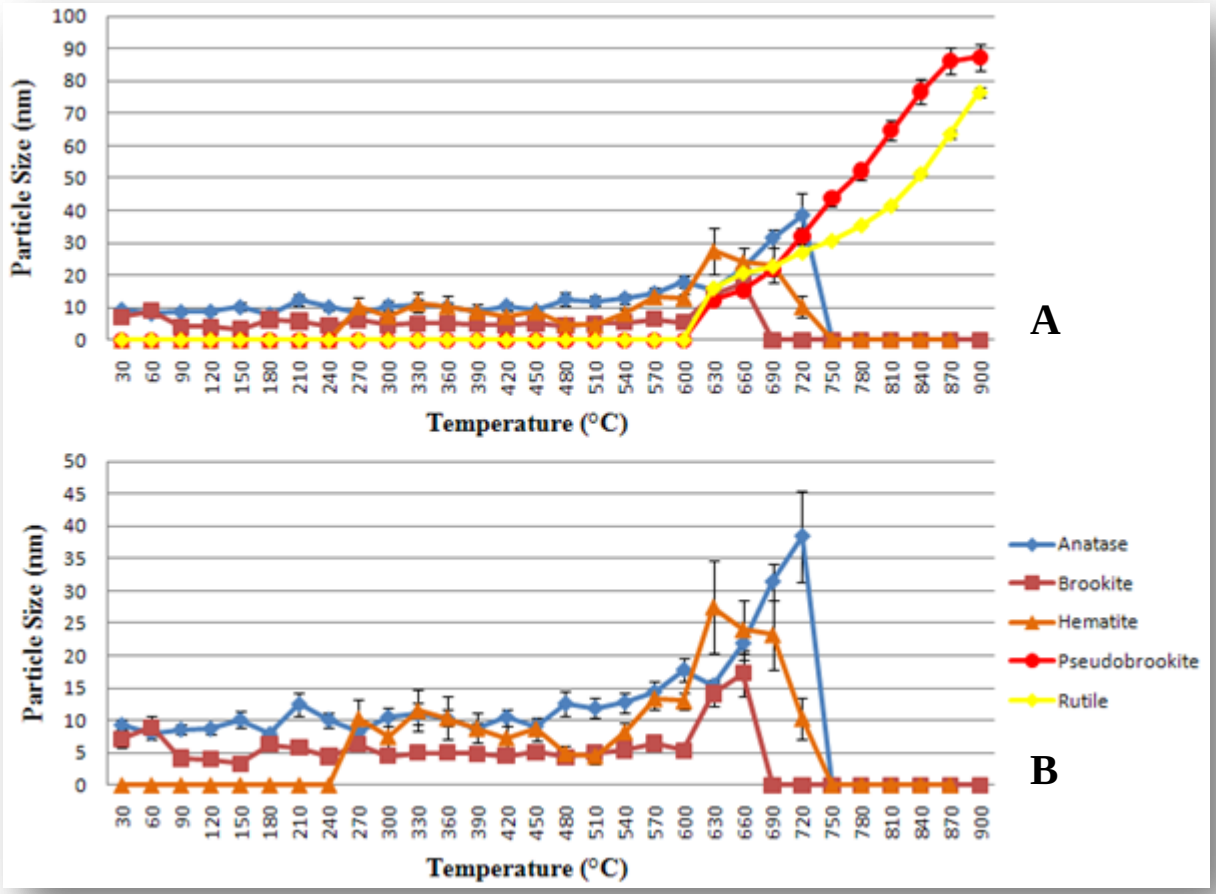

Figure 3.51. ***A*** *– particle size changes of the constituent phases in the Fe/NSA catalyst during heat treatment and* ***B*** *- magnified view of the minor phases*

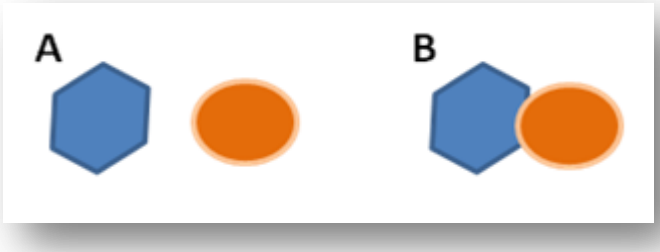

Figure 3.52. Diagrammatic representation of ***A*** *– unsupported and* ***B*** *– supported hematite in the Fe/NSA catalyst during heat treatment showing the similarity of the particle sizes (blue angular objects – anatase and orange circular objects – hematite)*

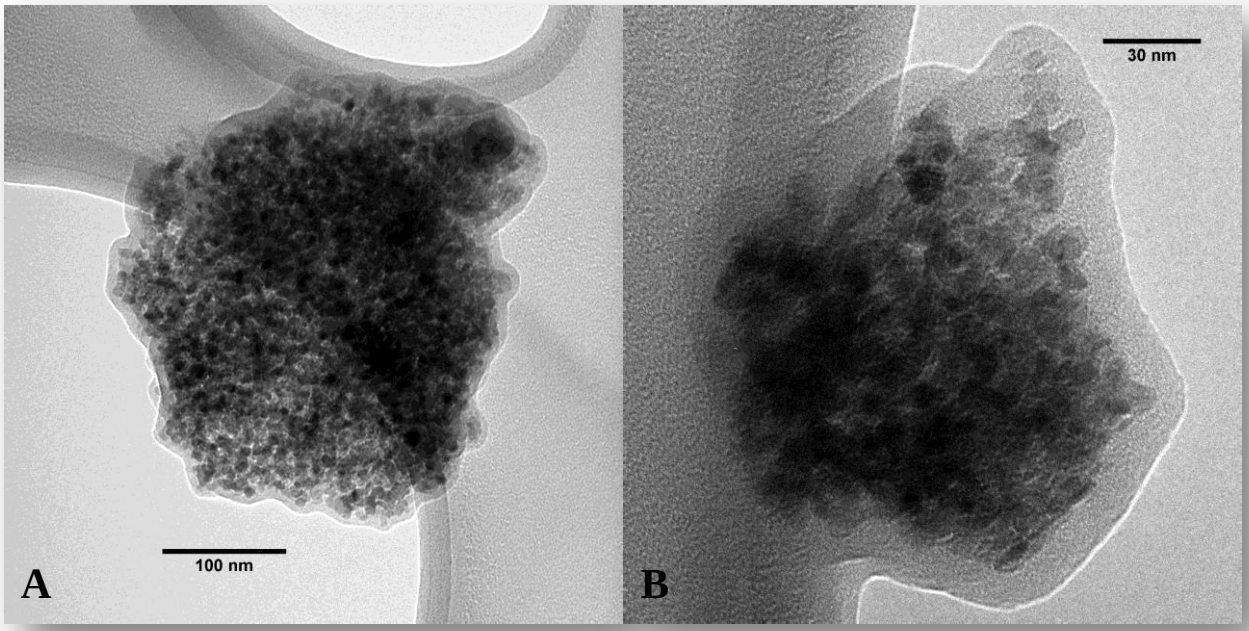

Figure 3.53. TEM images of the Fe/NSA catalyst after calcination showing what could possibly be support and hematite crystallites trapped in an amorphous Fe^{3+}AM matrix: ***A*** *– low magnification and* ***B*** *– high magnification*

The rate of growth of pseudobrookite particles was unlike any of those seen for the previous iron catalysts (Fig. 3.54). The initial growth rate was relatively fast with a value of approximately 0.5 nm/°C, in line with those seen before, after which there was a sudden decrease in the rate of particle size growth, which was also in line with previous observations. The difference arises when the temperature was increased above 690 °C, when the growth rate of pseudobrookite particles increased to a value close to that of the initial value, indicating that the rate of growth of pseudobrookite particles varied drastically with increasing temperature in this sample.

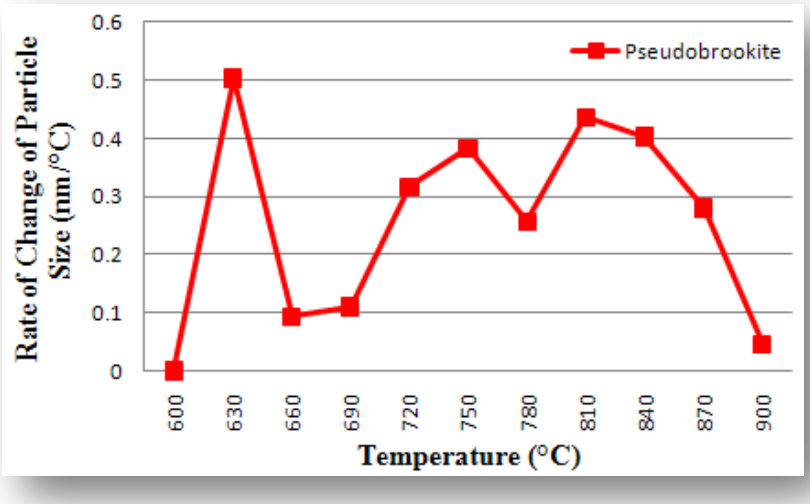

Figure 3.54. Rate of change of pseudobrookite particle size during the heat treatment of the Fe/NSA catalyst

3.2.4. Co/DEGUSSA P25

Preliminary Discussion

Cobalt (Co) catalysts are used in FT reactions due to their decreased affinity for the WGS reaction and higher consumption rate (in comparison with iron catalysts), which ultimately leads to higher first pass conversions and this increases reactor efficiency.[37] However, Co is significantly more expensive than iron and thus supported Co catalysts are used in industry to maximize the number of active metal sites for the FT reaction. Silica (SiO_2) supports are most commonly used.[43-47] However, many studies have been completed on TiO_2,[48-50] Al_2O_3[51-52] and other supports.[53-54] Unfortunately Co fluoresces intensely in an XRD system when a Cu source is used, leading background radiation, which decreases resolution and signal to noise ratios, making Rietveld refinement more difficult. The problem was further compounded by the additional sample penetration issues. For these reasons data was collected on a virtually identical system with a Co source in order to avoid fluorescence problems.

Quantitative Analysis

Baddeleyite (ZrO_2) was initially used as the spike in this experiment in order to suppress the amorphous contribution from the sample holder. Baddeleyite crystallizes in a monoclinic *P*21/*c* space group and is made up of edge-sharing ZrO_2 nonahedrons (Fig. 3.55).[55] However, this spike proved no more effective than silicon and caused significant peak overlap, resulting in a return to the use of silicon for the remaining catalyst samples. A shift of the peak position for the support and spike phases is noted in figure 3.56, when compared with previous data. This was due to the change in wavelength (λ) of the radiation when using the Co source. This dataset suffered from significant peak overlap, annotated as **X&Y** in figure 3.56. For example, at temperatures below 600 °C the peak at 41.2 ° 2-theta represents the 0 2 0 peak of the ZrO_2 spike. At temperatures above 600 °C there appears to be an increase in intensity of this peak. However, this is attributed to the emergence of the 1 1 0 peak of cobalt titanium oxide ($CoTiO_3$) denoted **C2**, which overlaps with the ZrO_2 peak (**Z&C2**). Similarly overlap of **C2** occurs with anatase (**A**) and rutile (**R**) peaks.

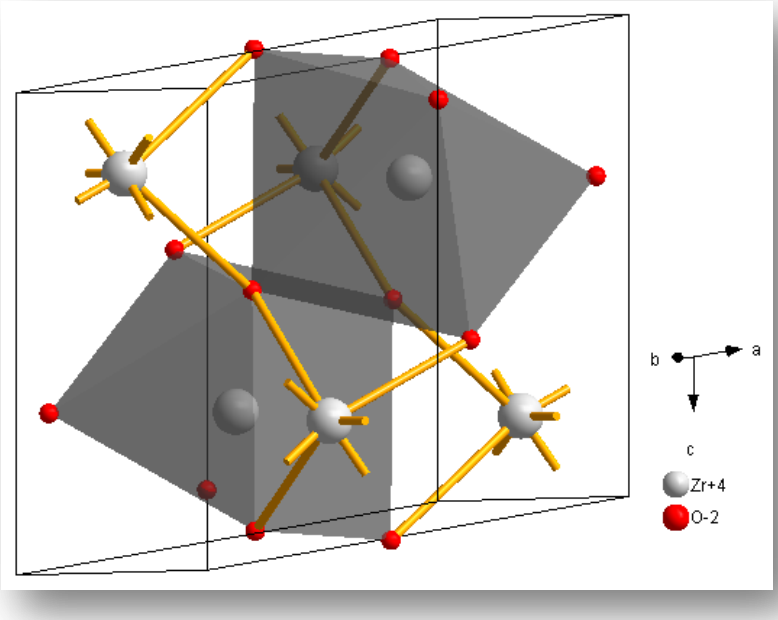

Figure 3.55. Crystallographic representation of baddeleyite (monoclinic P21/c)[55]

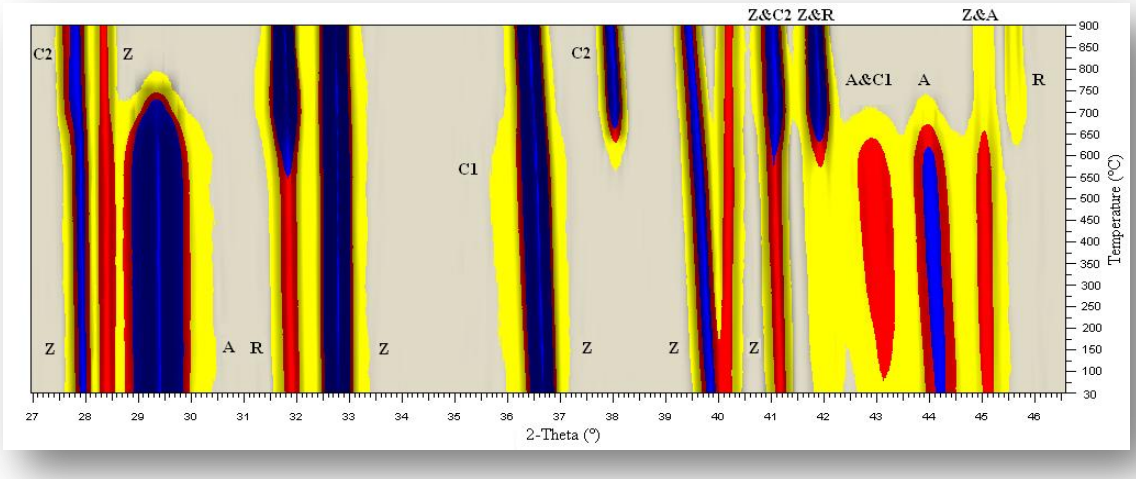

Figure 3.56. Intensity profile of the diffraction patterns collected during the heat treatment of the Co/Degussa P25 catalyst: ***A*** *– anatase,* ***R*** *– rutile,* ***Z*** *– baddeleyite spike,* ***C1*** *– cobalt oxide and* ***C2*** *– cobalt titanium oxide*

Quantitative Rietveld refinement showed the presence of the amorphous contribution from the sample holder and secondary corrections were thus applied to generate the results presented in figure 3.57. Figure 3.58 shows the instantaneous rates of formation of cobalt oxide and consumption of the amorphous component before and after this correction.

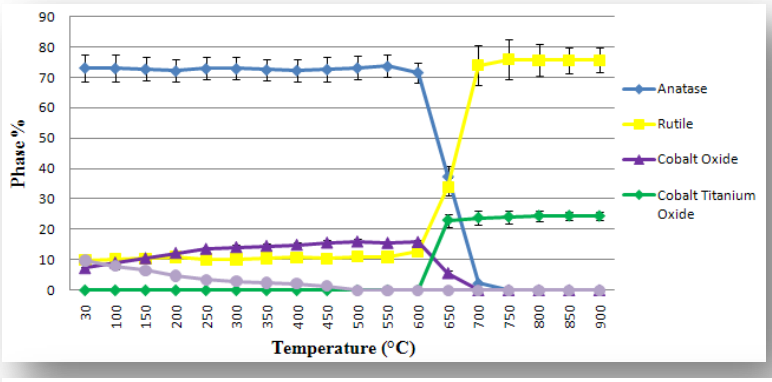

Figure 3.57. Secondary correction of the quantitative phase analysis of the Co/Degussa P25 catalyst during heat treatment (average GoF of 1.24)

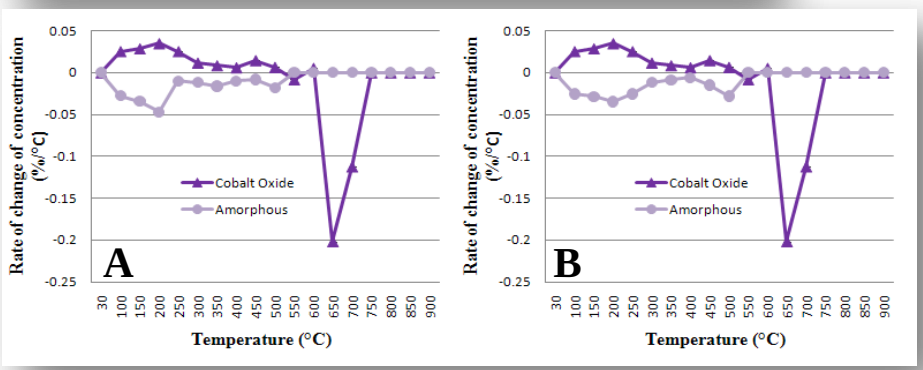

Figure 3.58. Instantaneous rates of change of concentration of cobalt oxide and amorphous $Co^{2+/3+}$/AM: ***A*** *– before and* ***B*** *– after data correction*

The data presented in figure 3.57 confirms that the maximum cobalt oxide concentration of 15.85 ± 0.7 % was achieved at a temperature of 500 °C. The anatase to rutile transition began at temperatures between 550 °C and 600 °C. Ti^{4+} migration was initiated at temperatures between 600 °C and 650 °C forming cobalt titanium oxide ($CoTiO_3$), the rate of which was identical to the combined rates of consumption of cobalt oxide and anatase not attributed to the transition (NAT), indicating that anatase was, once again, the only source of Ti^{4+} (Fig. 3.59). The calculated oxidation state of Co in cobalt oxide is 2.67, but in reality there are two octahedrally coordinated Co^{3+} metal sites for each Co^{2+} site in the structure.[56] The migration of Ti^{4+} into the structure causes a reduction of Co^{3+} metal sites to Co^{2+} along with significant structural changes, which ultimately form alternating layers of Co^{2+} and Ti^{4+} octahedra (Fig. 3.60).[57]

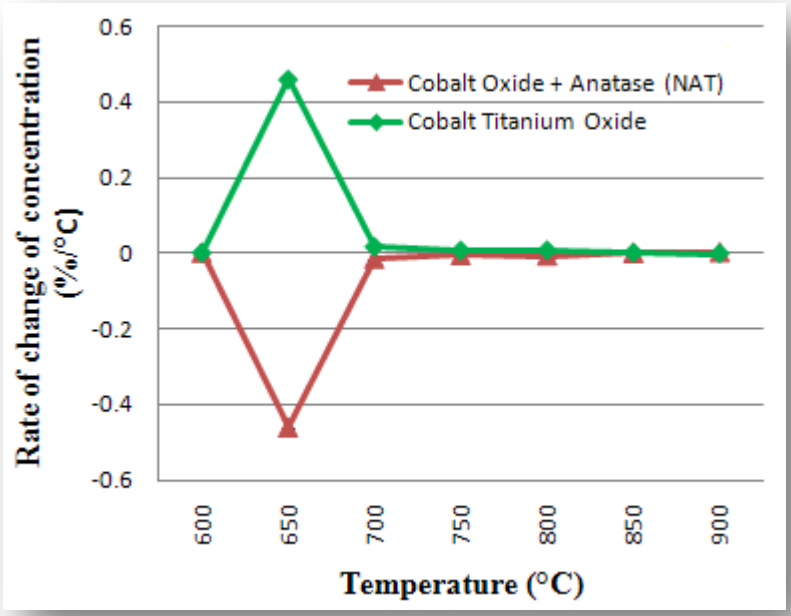

Figure 3.59. Instantaneous rates of change of concentration of cobalt titanium oxide and the combined rates of consumption of cobalt oxide and anatase not attributed to the phase transition (NAT)

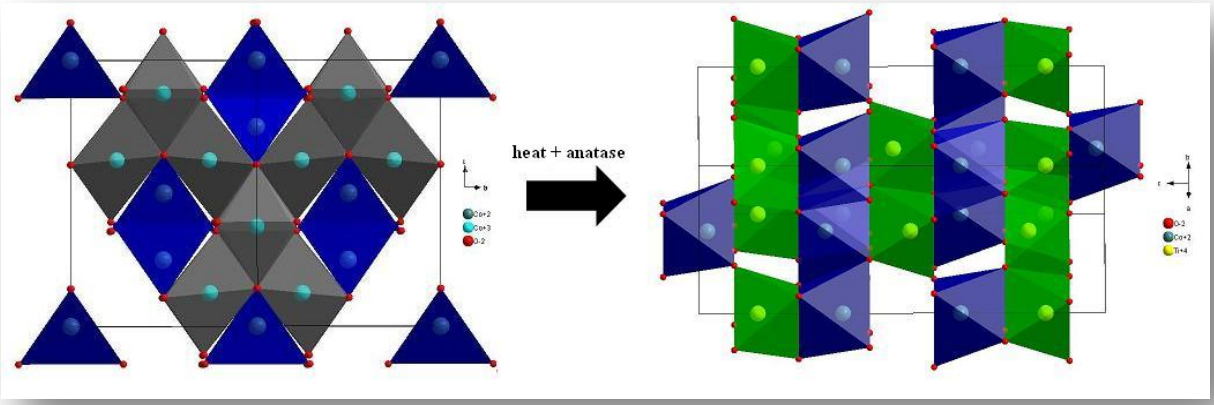

Figure 3.60. A structural representation of the conversion of cobalt oxide (cubic $Fd\bar{3}ms$) [56] *to cobalt titanium oxide(trigonal $R\bar{3}H$)* [57]

Particle Size Analysis

The particle size data in figure 3.61 indicates an initial decrease in average cobalt oxide particle size between 30 °C and 150 °C. This suggests that the cobalt oxide particles that had formed during the drying process were relatively large and the crystallization of other particles lowered the average value as temperature was increased. The average particle size increased steadily as the temperature exceeded 150 °C. At 500 °C, the temperature at which there was the largest concentration of cobalt oxide, the average particle size of cobalt oxide was found to be 14.8 ± 1 nm. The TEM image, presented as figure 3.62, revealed that the cobalt oxide particles had bound to the support phases but, due to the similarity in particle size, the degree of dispersion was very low. The cobalt oxide particles never exceeded an average value of 16.4 ± 1 nm. This indicates that this cobalt catalyst was less susceptible to physical changes and metal oxide agglomeration during heating, when compared to the equivalent iron catalyst.

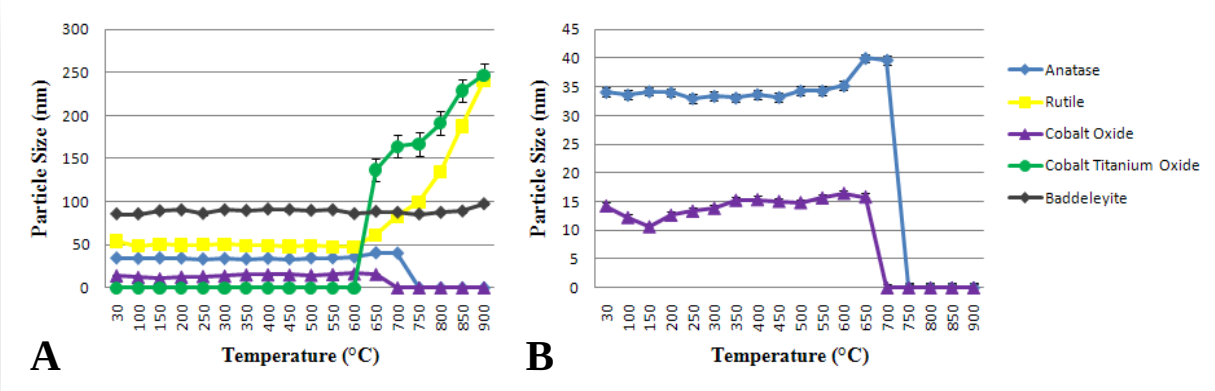

Figure 3.61. Particle size changes of the constituent phases present during the heat treatment of the Co/Degussa P25 catalyst: ***A*** *– all phases and* ***B*** *– anatase and cobalt oxide phases*

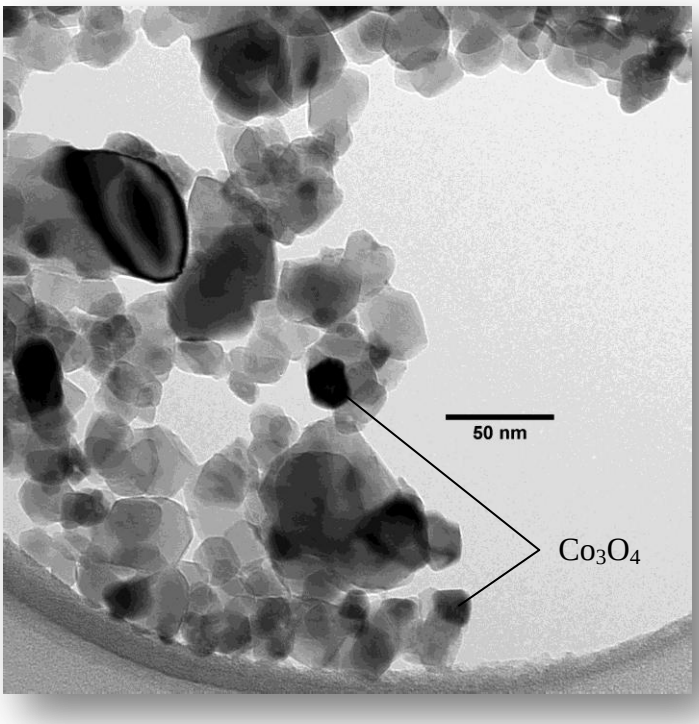

Figure 3.62. TEM image of the Co/Degussa P25 catalyst after calcination

The initial cobalt titanium oxide particle size, at 650 °C, was well above those of the reactant phases or combination thereof (Fig. 3.61), with an average value of 136.7 ± 13 nm. However, there may have been significant sintering during the 50 °C temperature interval between 600 °C and 650 °C. The rate of growth of the cobalt titanium oxide at 650 °C, with a value of ±2.7 nm/°C, was higher than any value seen previously for the iron titanates, indicating that the growth of these particles occurs rapidly (Fig. 3.63).

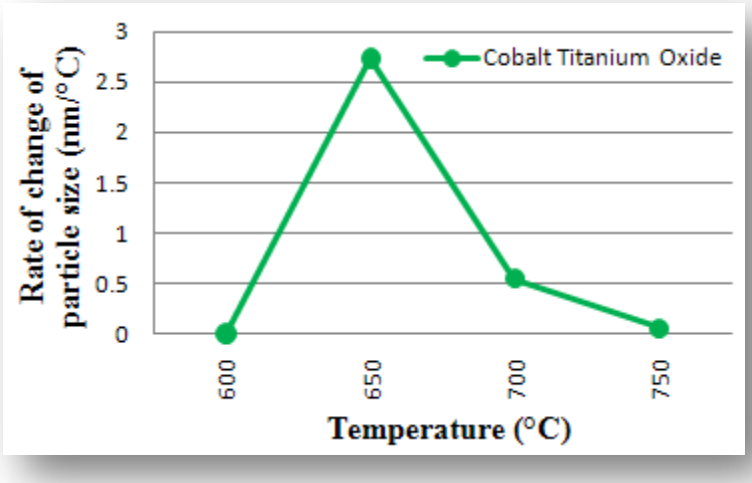

Figure 3.63. Instantaneous rates of change of cobalt titanium oxide particle size

3.2.5. Co/SIGMA ANATASE

Preliminary Discussion

Sigma anatase, with its high thermal stability and large particle size, proved ineffective as a support of iron-based systems. Its use as a support for cobalt was investigated in this section.

Quantitative Analysis

Figure 3.64 shows that crystalline cobalt nitrate tetrahydrate [$Co(NO_3)_2.4H_2O$], represented as **C3**, was present at the beginning of the heat treatment experiment, which was not observed in the Co/Degussa P25 catalyst. Cobalt nitrate crystallizes in a triclinic $P\bar{1}$ space group and is an ionic structure. It is made up of Co^{2+} ions that occupy the corners of the unit cell with nitrate (NO_3^-) molecules inside the unit cell, related by an inversion center (Fig. 3.65).[58] As the temperature was increased the cobalt nitrate was converted to amorphous material, a process that was complete at a temperature of 120 °C. The refinement results showed a significant amorphous contribution resulting in secondary corrections having to be applied to the data, the results of which are given in figure 3.66.

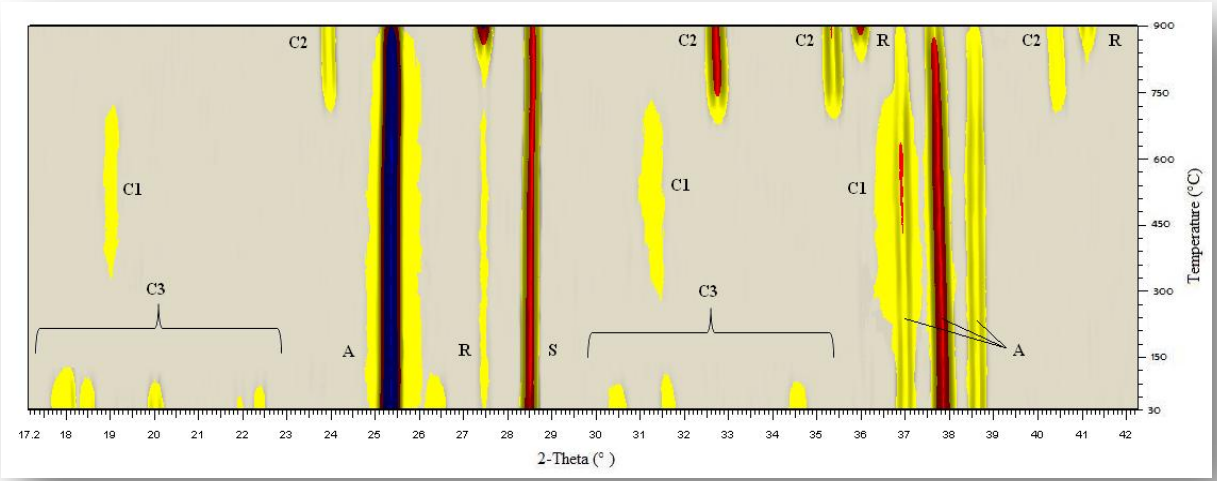

Figure 3.64. Intensity profile of the diffraction patterns collected during the heat treatment of the Co/Sigma catalyst: ***A*** *– anatase,* ***R*** *– rutile,* ***S*** *– silicon,* ***C1*** *– cobalt oxide,* ***C2*** *– cobalt titanium oxide and* ***C3*** *– cobalt nitrate tetrahydrate*

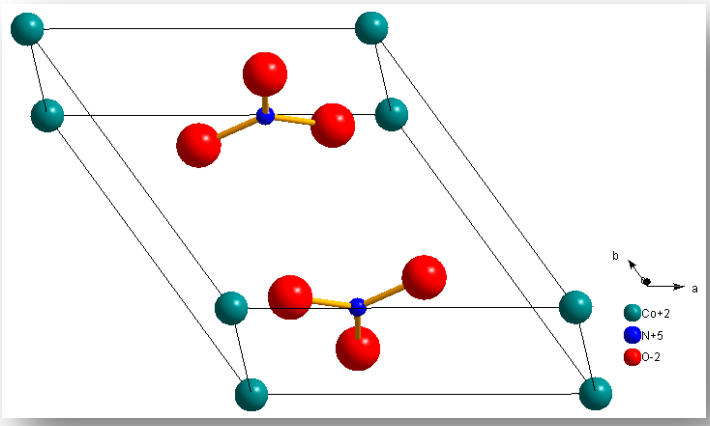

Figure 3.65. Crystallographic representation of cobalt nitrate [$Co(NO_3)_2.4H_2O$] (triclinic $P\bar{1}$)[58]

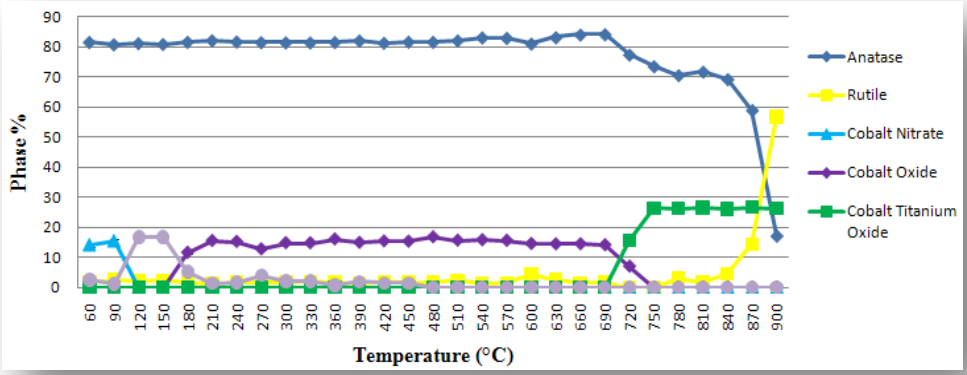

Figure 3.66. Corrected quantitative phase analysis of the Co/Sigma catalyst during heat treatment (average GoF of 1.08)

The quantitative data given in figure 3.66 suggests that the majority of cobalt nitrate had been deposited in crystalline form. Heating the sample resulted in the expulsion of water and nitrate molecules from the cobalt nitrate to form the amorphous Co^{3+}AM intermediate. The Co^{3+}AM was oxidized at temperatures above 150 °C, forming crystalline cobalt oxide. The cobalt oxide concentration remained relatively constant for the majority of the experiment, reaching a maximum of 16.64 ± 0.2 % at a temperature of 480 °C. This value appears rather high but it corresponds to a Co^0 loading of approximately 12 %, which is slightly higher than the loading value of 10 %. Cobalt titanium oxide formed at temperatures above 690 °C, via the anatase-cobalt oxide reaction. Interestingly, the reaction had reached completion before the anatase to rutile transition began at temperatures above 810 °C. Bearing in mind that the unloaded support did not undergo a phase transition, this result suggests that cobalt titanium oxide catalyzes the anatase to rutile transition at these elevated temperatures.

Particle Size Analysis

The particle size data presented in figure 3.67 shows that the anatase particle size remained relatively constant up to a temperature of 540 °C, after which the particles experienced irregular increases and decreases in size due to sintering (600 °C – 660 °C), formation of cobalt titanium oxide (690 °C – 810 °C) and agglomeration of the small amount of anatase remaining at temperatures above 810 °C. The average cobalt nitrate particle size was initially quite high but decreased dramatically upon heating, as water and nitrate molecules were driven off and the lattice was destroyed.

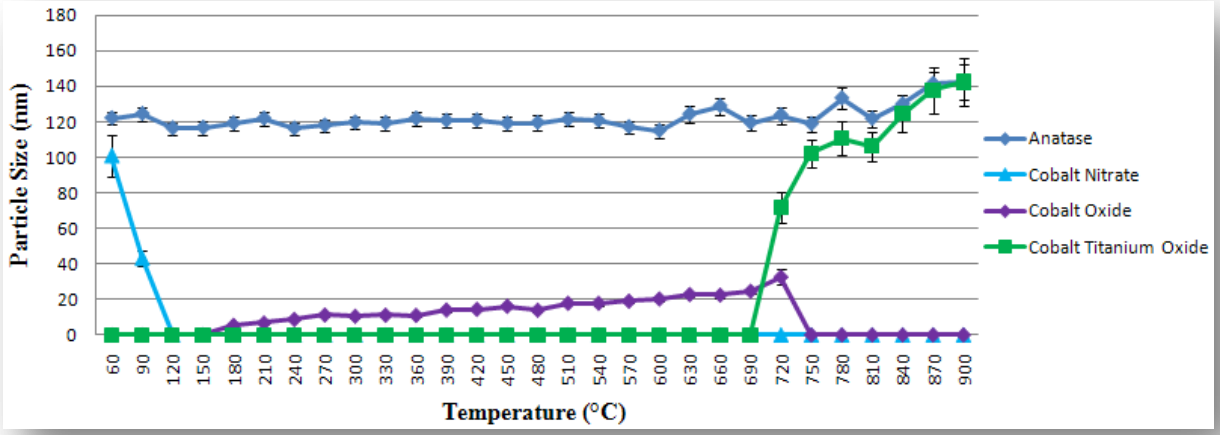

Figure 3.67. Particle size changes of the constituent phases during the heat treatment of the Co/Sigma catalyst

The presence of crystalline cobalt nitrate at the start of the experiment prompted investigation into the process of Co^{3+}AM and cobalt oxide formation. By assuming that the cobalt nitrate particles were spherical in nature and that the crystallization of cobalt oxide followed equation **(79)** below, we found that the calculated average particle size (using volume, density and mass calculations) should be approximately 50 nm upon completion of the calcination procedure. However, this was not the case and the particle size at maximum concentration, i.e. the point at which there should be no Co^{3+}AM left in the system, was approximately 13 nm (Fig. 3.67). This was confirmed by the TEM images in figure 3.68, which also shows good particle distribution on the surface of the support particles. Cobalt nitrate tetrahydrate is known to decompose at temperatures around 100 °C. We have shown that the decomposition process results in the formation of an amorphous intermediate that must have some degree of mobility on the surface of the support or undergo significant fracturing during the expulsion of the water and nitrate molecules in order to give rise to cobalt oxide particles with an average size smaller than 50 nm.

$$3[Co(NO_3)_2.4H_2O](s) + 2O_2(g) \xrightarrow{\Delta} Co_3O_4(s) + \underbrace{12H_2O(g) + 6NO_3^-}_{6HNO_3(g) + 6H_2O(g) + 6OH^-} \quad \textbf{(79)}$$

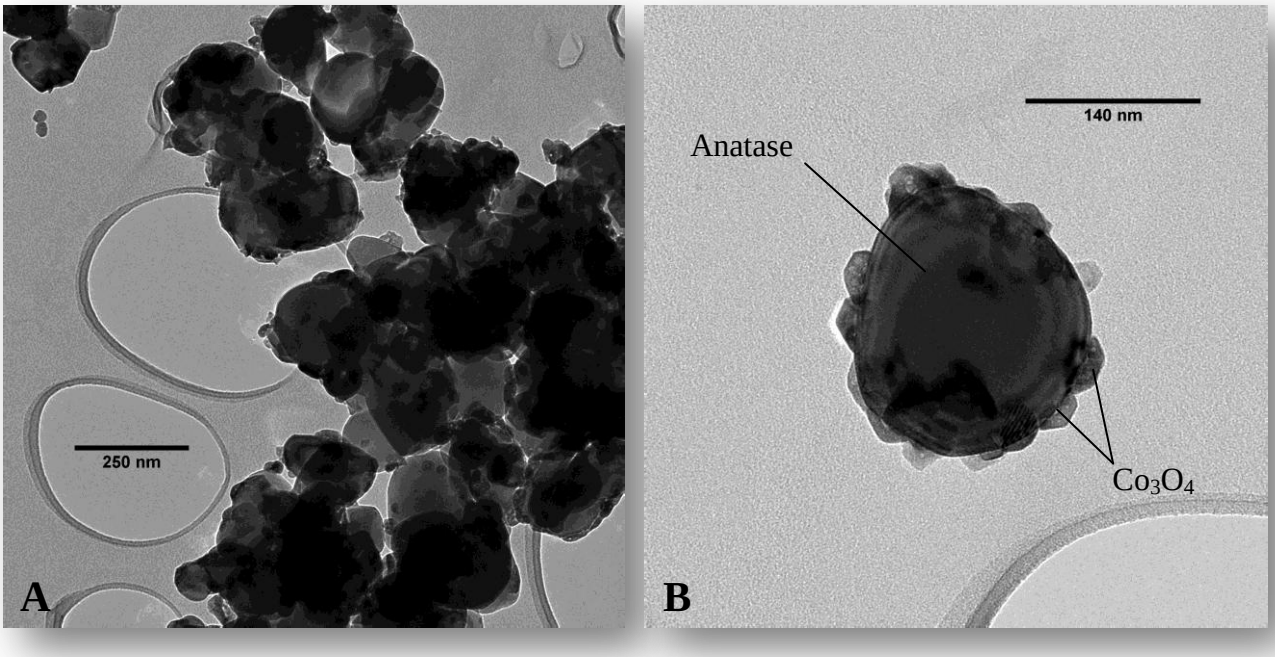

Figure 3.68. TEM images of the Co/Sigma catalyst after calcination: ***A*** *– sample representation and* ***B*** *– individual anatase particle supporting a number of cobalt oxide particles*

The cobalt oxide particle size increased gradually once the temperature exceeded 150 °C, reaching 13.9 ± 1 nm at 480 °C (the temperature of maximum concentration) and reaching a maximum of 32.5 ± 4 nm at 720 °C. The cobalt oxide particle size growth during heating indicates that this phase was more mobile on the Sigma support than on the Degussa P25 support. When the cobalt titanium oxide reaction began it resulted in the formation of relatively large particles (71.6 ± 9 nm) and achieved an initial growth rate of approximately 2.4 nm/°C at 720 °C (Fig. 3.69), which was comparable to that observed for the Degussa P25-supported cobalt catalyst. The growth process was halted at temperatures between 750 °C and 810 °C, after which a second growth regime began, which was attributed to agglomeration of the particles at elevated temperatures.

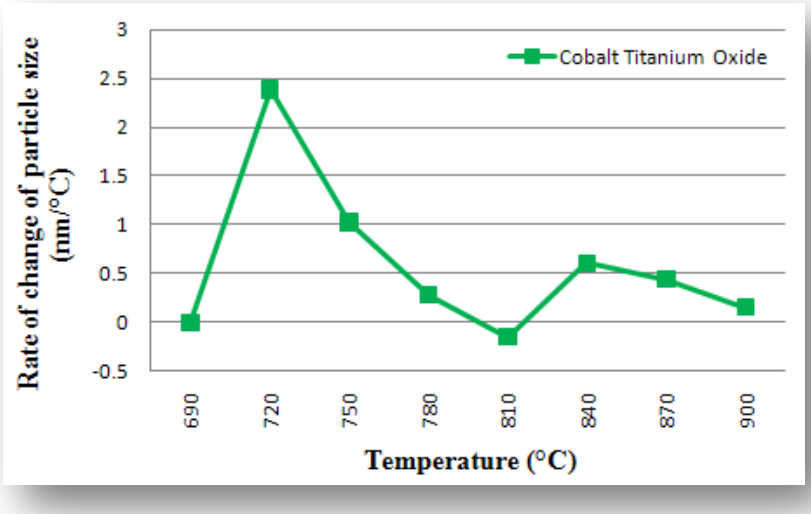

Figure 3.69. Instantaneous rates of change of cobalt titanium oxide particle size as a function of temperature during the heat treatment of the Co/Sigma catalyst

3.2.6. Co/NSA

Preliminary Discussion

We have shown that the NSA support is comprised of three phases, namely anatase, brookite and an amorphous material. The average anatase and brookite particle sizes are of the order of 9 nm. The presence of brookite catalyzed the anatase to rutile phase transition and the addition of hematite lowered the activation energy for the transition even further. Since the cobalt titanium oxide catalyzed the transition in the Sigma-supported catalyst, instead of cobalt oxide, it seemed fitting to determine if the same was true for the NSA-supported cobalt catalyst.

Quantitative Analysis

The intensity profile of the diffraction patterns collected during the heat treatment of this catalyst is given in figure 3.70 and shows the characteristic sharpening of the anatase peaks, the emergence of the cobalt oxide phase and the formation of cobalt titanium oxide with increasing temperature. The uncorrected concentration curves are given in figure 3.71 and show the distinctive anatase-amorphous material relationship observed before. Once again the data cannot be corrected by simply eliminating the amorphous contribution from the sample holder, since there was real amorphous material present in the support and as Co^{3+}AM. For this reason, as was the case for the Fe/NSA catalyst, overall quantitative trends were considered instead of actual values.

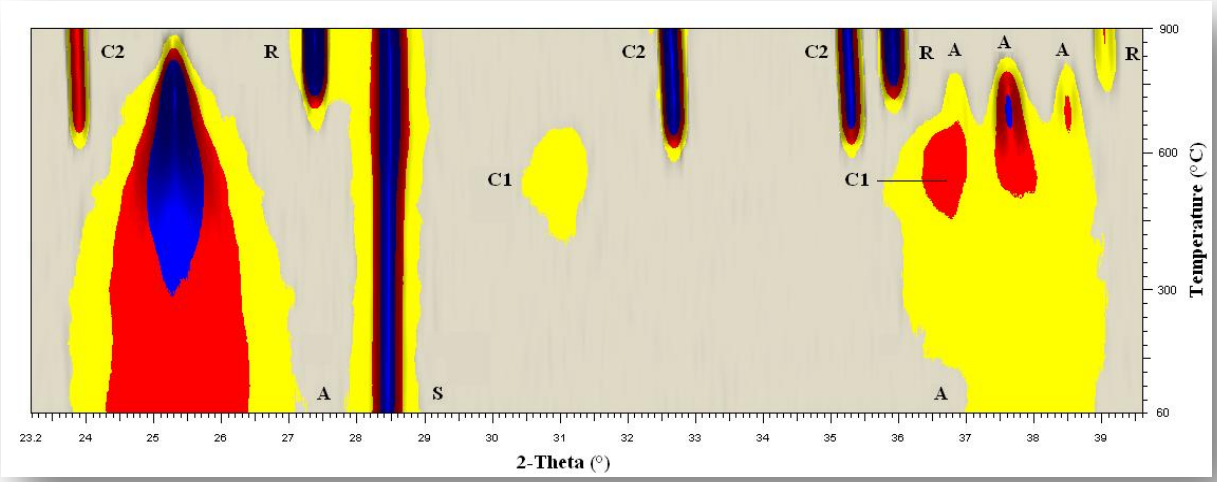

*Figure 3.70. Intensity profile of the diffraction patterns collected during the heat treatment of the Co/NSA catalyst: **A** – anatase, **R** – rutile, **S** – silicon, **C1** – cobalt oxide and **C2** – cobalt titanium oxide*

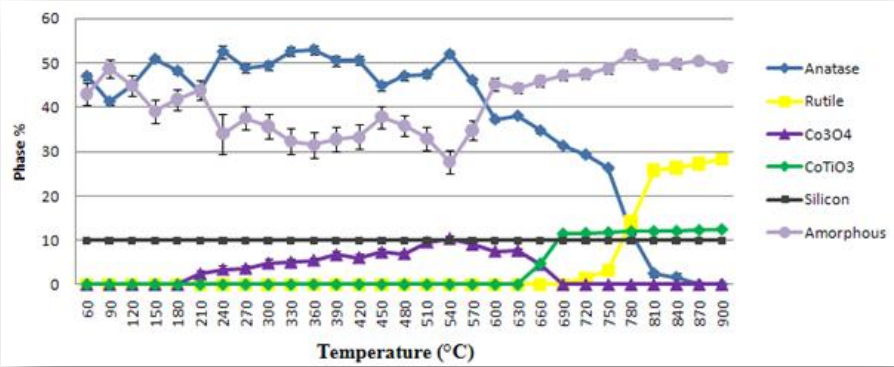

Figure 3.71. Quantitative phase analysis of the Co/NSA catalyst during heat treatment (average GoF of 1.03)

Unlike the Sigma-supported cobalt catalyst, there was no cobalt nitrate present at the start of the experiment, indicating that all of the cobalt was deposited as Co^{3+}AM. The Co^{3+}AM was converted to cobalt oxide at temperatures above 180 °C, reaching a maximum concentration at 540 °C. The cobalt titanium oxide reaction was initiated at temperatures above 630 °C, while the anatase to rutile phase transition was initiated at temperatures above 690 °C, which was considerably higher than was observed for the Fe/NSA catalyst at T > 600 °C and the unloaded support at T > 660 °C.

Particle Size Analysis

The changes in particle size of the constituent phases during heat treatment are given in figure 3.72**A**. Figure 3.72**B** shows only anatase and cobalt oxide and suggests that the anatase particle size remained constant until the reactor exceeded 420 °C. However, analysis of the rate of anatase particle growth in figure 3.73**A** suggests that the anatase particles actually began to increase in size at temperatures above 360 °C. Initially the changes were extremely small, however, as the reactor temperature exceeded 540 °C, the rate of growth accelerated. The anatase particles decreased in size at temperatures above 780 °C, as the phase transition was completed. Cobalt oxide particles, with sizes in the order of 8 nm, were present in the diffraction pattern collected at 210 °C. The particle size remained relatively constant until the reactor temperature exceeded 510 °C, at which point the cobalt oxide particles began to sinter and grow at a relatively consistent rate (Fig. 3.73**B**). At 540 °C, the temperature at which the maximum cobalt oxide concentration occurs, the cobalt oxide particles have an average size of 10.30 ± 0.5 nm, while anatase had an average value of 8.40 ± 0.2 nm. The similarity in particle size makes it difficult to distinguish the two type of particles in the TEM images, given in figure 3.74. The TEM images also show amorphous material that was distributed throughout the sample. The rate of growth of cobalt titanium oxide at 690 °C was an extraordinary 7 nm/°C (Fig. 3.73**C**), forming particles with an average size of 210.9 ± 8 nm. Increasing the temperature further resulted in a significant decrease in the cobalt titanium oxide particle size, reaching a minimum of 127.8 ± 5 nm at 780 °C, after which the particle size increases again. This oscillatory effect has not been observed in either of the previous samples and, as yet, defies explanation.

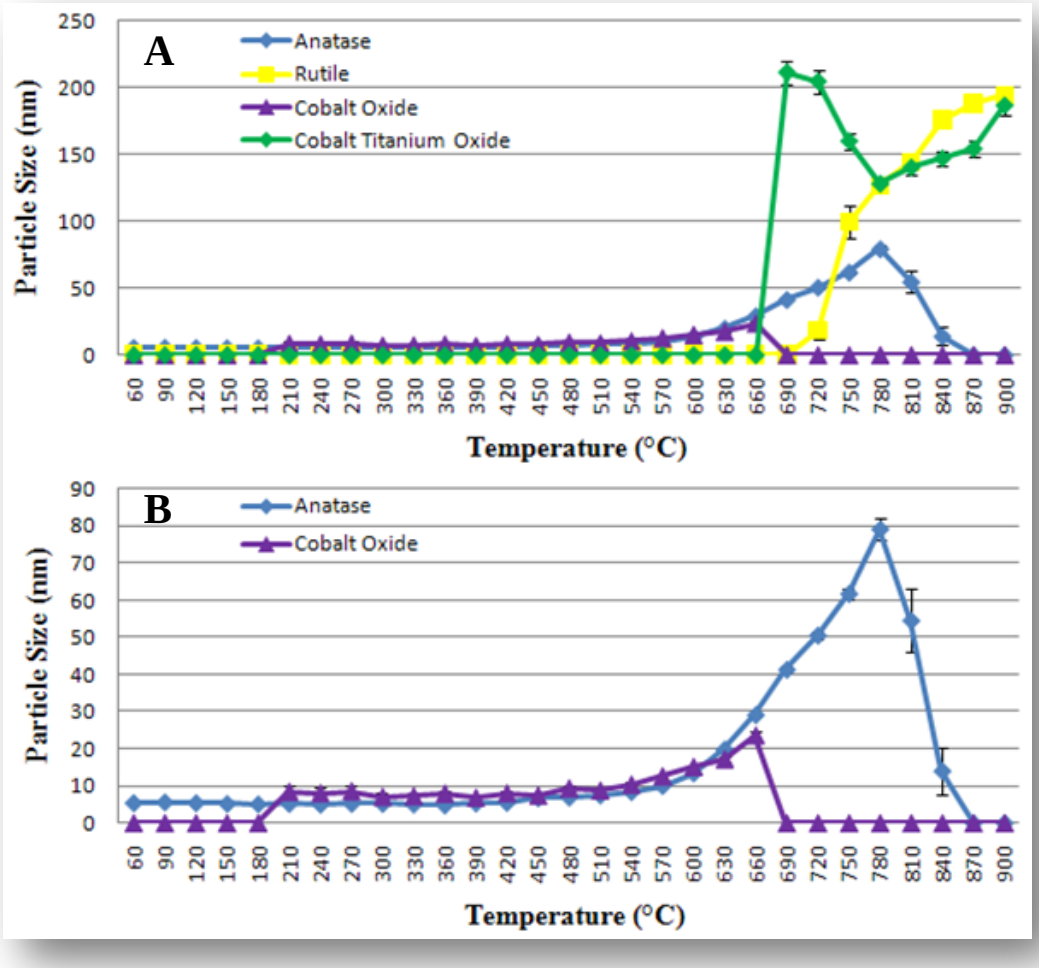

*Figure 3.72. Particle size changes of the constituent phases the during the heat treatment of the Co/NSA catalyst (**A** – all of the phases and **B** – anatase and cobalt oxide only)*

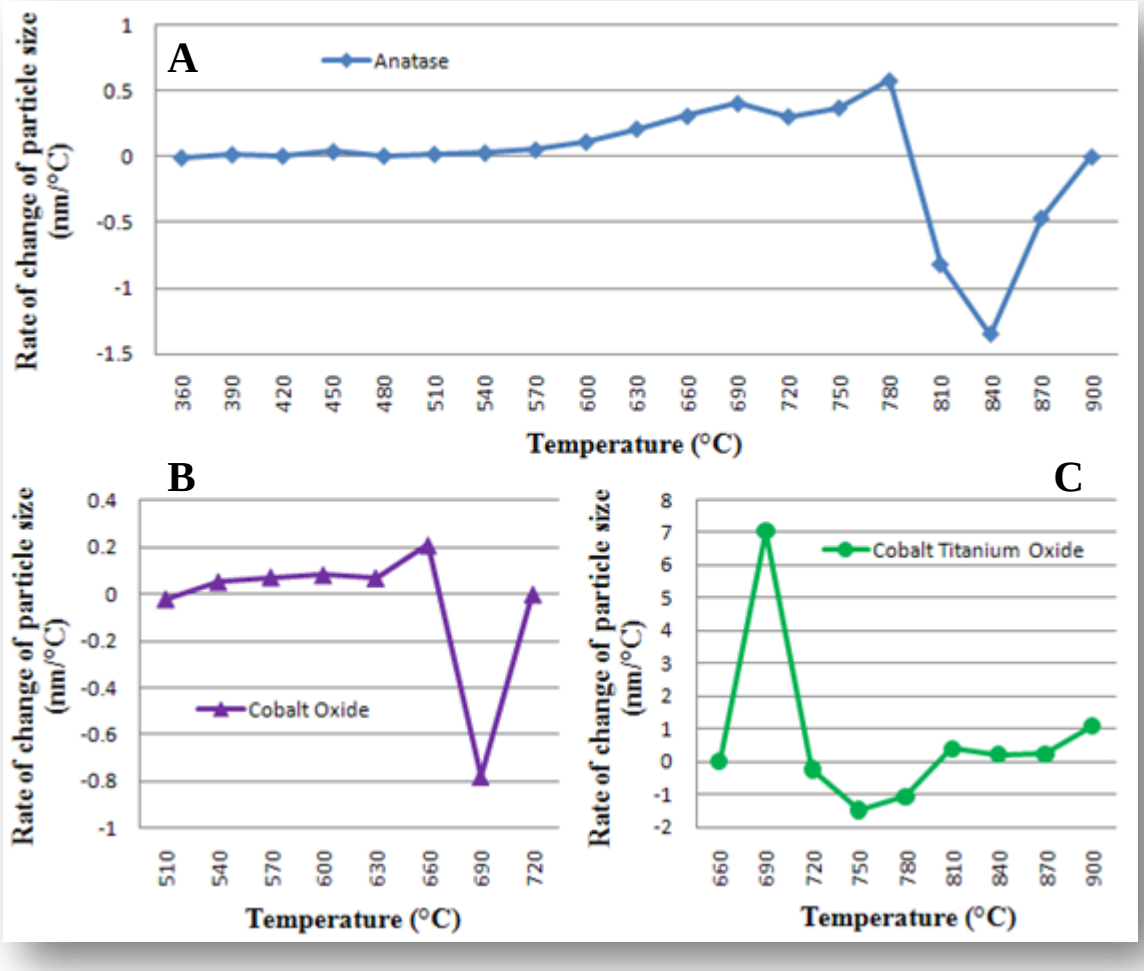

*Figure 3.73. Instantaneous rates of change of particle size of anatase (**A**), cobalt oxide (**B**) and cobalt titanium oxide (**C**)*

F

i

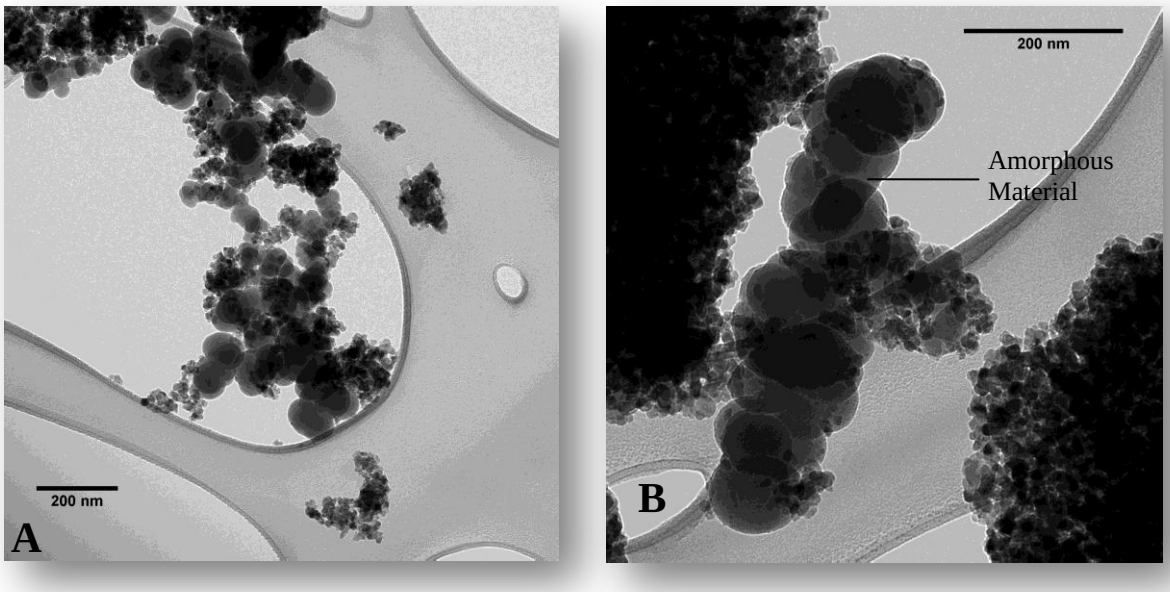

g

*Figure 3.74. TEM images of the Co/NSA catalyst after calcination showing amorphous component: **A** – sample representation and **B** – magnified region showing amorphous material*

3.2.7. Ru/DEGUSSA P25

Preliminary Discussion

Ru-based catalysts are extremely expensive, especially when compared to other FT metals, and are therefore not used as commercial catalysts. Ruthenium acetate [$Ru_2(OAc)_4$] was prepared from ruthenium chloride ($RuCl_3$) using the method proposed by Legzdins *et al.*.[59] Their work indicates that ruthenium acetate is formed during the reaction between ruthenium chloride and sodium acetate (NaOAc) in acetic acid (CH_3COOH) and ethanol (CH_3CH_2OH). They mentioned that it is difficult to isolate the product free from sodium acetate and sodium chloride (NaCl), an aspect that will become evident in the coming discussions, and suggest a further isolation experiment, which involves the formation of the triphenylphosphine adduct $Ru_2(OAc)_4,2PPh_3$. This step was not carried out when preparing the $Ru_2(OAc)_4$ for catalyst deposition and the results of the heat treatment procedure reflect this.

Quantitative Analysis

Figure 3.75 shows the progression of the heat treatment experiment and the emergence of the ruthenium oxide (RuO_2) phase with increasing temperature. Ruthenium oxide crystallizes in a tetragonal *P*42/*mnm* space group to form corner- and edge-sharing RuO_2 octahedra (Fig. 3.76).[60] There are two ruthenium oxide peaks present in the 2θ region provided in figure 3.75, the 1 1 0 peak at 27.9° and the 0 1 1 peak at 35.1°. Unfortunately the ruthenium oxide 1 1 0 peak falls directly between the rutile 1 1 0 peak at 27.3° and the baddeleyite 1 -1 -1 peak at 28.1°, while the 0 1 1 peak is overshadowed by the baddeleyite 2 0 0 peak at 35.0°. They are only evident from the slight increase in intensity (thickening of the red portion) of the baddeleyite peaks in these two regions (marked by *). In order to demonstrate these overlapping regions, the equivalent 2θ region from the refinement has been given in figure 3.77, in which the RuO_2 is highlighted in order to show the peak positions.

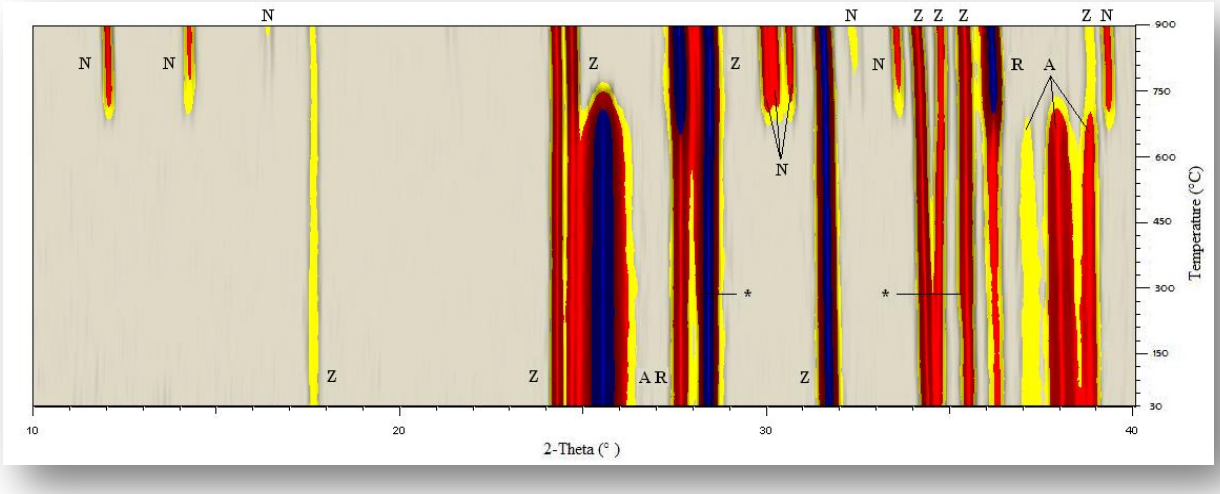

Figure 3.75. Intensity profile of the diffraction patterns collected during the heat treatment of the Ru/Degussa P25 catalyst: ***A*** *– anatase,* ***R*** *– rutile,* ***Z*** *– baddeleyite spike,* ***N*** *– disodium hexatitanate and* ******* *ruthenium oxide*

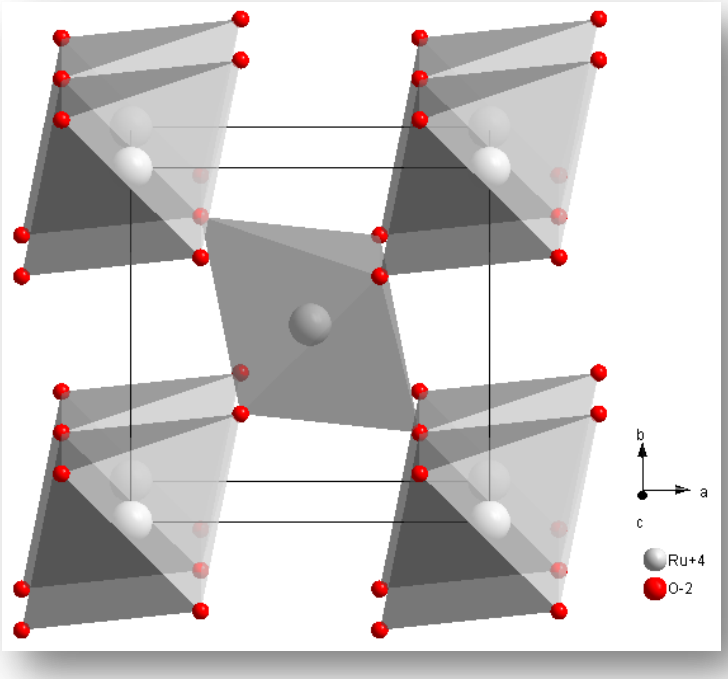

Figure 3.76. Crystallographic representation of ruthenium oxide (tetragonal P42/mnm)[60]

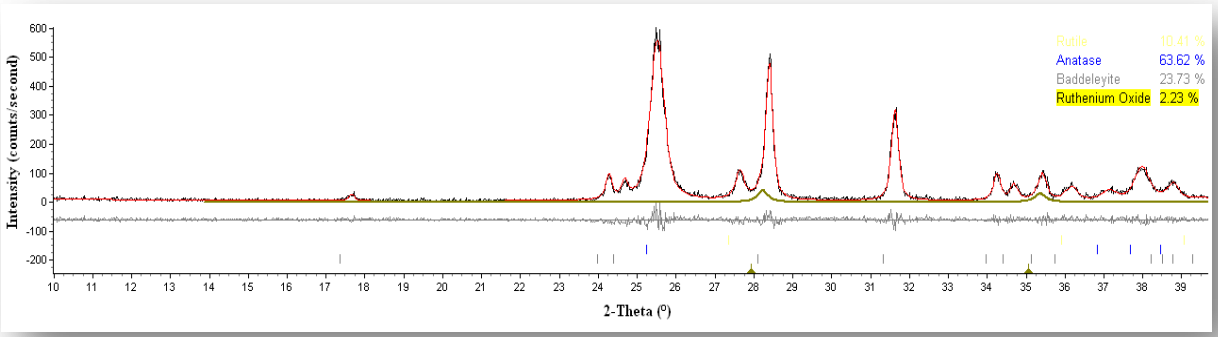

Figure 3.77. Individual refinement of the pattern collected at 420 °C showing the ruthenium oxide peak positions and contributions to overlapping peaks (brown)

The quantitative results of the multiple refinements are given in figure 3.78. No amorphous content was observed, which was surprising, since there should have been contributions from Ru^{4+}AM, carbonaceous deposits (in the form of unreacted acetic acid and other reactants used to prepare the ruthenium acetate). However, there was an unrealistic correlation between anatase and baddeleyite throughout the experiment but any attempt at logical corrections were further complicated by the apparent conversion of anatase to rutile at temperatures above 180 °C. Once again trends will be discussed rather than actual values.

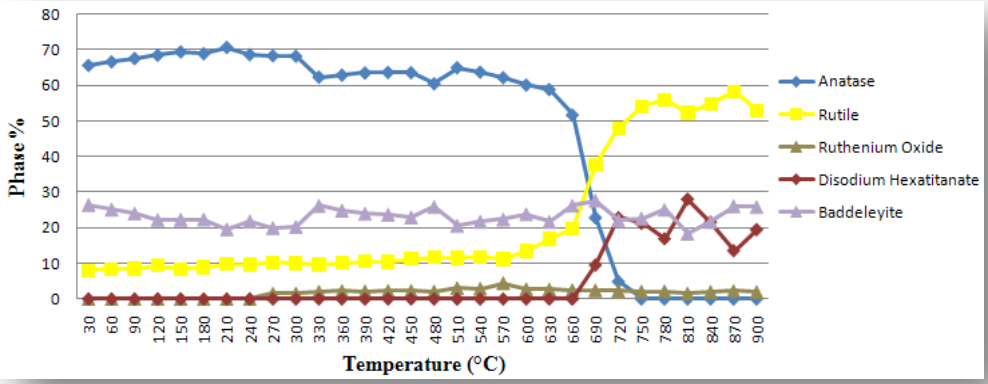

Figure 3.78. Quantitative phase analysis of the Ru/Degussa P25 catalyst during heat treatment (average GoF of 1.12)

The anatase to rutile phase transformation occurred at temperatures above 570 °C. The transformation and another, unexpected, reaction completely consumed the anatase phase. This second reaction was the formation of disodium hexatitanate ($Na_2Ti_6O_{13}$), a monoclinic structure that crystallizes in a *C*12/*m*1 space group, forming layers of edge-sharing TiO_2 octahedra with sodium cations separating the layers (Fig. 3.79).[61] The phase must have formed via the reaction between titania and sodium oxide (Na_2O) as outlined in equation **(80)**. Unfortunately the poor quality of the data did not allow for the conclusive determination of the phase of titania consumed to form the disodium hexatitanate. However, it seems likely that it was anatase due to the significantly larger rates of anatase consumption when compared to the rates of rutile formation at 690 °C and 720 °C (Table 3.4). The sodium oxide, which crystallizes in a cubic $Fm\bar{3}m$ space group,[62-63] is believed to have formed via the oxidation of the small amounts of sodium acetate that remained in the ruthenium acetate. However, no crystalline peaks for Na_2O were observed in any of the diffraction patterns collected during the experiment, which indicates it may have been present in an amorphous state.

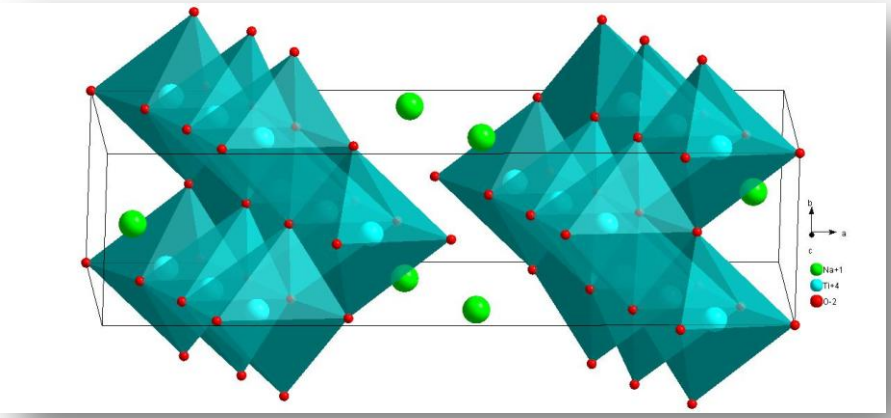

Figure 3.79. Crystallographic representation of disodium hexatitanate (monoclinic C12/m1)[61]

$$6TiO_2(s) + Na_2O(s) \xrightarrow{\Delta} Na_2Ti_6O_{13}(s) \quad \textbf{(80)}$$

Table 3.4. Instantaneous rates of change of concentration of anatase and rutile during the formation of disodium hexatitanate

Temp (°C)	Anatase (%/°C)	Rutile (%/°C)
690	-0.961	0.597
720	-0.597	0.346

The ruthenium oxide concentration reached a maximum at 570 °C and began to decrease thereafter. The fate of the ruthenium oxide was unclear, since no ruthenium species, in the form of reduced Ru^0, an oxide or a titanate, were detected as the concentration of ruthenium oxide decreased. Figure 3.78 suggests that disodium hexatitanate undergoes reversible transformations to rutile between 720 °C and 900 °C.

Particle Size Analysis

The particle size changes depicted in figure 3.80 indicates that the baddeleyite particles were relatively stable throughout the experiment. The anatase particle size remained relatively stable until the phase was consumed in the above processes. The rutile particle size was relatively stable until the reactor temperature exceeded 480 °C, at which point there was a significant increase in size, up to a temperature of 570 °C. This was followed by a decrease in size as the reactor approached 630 °C. A possible explanation for the latter decrease involves the anatase to rutile transition that increases in speed at temperatures above 570 °C and the smaller converted anatase particles decrease the average rutile particle size. The ruthenium oxide particle size curve followed a similar trend to that observed for hematite in the Fe/NSA catalyst. Once again the explanation involves consideration of the average particle size. It is possible that larger amorphous particles crystallize first, which would result in a large initial ruthenium oxide particle size, while smaller amorphous particles crystallize at higher temperatures, decreasing the overall particle size. The maximum ruthenium oxide concentration was observed at 570 °C and at this point the average particle size was 20.40 ± 0.8 nm. The TEM image, in figure 3.81, once again indicated that the ruthenium oxide particles had been bound to the support but had an extremely low distribution, due to the similarity in size. The disodium hexatitanate immediately formed relatively large particles, which continued to grow as the reaction proceeded.

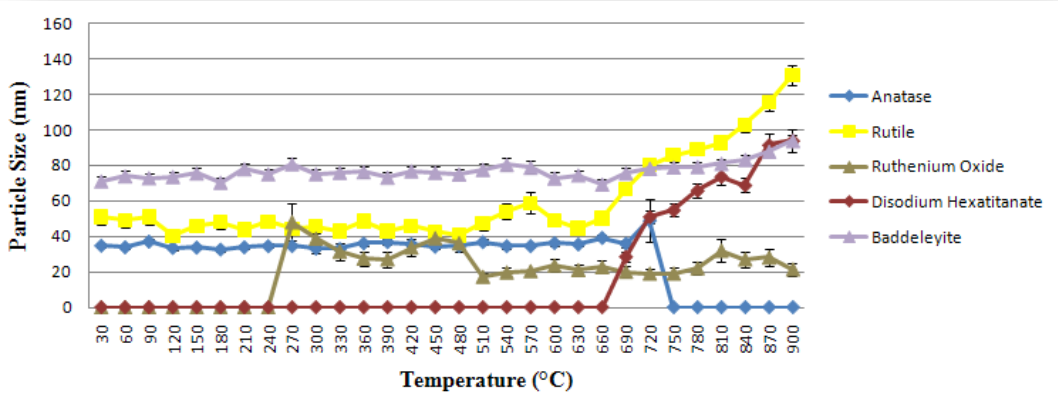

Figure 3.80. Particle size changes of the constituent phases during the heat treatment of the Ru/Degussa P25 catalyst

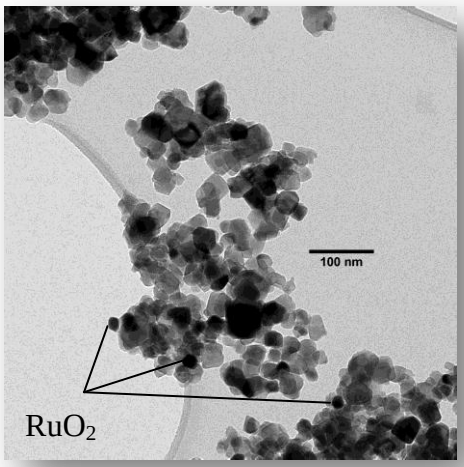

Figure 3.81. TEM image of the Ru/Degussa P25 catalyst after calcination

3.2.8. Ru/SIGMA ANATASE

Preliminary Discussion

The larger sizes of anatase particles and the small rutile concentration within the Sigma support make it much more attractive to study from a powder diffraction point of view, due to increased resolution and smaller number of support peaks, while the X-ray transparency seems to be easily corrected. The relevant diffraction results from the heat treatment of the 10 %Ru/Sigma catalyst are given as Figure 3.82.

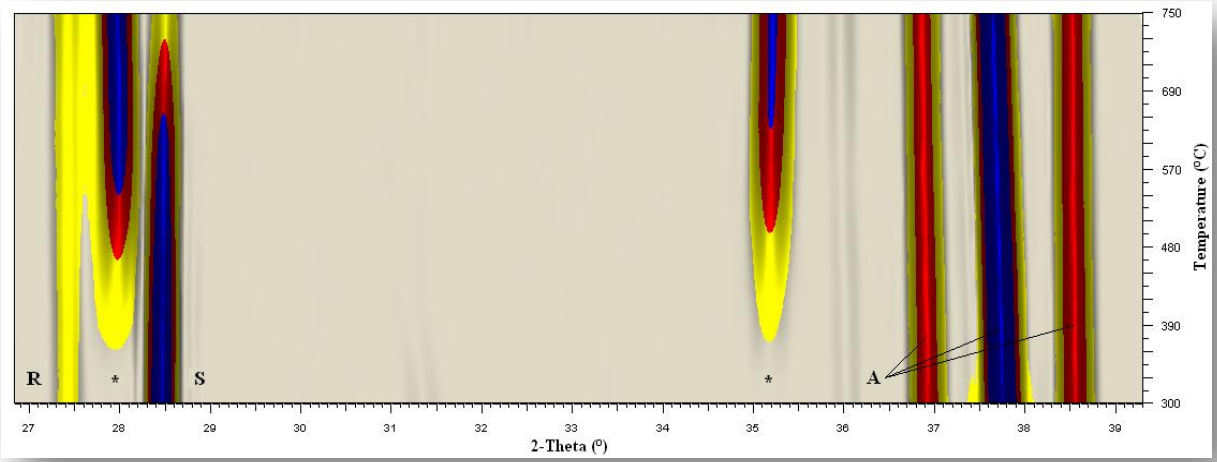

Figure 3.82. Intensity profile of the diffraction patterns collected during the heat treatment of the Ru/Sigma catalyst: ***A*** *– anatase,* ***R*** *– rutile,* ***S*** *– silicon and* ******* *- ruthenium oxide*

Quantitative Analysis

Figure 3.82 suggests that ruthenium oxide began crystallizing at temperatures above 330 °C, a fact that was confirmed by the corrected refinement results presented in figure 3.83. The ruthenium oxide reached a maximum concentration of 4.87 ± 0.1 % at 750 °C, crystallizing from the amorphous Ru^{4+}AM formed after drying the ruthenium acetate used to load the ruthenium. The anatase concentration decreased at temperatures above 450 °C, as the transition to rutile began. The most interesting observation during this experiment was the decrease in silicon concentration when the temperature exceeded 570 °C. Unfortunately, no peaks for a resultant silicon phase emerged during this decrease, however, there was an overall increase in amorphous material between 600 °C and 750 °C, suggesting that the silicon was converted to an amorphous species.

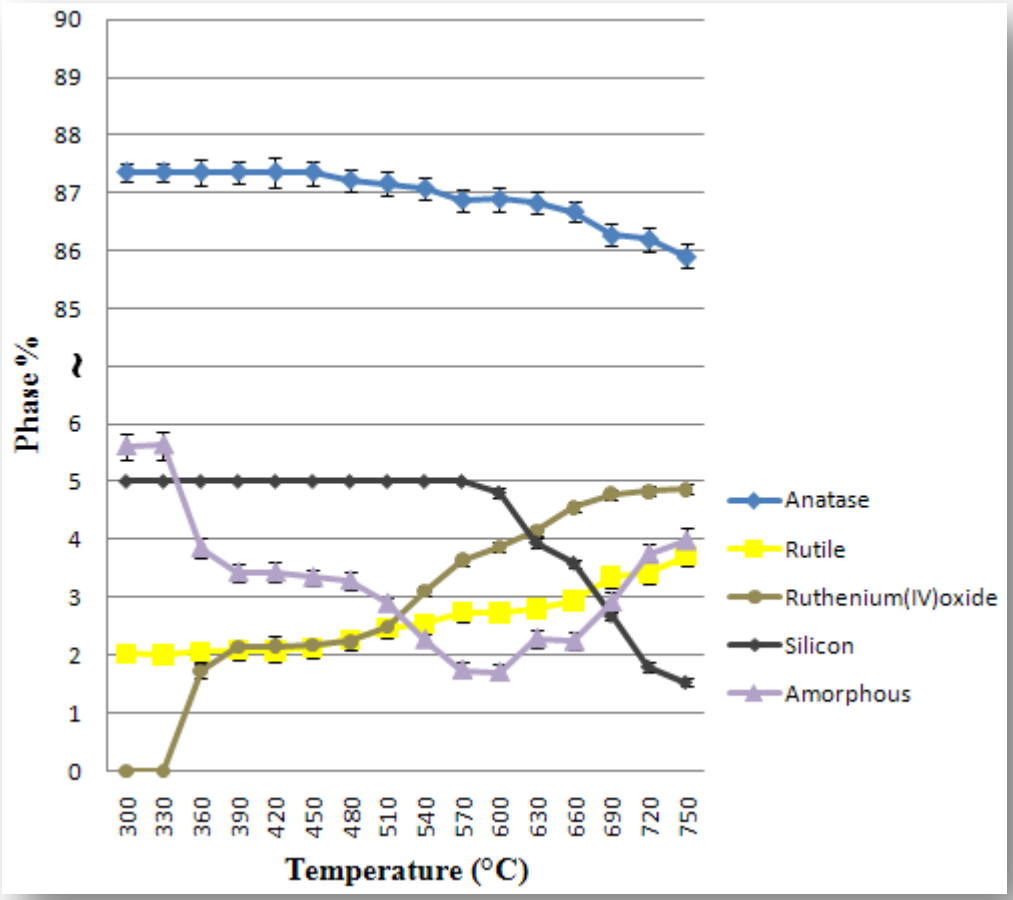

Figure 3.83. Quantitative phase analysis of the Ru/Sigma catalyst during heat treatment (average GoF of 1.24)

Particle Size Analysis

The changes in particle size of anatase and ruthenium oxide as a function of temperature are given in figure 3.84. The average anatase particle size increased by ±16 % over the temperature range of interest. When ruthenium oxide began to crystallize, at temperatures above 330 °C, it had an initial particle size of 14.0 ± 1 nm, which remained relatively constant until the temperature exceeded 420 °C, at which point the particle size increased dramatically. The ideal calcination temperature should, therefore, not be the above 750 °C, which marks the temperature of highest concentration, but at 450 °C, marking the point at which the particle size is 20.6 ± 1 nm. This was confirmed by the TEM images given in figure 3.85. The TEM images also suggest that the ruthenium oxide distribution on the surface of the anatase particles was good. Unfortunately the lower calcination temperature results in a low degree of oxidation of only 49 %.

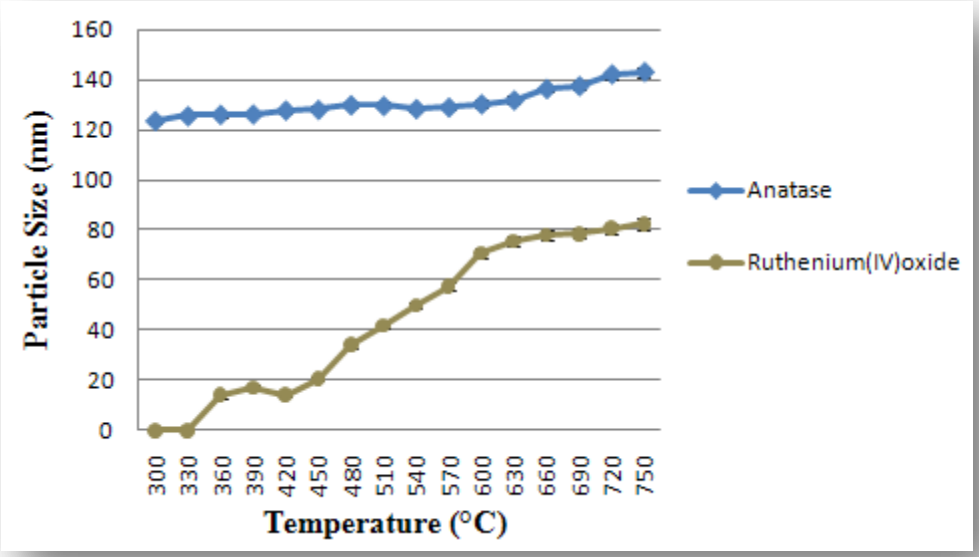

Figure 3.84. Particle size changes of anatase and ruthenium oxide during the heat treatment of the Ru/Sigma catalyst

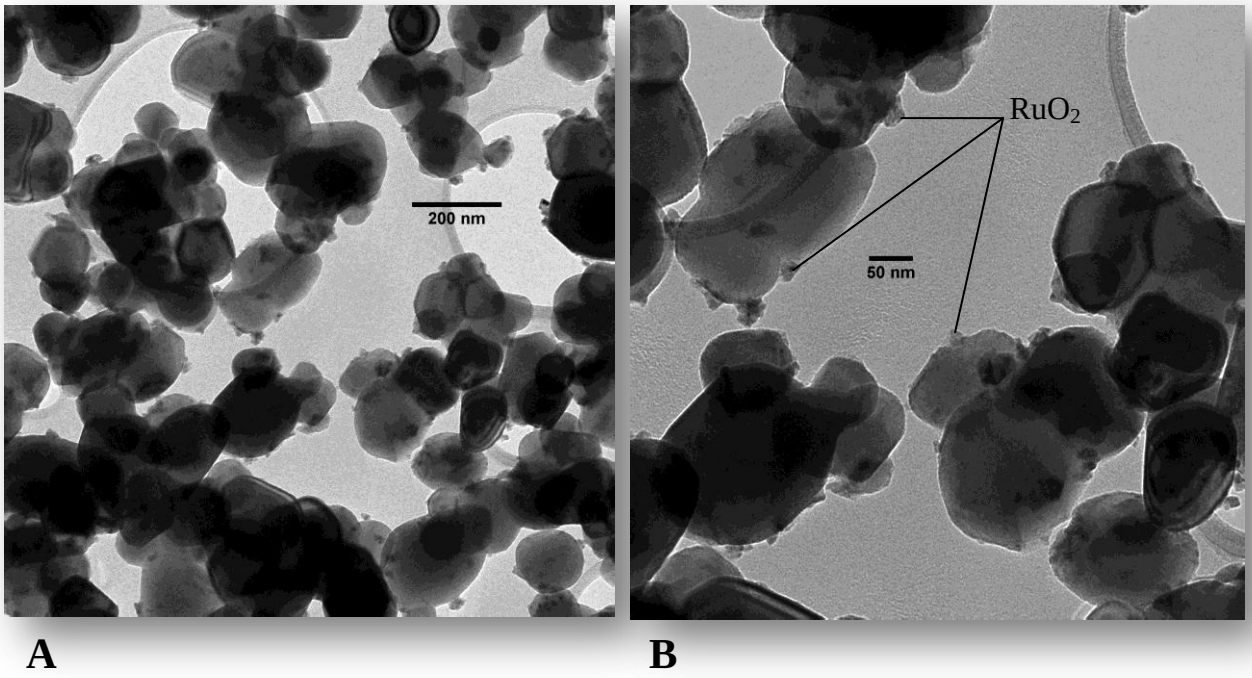

Figure 3.85. TEM images of the Ru/Sigma catalyst after calcination: ***A*** *– sample representation and* ***B*** *– magnified view for the determination of ruthenium oxide particle size*

3.2.9. Ru/NSA

Preliminary Discussion

Loading smaller metal particles onto the already small support particles is a challenge and as yet has not proved very successful with the series of catalysts used in this study. Unfortunately the problem persists when using ruthenium. The diffraction patterns collected during the heat treatment of the Ru/NSA catalyst are represented as an intensity profile in figure 3.86.

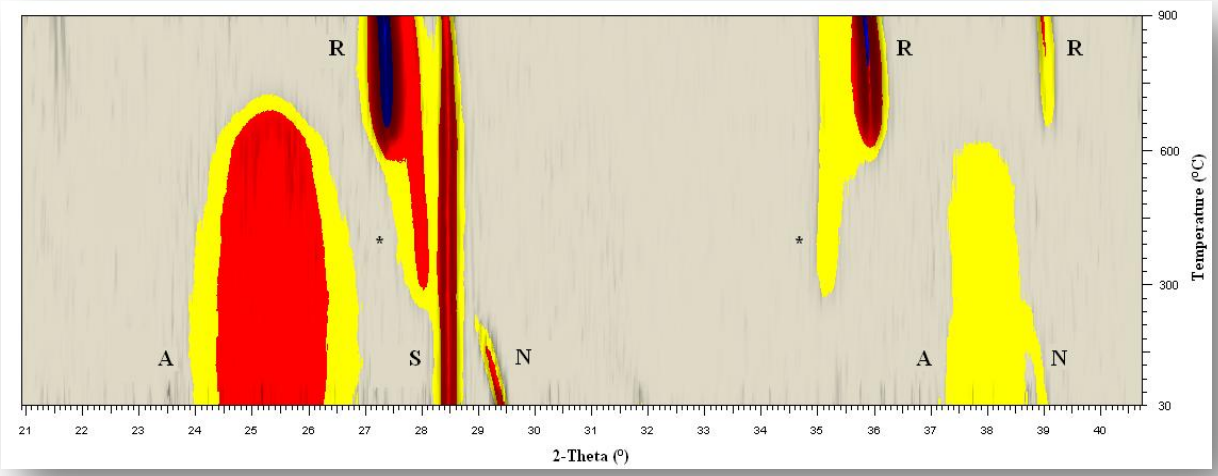

*Figure 3.86. Intensity profile of the diffraction patterns collected during the heat treatment of the Ru/NSA catalyst: **A** – anatase, **R** – rutile, **S** – silicon spike and **N** – nitratine*

Quantitative Analysis

The quantitative results shown in figure 3.87 are split into the support and spike phases (large concentration phases) and the low concentration phases. The first graph shows that there is a relationship between the anatase and brookite concentrations. However, it is likely that the relationship is entirely unrealistic, since the conversion of brookite to anatase under these conditions is thermodynamically impossible. Rutile generation occurred at temperatures above 480 °C, starting slowly reaching an initial plateau between 570 °C and 600 °C, after which there was an exponential increase in rutile concentration, resulting in the complete consumption of both anatase and brookite. It is clear that at temperatures above 720 °C silicon began to decompose as was observed during the analysis of the Sigma-supported ruthenium catalyst. The low concentration graph shows the presence of nitratine, a rhombohedral $R\bar{3}c$ phase with the chemical formula $NaNO_3$, the structure of which is given as figure 3.88. The nitratine structure is composed of corner-sharing sodium oxide octahedra, with intermittent nitrogen bridges.[64] The presence of nitratine in this system was completely unexpected and must have arisen from the presence of sodium acetate in the ruthenium acetate loading phase and a nitrate donor from the support. Nitratine is extremely hygroscopic and is not usually observed in crystalline form in areas with even the slightest humidity, so the presence of this material, although a contaminant, was rather special and quite noteworthy. The nitratine began to decompose at temperatures above 90 °C and was undetectable in the

pattern collected at 270 °C, possibly being converted to Na_2O. At the same temperature, ruthenium oxide became detectable and leveled off at temperatures between 330 °C and 360 °C. Between 360 °C and 510 °C, the phase percentages became rather erratic, making it difficult to determine if this was a real effect or an artifact from the refinement process. However, at temperatures above 510 °C there was a significant decrease in ruthenium oxide concentration, followed by a sudden increase at temperatures above 600 °C. This pattern was also shown by the Degussa P25-supported ruthenium catalyst during the heat treatment, lending credibility to the observation. The determination of the ideal calcination temperature was complicated by the erratic behavior between 360 °C and 510 °C, however, the trend in this region was for an increase in concentration and therefore the ideal calcination temperature (in terms of concentration) was deemed to be 480 °C, the point just before support modification occurs.

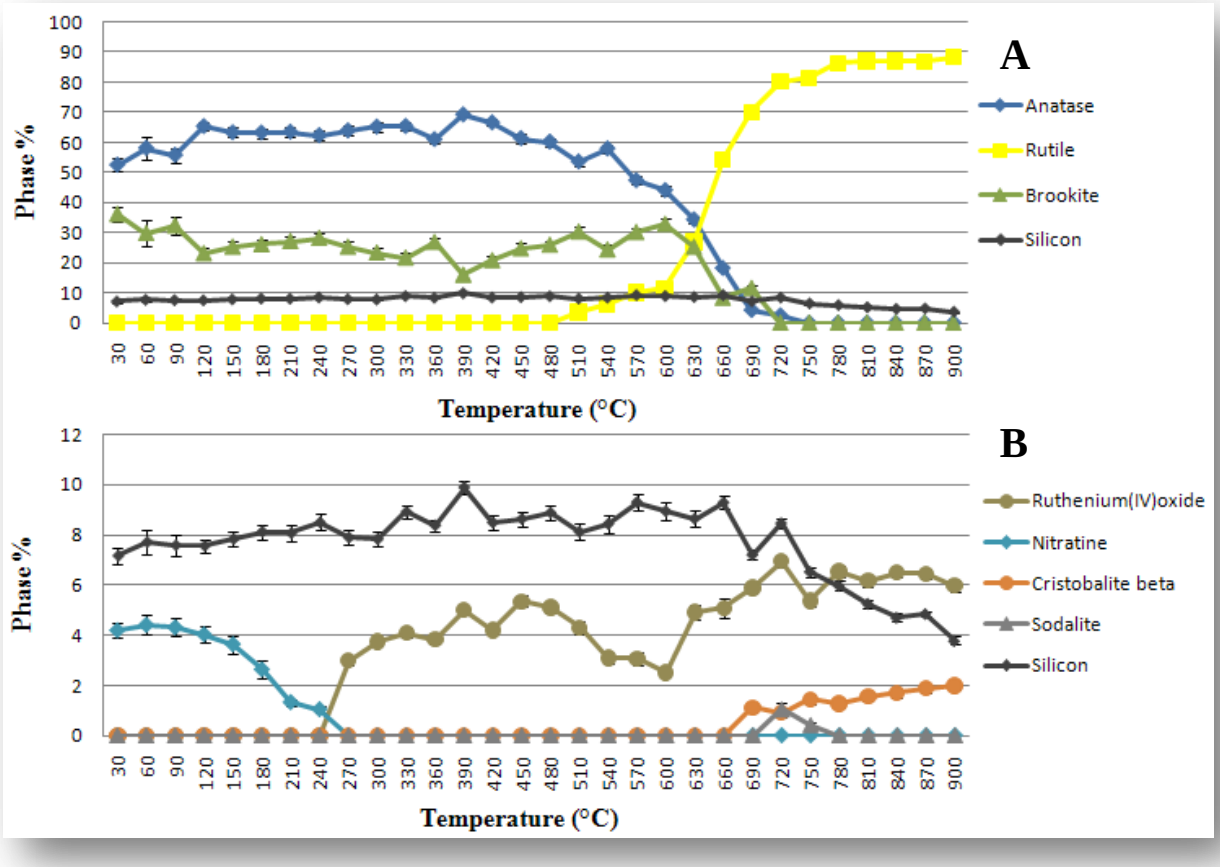

*Figure 3.87. Quantitative phase analysis of the Ru/Sigma catalyst during heat treatment, where **A** – major phases and **B** – minor phases (average GoF of 1.16)*

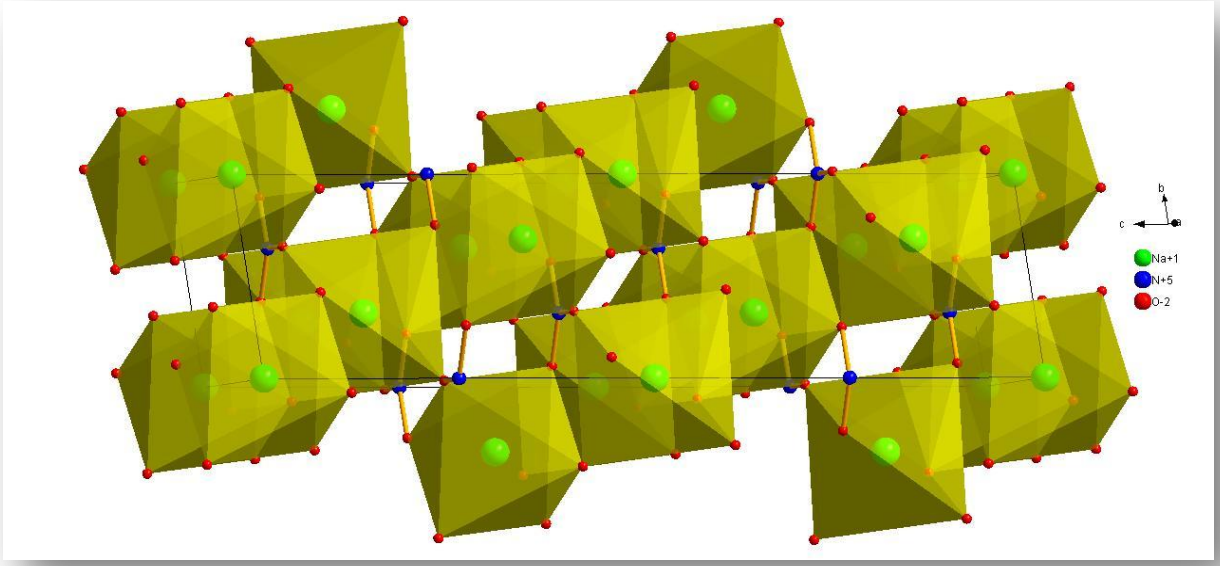

Figure 3.88. Crystallographic representation of nitratine (rhombohedral $R\bar{3}c$)[64]

The silicon spike was oxidized at temperatures above 660 °C to form β-cristobalite (SiO_2), which is a cubic *P*213 phase composed of corner-sharing SiO_2 tetrahedra (Fig. 3.89). [65] At 720 °C and 750 °C sodalite, another cubic phase that crystallizes in a $P\bar{3}4n$ space group with the chemical formula $Na_8(AlSiO_4)_6Cl_2$, was observed (Fig. 3.90). [66] Since the sample holder is comprised of aluminosilicates we had to ensure that the presence of this phase was not due to sample penetration. The diffraction pattern collected on the empty sample holder was checked for the presence of sodalite, which returned a negative result. The only possible explanation for the observation of this phase is that the sample must have reacted with the sample holder, or contaminants therein, at these elevated temperatures to incorporate aluminium. The sodalite phase was unstable at higher temperatures and was thought to be converted to cristobalite.

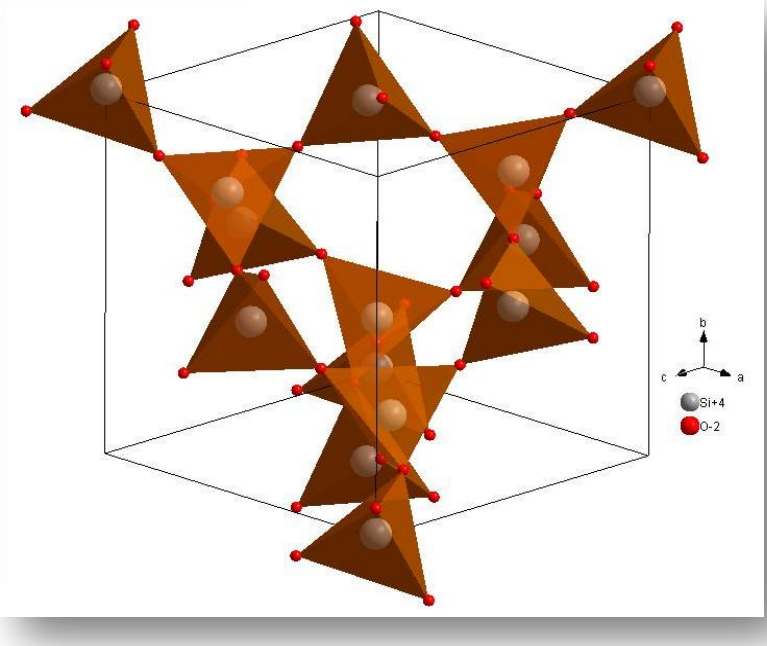

*Figure 3.89. Crystallographic representation of cristobalite (cubic P*213*)* [65]

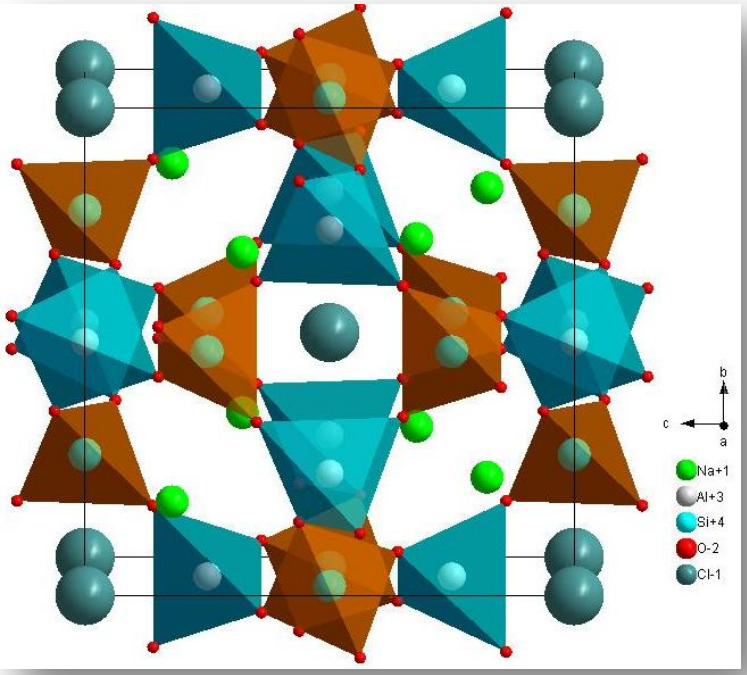

Figure 3.90. Crystallographic representation of sodalite (cubic $P\bar{3}4n$) [66]

Particle Size Analysis

The particle size changes that occurred during the experiment are given as figure 3.91. The anatase and brookite particle sizes increased slowly at temperatures above 270 °C in a similar fashion to previous experiments. When rutile was first detected at 510 °C it had already achieved a particle size of 17.9 ± 2 nm, which is two times larger than the average anatase particle size of 8.4 ± 1 nm at the corresponding temperature, once again lending credibility to the bridging-strain mechanism. When ruthenium oxide crystallized it formed particles with sizes in the order of 20 nm, a fact that was confirmed in the TEM images (Fig. 3.92).

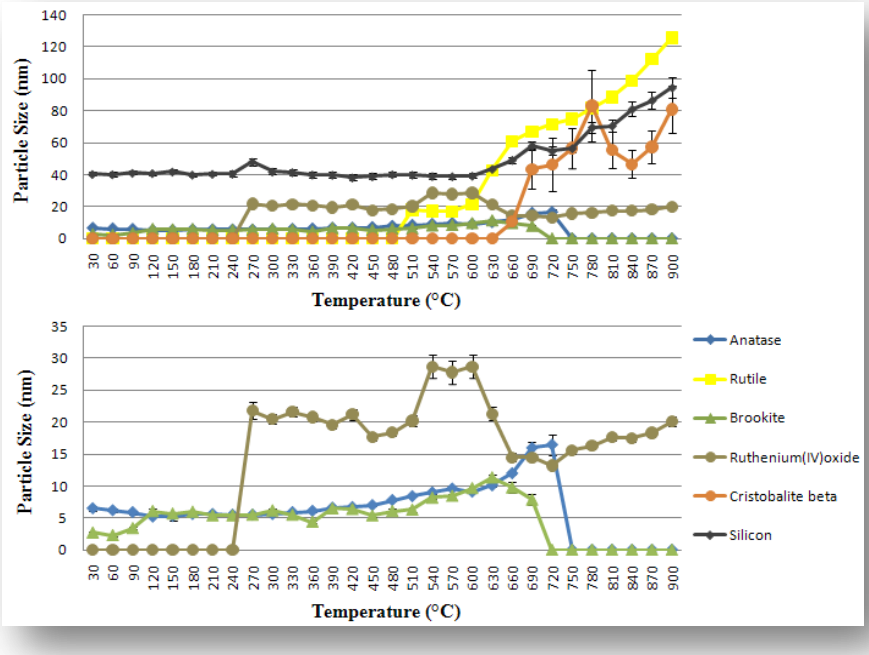

Figure 3.91. Particle size changes of the constituent phases during the heat treatment of the Ru/NSA catalyst

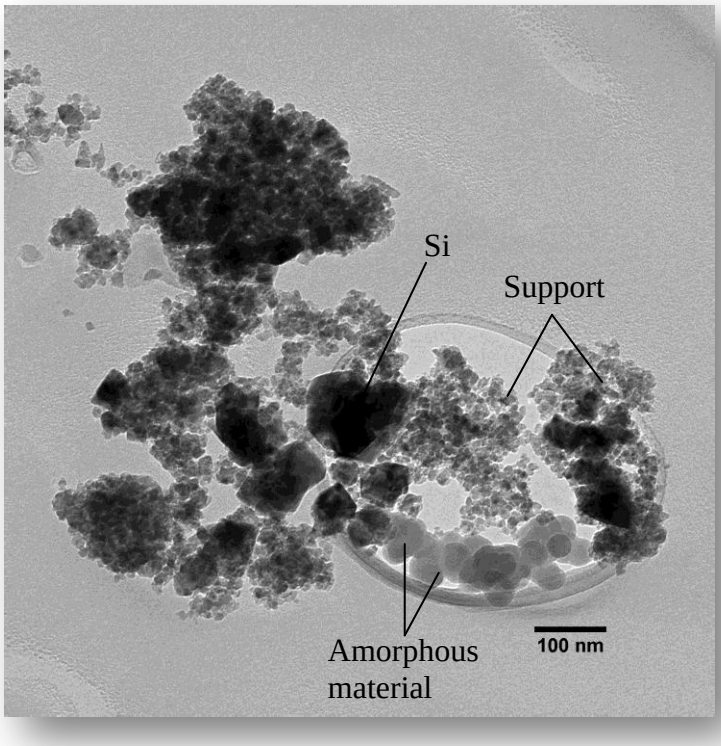

Figure 3.92. TEM image of the Ru/NSA catalyst after calcination

The instantaneous rates of rutile particle growth are shown in figure 3.93, and show a rather unusual pattern. When rutile was first detected at 510 °C, the rate of growth was approximately 0.6 nm/°C, after which the rate decreased to zero (or very slightly below) at 540 °C and 570 °C, indicating that the average particle size was not increasing at these temperatures. The rate increased when the reactor exceeded 570 °C, reaching a maximum at 630 °C. Thereafter the rate decreased until the reactor exceeded 750 °C, at which point the rate increased once again.

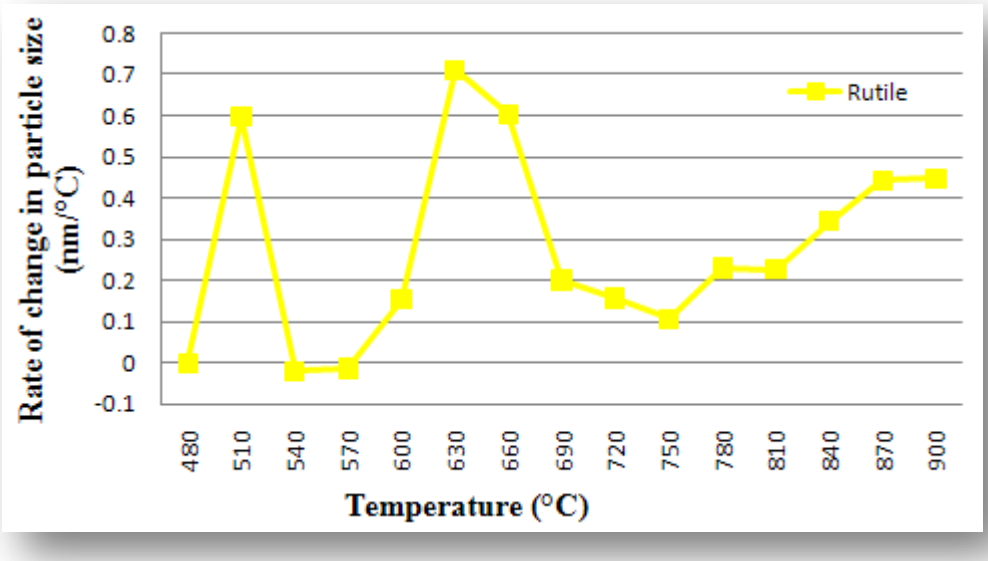

Figure 3.93. Instantaneous rates of change of rutile particle size as a function of temperature during the heat treatment of the Ru/NSA catalyst

3.3. SUMMARY

Table 3.5 outlines the findings of the heat treatment experiments. It shows the variation in the anatase to rutile transition temperature for all of the samples investigated. It is clear that the addition of metal oxides to the Degussa P25 support increased the temperature at which the anatase to rutile transition occurred. The addition of hematite and ruthenium oxide to the Sigma support caused decreases of 30 °C and 370 °C respectively, while the addition of cobalt(II/III) oxide increased the transition temperature by 30 °C. A similar result was observed for the NSA support.

Table 3.5 also summarizes the temperatures at which the maximum metal oxide concentration was observed and the ideal calcination temperature for each catalyst, after taking into account particle size data. There were only three catalysts that had to be calcined at lower temperatures, sacrificing metal oxide concentration for control over particle size. They were the Fe/Sigma, the Fe/NSA and the Ru/Sigma catalysts.

The temperatures at which metal titanate formation began in each catalyst are also given in table 3.5 and it suggests that metal titanate formation was initiated at temperatures between 600 °C and 760 °C, which is a rather narrow temperature range. This observation may indicate that the identity of the metal may have little influence on the activation temperature of the titanate formation reactions and may have more to do with the properties of the support at those temperatures.

Table 3.5. Summary of transition, maximum metal oxide, ideal calcination and metal titanate formation temperatures

	SUPPORTS			CATALYSTS								
Temperature (°C)	Degussa P25	Sigma Anatase	NSA	Fe/Degussa	Fe/Sigma	Fe/NSA	Co/Degussa	Co/Sigma	Co/NSA	Ru/Degussa	Ru/Sigma	Ru/NSA
Anatase - Rutile Transition	T>480	T>790	T>660	T>600	T>760	T>600	T>550	T>810	T>690	T>570	T>420	T>480
Maximum Metal Oxide				450	700	600	500	480	540	570	750	480
Ideal Calcination				450	460	510	500	480	540	570	450	480
Metal Titanate Formation				T>690	T>760	T>600	T>600	T>690	T>630			

3.4. *IN SITU* CATALYST REDUCTION

The catalyst samples were calcined *ex situ*, with an identical ramping program to that used for the heat treatment experiments. They were then reduced, *in situ*, using H_2 and various mixtures of H_2 and N_2. The aim of the reduction procedure was to convert the metal oxides (M_xO_y) to their metallic states (M^0), while maintaining small particle sizes. The reduction procedure took a similar form to that used in temperature programmed reduction (TPR) experiments. The sample was heated under a flow of H_2 gas but, unlike a TPR experiment, the sample was allowed to equilibrate for 15 minutes after each 20 °C interval before a diffraction pattern was collected. Once again mention must be made as to the non-equilibrium state that is set up in the reactor. When the temperature is high enough to initiate reduction, the process will continue while the diffraction pattern is collected. However, we have found that the reduction that occurred during the relatively short collection time could be neglected in the experiments.

3.4.1. Fe/DEGUSSA P25

In the early stages of this project the optimum calcination temperature for this catalyst was determined to be 600 °C, using the diffraction pattern that contained the most intense peaks for hematite. This process did not take into account the average size of the hematite particles, the importance of which has been discussed, and the fact that these high temperatures can result in the conversion of anatase to rutile. The data collected using this sample led to findings, which deserve mention in this study. This section is, therefore, divided into four parts, which cover the reduction of the catalyst calcined at 600 °C using 5 %, 10 % and 100 % H_2/N_2 gas mixtures and the reduction of the catalyst calcined at 450 °C (the best calcination temperature) using 100 % H_2.

3.4.1.1. Fe/DEGUSSA P25 Calcined at 600 °C and Reduced using 5 % H_2/N_2

Preliminary Discussion

The initial reduction experiment was carried out using a 5 % H_2/N_2 gas mixture. Hematite reacted with the support in the reducing atmosphere to form ilmenite ($FeTiO_3$), as witnessed by the emergence of diffraction peaks at 23.79 °, 32.49 °, 35.25 ° and 38.29 ° 2 - theta (Fig 3.94). Ilmenite crystallizes in a trigonal $R\bar{3}H$ space group with alternating layers of $Ti^{4+}O_6$ and $Fe^{2+}O_6$ octahedra (Fig. 3.95).[67] The reaction involves the reduction of Fe^{3+} in hematite to Fe^{2+} in ilmenite, via the reaction outlined in equation **(81)** below.

$$Fe_2O_3(s) + 2TiO_2(s) + H_2(g)\ [5\ \%\ H_2/N_2] \xrightarrow{\Delta} 2FeTiO_3(s) + H_2O(g) \qquad \textbf{(81)}$$

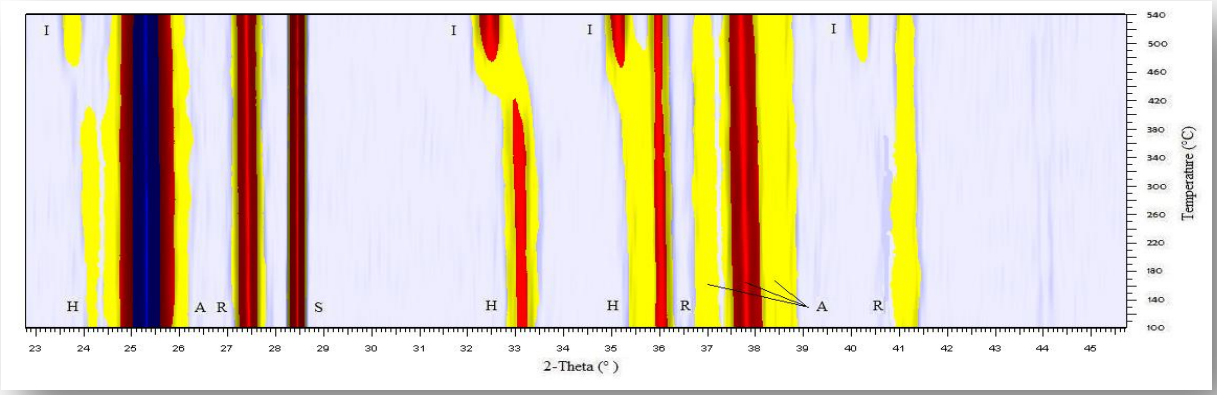

Figure 3.94. Intensity profile of the diffraction patterns collected during the reduction of the Fe/Degussa P25 catalyst calcined at 600 °C using a 5 % H_2/N_2 gas mixture: ***A*** *– anatase,* ***R*** *– rutile,* ***S*** *– silicon,* ***H*** *– hematite and* ***I*** *– ilmenite*

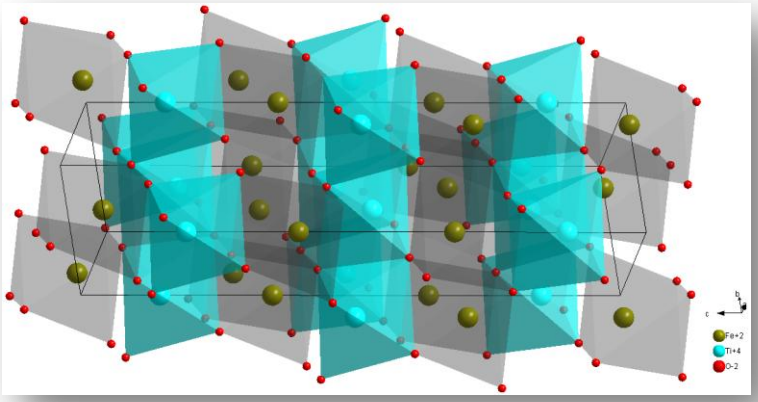

Figure 3.95. Crystallographic representation of ilmenite (trigonal $R\bar{3}H$)[67]

Quantitative Analysis

The quantitative data, extracted from the refinements, is given in figure 3.96. It shows that the sample was remarkably stable until the temperature exceeded 420 °C. The concentration of anatase and hematite decreased substantially between 420 °C and 500 °C as the ilmenite phase was formed. Figure 3.97**A** shows the rate of ilmenite formation and the combined rates of consumption of anatase and hematite. It is clear that the rates are not quite equal. However, combining the negative rate of rutile consumption yielded a curve that mirrors the rate of formation of ilmenite (Fig. 3.97**B**). This observation suggests that both anatase and rutile are consumed to form ilmenite in this process. The anatase was the major TiO_2 source, as witnessed by the higher rate of consumption of anatase (Fig. 3.98**A**) when compared to rutile (Fig. 3.98**B**). The formation of ilmenite appeared to be either diffusion-limited, since the reaction did not consume all of the hematite, or possibly reversible, since the hematite concentration increased at temperatures above 500 °C. The positive rate for rutile formation in figure 3.98**B** suggests that the anatase to rutile phase transition began at temperatures close to 460 °C, 140 °C lower than during the heat treatment process discussed earlier (chapter 3.2.1).

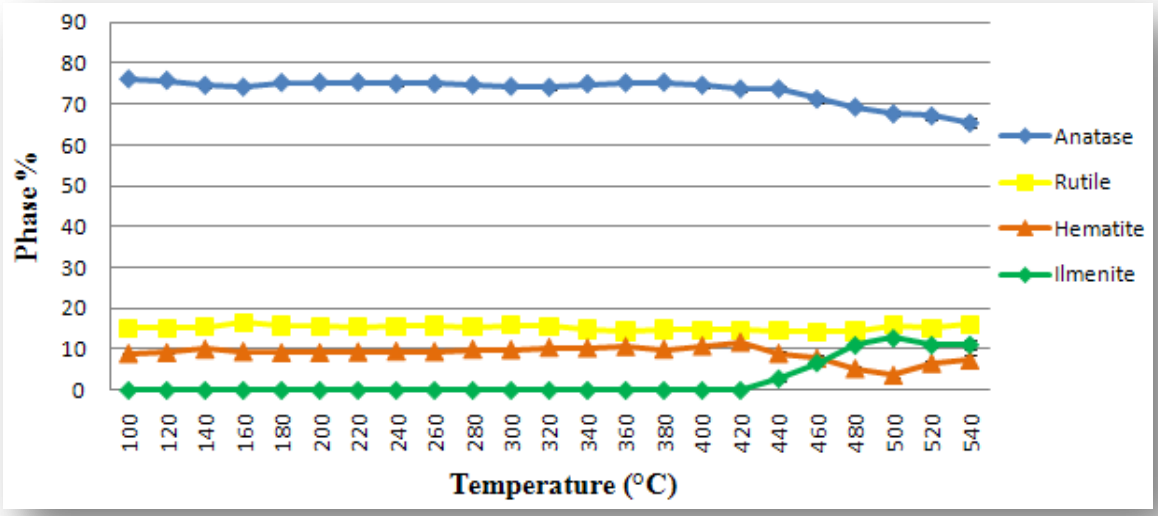

Figure 3.96. Quantitative phase analysis of the Fe/Degussa P25 catalyst calcined at 600 °C during reduction with a 5 % H_2/N_2 gas mixture (average GoF of 1.04)

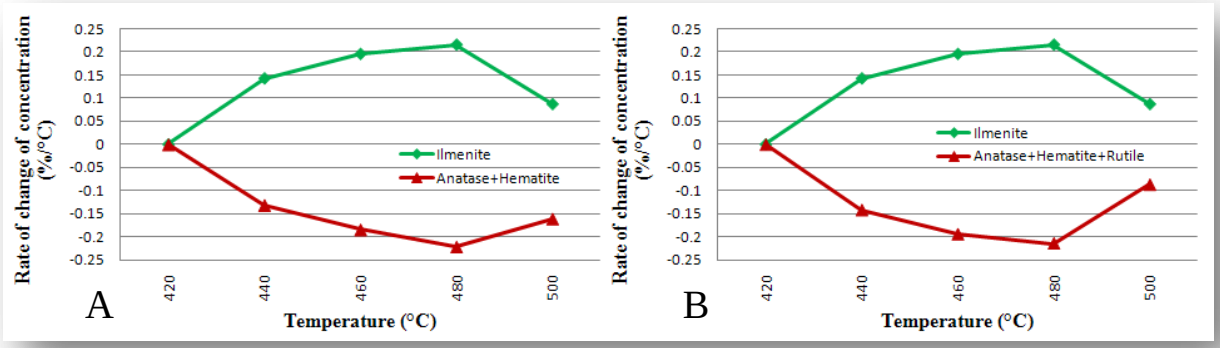

*Figure 3.97. Instantaneous rates of change of concentration. **A** – ilmenite vs. the combined rates of consumption of anatase and hematite and **B** – ilmenite vs. the combined rates of consumption of anatase, rutile and hematite*

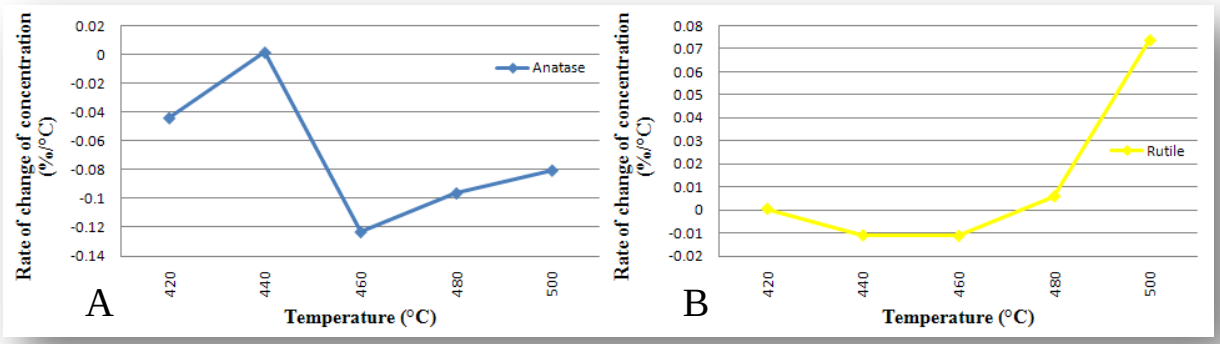

*Figure 3.98. Instantaneous rates of change of concentration. **A** – anatase and **B** – rutile during the reduction of the Fe/Degussa P25 catalyst calcined at 600 °C using a 5 % H_2/N_2 gas mixture*

Particle Size Analysis

Figure 3.99 shows the changes of the particle sizes of the constituent phases of the catalyst during the reduction procedure. The anatase and rutile particles remained relatively constant in size throughout the experiment. The hematite particle size fluctuated marginally in the beginning of the experiment but became more constant between 160 °C and 380 °C. The average hematite particle size decreased by 30 % between 380 °C and 420 °C and then stabilized. This observation adds credibility to the idea that the formation of ilmenite was diffusion limited. However, it is difficult to propose a mechanism based on these results. Ilmenite only became detectible in the pattern collected at 440 °C, but the hematite particle size decreased between 380 °C and 420 °C, indicating that there may have been a non-crystalline intermediate species or solid solution that formed before the crystallization of ilmenite. An amorphous material was observed in the high resolution transmission electron microscope (HRTEM) images given in figure 3.100. The hematite particle size remained constant until the temperature exceeded 500 °C, after which it began to increase in parallel with the increase in concentration discussed above. Although the ilmenite concentration decreased at temperatures above 500 °C, the remaining ilmenite particles in the system continued to grow quite dramatically.

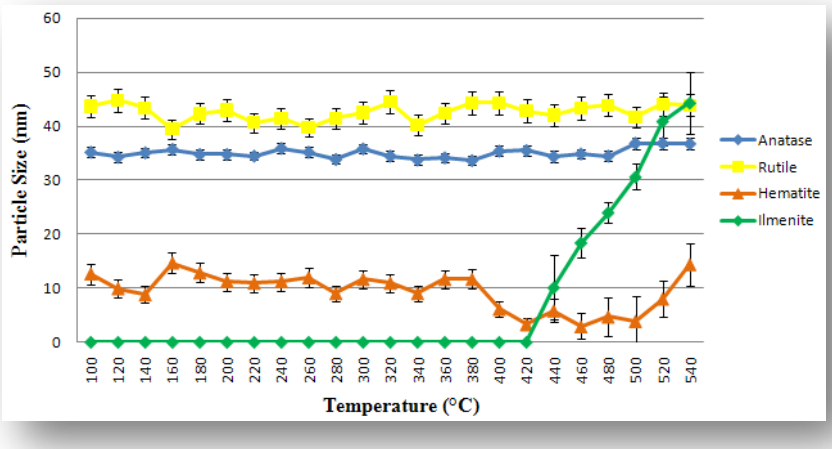

Figure 3.99. Particle size changes of the constituent phases in the Fe/Degussa P25 catalyst calcined at 600 °C during reduction with a 5 % H_2/N_2 gas mixture

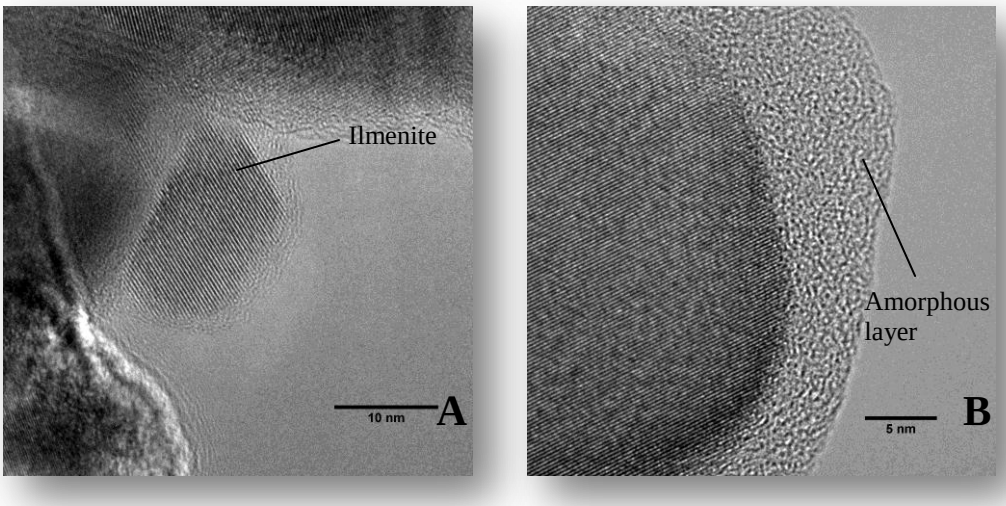

*Figure 3.100. HRTEM images of the Fe/Degussa P25 catalyst calcined at 600 °C and reduced using 5 % H_2/N_2: **A** – ilmenite particle and **B** – magnified view of amorphous layer*

3.4.1.2. Fe/DEGUSSA P25 Calcined at 600 °C and Reduced using 100 % H_2

Preliminary Discussion

The formation of ilmenite in the previous experiment prompted further investigation into the behavior of this catalyst under different reducing gas mixtures. The second step was to perform an identical *in situ* experiment replacing the 5%H_2/N_2 gas mixture with 100% H_2. The intensity profile for the experiment is given as figure 3.101 and shows a significantly different reduction profile. During this experiment hematite (Fe_2O_3) was reduced to magnetite (Fe_3O_4), which was ultimately reduced to iron (Fe^0). Magnetite crystallizes in a cubic $Fd\bar{3}mz$ space group to form a complex arrangement of $Fe^{3+}O_6$ octahedra and $Fe^{2+}O_4$ tetrahedra (Fig. 3.102**A**),[68] while iron crystallizes in a body-centered cubic (BCC) $Im\bar{3}m$ space group (Fig. 3.102**B**).[69]

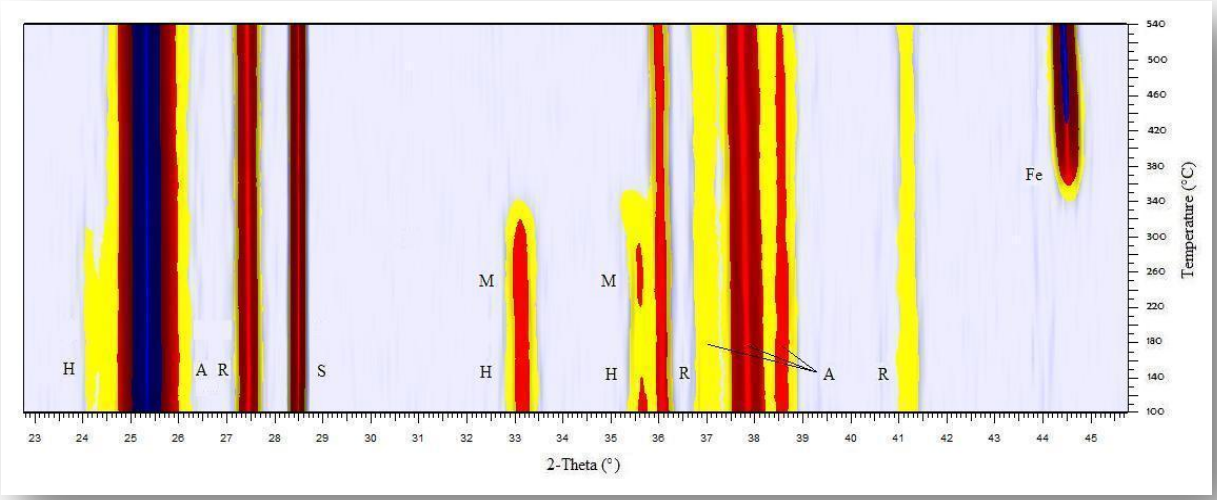

*Figure 3.101. Intensity profile of the diffraction patterns collected during the reduction of the 10Fe/Degussa P25 catalyst calcined at 600 °C using 100% H_2: **A** – anatase, **R** – rutile, **S** – silicon, **H** – hematite, **M** – magnetite and **Fe** – iron*

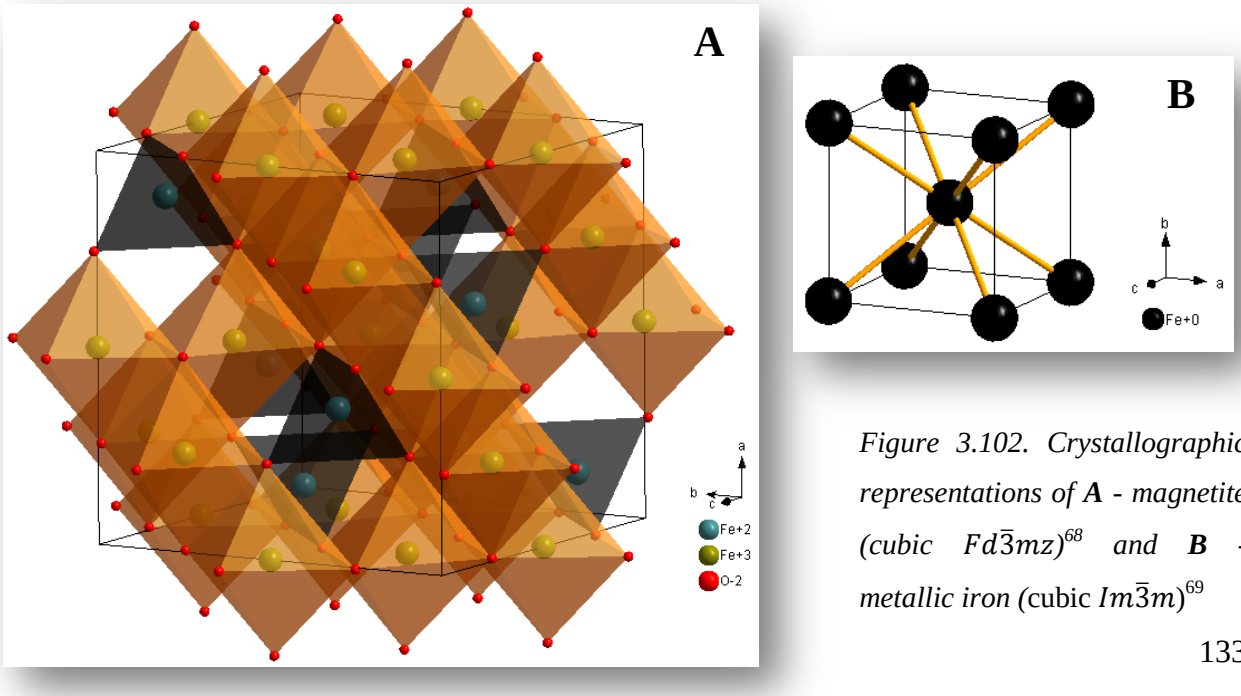

*Figure 3.102. Crystallographic representations of **A** - magnetite (cubic $Fd\bar{3}mz$)[68] and **B** - metallic iron (*cubic $Im\bar{3}m$)[69]*

Quantitative Analysis

The quantitative results of this experiment are given in figure 3.103. The anatase concentration remained relatively constant until the temperature exceeded 340 °C, at which point there was a significant decrease in anatase, which coincided with the formation of magnetite in the system. At temperatures above 300 °C, the hematite concentration decreased, forming an amorphous intermediate, which, at temperatures above 320 °C, was converted to magnetite with the remaining hematite. Iron was observed in the pattern collected at 340 °C and the concentration continued to increase along with an amorphous component. The iron concentration reached a maximum of 7.08 ± 0.1 %, representing a degree of reduction of 88 %. This indicates that 12 % of the iron in the system was likely incorporated into the amorphous component along with a significant amount of anatase. The anatase to rutile transition started at temperatures above 480 °C, which is 120 °C lower than was observed during the heat treatment of this sample (chapter 3.2.1).

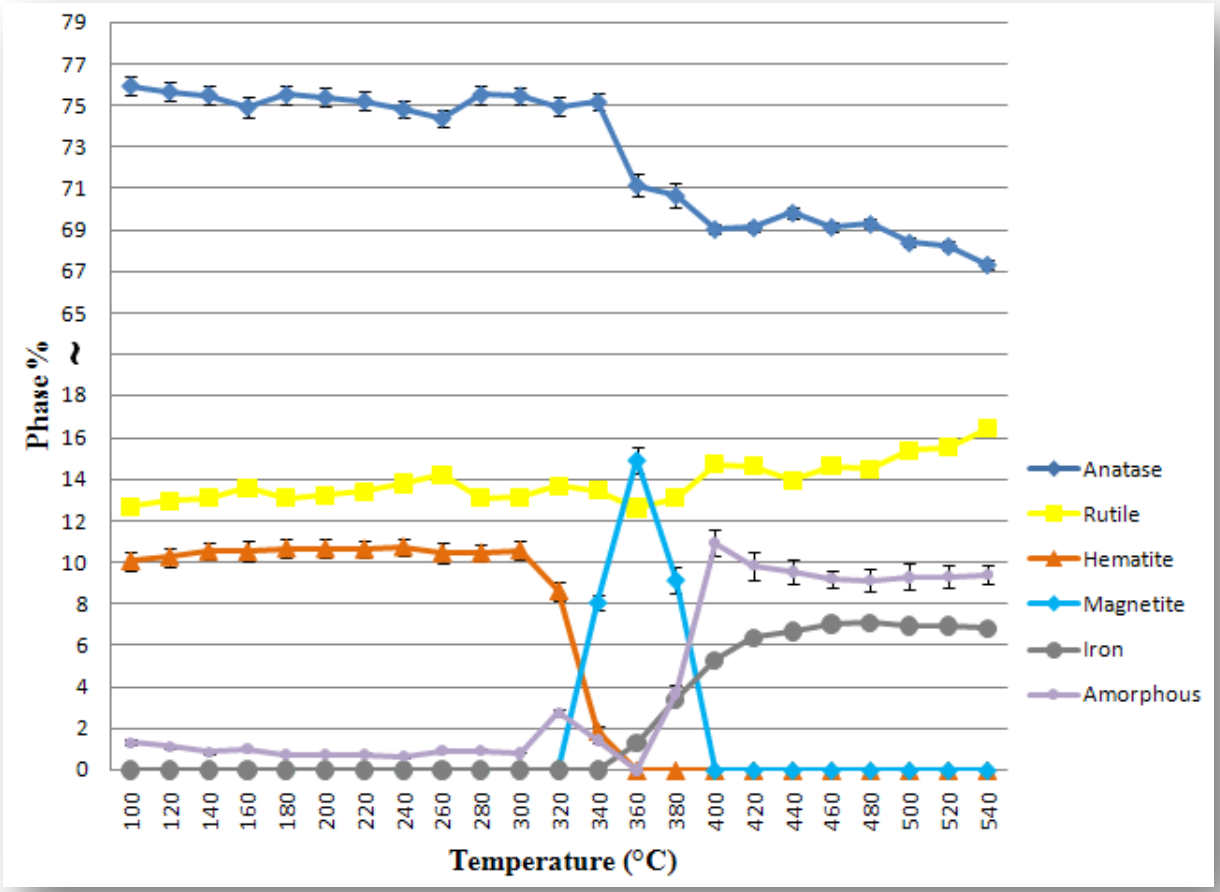

Figure 3.103. Quantitative phase analysis of the Fe/Degussa P25 catalyst calcined at 600 °C during reduction with 100 % H_2 (average GoF of 1.05)

Particle Size Analysis

The anatase and rutile particle sizes remained relatively stable throughout the experiment (Fig. 3.104). Magnetite was observed in the pattern collected at 340 °C and had a small average particle size, while the hematite particle size appeared to increase slightly. This suggests that smaller hematite particles are reduced first, while larger particles require higher temperatures. The overlap of hematite – magnetite and magnetite – iron reduction temperatures makes it difficult to speculate on the formation of iron particles. It is clear that the majority of the reduction process took place between 340 °C and 360 °C, with iron particles growing extensively with increasing temperature due to sintering.

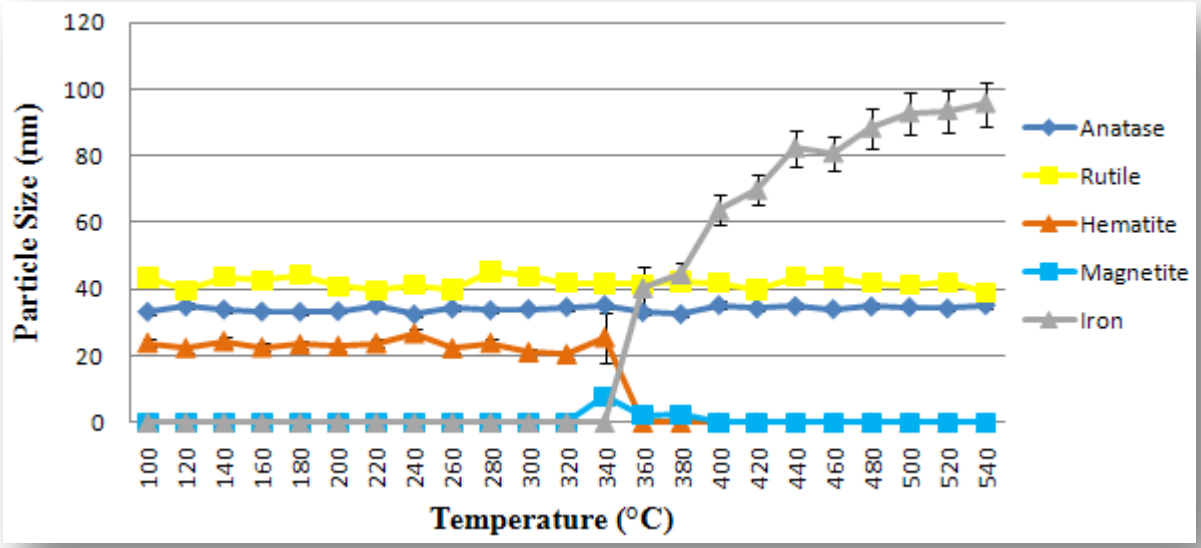

Figure 3.104. Particle size changes of the constituent phases during the reduction of the Fe/Degussa P25 catalyst, calcined at 600 °C, with 100% H_2

3.4.1.3. Fe/DEGUSSA P25 Calcined at 600 °C and Reduced using 10 % H_2/N_2

Preliminary Discussion

The previous two experiments demonstrated two different reduction profiles, which were dependant on the concentration of hydrogen in the reducing gas mixture, as outlined in equations **(82)** and **(83)**.

$$Fe_2O_3(s) + 2TiO_2(s) + H_2(g)\ [5\%H_2/N_2] \rightarrow 2FeTiO_3(s) + H_2O(g) \quad \textbf{(82)}$$

$$3Fe_2O_3(s) + H_2(g) \rightarrow 2Fe_3O_4(s) + H_2O(g)$$

$$\hookrightarrow Fe_3O_4(s) + 4H_2(g) \rightarrow 3Fe(s) + 4H_2O(g) \quad \textbf{(83)}$$

The experiment was repeated using 10 %, 25 % and 50 % H_2/N_2 gas mixtures in order to determine the hydrogen concentration required for the transition from the reaction outlined in equation **(82)** to that in equation **(83)** and *vice versa* (table 3.6). It was found that a 10 % H_2/N_2 gas mixture resulted in a combination of reduction products (Fig. 3.105).

Table 3.6. Results of in situ experiments performed using reducing gas mixtures with increasing hydrogen concentrations

Hydrogen Concentration	Outcome
5 % H_2 / N_2	$Fe_2O_3 \rightarrow FeTiO_3$
10 % H_2 / N_2	$Fe_2O_3 \rightarrow FeTiO_3 + Fe^0$
25 % H_2 / N_2	$Fe_2O_3 \rightarrow Fe_3O_4 \rightarrow Fe^0$
50 % H_2 / N_2	$Fe_2O_3 \rightarrow Fe_3O_4 \rightarrow Fe^0$
100 % H_2 / N_2	$Fe_2O_3 \rightarrow Fe_3O_4 \rightarrow Fe^0$

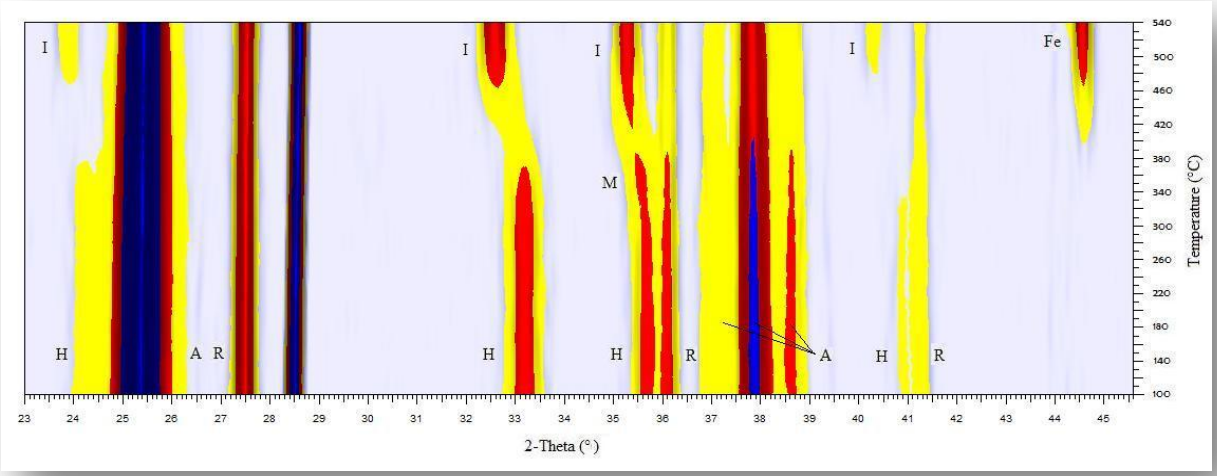

*Figure 3.105. Intensity profile of the diffraction patterns collected during the reduction of the Fe/Degussa P25 catalyst calcined at 600 °C with 10% H_2: **A** – anatase, **R** – rutile, **S** – silicon, **H** – hematite, **M** – magnetite **I** – ilmenite and **Fe** – iron*

Quantitative Analysis

The catalyst was remarkably stable up to a temperature of 320 °C (Fig. 3.106). Hematite was slowly reduced to magnetite at temperatures above 320 °C, with magnetite reaching a maximum concentration of 4.44 ± 0.3 % at 400 °C, leaving the majority of the hematite unreduced. A possible explanation of this phenomenon takes into account the inability of hydrogen to penetrate the unit cells of either iron oxide species to extract oxygen atoms (Fig. 3.107). Therefore, surface modification must be responsible for continued reduction of the hematite core. Our data clearly shows that reducing gases with low hydrogen concentrations are less effective surface modifiers, leading to incomplete reduction and the formation of ilmenite at the interface between the titania support and hematite. At temperatures above 340 °C an amorphous component was formed in parallel with the reduction of hematite. This amorphous component reached a maximum concentration at 400 °C, which also happens to be the temperature of maximum magnetite concentration. This amorphous component is thought to be the interface material generated between the newly formed magnetite shells and the support. At temperatures above 400 °C, the amorphous concentration decreased to zero as ilmenite (T > 380 °C) and iron (T > 400 °C) were formed. It is not possible to tell if the amorphous material was converted to ilmenite or if some modification occurs that allows iron to be liberated at these high temperatures. The ilmenite concentration increased rapidly between 460 °C and 520 °C, reaching a maximum concentration of 21.55 ± 0.9 %, completely consuming the remaining hematite phase. The ilmenite phase was then consumed, at temperatures above 520 °C, leading to the formation of more amorphous material. 73 % of the magnetite in the sample was reduced to iron at temperatures above 400 °C. Iron only reached a maximum concentration of 2.33 ± 0.1 % at 540 °C.

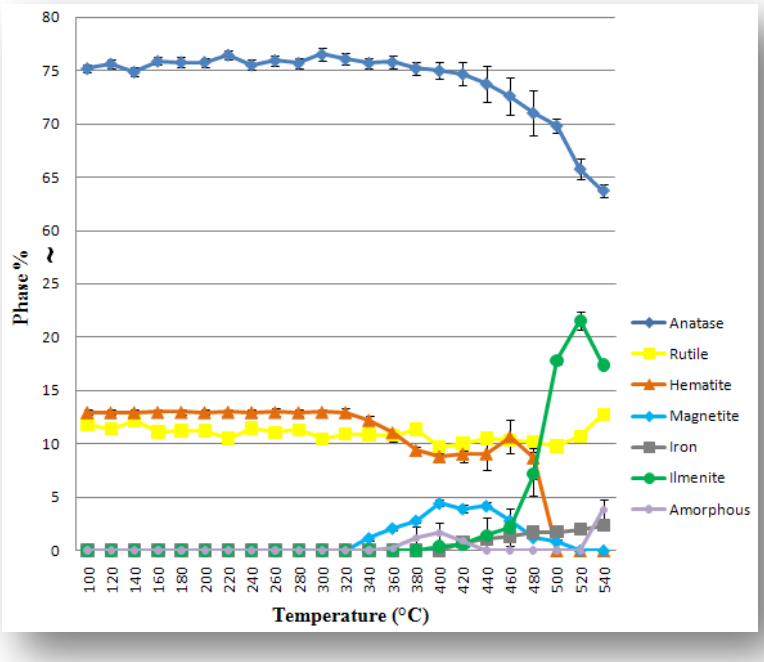

Figure 3.106. Quantitative phase analysis of the Fe/Degussa P25 catalyst, calcined at 600 °C, during reduction with 10 % H_2 (average GoF of 1.13)

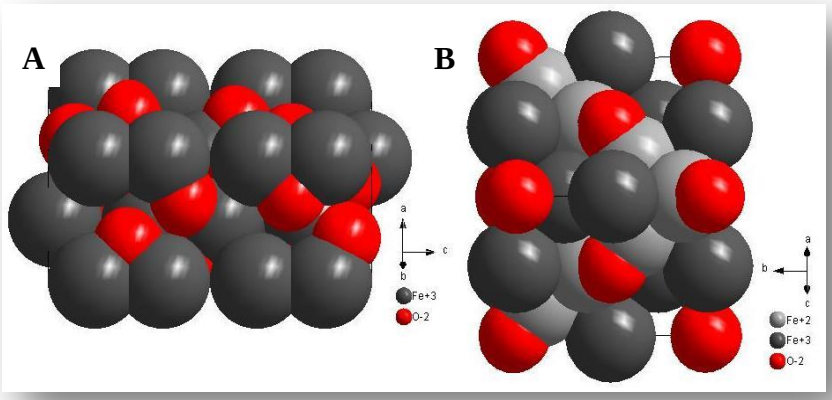

*Figure 3.107. Space-filling unit cell structures of hematite[40] (**A**) and magnetite[68] (**B**)*

Particle Size Analysis

The anatase and rutile particles remained relatively constant in size throughout the experiment (Fig. 3.108**A**). The average hematite particle size began to decrease upon reduction to magnetite at temperatures above 320 °C (Fig. 3.108**B**). The average magnetite particle size was significantly larger than the parent hematite particles at 340 °C, suggesting that larger hematite particles were reduced first, the opposite of what was observed when using 100 % H_2. Smaller hematite particles were reduced at higher temperatures, decreasing the average size of magnetite particles until the reactor reached 440 °C. At temperatures above 440 °C, as the reduction of magnetite to iron gained momentum, the average magnetite particle size increased quite dramatically, indicating that, unlike the hematite – magnetite reduction step, smaller magnetite particles were initially reduced to form iron (Fig. 3.108**C**). There could, however, have been magnetite sintering taking place at these temperatures. The average iron particle size increased dramatically between 400 °C and 420 °C as the small amount of magnetite was reduced to iron. Ilmenite became visible in the pattern collected at 400 °C and had already attained an average particle size of 28.3 ± 2 nm, which then oscillated around this value as the temperature was increased further (Fig. 3.108**D**).

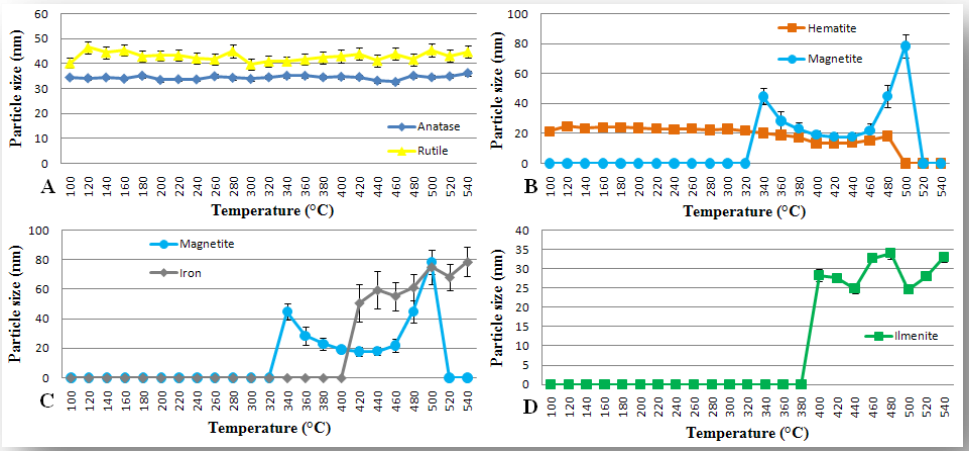

*Figure 3.108. Particle size changes of anatase and rutile (**A**), hematite and magnetite (**B**), magnetite and iron (**C**) and ilmenite (**D**) during the reduction of the Fe/Degussa P25 catalyst, calcined at 600°C, with a 10 % H_2/N_2 gas mixture*

3.4.1.4. Fe/DEGUSSA P25 Calcined at 450 °C and Reduced using 100 % H_2

The appropriate calcination temperature for the Fe/Degussa P25 catalyst was found to be 450 °C (chapter 3.2.1). The *in situ* PXRD experiment was repeated using 100 % H_2 to monitor the reduction profile of this system after calcination at 450 °C. The catalyst displayed the standard reduction profile for iron as can be seen in the intensity profile given as figure 3.109.

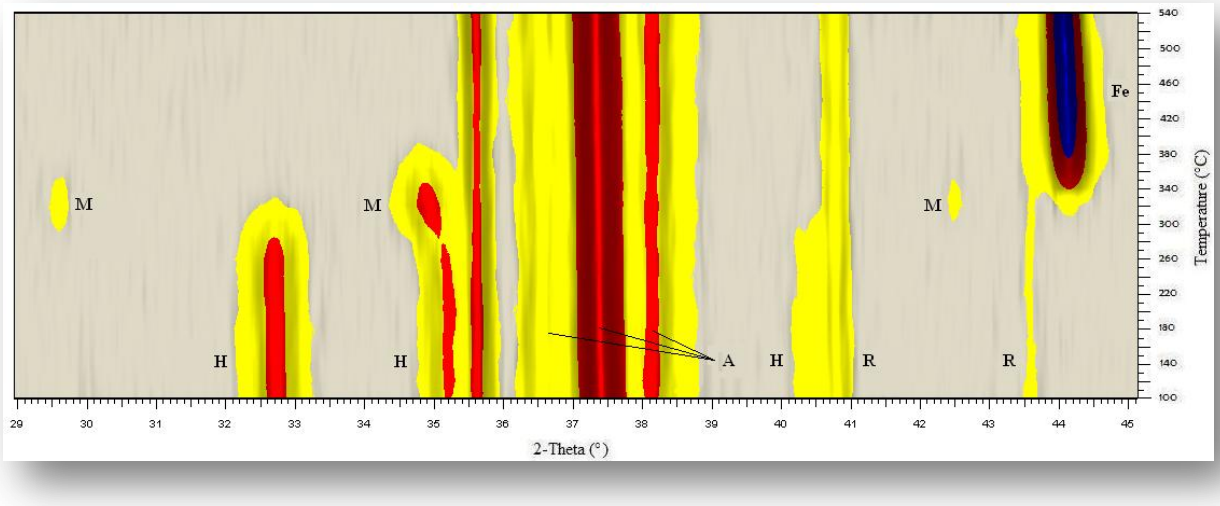

*Figure 3.109. Intensity profile of the powder diffraction patterns collected during the reduction of the Fe/Degussa P25 catalyst calcined at 450°C with 100 % H_2: **A** – anatase, **R** – rutile, **H** – hematite, **M** – magnetite and **Fe** – iron*

Quantitative Analysis

The anatase concentration remained relatively stable throughout the reduction experiment (Fig. 3.110), unlike the catalyst calcined at 600 °C. The absence of a decrease in anatase concentration, during the reduction of hematite to magnetite suggests that there was limited, if any, interaction between the two phases. However, a small amount of amorphous material was produced at temperatures above 280 °C, after the start of the reduction of hematite at temperatures above 260 °C. Magnetite reached a maximum concentration of 9.51 ± 0.3 % at 320 °C, after which it was reduced to iron, forming more amorphous material in the process. The amorphous concentration continued to increase while iron was formed, reaching a maximum concentration of 3.96 ± 0.1 %. The amorphous concentration then decreased as the temperature was increased, liberating a small amount of iron. Iron reached a maximum concentration of 8.52 ± 0.1 % at 500 °C, resulting in a calculated degree of reduction of 104 % (8.19 % marks the 100 % degree of reduction).

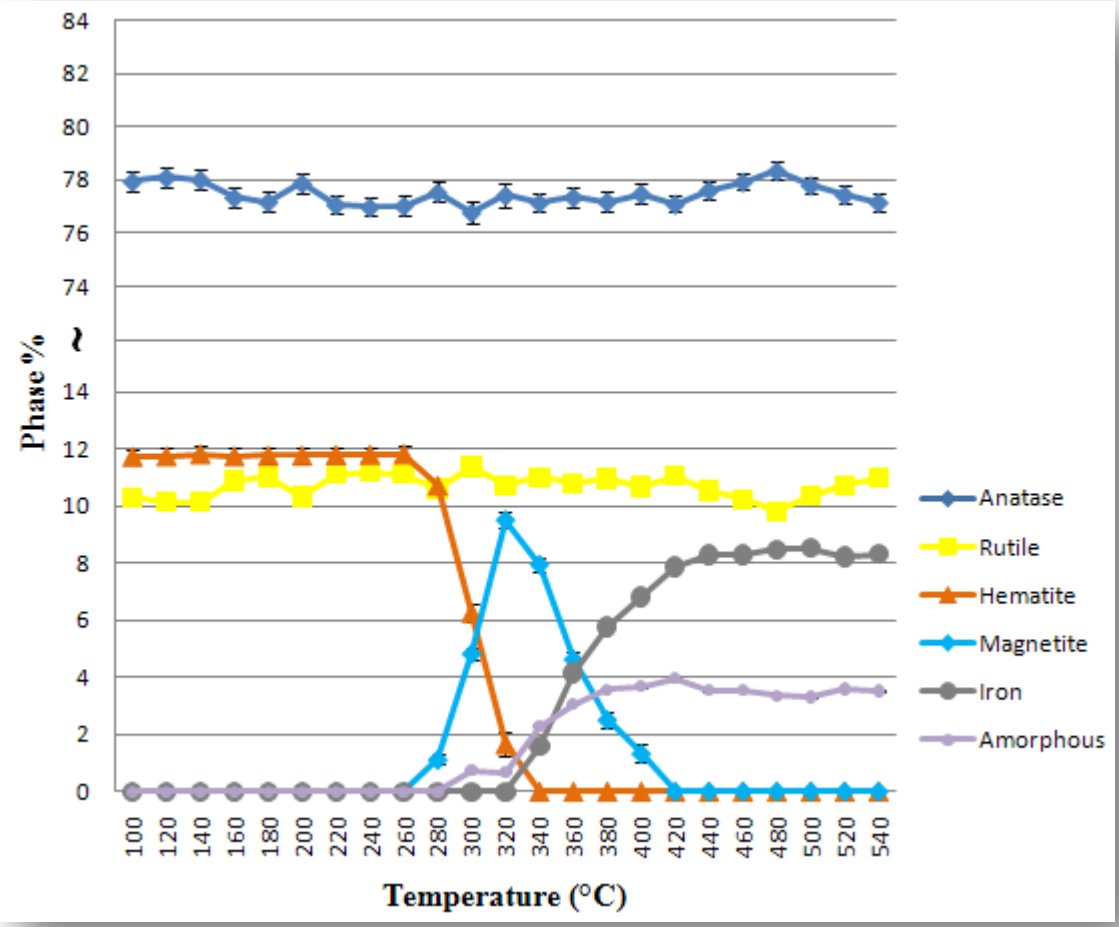

Figure 3.110. Quantitative phase analysis of the Fe/Degussa P25 catalyst, calcined at 450 °C, during reduction with 100 % H_2 (average GoF of 1.13)

Particle Size Analysis

The changes in particle size of the constituent phases during the reduction process are given in figure 3.111. Once again the anatase and rutile particle size remained relatively constant throughout the experiment. The hematite particle size began to decrease at temperatures above 260 °C, during the reduction to magnetite. The small decrease in the average hematite particle size and the initially large average particle size of magnetite suggests that larger hematite particles were reduced first, while the reduction of smaller hematite particles required more energy in order to overcome a higher activation energy. The average magnetite particle size decreased with increasing temperature and stabilized between 320 °C and 340 °C, with values in the region of 17 nm. The average magnetite particle size then decreased at temperatures above 340 °C, as magnetite was reduced to iron, a process which started at temperatures above 320 °C. The initial average iron particle size, at 340 °C, was 35.0 ± 3 nm, which remained constant when the temperature was increased by 20 °C . The iron particle size then increased with increasing temperature, due to sintering.

In an effort to produce iron particles with an average size of 20 nm or less, an identical experiment was performed where diffraction patterns were collected at 1 °C intervals in the 320 °C – 340 °C temperature range. The reduction of magnetite to iron was found to occur at 329 °C. A third experiment was performed in which the reactor was ramped to 320 °C in the same way as the other experiments and then ramped to 329 °C at 15 °C/min and held at this temperature, while consecutive diffraction patterns were collected (Fig. 3.112). The results suggest that, even at this constant temperature, the initial iron particles formed by reduction of magnetite had an average particle size of 56 ± 15 nm. However, this data also suggests that the average particle size decreased with increasing time at constant temperature, to a minimum value of 37 ± 2 nm, after which it began to increase once again but to a lesser extent than before. The TEM image, given in figure 3.113, resembles those taken for the calcined catalyst, where the iron particles are supported but have a very low degree of dispersion.

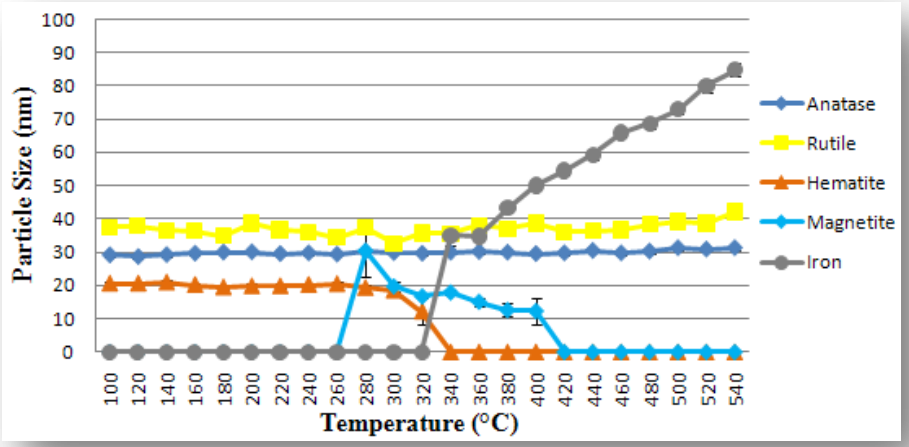

Figure 3.111. Particle size changes of the constituent phases in the Fe/Degussa P25 catalyst, calcined at 450 °C, during reduction with 100 % H_2

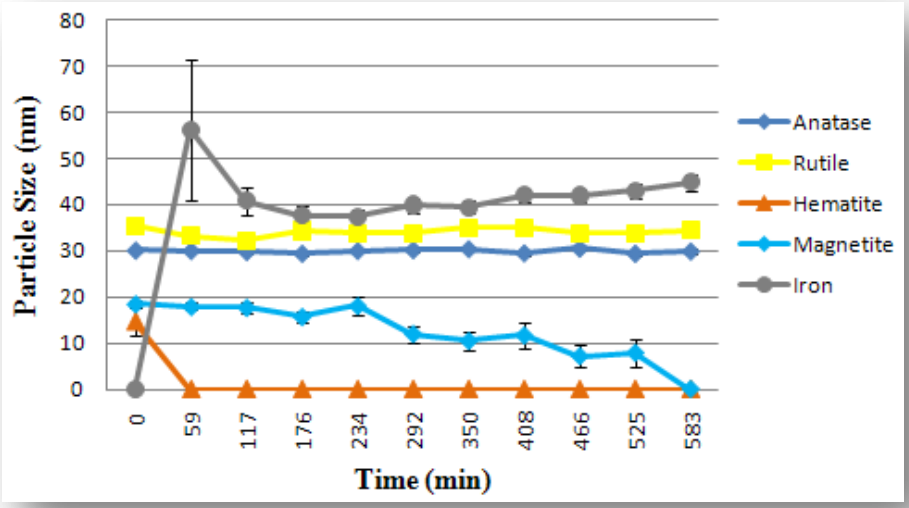

Figure 3.112. Particle size changes of the constituent phases in the Fe/Degussa P25 catalyst, calcined at 450 °C, during reduction with 100 % H_2 at 329 °C (average GoF of 1.16)

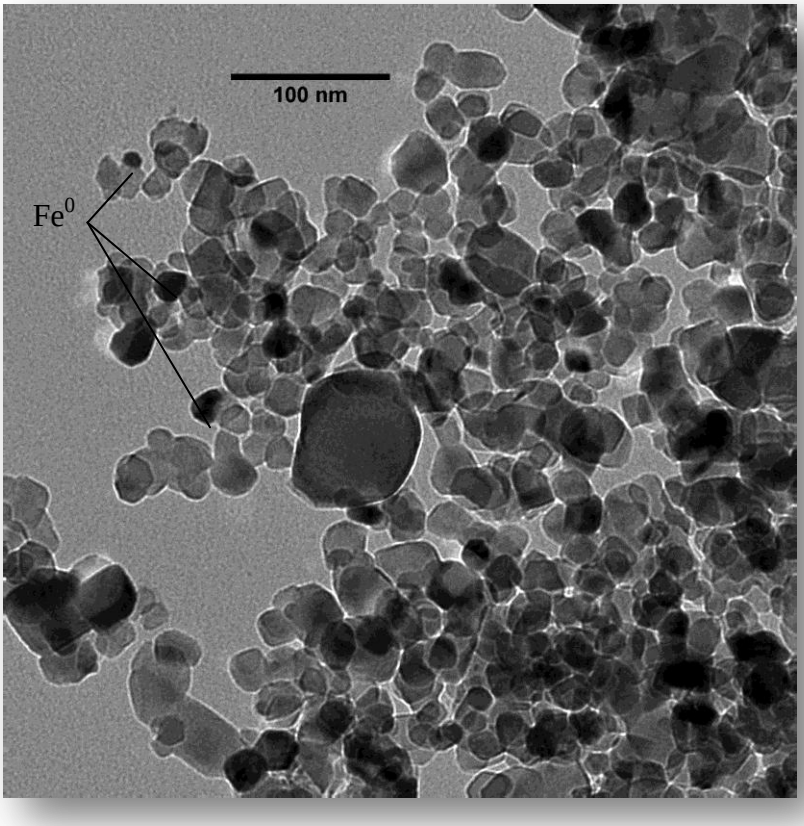

Figure 3.113. TEM image of the Fe/Degussa P25 catalyst, calcined at 450 ℃, after reduction at 329 ℃

3.4.2. Fe/SIGMA ANATASE

Preliminary Discussion

The heat treatment of the Fe/Sigma Anatase catalyst revealed that the temperature at which maximum hematite concentration was attained was 700 °C. However, the hematite particle size was in the order of 35 ± 2 nm. The catalyst was, therefore, calcined at 460 °C, where only 42 % of the possible hematite concentration could be detected, to ensure a small average particle size. TEM images of the calcined catalyst showed that the hematite was entirely unsupported and, as such, the following discussion covers the reduction of a catalyst – support mixture, rather than a supported catalyst. The intensity profile of the diffraction patterns collected during the reduction experiment is given as figure 3.114. The catalyst follows a slightly different reduction profile in that there was an additional iron oxide phase present in the form of wuestite. Wuestite crystallizes in a cubic $Fm\bar{3}m$ space group (Fig. 3.115) and represents an Fe^{2+} system (FeO), completing the reduction sequence Fe^{3+} (hematite)→ $Fe^{2+/3+}$ (magnetite) → Fe^{2+} (wuestite) → Fe^{0} (metallic iron).[70] It is possible that wuestite formed during the reduction of the Fe/Degussa P25 catalyst, however, the relatively small anatase particle size results in broad peak widths and, therefore, significant peak overlap (decreased resolution), making it difficult to observe the wuestite peaks.

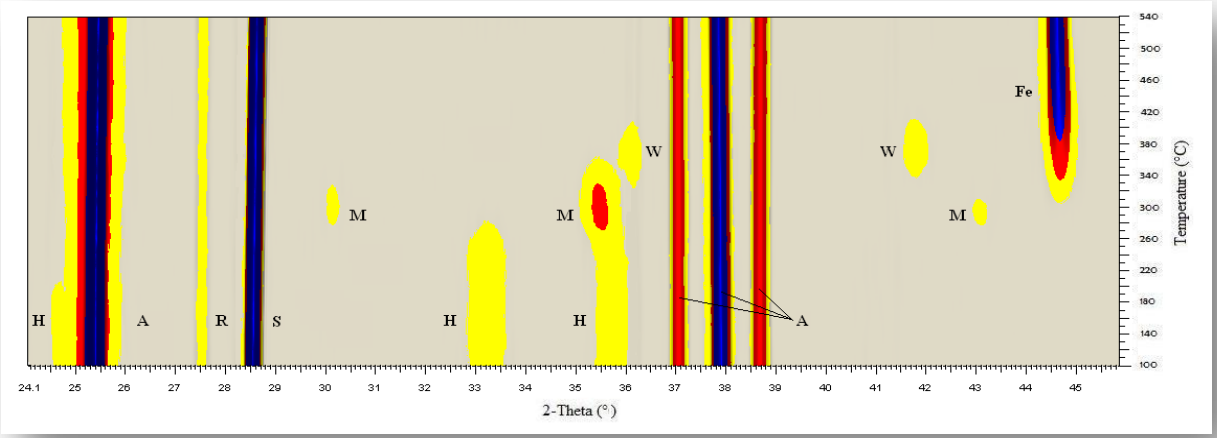

Figure 3.114. Intensity profile of the diffraction patterns collected during the reduction of the Fe/Sigma catalyst: ***A*** *– anatase,* ***R*** *– rutile,* ***S*** *– silicon,* ***H*** *– hematite,* ***M*** *– magnetite,* ***W*** *– wuestite and* ***Fe*** *– iron*

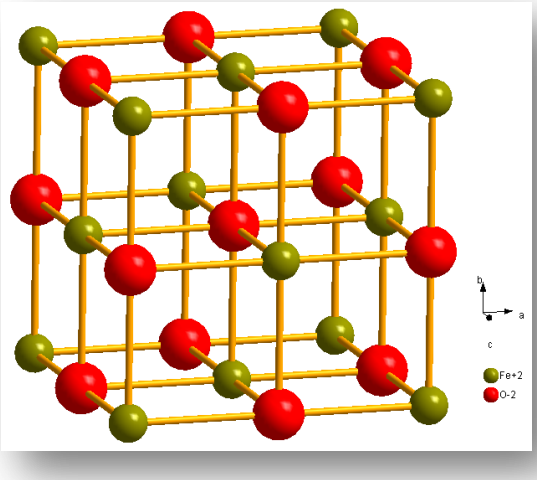

Figure 3.115. Crystallographic representation of wuestite (cubic $Fm\bar{3}m$)[70]

Quantitative Analysis

Figure 3.116 shows the variation in phase composition as the catalyst underwent reduction. As expected the anatase and rutile phases remained relatively stable throughout the experiment. The incomplete calcination of this sample resulted in the presence of Fe^{3+}AM at the start of the experiment, which was converted to crystalline hematite between 100 °C and 200 °C. The hematite concentration began to decrease at temperatures above 220 °C, forming an amorphous component. Since the hematite particles were unsupported, it seems likely that this material represents an amorphous intermediate species that represents the oxygen deficient hematite particles before lattice rearrangement to form magnetite. It is also possible that the reduction process initiates the hematite-anatase interaction to form amorphous iron titanates but, as was shown in the previous chapter, the formation of these iron titanates occurs to a much larger extent during the reduction of magnetite. The amorphous component continued to increase in concentration, even after the formation of magnetite had begun (T > 260 °C), and accounted for the apparent loss of iron species in the system after the reduction of hematite. Iron was first observed in the pattern collected at 320 °C, while wuestite, was only observed in the pattern collected at 340 °C. There are two possible explanations for the observation of wuestite in this sample. The first takes into account the possibility that the reduction of magnetite to iron always passes through the wuestite intermediate, which is possibly very short-lived, and the resolution of the diffraction patterns collected during *in situ* reduction determine if it is observed. The second explanation takes into account the possibility that two competing reactions may have taken place during the reduction of magnetite, i.e the reduction of magnetite directly to iron and the reduction of magnetite to wuestite, which was inevitably reduced to iron during the course of the reduction process. The two reduction pathways may be particle size related. The amorphous concentration continued to increase during the reduction of magnetite. The wuestite concentration began to decrease at temperatures above 360 °C, as it was reduced to form iron. The amorphous concentration decreased somewhat, at temperatures above 360 °C, liberating iron. Even with this amorphous component, the overall degree of reduction for this catalyst was 84 %, meaning that 16% of the iron is not available in metallic form and likely formed part of the amorphous component.

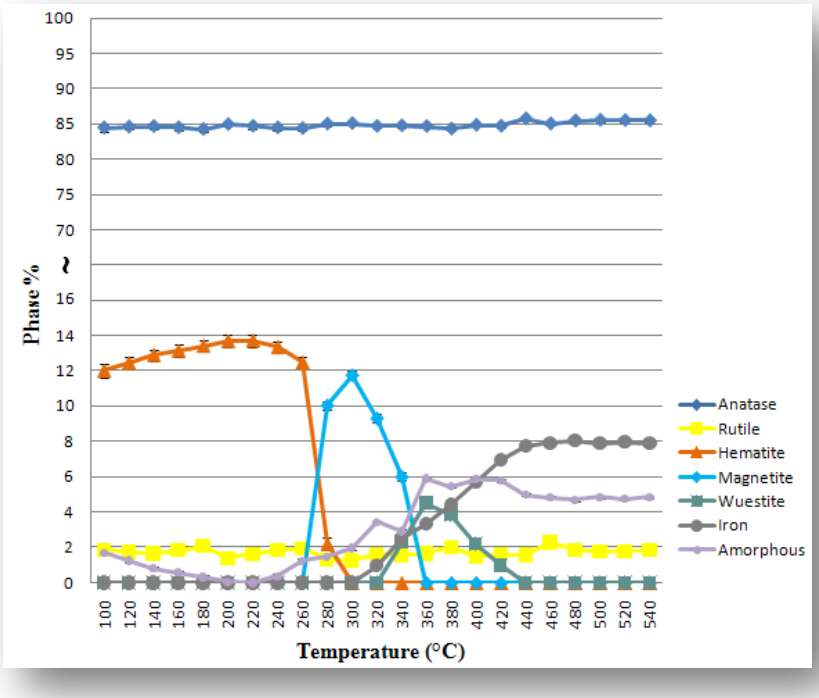

Figure 3.116. Quantitative phase analysis of the Fe/Sigma catalyst during reduction (average GoF of 1.22)

Particle Size Analysis

The changes in average particle size of the phases, present during the reduction process, are given in figure 3.117. Unlike in the Fe/Degussa P25 catalyst, the average anatase particle size increased steadily throughout the experiment. It was initially thought to be due entirely to thermal expansion but calculations, performed using unit cell volumes at the two extremes of temperature, revealed that this would only result in an increase in particle size of only 1.13 %, increasing the initial average anatase particle size of 122 ± 1 nm at 100 °C to ±123 nm at 540 °C, which is far from the observed value of 141 nm. The anatase particle size did decrease to an average value of 128 ± 2 nm upon cooling, suggesting that some agglomeration occurred during the reduction process. This could be another observation of anatase growth via the bridging mechanism proposed by Kim *et al.*.[18]

The hematite particle size remained relatively constant up to a temperature of 260 °C, at which point the first reduction step was initiated. Magnetite particles had a similar size to that of the parent hematite particles and the absence of a particle size decrease at higher temperatures, suggests that the hematite, and thus the magnetite particles, had a very narrow particle size distribution in the sample. The reduction of magnetite to iron was found to begin at 301 °C and at 320 °C had already attained an average particle size of 39 ± 6 nm.

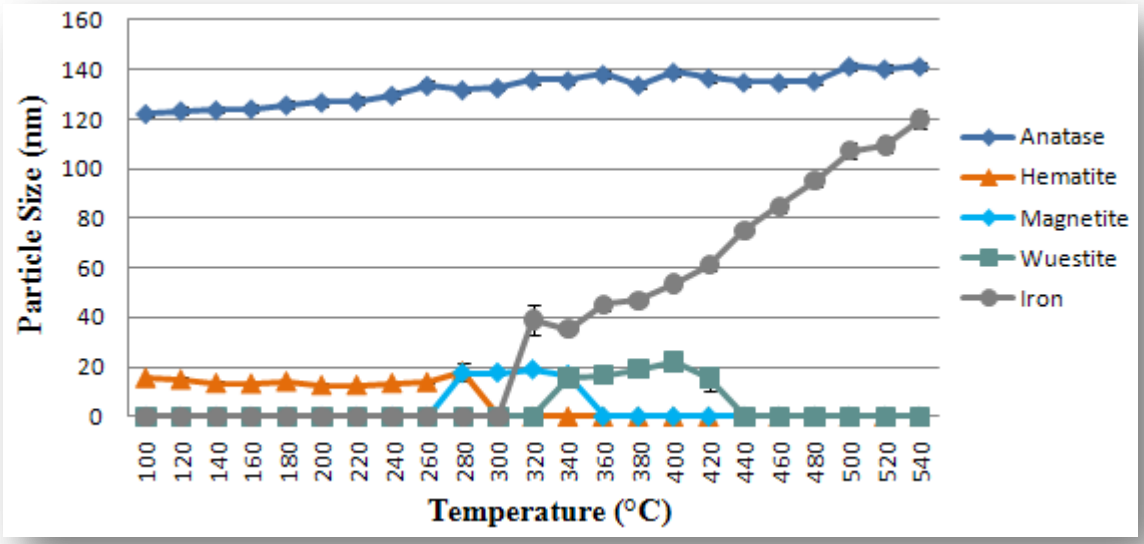

Figure 3.117. Particle size changes of the constituent phases of the Fe/Sigma catalyst during reduction

The sample was reduced at a constant temperature of 301 °C in order to determine if the particle size could be controlled. However, figure 3.118 shows that the iron particles that formed initially had an average particle size of 32 ± 6 nm, which then decreased to a minimum value of 27 ± 1 nm as the reduction process continued. The particle size distribution of iron also decreased as the reduction process progressed, while the magnetite particle size distribution increased. The TEM images in figure 3.119 indicate that, during the reduction process, the iron particles became bound to the anatase particles in the

support, forming clusters of iron particles attached to individual anatase particles. This is a dramatic difference in morphology when compared to the TEM images of the catalyst produced after calcination (Fig. 3.47), which showed entirely unsupported hematite particles. This observation indicates that, under reduction conditions, there is a significant Fe^0/Fe_xO_y – anatase interaction and adds credibility to the proposal that under reduction conditions an amorphous species is formed at the Fe^0/Fe_xO_y – anatase interface that anchors the particles.

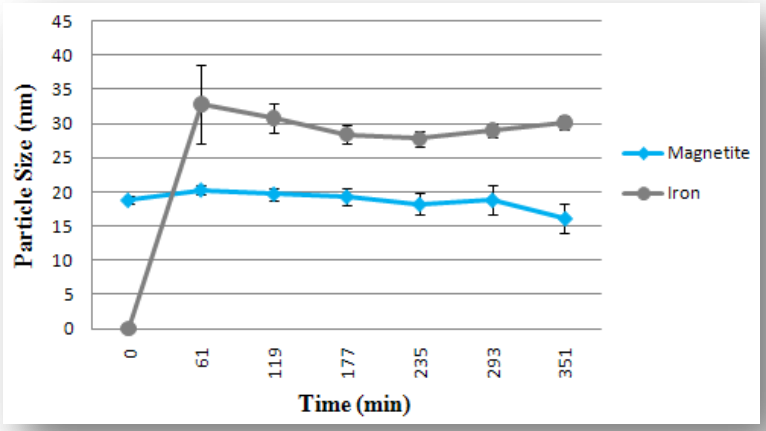

Figure 3.118. Particle size changes of the constituent phases in the Fe/Sigma catalyst during reduction at 321 °C (average GoF of 1.15)

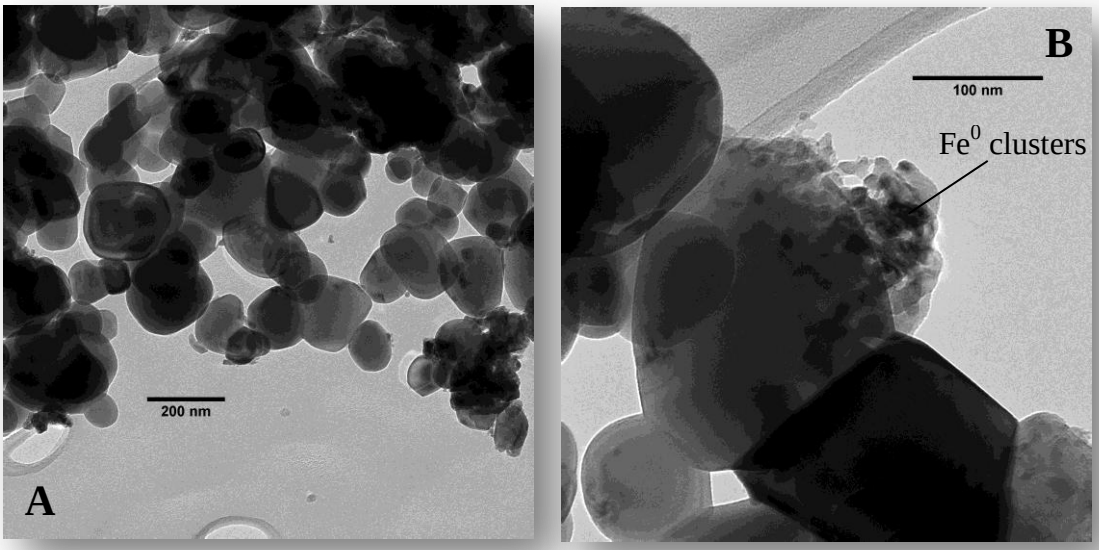

*Figure 3.119. TEM images of the Fe/Sigma catalyst after reduction at 301 °C: **A** – sample representation and **B** – magnified view of the supported iron clusters*

3.4.3. Fe/NSA

Preliminary Discussion

This sample was calcined at 510 °C, the temperature corresponding to the largest anatase to hematite particle size ratio (chapter 3.2.3). The *in situ* reduction experiment discussed here is one in which the reactor was ramped to 300 °C in the normal way, i.e. 20 °C increments etc., and then ramped to 323 °C and held constant while diffraction patterns were consecutively collected (note the nonlinear scale in figure 3.120). This temperature was found to be the temperature at which iron was first observed in an earlier experiment. The intensity profile shows peaks for anatase, brookite, silicon and iron but none for hematite and magnetite. It was likely that the hematite and magnetite particles were too small to be resolved in the diffraction patterns, a problem compounded by the broad anatase peaks.

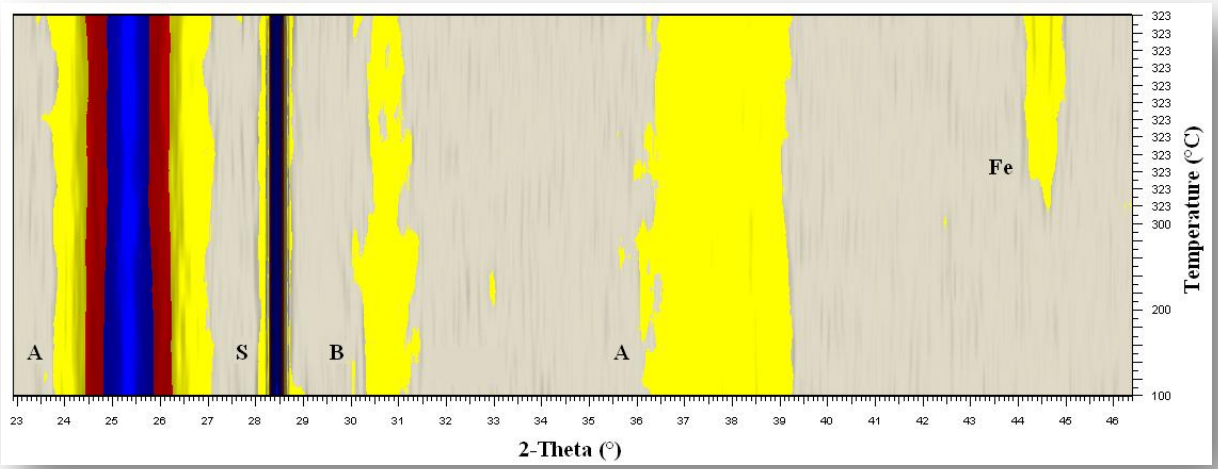

Figure 3.120. Intensity profile of the powder diffraction patterns collected during the reduction of the Fe/NSA catalyst: ***A*** *– anatase,* ***B*** *– brookite,* ***Fe*** *– iron and* ***S*** *– silicon*

Quantitative Analysis

The refinement results in figure 3.121 suggest that there was a large amount of amorphous material present at the start of the experiment. Brookite was converted to amorphous material between 100 °C and 160 °C, while the anatase concentration remained constant. The brookite concentration then stabilized for the remainder of the experiment. At temperatures between 200 °C and 323 °C the anatase concentration decreased, generating more amorphous material and then leveled off. The first pattern collected at 323 °C did not have any iron peaks, however, the subsequent patterns, collected at increasing time intervals, showed the emergence and increase in concentration of iron with a parallel decrease in amorphous material, indicating that iron can be generated from the amorphous material.

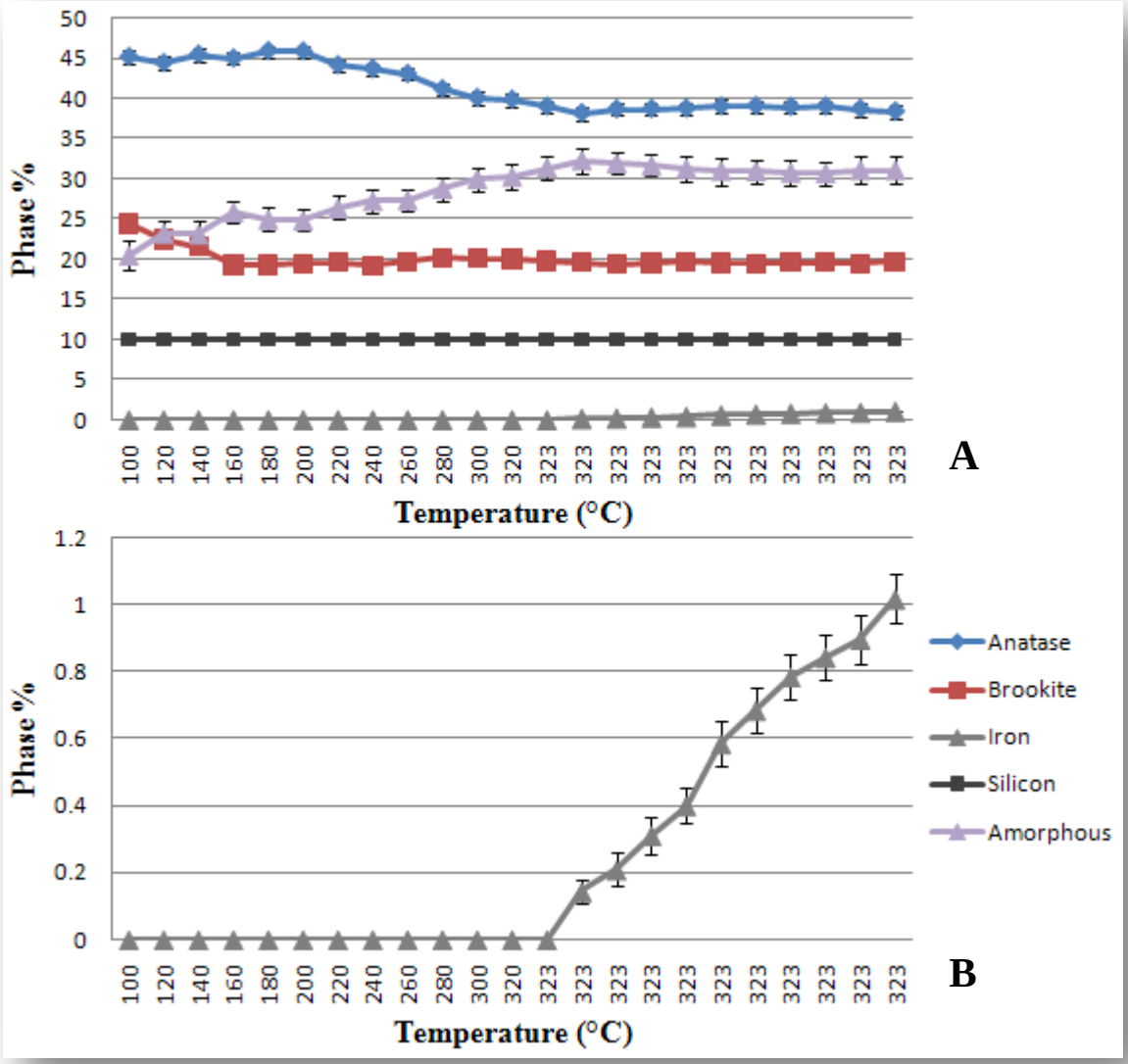

*Figure 3.121. Quantitative phase analysis of the Fe/NSA catalyst during reduction with 100% H_2: **A** – all phases and **B** – iron (average GoF of 1.13)*

Particle Size Analysis

Figure 3.122 indicates that the anatase particle size remained relatively constant throughout the reduction process, while the brookite particle size appeared to oscillate erratically. It is likely that the average brookite size was relatively constant and the oscillation was due to anomalies in the refinement procedure that arise due to the small, broad diffraction peaks produced by the brookite phase. When iron emerged it had an average particle size of 137 ± 91 nm. The large error associated with this value suggests that it is likely to be inaccurate and the real particle size is probably closer to 50 nm. The difficulty in measuring the particle size accurately is due to the small size of the emerging iron peak. The iron particles matured to an average particle size of approximately 25 nm, while the concentration continued to increase. This suggests that the iron particle size can be controlled by not exceeding the ideal reduction temperature of 323 °C. It is to be noted that the iron particle size exceeds the support particle size by almost four times.

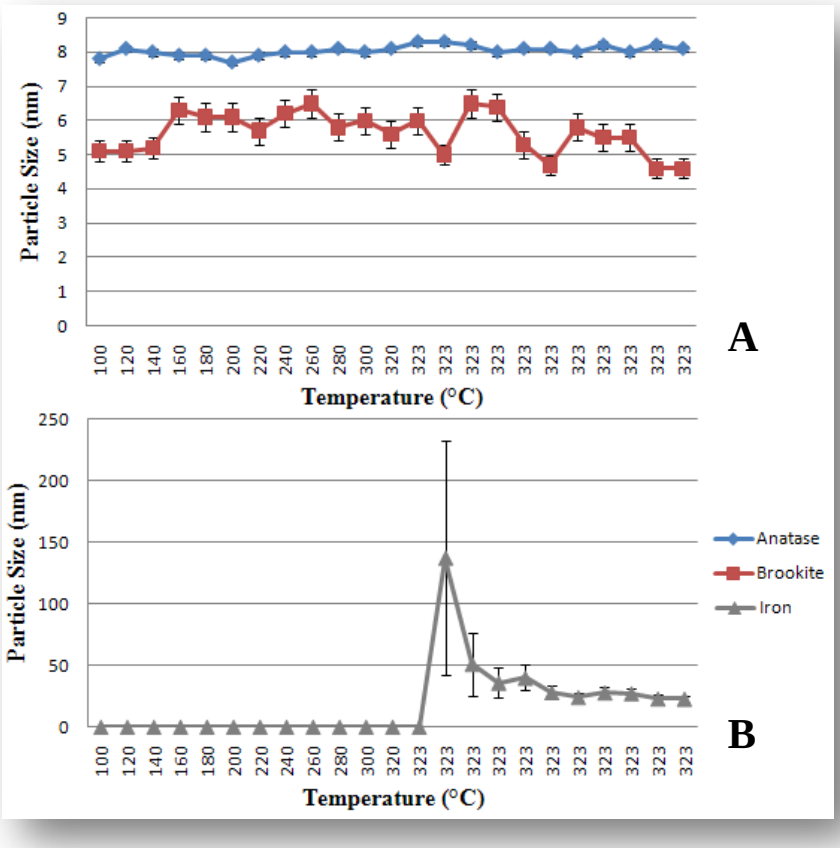

Figure 3.122. Particle size changes of the constituent phases present during the reduction of the Fe/NSA catalyst: ***A*** *– anatase and brookite and* ***B*** *– iron*

It is difficult to differentiate the iron particles from the support particles in the TEM images, given in figure 3.123. However, it appears that the darker regions in the micrograph represent iron particles that are surrounded by support particles. This arises since there would be less electron penetration, due to the increased density.

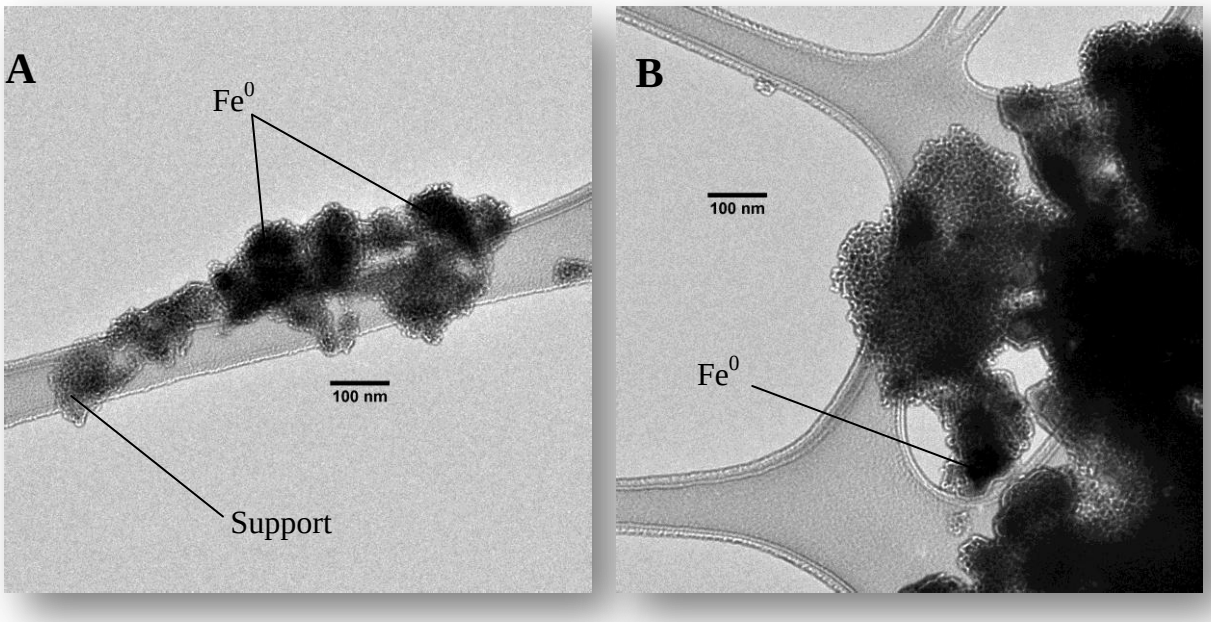

Figure 3.123. TEM images of the Fe/NSA support after reduction: ***A*** *– small iron-support cluster and* ***B*** *– sample representation*

3.4.4. Co/DEGUSSA P25

Preliminary Discussion

The optimum calcination temperature for this catalyst was found to be 500 °C, which resulted in a maximum cobalt oxide concentration of 15.85 ± 0.69 % with an average particle size of 14.8 ± 0.6 nm (chapter 3.2.4). The intensity profile of the diffraction patterns collected during the reduction experiment is given as figure 3.124. It shows that cobalt(II/III)oxide (Co_3O_4), was reduced to cobalt(II)oxide (CoO) at temperatures above 200 °C. CoO is a cubic $Fm\bar{3}m$ phase (Fig. 3.125**A**).[71] The CoO, was then reduced to metallic cobalt at temperatures above 250 °C, which is also a cubic $Fm\bar{3}m$ phase (Fig. 3.125**B**).[72]

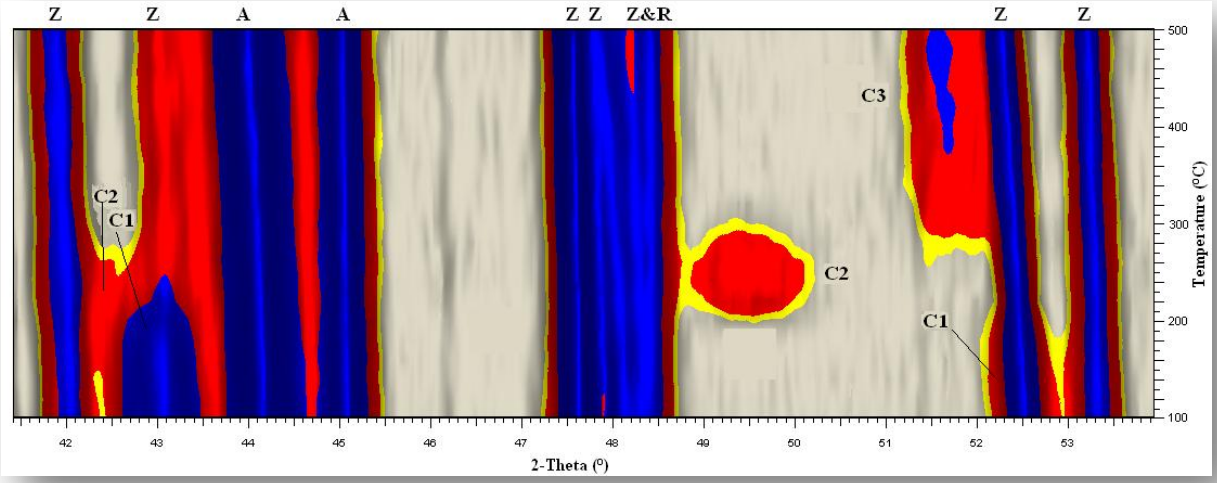

Figure 3.124. Intensity profile of the diffraction patterns collected during the reduction of the Co/Degussa P25 catalyst: ***A*** *– anatase,* ***R*** *– rutile,* ***Z*** *– baddeleyite,* ***C1*** *–* Co_3O_4*,* ***C2*** *– CoO and* ***C3*** *–* Co^0

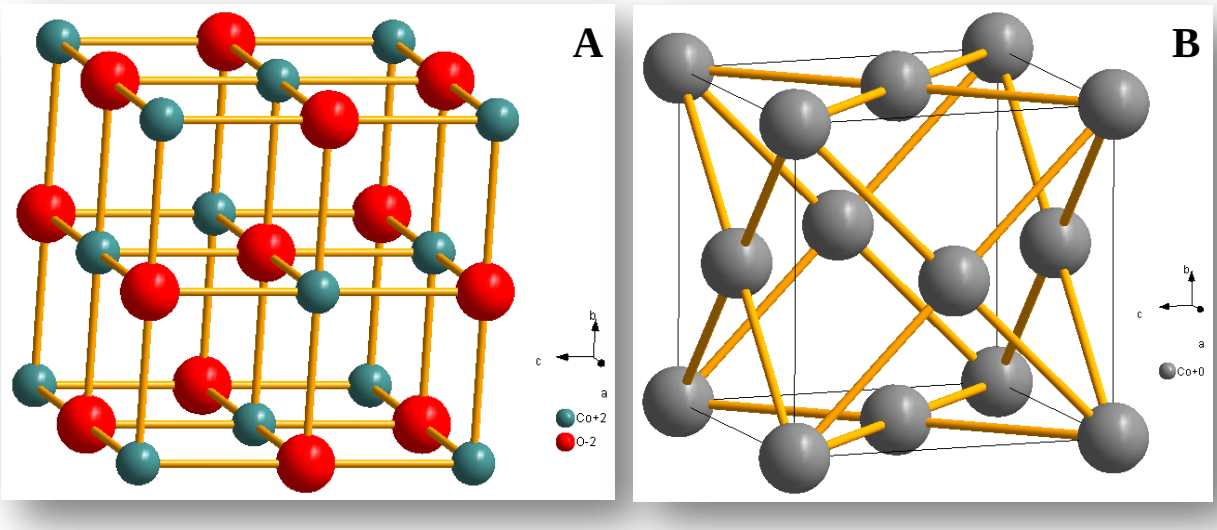

Figure 3.125. Crystallographic representations of ***A*** *- CoO (cubic* $Fm\bar{3}m$*)*[71] *and* ***B*** *– metallic cobalt (cubic* $Fm\bar{3}m$*)*[72]

Quantitative Analysis

The quantitative data in figure 3.126 shows that the Co_3O_4 concentration began to decrease at temperatures above 120 °C, forming a small amount of amorphous intermediate. We believe that this intermediate represents the interface between the Co_3O_4 species and the support as was the case with the iron catalysts discussed above. At temperatures above 180 °C both the amorphous and Co_3O_4 concentrations decreased as the reduction of Co_3O_4 to CoO gained momentum. CoO reached its maximum concentration at 240 °C and more amorphous material was detected. The formation of this amorphous material coincides with a small, but noticeable, decrease in the anatase concentration between 200 °C and 220 °C, indicating that the amorphous material is likely to be a result of the adhesion of the CoO to the anatase support. Jongsomjit *et al.* reported the formation of a Co-support compound (Co-SC) during the reduction of Co/TiO_2 catalysts that was different to $CoTiO_3$, using Raman spectroscopy.[73] However, they were unable to determine the structure of the material and proposed that is was too well dispersed on the surface of the support to be detected by X-ray diffraction. In 2007 Suriye *et al.* used electron spin resonance (ESR) to study the Co-SC structure and proposed a mechanism for the formation of Co-SC.[74] They were able to show that cobalt interacts with the support via hydrogen facilitation to form $Co^0(H_xTiO_y)$ materials. Our data confirms that the reason that it was not detected by standard laboratory based X-ray diffraction equipment was because it is an amorphous compound, i.e. it has no long range crystalline order. Our data also suggests that this amorphous material is formed at the interface between anatase and cobalt particles during the reduction of CoO to metallic cobalt.

Metallic cobalt was first observed in the pattern collected at 280 °C and increased in concentration, along with the amorphous material, as the temperature was increased. This increase in concentration of the amorphous material appeared to be driven by a decrease in rutile concentration at temperatures above 280 °C. This was the first time, in this study, that the rutile phase was seen to interact with metallic species in the sample. At temperatures above 280 °C metallic cobalt reached its maximum concentration, with a value of 7.58 ± 0.5 %, at 400 °C, resulting in a calculated degree of reduction of 80 %.

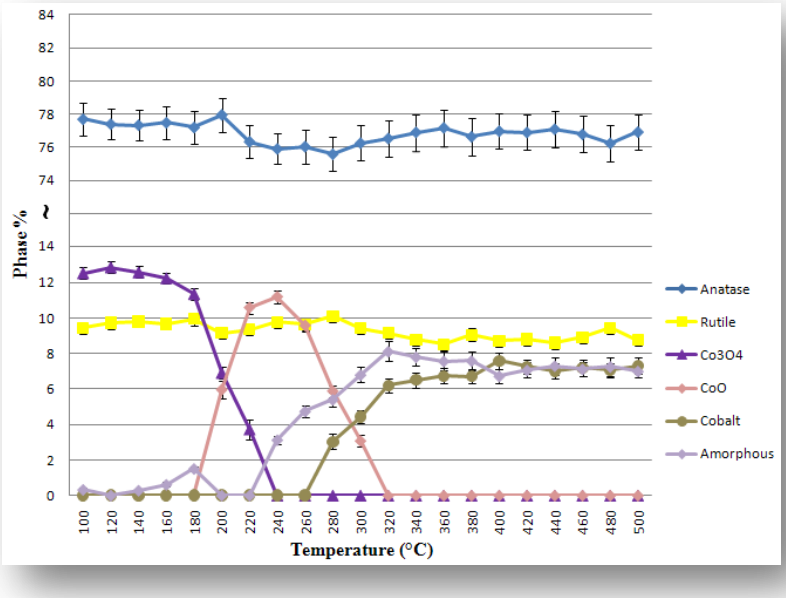

Figure 3.126. Quantitative phase analysis of the Co/Degussa P25 catalyst during reduction (average GoF of 1.27)

Particle Size Analysis

The changes in particle size during the reduction reaction are given as figure 3.127. The anatase particle size remained relatively constant throughout the experiment. The Co_3O_4 particles started out at approximately 16 nm and, upon reduction, formed CoO particles with an average size of 8.7 ± 1 nm. In an attempt to explain the observation, we calculated the expected CoO particle size by assuming that the particles had a dome shape on the surface of the support particles. The results indicated that the CoO particles should have an average size of approximately 12 nm, assuming that all of the Co_3O_4 was reduced to CoO. However, the results presented in the previous section indicate that there was an amorphous interfacial component that formed during the reduction process, which appears to anchor the particle to the support. The large discrepancy between the expected and observed particle size can, therefore, be attributed to the apparent loss of cobalt species that takes place in this anchoring process. The reduction of CoO to metallic cobalt formed cobalt particles with an average size of 14 ± 2 nm, which remained relatively stable upon further heating. The stability of the cobalt particle size at higher temperatures indicates that the Co/Degussa P25 catalyst is not as prone to metal sintering as the iron catalysts. The TEM images, given in figure 3.128, confirms the size of the cobalt particles and the binding of the particles to the support phase. They also show a much better degree of dispersion of the cobalt particles on the surface of the support, when compared to the Fe/Degussa P25 catalyst.

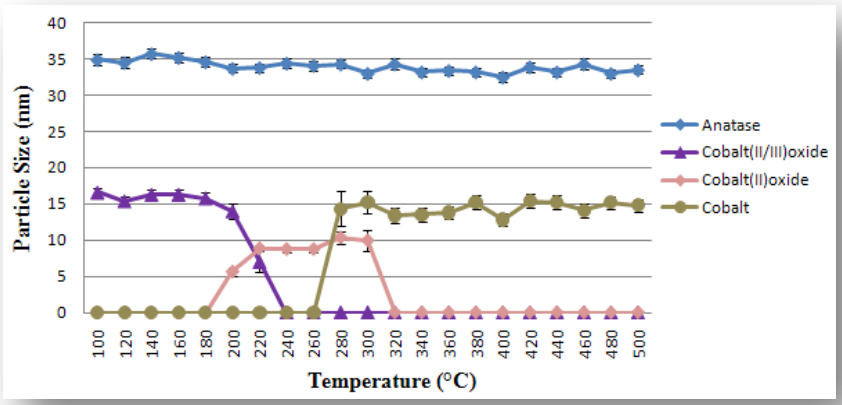

Figure 3.127. Particle size changes of the constituent phases present during the reduction of the Co/Degussa P25 catalyst

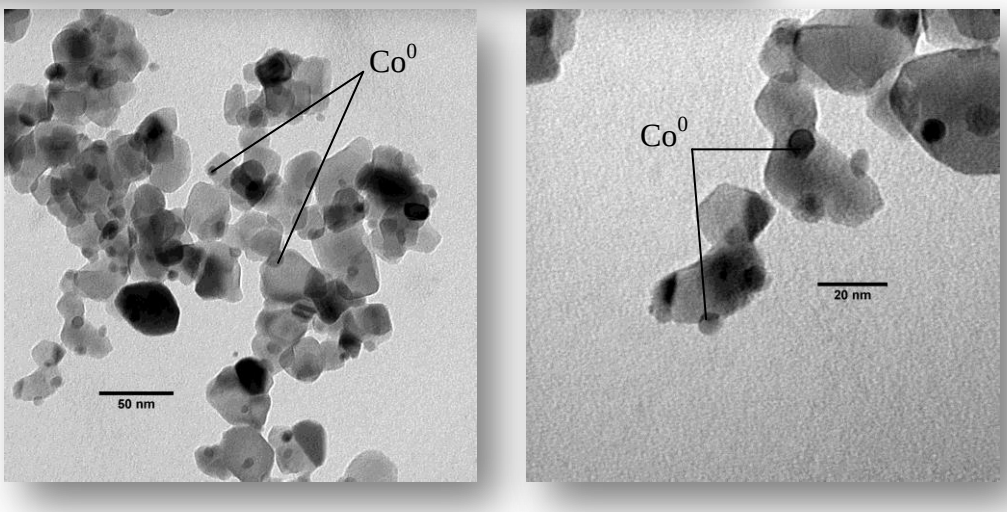

Figure 3.128. TEM images of the Co/Degussa P25 catalyst after reduction

3.4.5. Co/SIGMA ANATASE

Preliminary Discussion

In chapter 3.2.5 we determined that the ideal calcination temperature for this catalyst was 480°C, yielding Co_3O_4 particles with an average size in the order of 14 nm. The diffraction patterns collected during the reduction of this catalyst are given as an intensity profile in figure 3.129 and indicate that the catalyst followed an identical reduction profile to the Co/Degussa P25 catalyst discussed above.

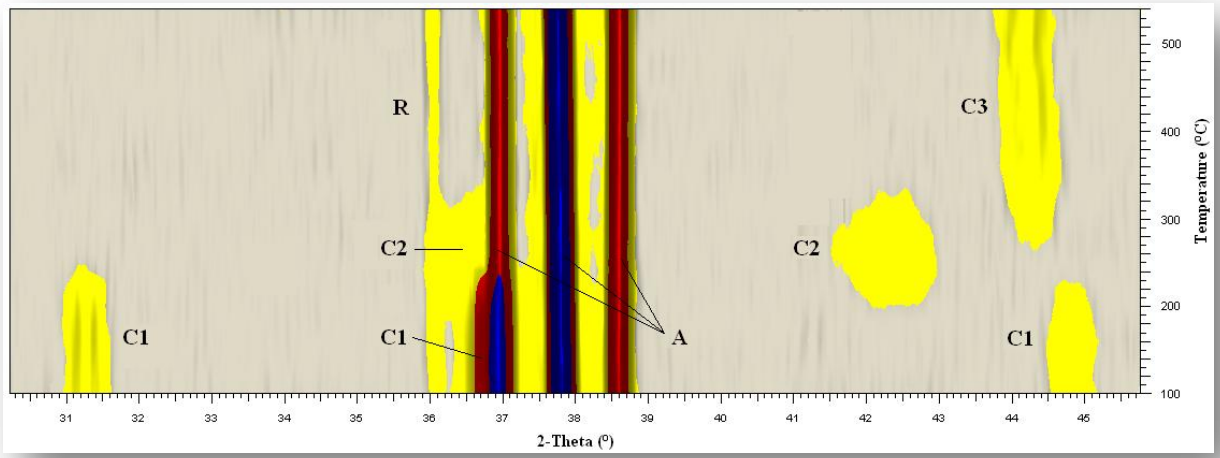

Figure 3.129. Intensity profile of the diffraction patterns collected during the reduction of the 10%Co/Sigma catalyst: ***A*** *– anatase,* ***R*** *– rutile,* ***C1*** *–* Co_3O_4*,* ***C2*** *– CoO and* ***C3*** *–* Co^0

Quantitative Analysis

Co_3O_4 was reduced to CoO, which was ultimately reduced to metallic cobalt at temperatures above 180 °C and 260 °C respectively (Fig. 3.130). The degree of reduction of the first step was approximately 90 %, while that of the second step was only ±32 %, leading to an overall degree of reduction of 29 %. The reason for this low value is the fact that a significant amount of cobalt was lost during the development of the interfacial amorphous material formed by reaction between the anatase and CoO particles. This observation suggests that there was a much higher metal/metal oxide – support interaction that occurred under reduction conditions, than was observed for the Co/Degussa P25 catalyst. It is difficult to say what the possible cause of this phenomenon might be, since the only differences between the two supports are the the particle size and the anatase to rutile ratio.

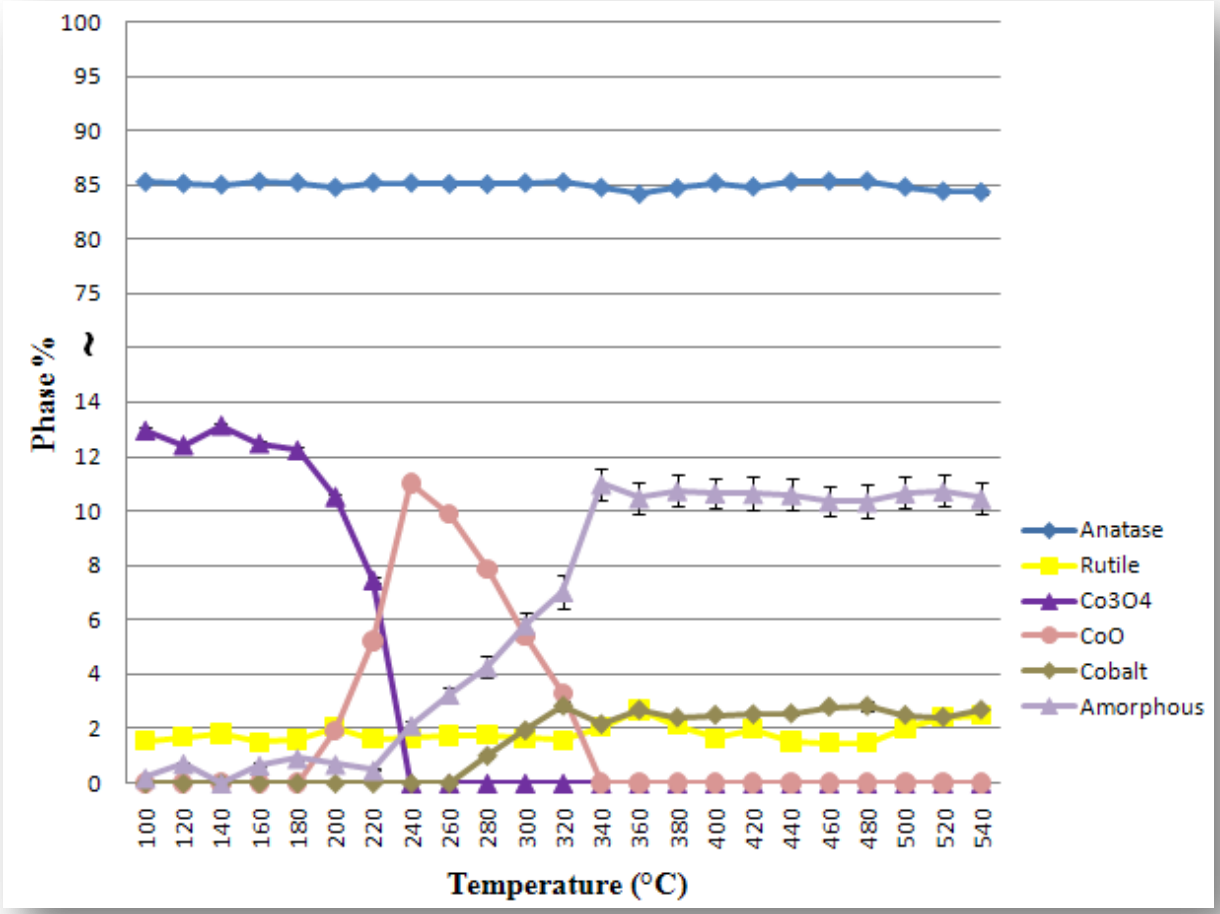

Figure 3.130. Quantitative phase analysis of the Co/Sigma catalyst during reduction (average GoF of 1.19)

Particle Size Analysis

The anatase particle size remained relatively constant throughout the experiment (Fig. 3.131). The average Co_3O_4 particle size, at the start of the experiment, was slightly larger than expected, with average values between 25 nm and 30 nm. These particles were reduced to CoO particles with an average size of between 10 nm and 13 nm and the increasing trend of the graph suggests that smaller particles were formed first, while larger ones were formed at higher temperatures. The reduction of CoO led to the formation of metallic cobalt particles with an average size of ±20 nm that remained fairly stable with increasing temperature. This, once again, confirms that the supported cobalt catalysts were much less prone to sintering at elevated temperatures than the iron catalysts. The TEM images, given in figure 3.132, show that the metallic cobalt particles were supported and had a good degree of dispersion. They also show that the cobalt particles were cratered.

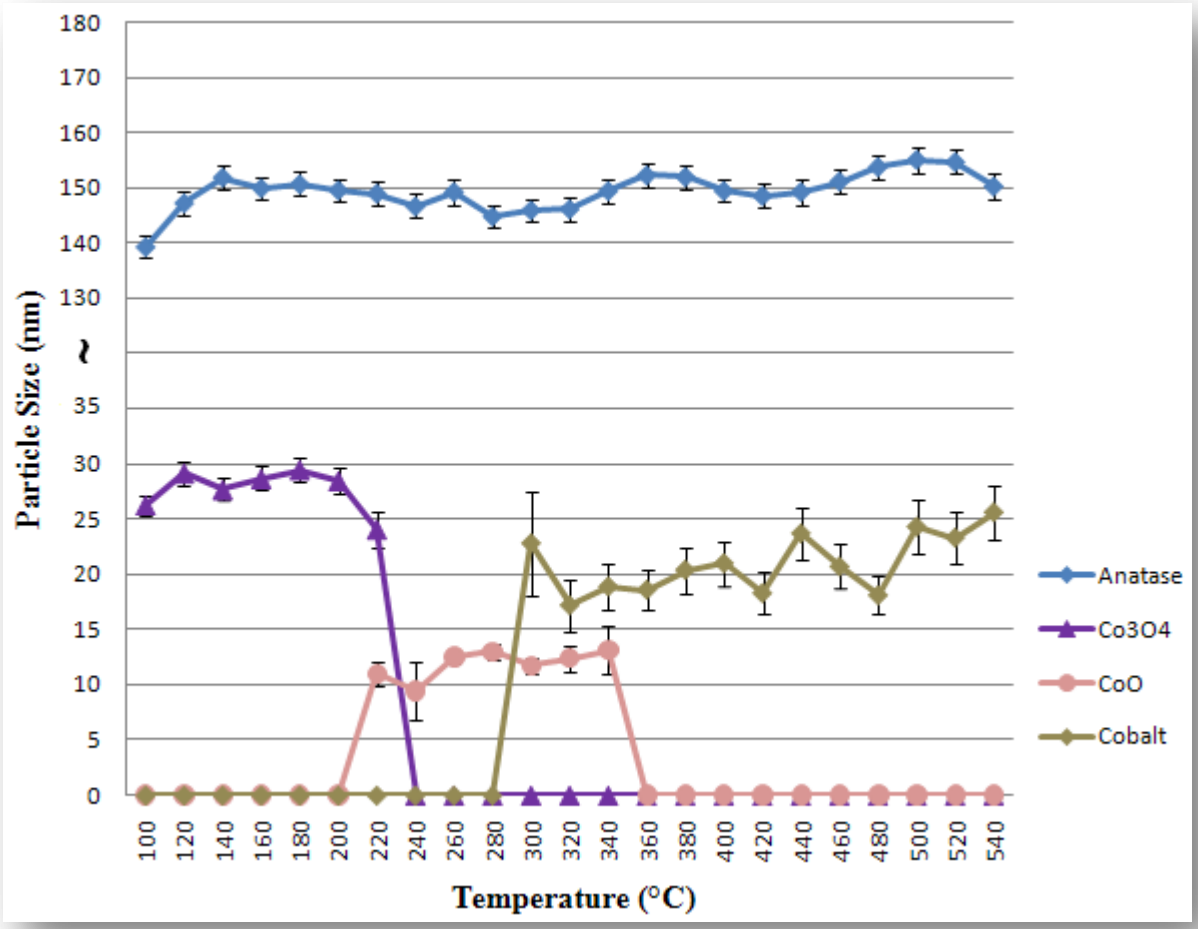

Figure 3.131. Particle size changes of the constituent phases present during the reduction of the Co/Sigma catalyst

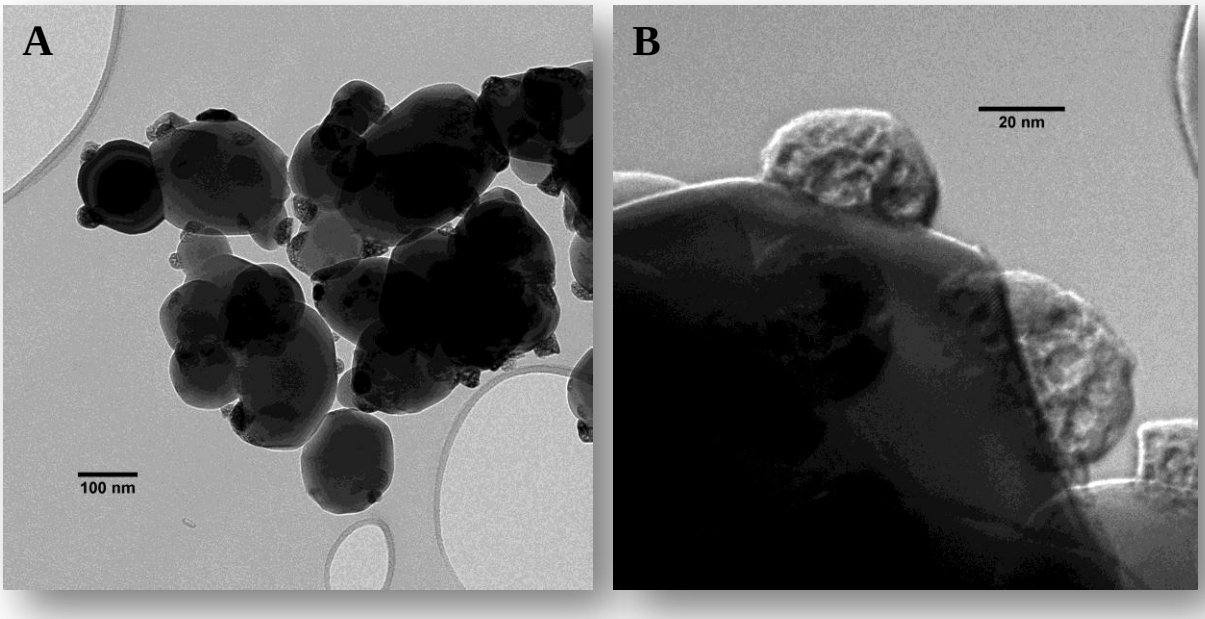

*Figure 3.132. TEM images of cobalt particles supported on anatase (**A**) and cratered cobalt particles (**B**)*

3.4.6. Co/NSA

Preliminary Discussion

The ideal calcination temperature for this catalyst was 540 °C (chapter 3.2.6), which produced Co_3O_4 particles with an average diameter of 10.3 ± 0.5 nm. The powder diffraction patterns, presented in the intensity profile given as figure 3.133, demonstrate the phase changes that occurred during the reduction of this catalyst between 100 °C and 300 °C in 20 °C intervals and between 300 °C and 310 °C in 1 °C intervals. This program was set up to determine the exact temperature at which metallic cobalt became detectable.

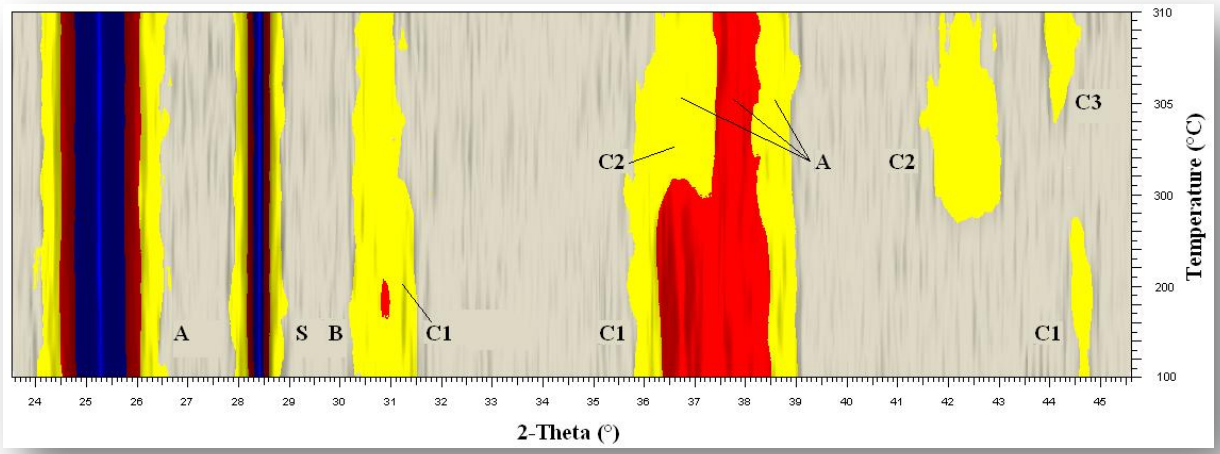

Figure 3.133. Intensity profile of the diffraction patterns collected during the reduction of the Co/Sigma catalyst: ***A*** *– anatase,* ***B*** *– brookite,* ***S*** *- silicon,* ***C1*** *–* Co_3O_4*,* ***C2*** *– CoO and* ***C3*** *–* Co^0

Quantitative Analysis

The quantitative curves, shown in figure 3.134, show that the anatase and brookite concentrations remained relatively constant until the temperature exceeded 260 °C, at which point both concentrations decreased as the temperature was increased. The decreases coincided with the reduction of Co_3O_4 and the formation of the amorphous intermediate phase, as was shown for the previous experiments. The rate of increase in the amorphous concentration, between 260 °C and 300 °C, was equal in magnitude to the combined rates of consumption of anatase, brookite and Co_3O_4 not consumed by reduction (denoted NCBR), with anatase and Co_3O_4 being the major contributors (Table 3.7). Brookite, Co_3O_4 and CoO were consumed to form more amorphous material and a small amount of anatase between 300 °C and 301 °C. The amorphous concentration increased between 303 °C and 304 °C. The rate of this increase was proportional to the combined rates of consumption of anatase, brookite and CoO (no CoO had been reduced to metallic cobalt at 304 °C), with brookite and CoO being the main contributors. These observations suggest that Co_3O_4 preferentially reacts with anatase during the reduction of Co_3O_4 to CoO and CoO preferentially reacts with brookite during the reduction of CoO to metallic cobalt. Both of these reactions generated amorphous materials. The maximum cobalt concentration achieved was 2.02 ± 0.2 %,

giving this catalyst a poor degree of reduction of 18 %. This value suggests that 82 % of the cobalt loaded onto this catalyst was consumed via the processes that generated the amorphous material.

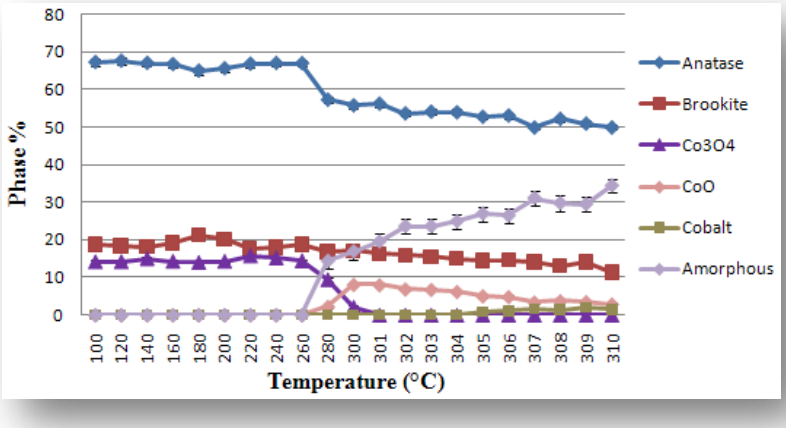

Figure 3.134. Quantitative phase analysis of the Co/NSA catalyst during reduction (average GoF of 1.08)

Table 3.7. Instantaneous rates of change of concentration of the phases present during the reduction of the Co/NSA catalyst (NCBR – not consumed by reduction)

Temperature (°C)	Instantaneous Rates of Change of Concentration (%/°C)										
	Anatase	Brookite	Co3O4	CoO	Cobalt	Amorphous	Co3O4 (NCBR)	CoO (NCBR)	Anatase+Brookite+Co3O4 (NCBR)	Anatase+Brookite+Co3O4+CoO	Anatase+Brookite+CoO (NCBR)
280	-0.481	-0.101	-0.250	0.113	0.000	0.719	-0.137		-0.719		
300	-0.074	0.018	-0.365	0.295	0.000	0.126	-0.070		-0.126		
301	0.452	-0.854	-2.107	-0.107	0.000	2.616	-2.213			-2.616	
302	-2.574	-0.359	0.000	-1.113	0.000	4.047					-4.047
303	0.442	-0.328	0.000	-0.114	0.000	0.000					0.000
304	-0.173	-0.564	0.000	-0.564	0.000	1.302					-1.302
305	-1.172	-0.476	0.000	-1.156	0.781	2.022		-0.374			-2.022

Particle Size Analysis

The particle size changes of the phases present in the catalyst during the reduction process are given in figure 3.135. The anatase and brookite average particle size values remained relatively constant throughout the reduction process, with the average brookite particle size only increasing significantly between 309 °C and 310 °C. This increase corresponds to a significant decrease in concentration in figure 3.134 and suggests that a large number of the smaller brookite particles were consumed to form more amorphous material at those temperatures. The reduction of the Co_3O_4 particles led to the formation of smaller CoO particles than was expected, with average values of around 10 nm. The CoO particle size decreases slightly between 301 °C and 303 °C to a value of approximately 9 nm, which corresponds to a significant increase in amorphous material (Fig. 3.134), confirming the reaction between CoO and the support materials under those conditions. The reduction of CoO resulted in the formation of metallic cobalt particles with an average particle size of approximately 20 nm over the 305 °C to 310 °C temperature range.

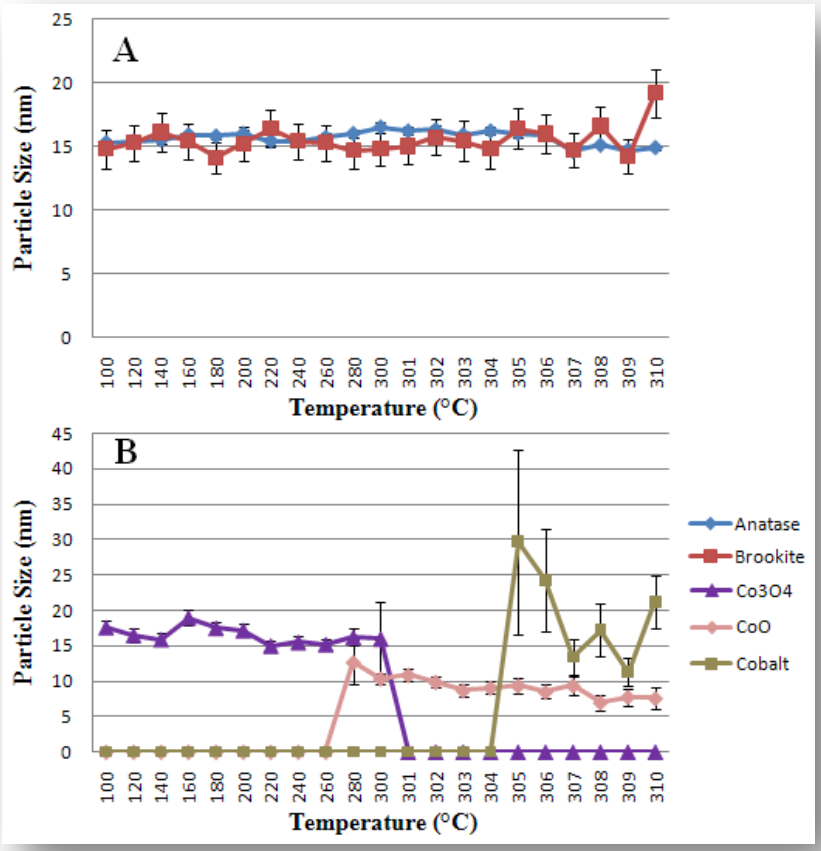

*Figure 3.135. Particle size changes of **A** – the support phases and **B** – the cobalt and cobalt oxide phases present in the Co/NSA catalyst during reduction*

It was difficult to differentiate the particles in the TEM images in figure 3.136 due to the similarity of the anatase, brookite and cobalt particle sizes. However, it is reasonable to suggest that the particles that appear darker in the TEM images are metallic cobalt particles, since they have a higher density than the support particles and they are the appropriate size. There was also a significant amount of amorphous material observed throughout the sample.

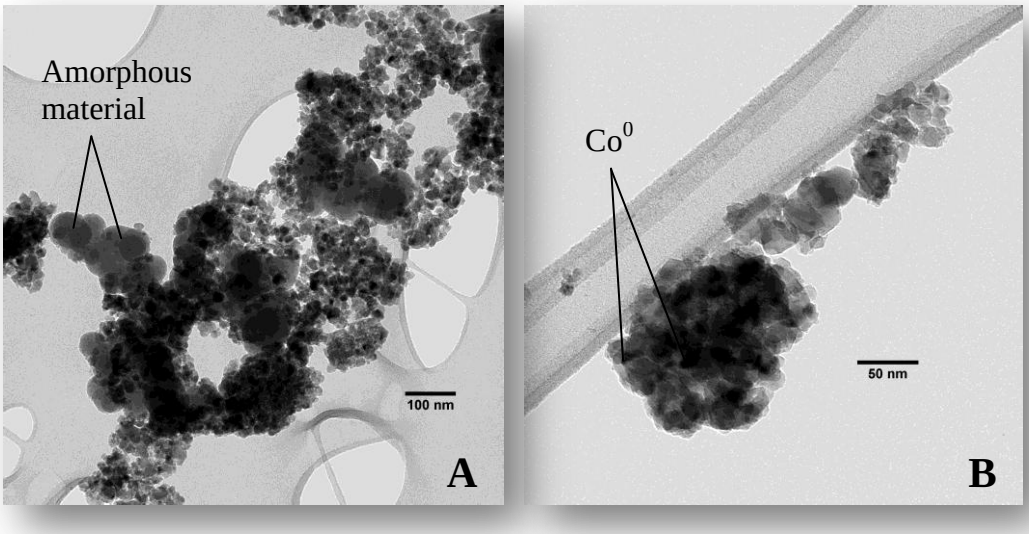

*Figure 3.136. TEM images of the Co/Degussa P25 catalyst after reduction with 100% H_2: **A** – sample representation and **B** – cobalt-support cluster*

3.4.7. Ru/DEGUSSA P25

Preliminary Discussion

The ideal calcination temperature for this catalyst was 570 °C (chapter 3.2.7) and the reduction of the ruthenium oxide catalyst particles occurred at significantly lower temperatures than had been observed for the iron and cobalt catalysts (Fig. 3.137).

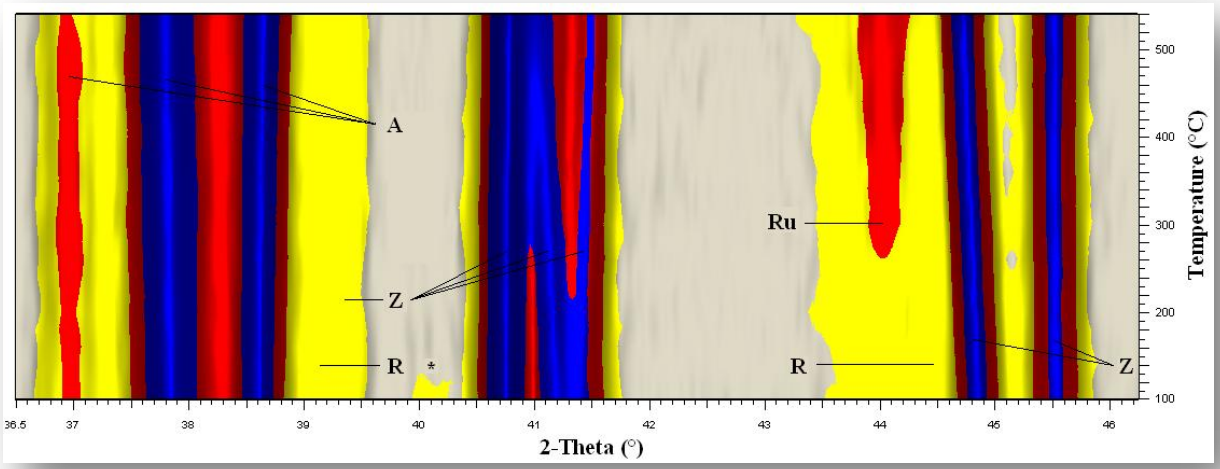

Figure 3.137. Intensity profile of the diffraction patterns collected during the reduction of the Ru/Degussa P25 catalyst: ***A*** *– anatase,* ***R*** *– rutile,* ***Z*** *– baddeleyite,* ******* *– ruthenium oxide and* ***Ru*** *– metallic ruthenium*

Quantitative Analysis

The quantitative results show that the anatase and rutile concentrations remained relatively constant throughout the reduction procedure (Fig. 3.138). There was a small amount of amorphous material present at the start of the reduction procedure, which is attributed to the carbonaceous deposits or coke, generated during the calcination process. Ruthenium oxide was reduced to metallic ruthenium when the temperature exceeded 120 °C with the concurrent formation of a significant amount of amorphous material. The maximum concentration of ruthenium was 0.72 ± 0.1 % at 280 °C, which represents a calculated degree of reduction, using the maximum concentration of RuO_2 observed at 120 °C, of 55 %. The remaining 45 % was incorporated into the amorphous material produced at these temperatures. Once the two reactions were complete, the catalyst remained stable (in terms of concentration) when exposed to increasing temperatures.

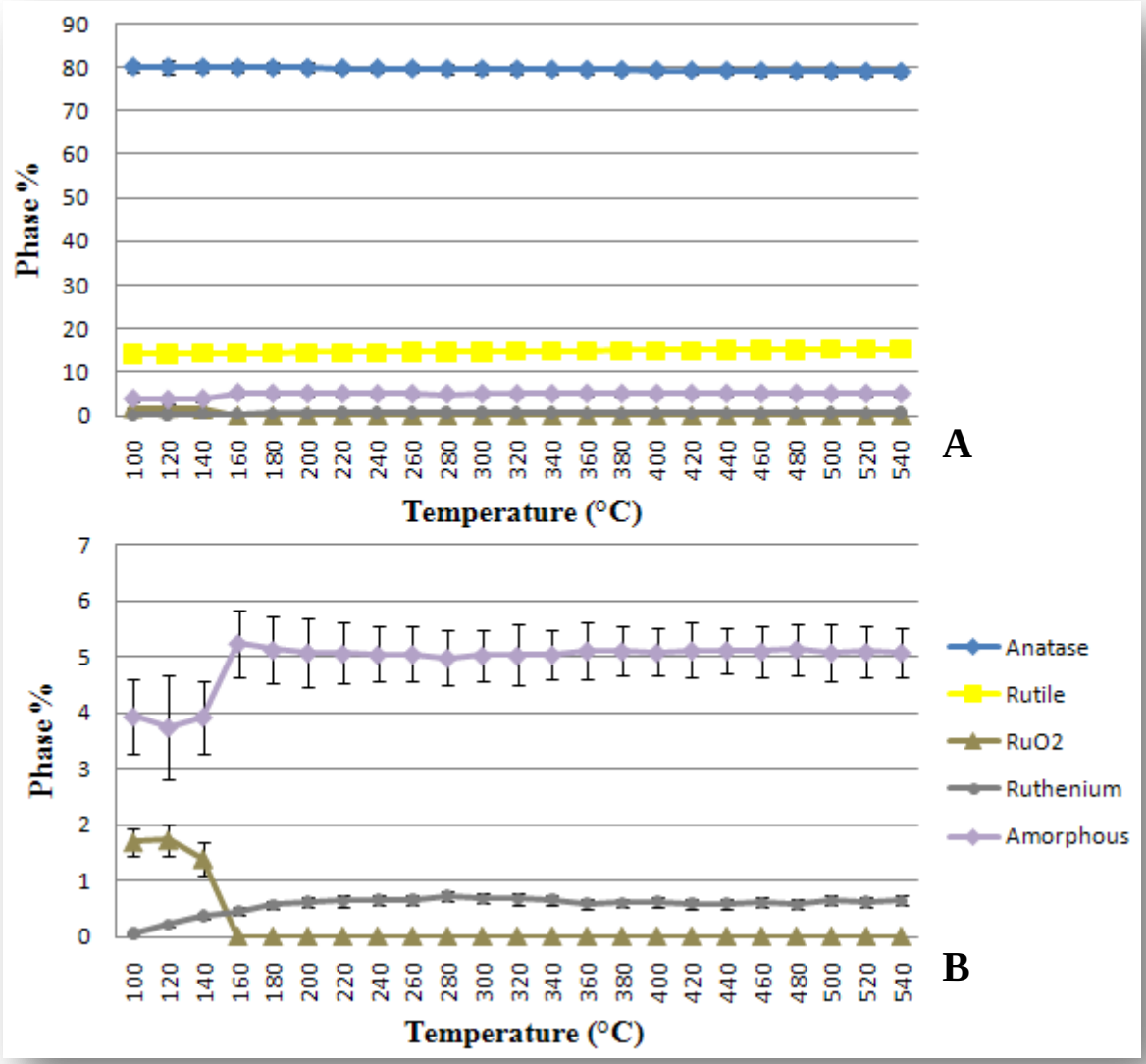

*Figure 3.138. Quantitative phase analysis of the Ru/Degussa P25 catalyst during reduction where **A** – all phases and **B** – minor phases (average GoF of 1.08)*

Particle Size Analysis

Figure 3.139 shows the changes in particle size of the constituent phases during the reduction process. The baddeleyite phase was relatively stable, with the small increase in size attributed to thermal expansion. The average anatase particle size was extremely stable throughout the experiment, while the average rutile particles appeared to increase slightly as the experiment progressed. When RuO_2 was reduced to metallic ruthenium, at temperatures above 120 °C, the average particle size of the ruthenium particles formed was 15 ± 3 nm, which decreased as the reduction process continued, reaching a minimum value of 8 ± 1 nm at 200 °C. This decrease suggests that larger ruthenium oxide particles were reduced first, while smaller particles required higher temperatures. The ruthenium particles increased in size marginally at temperatures above 200 °C, due to sintering.

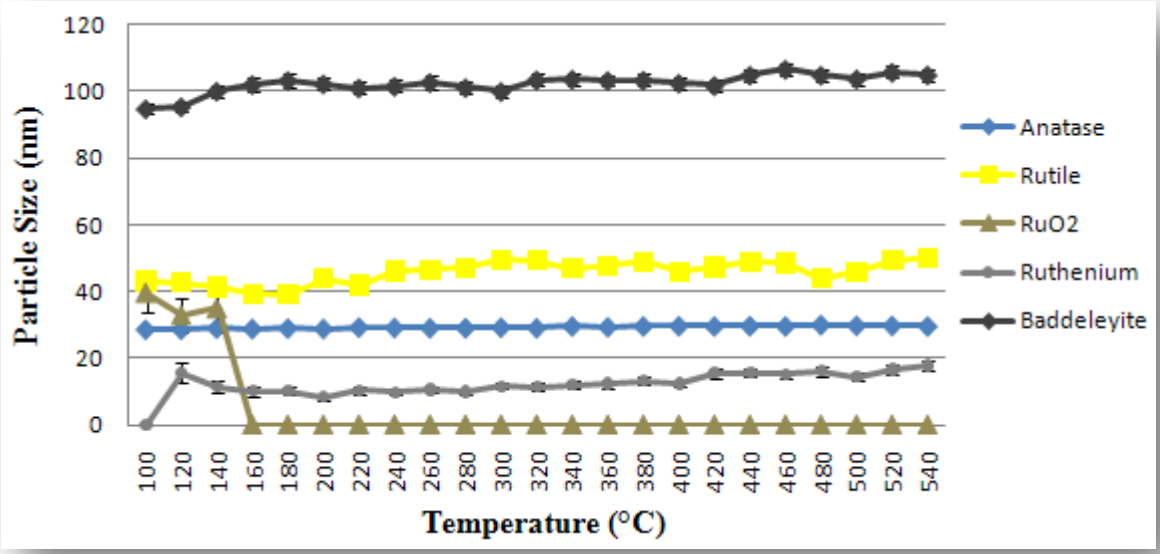

Figure 3.139. Particle size changes of the constituent phases present during the reduction of the Ru/Degussa P25 catalyst

The similarity between the particle sizes of anatase, rutile and the metallic ruthenium made it difficult to distinguish the phases in the TEM images (Fig. 3.140**A**). Metallic ruthenium has a much higher elemental mass and density, which makes it less transparent to electrons and it will appear as darker particles in the TEM images. Figure 3.140**B** shows the presence of dark spots on the surface of anatase particles. The spots are smaller than the ruthenium particle size determined by diffraction and could represent the amorphous material generated by the interaction between the ruthenium species and the support.

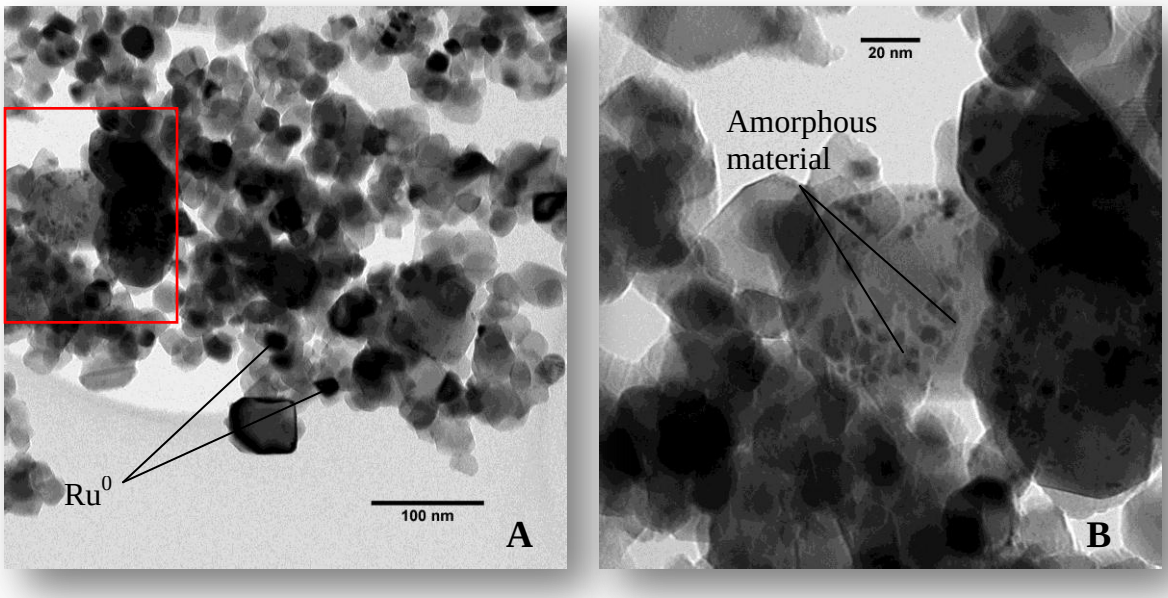

*Figure 3.140. TEM images of the Ru/Degussa P25 catalyst after reduction using 100 % H_2: **A** – sample representation and **B** – magnified view of the region outlined in red*

3.4.8. Ru/SIGMA ANATASE

Preliminary Discussion

The ideal calcination temperature for the Ru/Sigma catalyst was found to be 450 °C (chapter 3.2.8), which led to the formation of small RuO_2 particles with average sizes of approximately 20 nm. TEM confirmed that the RuO_2 oxide particles were supported on the surfaces of anatase particles with a relatively good degree of dispersion. The reduction of the catalyst followed a similar process to that of the Ru/Degussa P25 catalyst, where RuO_2 was reduced at extremely low temperatures to yield a very small amount of metallic ruthenium in the sample (Fig. 3.141). Figure 3.141 also shows the presence of sodium chloride (NaCl) at the start of the reduction process, which eventually disappears at elevated temperatures. NaCl crystallizes in a face-centered cubic (FCC) $Fm\bar{3}m$ space group (Fig. 3.142).[75] The slope of the NaCl (0 0 2) peak with increasing temperature is due to its significantly higher thermal expansion coefficient, when compared with the other phases.

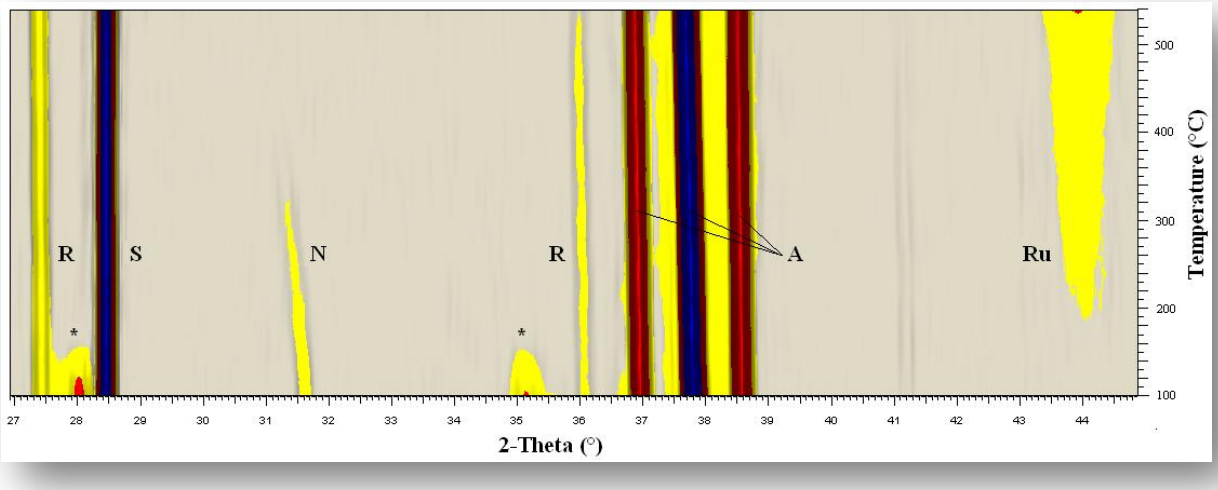

*Figure 3.141. Intensity profile of the diffraction patterns collected during the reduction of the Ru/Sigma catalyst using 100 % H_2: **A** – anatase, **R** – rutile, **S** – silicon, **N** – sodium chloride, ***** - ruthenium oxide and **Ru** – metallic ruthenium*

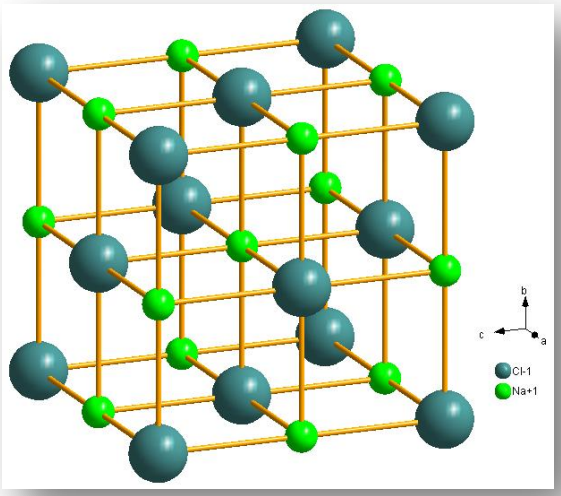

Figure 3.142. Crystallographic representation of sodium chloride (FCC $Fm\bar{3}m$)[75]

Quantitative Analysis

The quantitative analysis of this sample, given in figure 3.143, revealed that RuO_2 was reduced to metallic ruthenium at temperatures above 140 °C. This reduction step coincided with a decrease in the anatase concentration and the appearance of an amorphous phase. The amorphous phase decreased in concentration after its initial formation to a minimum at 280 °C. Calculations indicated that 57 % of the RuO_2 available at the start of the reduction process was consumed to form the amorphous material along with a small percentage of anatase. The NaCl concentration decreased to zero as the temperature approached 380 °C but yielded no crystalline product phase. The disappearance of NaCl in the system was surprising, since the melting and boiling points are 801 °C and 1413 °C respectively. The only possible explanation for this observation is that ruthenium catalyses the degradation of NaCl to form amorphous material, since the 0 0 2 peak is absent in the pattern collected at 100 °C after completion of the reduction experiment. Our data suggests that much of the amorphous material formed at temperatures above 280 °C was due to NaCl and not necessarily the interaction between Ru or RuO_2 and the support. This amorphous material is relatively dynamic in that metallic ruthenium is continually liberated from it at temperatures above 420 °C. The metallic ruthenium concentration reached a maximum value of 0.80 ± 0.02 % at 540 °C, with a calculated degree of reduction of 51 %.

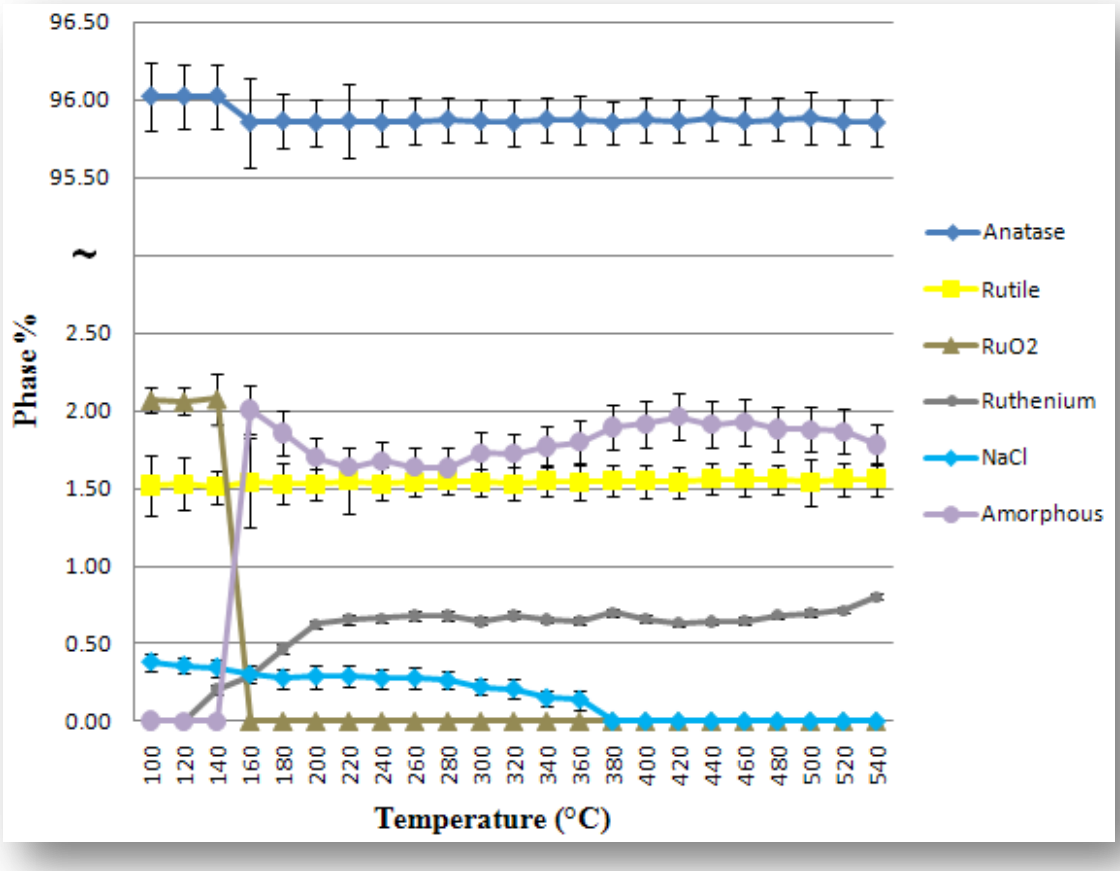

Figure 3.143. Quantitative phase analysis of the Ru/Sigma catalyst during reduction (average GoF of 1.24)

Particle Size Analysis

Figure 3.144 shows that the average anatase particle size increased gradually throughout the experiment. This increase was due to thermal expansion. The reduction process led to the formation of metallic ruthenium particles with an initial average size of approximately 6 nm. The average particle size decreased, once again, with increasing temperature, suggesting that larger ruthenium oxide particles were reduced initially, followed by smaller particles, decreasing the average particle size. The minimum particle size attained during the reduction process was 5.2 ± 0.3 nm at 220 °C, which coincides with a concentration plateau (Fig. 3.143). The ruthenium particles increased in size fairly consistently when the temperature exceeded 220 °C and reached a maximum size of 13.3 ± 0.5 nm at 540 °C, coinciding with the maximum ruthenium concentration.

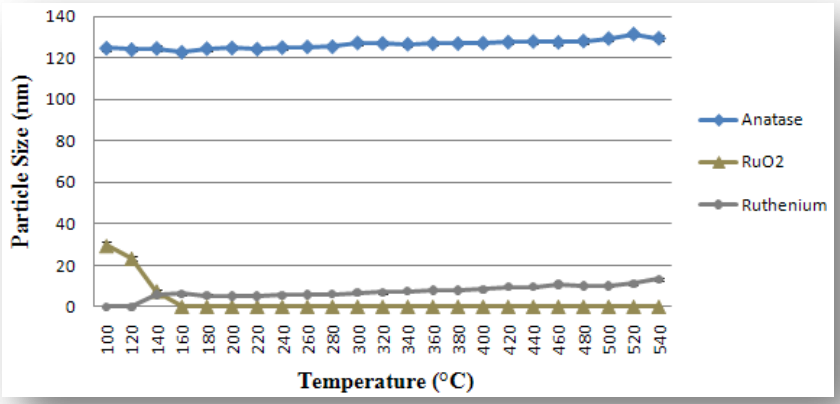

Figure 3.144. Particle size changes of anatase, ruthenium oxide and metallic ruthenium during the reduction of the Ru/Sigma catalyst

The TEM images in figure 3.145 show that there were a small number of unevenly distributed ruthenium particles on the surface of the support. This could be due to the small concentration of metallic ruthenium in the sample at the end of the reduction process.

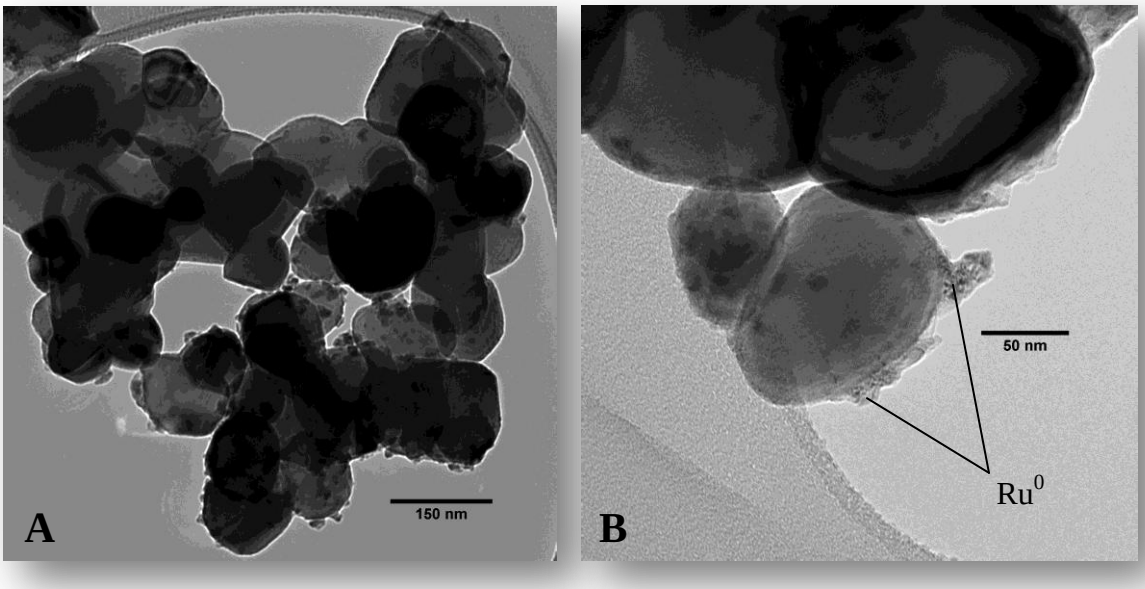

Figure 3.145. TEM images of the Ru/Sigma catalyst after reduction: ***A*** *– sample representation and* ***B*** *– ruthenium particles supported on an anatase particle*

3.4.9. Ru/NSA

Preliminary Discussion

The intensity profile of the diffraction patterns collected during the reduction of the Ru/NSA catalyst is given as figure 3.146. The most notable feature in this dataset is the formation of a significant amount of rutile at temperatures just below 200 °C and the consumption of the rutile as the temperature was increased. This is the lowest temperature at which this phase transition has been observed at atmospheric pressure. This data also shows that rutile can be consumed during reduction.

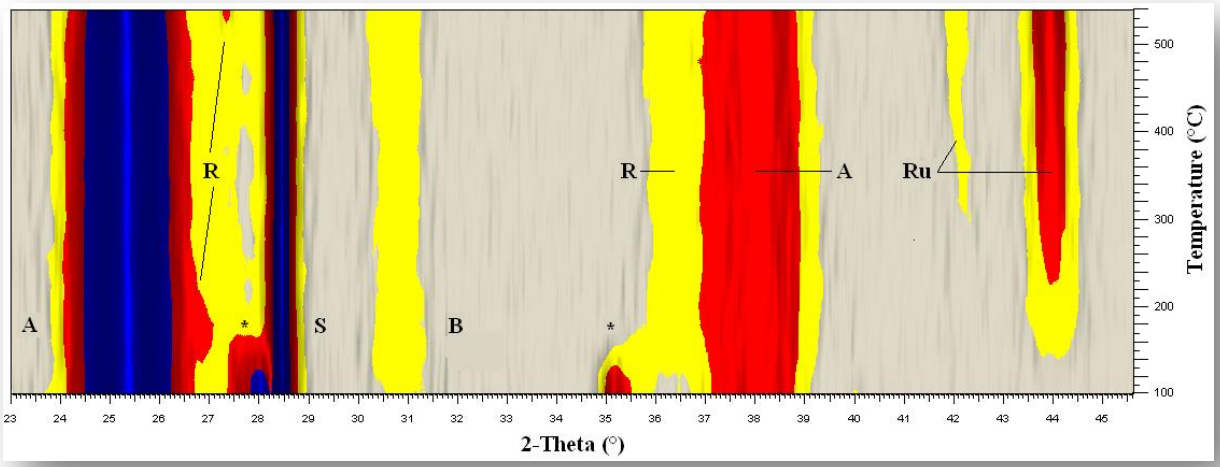

Figure 3.146. Intensity profile of the diffraction patterns collected during the reduction of the Ru/NSA catalyst: ***A*** *– anatase,* ***R*** *– rutile,* ***B*** *– brookite,* ***S*** *– silicon,* ******* *- ruthenium oxide and* ***Ru*** *– metallic ruthenium*

Quantitative Analysis

The quantitative curves (Fig. 3.147**A**) show that the anatase, brookite and silicon concentrations remained relatively stable throughout the reduction process. Correction of this data proved impossible, since there were multiple, competing phase changes occurring throughout the experiment, the most important of which was the formation of rutile as discussed earlier. Figure 3.147**B** confirms the formation of rutile at temperatures above 180 °C and it is clear that, with increasing temperature, the concentration of rutile decreased. The RuO_2 concentration decreases to zero between the temperatures of 100 °C and 200 °C. The formation of rutile coincided with the most significant decrease in the RuO_2 concentration, which may suggest that the formation of rutile in this system is somehow catalyzed by either the presence of ruthenium oxide or metallic ruthenium. Metallic ruthenium is present in the pattern collected at 120 °C, which indicates a much lower reduction temperature than observed for the Ru/Degussa P25 and the Ru/Sigma catalysts. Ruthenium reached a maximum concentration of 0.94 ± 0.02 % at 540 °C, representing a calculated degree of reduction of only 27 %. The low degree of reduction suggests that much of the ruthenium was lost to amorphous species formed in similar ways to those discussed previously.

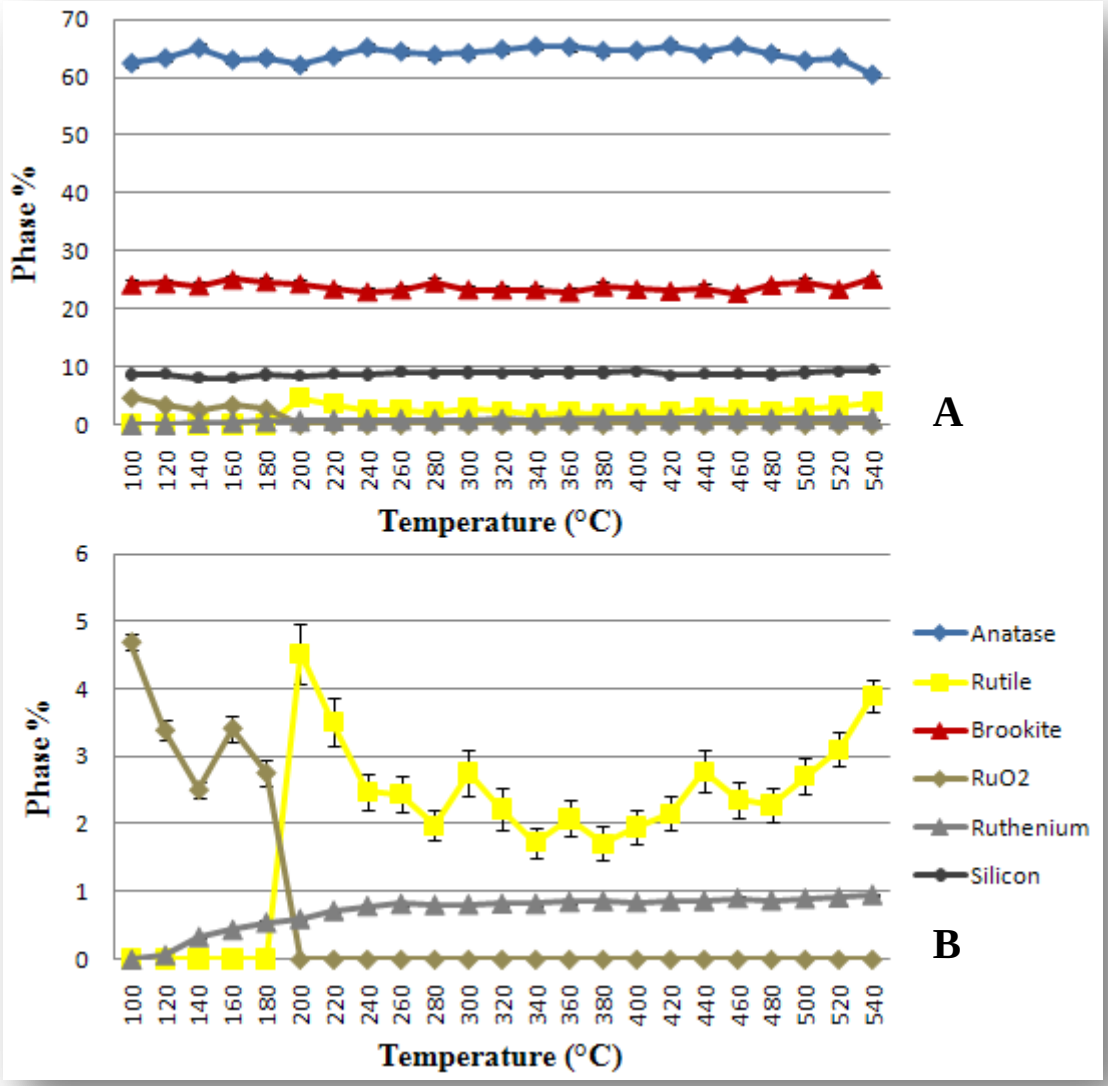

*Figure 3.147. Quantitative phase analysis of the Ru/NSA catalyst during reduction where **A** – all phases and **B** – minor phases (average GoF of 1.19)*

Particle Size Analysis

The average anatase and brookite particle size remained relatively constant throughout the reduction process (Fig. 3.148**A**). The ruthenium oxide particle size decreased as soon as the experiment was started to yield metallic ruthenium particles with an initial size of 22 ± 7 nm, which decreased to a minimum value of 8.7 ± 0.4 nm at 220 °C (Fig. 3.148**B**). The ruthenium particle size increased slowly at higher temperatures but never exceeded 16 nm. The average rutile particle size appeared to oscillate in the 15 – 20 nm region and the relatively large error bars suggest that there was a large degree of uncertainty associated with these values but it probably safe to assume that the real value lies somewhere between the two extremes.

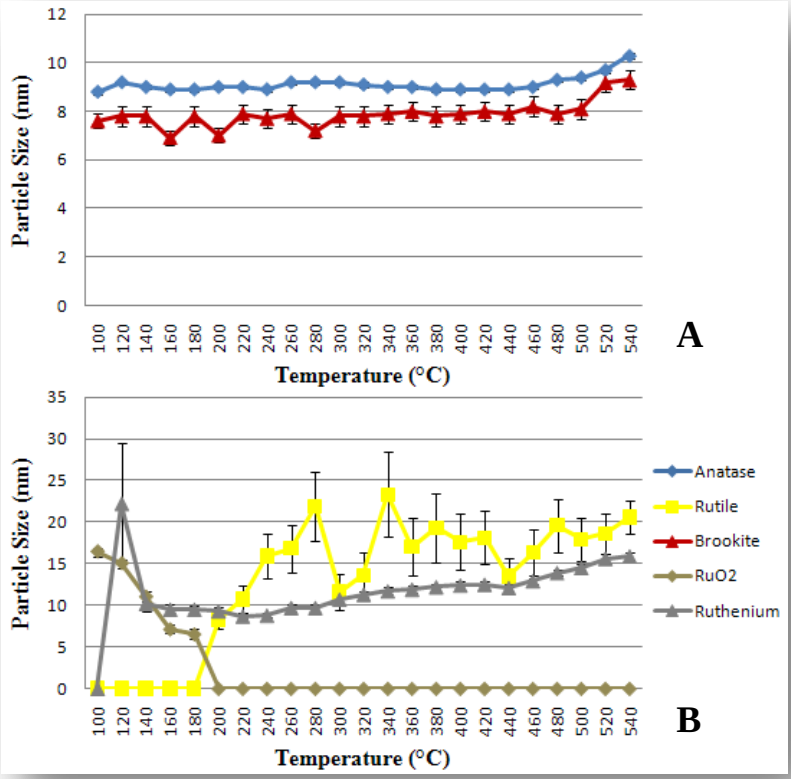

Figure 3.148. Particle size changes of the constituent phases present during the reduction of the Ru/NSA catalyst: ***A*** *– support phases and* ***B*** *– minor and product phases*

The TEM images, given in figure 3.149, show the presence of an amorphous species, which was present in a significant concentration. The similarity of the anatase, brookite, rutile and ruthenium particle sizes results in the phases being indistinguishable from one another. The only phase that could be resolved was the silicon spike phase. Following on from the trends observed above, it is likely that the ruthenium particles were bound to support phases but, because of the similarity in particle size, the distribution of the ruthenium was extremely low.

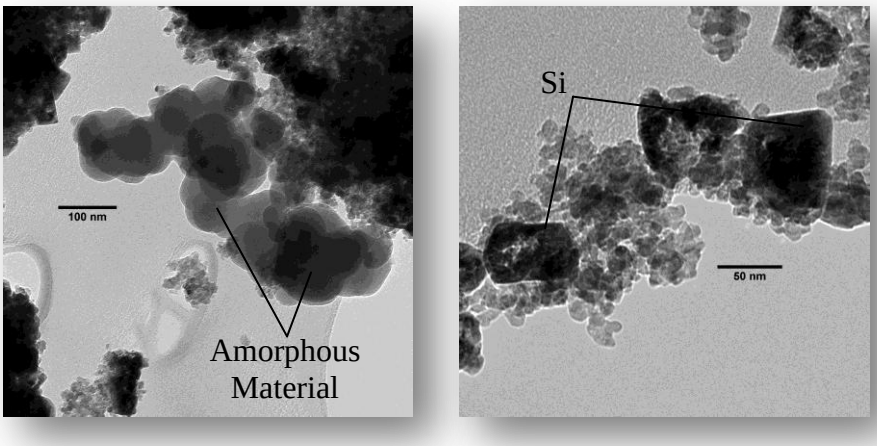

Figure 3.149. TEM images of the Ru/NSA catalyst after reduction with 100% H_2: ***A*** *– amorphous phase and* ***B*** *– magnified view of the reduced sample highlighting the silicon spike phase*

3.5. SUMMARY

In the discussion above, we were able to show that the concentration of H_2 in the reducing gas mixture affected the reduction pathway of titania-supported iron catalysts. Reduction using low hydrogen concentrations led to the formation of ilmenite ($FeTiO_3$), where Fe^{3+} in hematite (Fe_2O_3) was reduced to Fe^{2+} during a reaction with both anatase and rutile phases. A hydrogen concentration of 10 % resulted in the formation of both ilmenite and iron reduction products, namely magnetite (Fe_3O_4) and metallic iron (Fe^0). H_2 concentrations above 10% resulted in natural reduction products only.

Data analysis led to the discovery of amorphous materials that were generated during the reduction of the supported metal oxides (Fig. 3.150). Although there has been speculation regarding the formation of metal-support materials, especially for titania-supported cobalt catalysts,[73-74] quantification of these amorphous phases or determination of when they form has not been discussed previously. We have been able to quantify the amorphous materials in many instances and have found that they usually form during the second stage of reduction, i.e. magnetite → metallic iron and cobalt(II) oxide → metallic cobalt. The formation of the amorphous materials decreased the reducibility of the catalysts drastically for cobalt and ruthenium catalysts, while the iron catalysts were less affected.

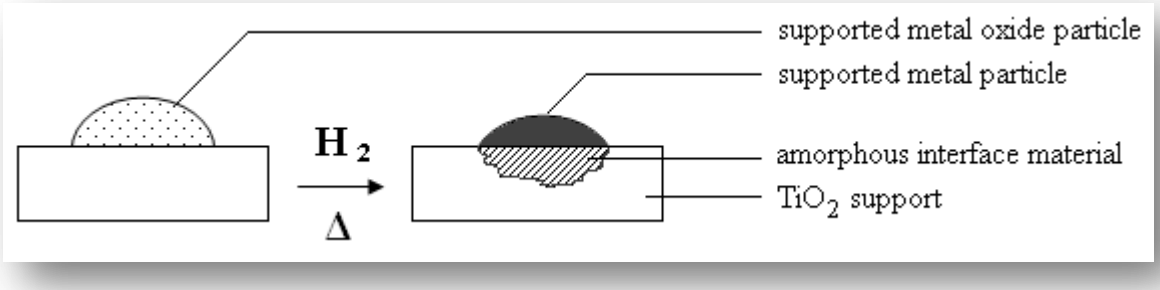

Figure 3.150. Formation of the amorphous interfacial material between metal particles and TiO_2 supports during reduction

Table 3.8 summarizes the reduction data and was compiled to permit comparisons between the catalysts and supports. The iron catalysts all followed very similar reduction patterns. However, the Fe/NSA catalyst suffered a dramatic decrease in its degree of reduction, losing 60 % of its iron to the amorphous component. The Co/Degussa P25 and Co/Sigma catalysts were reduced at very similar temperatures but 71 % of the cobalt in the Co/Sigma catalyst was lost during the formation of the interfacial amorphous material, while only 20 % was lost during the reduction of the Co/Degussa P25 catalyst. The Co/NSA catalyst required much higher temperatures to initiate reduction and 82 % of the cobalt content was incorporated into the amorphous material. The ruthenium catalysts were reduced at significantly lower temperatures than the iron and cobalt catalysts but also suffered from severe loss of ruthenium concentration to the amorphous component. The Ru/Sigma and Ru/NSA catalysts could be reduced at high temperatures, with little effect on the average particle size, to increase the ruthenium concentration in the sample.

Table 3.8. Summary of the reduction data in terms of the temperature at which the first and second reduction steps occurred, the degree of reduction achieved, the smallest M^0 particle size that could be achieved and the ideal reduction temperature, taking into account maximum concentration and particle size (N/O – not observed)

	CATALYSTS								
	Fe/Degussa	Fe/Sigma	Fe/NSA	Co/Degussa	Co/Sigma	Co/NSA	Ru/Degussa	Ru/Sigma	Ru/NSA
First Reduction (°C)	T>260	T>260	N/O	T>180	T>180	T>260	T>100	T>140	T>100
Second Reduction (°C)	T>320	T>300	T>320	T>260	T>260	T>304			
Degree of Reduction (%)	104	84	40	80	29	18	55	51	27
Minimum Metal Particle Size (nm)	37	28	25	14	20	20	8.5	5.2	8.7
Ideal Reduction temperature (°C)	329	301	323	280	224	305	280	540	540

3.6. REFERENCES

1. A. Rubio-Ponce, A. Conde-Gallardo and D. Olguin, *Phys. Rev.*, **B78**, 035107-1 (1978).
2. V. I. Khitrova, M. F. Bandule and Z. G. Pinsker, *Kristallografiya*, **22**, 714 (1977).
3. A. Suzuki and Y. Kotera, *Bull. Chem. Soc. Jpn.*, **35**, 1353 (1962).
4. R. D. Shannon and J. A. Pask, *J. Am. Ceram. Soc.*, **48**, 391 (1965).
5. E. F. Heald and C. W. Weiss, *Am. Mineral.*, **57**, 10 (1972).
6. K. J. D. MacKenzie, *Trans. J. Br. Ceram. Soc.*, **74**, 77 (1975).
7. S. Hishita, I. Mutoh, K. Koumoto, H. Yanagida, *Ceram. Int.*, **9**, 41 (1983).
8. J. F. Banfield, B. L. Bischoff and M. A. Anderson, *Chem. Geol.*, **110**, 211 (1993).
9. A. A. Gribb and J. F. Banfield, *Am. Mineral.*, **82**, 717 (1997).
10. H. Zhang and J. F. Banfield, *Phase Transformations and Systems Driven Far From Equilibrium*, Materials Research Society, Pennsylvania (1998), p619-624.
11. H. Zhang and J. F. Banfield, *J. Mater. Sci.*, **8**, 2073 (1998).
12. X. Z. Ding, X. H. Liu and Y. Z. He, *J. Mater. Sci. Lett.*, **15**, 1789 (1996).
13. S. C. Liao, K. D. Pae and W. E. Mayo, *Nanostruct. Mater.*, **5**, 319 (1995).
14. X. Z. Ding, L. Liu, X. M. Ma, Z. Z. Qi and Y. Z. He, *J. Mater. Sci. Lett.*, **13**, 462 (1994).
15. Q. Xu, J. Zhang, Z. Feng, Y. Ma, X. Wang and C. Li, *Chem. Asian J.*, **5**, 2158 (2010).
16. W. T. Pennington, *J. Appl. Cryst.*, **32**, 1028 (1999).
17. C. Buchsbaum and M. U. Schmidt, *Acta Crystallogr.*, **B63**, 926 (2007).
18. K. Kim, H. Park, J. Ahn, J. Lee and J. Park, *Mater. Sci. Forum*, **534-536**, 65 (2007).
19. M. R. Ranade, A. Navrotsky, H. Z. Zhang, J. F. Banfield, S.H. Elder, A. Zaban, P. H. Borse, S. K. Kulkarni, G. S. Doran and H. J. Whitfield, *PNAS*, **99**, 6476 (2002).
20. N. Shaw and Y. Liu, *Acta Phys. Sinica*, **20**, 699 (1964).
21. B. N. Dutta, *Phys. Status Solidi B*, **2**, 984 (1962).
22. L. Maissel, *J. Appl. Phys.*, **31**, 211 (1960).
23. W. M. Yim and R. J. Paff, *J. Appl. Phys.*, **45**, 1456 (1974).
24. V. V. Zhdanova, M. G. Kekua and T. Z. Samadashvili, *Inorg. Mater. (USSR)*, **3**, 1112 (1967).
25. J. P. Dismukes, L. Ekstrom and R. J. Paff, *J. Phys. Chem.*, **6**, 3021 (1964).
26. R. O. A. Hall, *Acta Crystallogr.*, **14**, 1004 (1961).
27. G. I. Dolivo-Dobrovol'skaya, V. V. Zhdanova and V. P. Sergeev, *Sov. Phys. Solid State*, **15**, 933 (1973).
28. H. Ibach, *Phys. Status Solidi B*, **31**, 625 (1969).
29. R. B. Roberts, *J. Phys. D*, **14**, L163 (1981).
30. Y. Okada and Y. Tokumaru, *J.Appl. Phys.*, **56**, 314 (1984).
31. M. E. Straumanis and E. K. Aka, *J.Appl. Phys.*, **23**, 330 (1952).
32. M. Sljukic, B. Matkovic, B. Prodic and D. Anderson, *Powder Diffr.*, **2**, 41 (1987).
33. Makor^{TM} specification sheet, Corning Inc. New York.
34. S. Sivakumar, P. K. Pillai, P. Mukundan and K. G. K. Warrier, *Mater. Lett.*, **57**, 330 (2002).

35. E. P. Meagher and G. A. Lager, *Can. Mineral.*, **17**, 77 (1979).
36. Y. Hu, H. Tsai and C. Huang, *J. Eur. Ceram. Soc.*, **23**, 691 (2003).
37. M. E. Dry, *J. Chem. Technol. Biotechnol.* **77**, 43 (2001).
38. A. N. Pour, M. R. Housaindonkht, S. F. Tayyari and J. Zarkesh, *J. Nat. Gas Chem.*, **19**, 107 (2010).
39. L. A. Cano, M. V. Cagnoli, N. A. Fellenz, J. F. Bengoa, N. G. Gallegos, A. M. Alvarez and S. G. Marchetti, *Appl. Catal. A*, **379**, 105 (2010).
40. E. N. Maslen, V. A. Strel'tsov, N. R. Strel'tsova and N. Ishizawa, *Acta Crystallogr.*, **B50**, 435 (1994).
41. I. E. Grey, C. Li and T. Ness, *J. Solid State Chem.*, **141**, 221 (1998).
42. F. C. Gennari, J. J. Andrade Gamboa and D. M. Pasquevich, *J. Mater. Sci.*, **33**, 1563 (1998).
43. Y. Zhang, Y. Liu, G. Yang, S. Sun and N. Tsubaki, *Appl. Catal. A*, **321**, 79 (2007).
44. I. Puskas, T. H. Fleisch, J. A. Kaduk, C. L. Marshall, B. L. Meyers, M. J. Castagnola and J. E. Indacochea, *Appl. Catal. A*, **316**, 197 (2007).
45. S. Song, S. Lee, J. Bae, P. S. Sai Prasad, K. Jun and Y. Shul, *Catal. Lett.*, **129**, 233 (2009).
46. I. Puskas, T. H. Fleisch, P. R. Full, J. A. Kaduk, C. L. Marshall and B. L. Meyers, *Appl. Catal. A*, **311**, 146 (2006).
47. A. M. Saib, A. Borgna, J. van de Loosdrecht, P. J. van Berge and j. W. Niemantsverdriet, *J. Phys Chem. B*, **110**, 8657 (2006).
48. J. Li and N. J. Coville, *S.Afr. J. Chem.*, **57**, 49 (2004).
49. J. Li and N. J. Coville, *S.Afr. J. Chem.*, **56**, 1 (2003).
50. T. Petsi, G. D. Panagiotou, C. S. Garoufalis, C. Kordulis, P. Stathi, Y. Deligiannakis, A. Lycourghiotis and K. Bourikas, *Chem. Eur. J.*, **15**, 13090 (2009).
51. S. Rane, O. Borg, J. Yang, E. Rytter and A. Holmen, *Appl. Catal. A*, **388**, 160 (2010).
52. J. Yang, E. Z. Tveten, D. Chen and A. Holmen, *LANGMUIR*, **26**, 16558 (2010).
53. S. S. Lin, D. H. Kim, M. H. Engelhard and S. Y. Ha, *J. Catal.*, **273**, 229 (2010).
54. H. X. Zhao and H. L. Lu, *React. Kinet. Catal. Lett.*, **97**, 289 (2009).
55. R. J. Hill and L. M. D. Cranswick, *J. Appl. Cryst.*, **27**, 802 (1994).
56. W. L. Smith and A. D. Hobson, *Acta Crystallogr.*, **B29**, 362 (1973).
57. K. Kidoh, K. Tanaka, F. Marumo and H. Takei, *Acta Crystallogr.*, **B40**, 92 (1984).
58. B. Ribar, N. Milinski, R. Herak, I. Krstanovic and S. Djuric, *Z. Kristallogr.*, **144**, 133 (1976).
59. P. Legzdins, R. W. Mitchell, G. L. Rempel, J. D. Ruddick and G. Wilkinson, *J. Chem. Soc. A*, **19**, 3322 (1970).
60. J. Haines, J. M. Leger, O. Schulte and S. Hull, *Acta Crystallogr.*, **B53**, 880 (1997).
61. S. Andersson and A. D. Wadsley, *Acta Crystallogr.*, **15**, 194 (1962).
62. E. Zintl and H. H. von Baumbach, *Z. Anorg. Allg. Chem.*, **198**, 88 (1931).
63. E. Zintl, *Z. Elektrochem. Angew. Phys. Chem.*, **40**, 558 (1934).
64. P. Cherin, W. C. Hamilton and B. Post, *Acta Crystallogr.*, **23**, 455 (1967).
65. T. Demuth, Y. Jeanvoine, J. Hafner and J. G. Angyan, *J. Phys. Condens. Matter*, **11**, 3833 (1999).
66. M. M. Murshed and T. M. Gesing, *Z. Kristallogr.*, **222**, 341 (2007).

67. T. Yamanaka, *J. Synchrotron Radiat.*, **12**, 566 (2005).
68. W. O'Reilly, *Acta Crystallogr.*, **B24**, 422 (1968).
69. D. R. Wilburn and W. A. Bassett, *Am. Mineral.*, **63**, 591 (1978).
70. R. W. G. Wyckoff and E. D. Crittenden, *Z. Kristallogr.*, **63**, 144 (1926).
71. N. G. Schmahl and G. F. Eikerling, *Z. Phys. Chem.*, 62, 268 (1968).
72. F. Vincent and M. Figlarz, *C. R. Hebd. Seances Acad. Sci.*, **264**, 1270 (1967).
73. B. Jongsomjit, C. Sakdamnuson, J. G. Goodwin Jr, and P. Praserthdam, *Catal. Lett.*, **94**, 209 (2004).
74. K. Suriye, P. Praserthdam and B. Jongsomjit, *Catal. Commun.*, **8**, 1772 (2007).
75. H. E. Swanson, R. K. Fuyat, *J. Res. Nat. Bur. Stand.*, **539**, 41 (1953).

CHAPTER 4 – GENERAL CONCLUSIONS

The main aim of this study was to develop *in situ* PXRD methods to monitor the properties of catalysts during heat treatment (calcination) and activation (reduction). The TiO_2-supported FT catalysts, used in this study, highlighted the importance of internal standard (spike) addition, which allows for the determination of the exact, rather than relative, concentrations of the crystalline phases during Rietveld refinement procedures. The addition of a spike phase also allows for the calculation of amorphous and/or unidentified minor crystalline phases.

The difficulty with laboratory-based investigations of this kind is the time required to collect diffraction data of sufficient quality that can be used in a Rietveld refinement. Ideally, a wide angle diffraction pattern, with good intensity and resolution, should be collected in as short a time as possible to improve the time resolution and accuracy of the experiment. Although the time resolution of the experiments performed in this study was relatively poor, we were able to show that studies of this kind can provide insight into the properties of a catalyst during pretreatment procedures.

In Chapter 3.1 the effect of heat treatment on the three TiO_2 support materials was evaluated. Refinement of the powder patterns, collected during heat treatment, allowed us to monitor the solid-state phase changes that occurred in the three supports, estimate the rates of these transformations and monitor particle size changes that occurred with increasing temperature. Mathematical correction procedures were developed to eliminate the effects of sample holder contribution that arose due to sample penetration. The order of thermal stability of the three supports, in terms of anatase to rutile transition temperature, was; Sigma anatase > NSA > Degussa P25. The growth of anatase particles, due to particle bridging before transition to rutile, was confirmed and a decrease in anatase particle size was observed once the transition had been initiated.

In Chapter 3.2 the effects of excessive heat treatment of the catalyst samples was investigated. The *in situ* heat treatment experiments provided a means to determine the ideal calcination temperature for each catalyst in terms of maximum concentration and particle size. By adding an internal standard to each sample, the refinements yielded insight into the conversion of amorphous metal precursors to crystalline metal oxides. The addition of metal oxides resulted in the shift of the anatase-rutile transition temperature to varying degrees in the different supports and also resulted in the formation of metal titanates at high temperatures. By considering the rates of change of concentration of the various phases in the sample at each temperature interval, we were able to determine if the formation of a particular metal titanate occurred via a metal oxide reaction with anatase or rutile or both phases. The excessive heat treatment experiments demonstrate what happens to the catalysts in a calcination reactor containing hot spots (regions of elevated temperature due to thermal gradients).

In Chapter 3.4 *in situ* reduction experiments were performed on the catalysts, to monitor the phase changes that occurred during catalyst activation. We were able to show that the reduction profile of a Degussa P25-supported Fe catalyst changed according to the concentration of H_2 in H_2/N_2 reducing gas mixtures, which could have far-reaching consequences for traditional reduction procedures based on TPR measurements. The formation of reduction products was monitored as a function of temperature in order to determine the ideal reduction procedure that would yield the maximum possible concentration of the active metal species with particle sizes in the range known to be active for FT synthesis. We found that particle size control was difficult for the supported Fe catalysts but less difficult for the Co and Ru catalysts. Spike addition and Rietveld refinement made it possible to monitor the formation of amorphous interfacial species that appear to be produced during reduction of the metal oxides, especially during the reduction of magnetite (Fe_3O_4) to Fe^0 and CoO to Co^0. The formation of this amorphous material severely decreases the amount of metal formed on the surface of the support, as witnessed by the low degrees of reduction observed for the majority of the catalysts. The formation and detection of these amorphous species provides a good platform for an application for synchrotron beam time in order to collect diffraction data for pair distribution function (PDF) analysis, which would yield short-range structural information about the amorphous material.

Besides the PDF investigation mentioned above, future investigations could include *in situ* FT experiments on the optimized catalysts with a comparison to similar catalysts prepared via traditional methods. This work would benefit from the installation of the GC system on the exit side of the XRK, which has been completed recently. Definitive determination of the phase transition kinetics could be achieved if the time resolution of the diffractometer was improved. This could be accomplished by installing an X-ray mirror, to increase flux on the sample, and a monochromator, which would limit peak broadening when using the VÅntec detector in "snap-shot" mode to collect an angular region of interest in a very short time. This would allow collection of diffraction patterns, with an angular range of up to 12 ° 2-theta, without having to stabilize the cell at specific temperature intervals. The exact temperature of the sample at every collection could be determined using the lattice parameter of the spike, as was shown in Chapter 3.1.1 and figure 3.18.

Although the catalyst systems used in this study are unlikely to find application in FT processes, they have served to develop *in situ* PXRD pretreatment procedures that combine quantitative and particle size analysis in a single experiment. This information can be used to optimize catalyst pretreatment procedures in order to produce better, and more consistent, catalysts.

APPENDIX A – LIST OF ITEMS ON ACCOMPANYING DISC

Diffraction Data	Supports	Degussa P25	Heat Treatment	Degussa P25 Heat Treatment.raw
				Degussa P25 Heat Treatment.pro
		Sigma Anatase	Heat Treatment	Sigma Anatase Heat Treatment.raw
				Sigma Anatase Heat Treatment.pro
		NSA	Heat Treatment	NSA Heat Treatment.raw
				NSA Heat Treatment.pro
	Catalysts	Fe/Degussa P25	Heat Treatment	Fe/Degussa P25 Heat Treatment.raw
				Fe/Degussa P25 Heat Treatment.pro
			Reduction	Fe/Degussa P25 Incorrectly Calcined 5%H2.raw
				Fe/Degussa P25 Incorrectly Calcined 5%H2.pro
				Fe/Degussa P25 Incorrectly Calcined 10%H2.raw
				Fe/Degussa P25 Incorrectly Calcined 10%H2.pro
				Fe/Degussa P25 Incorrectly Calcined 100%H2.raw
				Fe/Degussa P25 Incorrectly Calcined 100%H2.pro
				Fe/Degussa P25 Correctly Calcined 100%H2.raw
				Fe/Degussa P25 Correctly Calcined 100%H2.pro
				Fe/Degussa P25 Correctly Calcined 100%H2 Search.raw
		Fe/Sigma Anatase	Heat Treatment	Fe/Sigma Anatase Heat Treatment.raw
				Fe/Sigma Anatase Heat Treatment.pro
			Reduction	Fe/Sigma Anatase Reduction 100%H2.raw
				Fe/Sigma Anatase Reduction 100%H2.pro
				Fe/Sigma Anatase Reduction at Constant Temperature.raw
				Fe/Sigma Anatase Reduction at Constant Temperature.pro
		Fe/NSA	Heat Treatment	Fe/NSA Heat Treatment.raw
				Fe/NSA Heat Treatment.pro
			Reduction	Fe/NSA Final Reduction 100%H2.raw
				Fe/NSA Final Reduction 100%H2.pro
		Co/Degussa P25	Heat Treatment	Co/Degussa P25Heat Treatment.raw
				Co/Degussa P25 Heat Treatment.pro
			Reduction	Co/Degussa P25 Reduction.raw
				Co/Degussa P25 Reduction.pro
		Co/Sigma Anatase	Heat Treatment	Co/Sigma Anatase Heat Treatment.raw
				Co/Sigma Anatase Heat Treatment.pro
			Reduction	Co/Degussa P25 Reduction.raw
				Co/Degussa P25 Reduction.pro
		Co/NSA	Heat Treatment	Co/NSA Heat Treatment.raw
				Co/NSA Heat Treatment.pro
			Reduction	Co/NSA Reduction Search.raw
				Co/NSA Reduction Search.pro
		Ru/Degussa P25	Heat Treatment	Ru/Degussa P25 Heat Treatment.raw
				Ru/Degussa P25Heat Treatment.pro
			Reduction	Ru/Degussa P25 Reduction.raw
				Ru/Degussa P25 Reduction.pro
		Ru/Sigma Anatase	Heat Treatment	Ru/Sigma Anatase Heat Treatment.raw
				Ru/Sigma Anatase Heat Treatment.pro
			Reduction	Ru/Sigma Anatase Reduction.raw
				Ru/Sigma Anatase Reduction.pro
		Ru/NSA	Heat Treatment	Ru/NSA Heat Treatment.raw
				Ru/NSA Heat Treatment.pro
			Reduction	Ru/NSA Reduction.raw
				Ru/NSA Reduction.pro